Erosion-Corrosion Characterisation for Pipeline Materials Using Combined Acoustic Emission and Electrochemical Monitoring

by

Jonathan Item Ukpai

Submitted in accordance with the requirements for the degree of

Doctor of Philosophy

The University of Leeds

School of Mechanical Engineering

July 2014

The candidate confirms that the work submitted is his own, except where work which has formed part of jointly authored publications has been included. The contribution of the candidate and the other authors to this work has been explicitly indicated below. The candidate confirms that appropriate credit has been given within the thesis where reference has been made to the work of others.

The publications related to this work are as follows:

1. Ukpai J.I.; Barker R.; Hu X.; Neville A.; Exploring the erosive wear of X65 carbon steel by acoustic emission method. Wear, Volume 301, Issues 1-2, pp. 370-382, 2013.

2. Ukpai J.I.; Barker R.; Hu X.; Neville A.; Determination of particle impacts and impact energy in the erosion of X65 carbon steel using acoustic emission technique. Tribology International Journal, Volume 65, pp. 161-170, 2013.

3. Ukpai J.I.; Barker R.; Hu X.; Neville A.; An *in-situ* investigation of flow-induced corrosion and erosion-corrosion degradation of X65 pipeline materials using combined acoustic emission and electrochemical techniques. CORROSION/2013 paper no. 2305, NACE International Conference, Orlando, FL 2013.

4. Ukpai J.I.; Barker R.; Neville A., A combined electrochemical and acoustic emission technique for mechanistic and quantitative evaluation of erosion-corrosion and its components. CORROSION/2014 paper no. 4180, NACE International Conference, San Antonio, TX, 2014.

All the work in the papers mentioned above is a contribution of the candidate, under the supervision of the co-authors.

Acknowledgements

I want to thank my supervisors, Professor Anne Neville and Dr. Simon Hu for their kind words of advice, encouragement, guidance, exposure and for taking me round the world during conferences and symposia. I also thank my colleagues, Richard Barker and Michael Bryant for answering all my numerous questions. My gratitude goes to our lab technicians Ron Cellier, Graham Jakeman (of blessed memory) and Brian Leach for their assistance in the production of component parts of my research facilities and fixtures, and for constantly replenishing the laboratory consumables, and to Jacqueline Kidd and Fiona Slade for their sincere and warm administrative support.

I am very grateful to all the people who made enormous sacrifices of their time, energy, and resources to make this project possible. I will not be able to name them one by one because of space. Specifically, I thank my wife (Alice) and my kids (David, Jonathan and Michelle) for their love, patience and understanding throughout the period of the PhD study. I promise to compensate you all for the fatherly love and care I denied you during my late night research activities. I also thank my late father, *Omezue* (Chief) Ukpai Item (who did not live to see the end of this project) and Mother, Mrs. Ugo Ukpai for their prayers and parental support.

The staff and management of Petroleum Technology Development Fund (PTDF), Abuja, Nigeria, I cannot thank you enough for paying my tuition fees and maintenance allowance for three years in United Kingdom. All I have to say to you is, please do not relent in your good work, always keep the flag flying. My gratitude also goes to the staff and management of National Board for Technical Education (NBTE), Kaduna, Nigeria for all their support.

Above all, I say a big thank you to God almighty, for His grace, provisions, protection, good health and mercies throughout the period of this research. To Him alone I give all the glory.

Abstract

The prediction and monitoring of erosion and erosion-corrosion attack on oil and gas pipeline materials in service is useful for facilities design, material selection and maintenance planning so as to predict material performance accurately, operate safely, and prevent unplanned production outages. Conventional methods such as failure records, visual inspection, weight-loss coupon analysis, can be time-consuming and can only determine erosion or erosion-corrosion rates when the damage has already occurred.

To improve on this, the acoustic emission (AE) technique combined with electrochemical monitoring was chosen and implemented in this study to investigate and characterize erosion and erosion-corrosion degradation rates of oil and gas pipeline materials (X65) under Submerged Impinging Jet (SIJ) systems in a saturated CO_2 environment. Measured acoustic emission energy was correlated with the mass loss from gravimetric measurement for different flow velocities and sand loadings. Sand particle impacts were quantified and compared with theoretical predictions, and the associated impact energies predicted from Computational Fluid Dynamics (CFD) were correlated with measured acoustic emission energy and mass loss.

The combined acoustic emission and electrochemical monitoring (involving Linear Polarisation Resistance (LPR) and Electrochemical Impedance spectroscopy (EIS)) helped to simultaneously investigate the surface reactivity of the corroding materials as well as capture the sand impacts contribution during the erosion-corrosion degradation processes. Results reveal that the effect of the mechanical damage which is not sensed by *in-situ* electrochemical measurement is adequately captured by the AE method, thus making the combined technique a novel approach for *in-situ* monitoring of both the electrochemical and mechanical damage contributions of erosion-corrosion degradation processes.

Contents

List of Figures

List of Tables

Nomenclature

A	Surface Area (cm^2) or Constant
A_{AE}	Acoustic Emission Amplitude (dB)
a,b,c	Material Geometry and Flow Pattern Constants
B	Stern-Geary Coefficient (mV)
β	Cathodic Transfer Coefficient
β_a, β_c	Anodic and Cathodic Tafel Slopes (mV/decade)
C	Concentration (mg/L) or Capacitance (F) or Mass Loss Due to Pure Corrosion
dC_E	Mass Loss Due to Influence of Erosion on Corrosion
C_{edl}	Electrical Double Layer (EDL) Capacitance (F)
C_p	Specific Heat Capacity (K/Kg.K)
D	Diffusion Coefficient (m^2/sec) or Diameter (m)
D_r	Ratio of Contact to Depth of Cut
e	Coefficient of Restitution
ϵ, ϕ	Deformation and Scratch Wear Factors
E	Electrode Potential (V) or Mass Loss Due to Pure Erosion
dE_C	Mass Loss Due to Influence of Corrosion on Erosion
E_e	Young Modulus of Elasticity (Pa)
E_1 and E_2	Young Modulus of Particle and Target Materials Respectively
E_{corr}	Corrosion Potential (V)
F	Faraday's Constant (96,485 C)

f_{CO_2}	CO_2 Fugacity (bar)
f_t	Numerical Constant
F_R	Ratio of Vertical Force to Horizontal Force
ΔG	Gibbs Free Energy (J/mol)
H_S	Hardness of Particle (Pa)
n	Number of electrons in a Reaction
i	Current Density (A/cm^2)
i_{corr}	Corrosion Current Density (A/cm^2)
J	Material Flux (mol/sec.m^2)
k	Reaction Rate Constant
K_t	Temperature Dependent Constant
K_{sp}	Solubility Limit (M)
m	Mass of particle (g)
M	Atomic Weight of a Metal (g)
n_c	Strain Hardening Coefficient
p_{CO_2}	CO_2 Partial Pressure (bar)
P	Eroding Flow Stress (Pa)
Pe	Peclet Number
q	Charge (C)
Q	Volume of Material Removed (m^3) by Particles
r_{corr}	Corrosion Pentration Rate (cm/s)
R	Universal Gas Constant (J/mol.K)

Re	Reynolds Number
R_p	Polarisation resistance ($\Omega.cm^2$)
R_{ct}	Charge-Transfer Resistance ($\Omega.cm^2$)
R_s	Solution Resistance ($\Omega.cm^2$)
Sh	Sherwood Number
St	Stokes Number
t	Time (s)
T	Temperature (K)
τ_w	Wall Shear Stress (Pa)
μ	Coefficient of Friction
ρ	Density (g/cm^3)
$\vec{v}$	Mean Flow velocity (m/s)
υ	Kinematic Viscosity (Pa.s)
υ_1, υ_2	Poison's Ratio of Particle and Target Materials Respectively
η	Overpotential (V)
V_{out}	Sensor Output Voltage (mV)
V_{in}	Sensor Input (Reference) Voltage (1μV)
V	Particle Velocity (m/s)
θ	Particle Impact Angle
ω	Angular Frequency (rad/sec)
W_t	Weight loss at the anode (g)
Z	Impedance ($Ohm.cm^2$)

Abbreviations

AC	Alternating Current
AE	Acoustic Emission
API	American Petroleum Institute
ASTM	American Society for Testing and Materials
CA	Corrosion Allowance
CPU	Central Processing Unit
CFD	Computational Fluid Dynamics
CP	Cyclic Polarisation or Cathodic Protection
CR	Corrosion Rate
CUI	Corrosion Under Insulation
DC	Direct Current
DDT	Duration Discrimination Time
FFT	Fast Fourier Transform
EAS	Electrochemical Active Species
EDL	Electrical Double Layer
EIS	Electrochemical Impedance Spectroscopy
ER	Electrical Resistance
HB	Brinell Hardness
IHP	Inner Helmoltz Plane
KE	Kinetic Energy
LPR	Linear Polarisation Resistance
LHS	Left Hand Side

MIC	Microbial Induced Corrosion
OHP	Outer Helmoltz Plane
OCP	Open Circuit Potential
PDS	Potentiodynamic Scanning
PR	Precipitation Rate
PWC	Preferential Weld Corrosion
RCE	Rotating Cylinder Electrode
RDS	Rate Determining Step
RHS	Right Hand Side
RMS	Root Mean Square
RP	Recommended Practice
RPM	Revolution Per Minute
SCE	Saturated Calomel Electrode
SEM	Scanning Electron Microscope
SHE	Standard Hydrogen Electrode
SIJ	Submerged Impinging Jet
SS	Supersaturation
ST	Scaling Tendency
TML	Total Mass Loss
VS	Vallen Sensor
WT	Wavelet Transform

Chapter 1 Introduction

1.1 Motivation

Carbon dioxide (CO_2) corrosion, sand erosion and erosion-corrosion are important and inevitable challenges in oil and gas production which normally result in severe damage by attacking the materials used in production, gathering and processing facilities. They occur due to the presence of water, CO_2 gas and sand particles co-produced with the hydrocarbon [1]. CO_2 dissolves in water to form carbonic acid which directly deteriorates materials [2] or partially dissociates to form corrosive species [3] that degrade carbon steel pipeline materials in service. Depending on the operating conditions, protective iron carbonate ($FeCO_3$) films tend to form on the steel surface to prevent further corrosion attack [4]. However, this protective film is continuously eroded by sand particle impingement thereby exposing fresh surfaces to further corrosion attack. The combined effect of CO_2 corrosion and sand erosion is known as erosion-corrosion [1] and a pictorial example of the nature of the attack is shown in Figure 1.1.

(a) (b)

Figure 1.1: Typical CO_2 erosion-corrosion damage in (a) X65 carbon steel pipeline and (b) in a choke (a device used to control the flow of fluid in pipelines) [5].

The erosion-corrosion degradation of materials is a complex phenomenon because it emanates from the combined effects of mechanical forces (caused by flowing fluid in the presence and absence of solid particles destroying the surface layer/base metal) and electrochemical or chemical dissolution of metallic ions which can be enhanced by mass transfer increases at the surfaces. This damage results in more material loss than the sum of the losses caused by pure mechanical erosion and pure electrochemical corrosion.

The consequences and costs associated with CO_2 corrosion and erosion-corrosion damage in oil and gas facilities are enormous and cannot be over-emphasized. The UK Piper-Alpha disaster of 1988 [6] and the recent BP Gulf of Mexico oil spill [7] are typical examples. Kermani and Harrop [8] in an industry-wide survey in 1980s showed that corrosion-related failures constitute 33% of failures in oil and gas industry and that 28% of these failures are attributed to CO_2 corrosion. A summary of their analysis is shown in Figure 1.2. They maintained that the cost of corrosion to the BP Group gives a reasonable estimation of such corrosion costs and can be viewed in terms of capital expenditure (CAPEX); operating expenditure (OPEX); replacement expenditure; lost revenue; Health, Safety and Environment (HSE); and drilling costs.
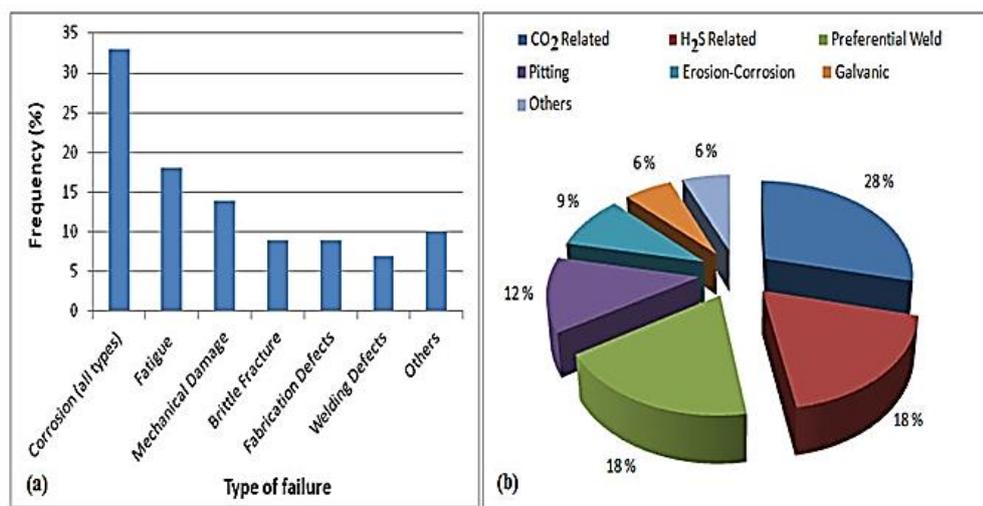
Figure 1.2 (a) Survey of selected number of failures and (b) causes of corrosion related failures in oil and gas related industries [8].

Kermani and Harrop [8] further observed that the costs can be minimized through adequate corrosion enlightenment campaigns, and training coupled with preventive measures such as controlling flow conditions, selecting corrosion resistant alloys, applying inhibitors, etc. However, in spite of their low resistance to CO_2 corrosion and erosion-corrosion attack when compared with corrosion resistant alloys (CRAs), carbon steel materials are still widely used by industry with the application of corrosion inhibitors because they are relatively cheap, readily available and can easily be fabricated [9].

As a result, efforts have been made by researchers and industries world-wide to understand the mechanisms and predict CO_2 corrosion and erosion-corrosion so as to reduce or eliminate the costs and consequences associated with the damage, operate safely and avoid unplanned production outages. The development of de-Waard and Milliams model in 1975 [2] with its modifications [10-12] has helped in understanding and predicting CO_2 corrosion and it has led to development of several empirical [13-17], semi-empirical [18-22] and mechanistic [3, 4, 23-30] models. However, these models do not take into account effect of sand erosion. On the other hand, the sand erosion models [31-34] developed over the years do not take into account the effect of corrosion. As a result, various experimental, empirical and computational techniques that tend to combine the effects of corrosion and erosion with their synergism have been developed by leading researchers such as the Tulsa group [1, 35-38], Ohio group [39, 40], Leeds group [41-43], Glasgow group [44, 45], Alberta group [46-48], etc and are used to predict erosion-corrosion damage.

It has been observed that despite the development over the years, the oil and gas industries still use the de-Waard and Milliams model [2, 10-12] and API RP 14E [32] erosion relation in design and operations because of their simplicity and ease of application as most of the models developed by researchers are complex and difficult to implement in day to day design and operations of oil and gas production [49]. The

models can be conservative and tend to impose a limit on production rates so as to avoid severe damage. Sometimes, they are unreliable in predicting the actual long term damage and indirectly results in over-specification of material which affects cost of production of oil and gas [9]. This is because of the poor understanding of erosion-corrosion phenomenon occasioned by the complex nature of the process.

Therefore, it is necessary to continuously monitor flow streams to determine the onset of sand production and predict the extent of damage to the material and take action when excessive sand is noticed or damage becomes significant. The sand and material damage monitoring can be achieved by combining acoustic emission (AE) method with electrochemical monitoring. AE is non-intrusive, fast, cost effective, easily and cheaply maintained, and can monitor long pipelines from a single sensor location. The method can enhance long distance or remote monitoring of the oil and gas pipelines from single sensor location. This can be very helpful in preventive and predictive maintenance strategies that will detect onset of sand production, impending failures and allow for proper planning and scheduling of pipeline repairs and replacements. Furthermore, buried or remote pipes can be monitored from single sensor location, thereby reducing cost and time of inspection. It can also allow for full capacity production without shutting production lines at fixed periods for visual inspection of corrosion coupons and other convectional tests as currently practised in oil and gas industries.

However, the AE method requires highly specialised sensors and signal processing/interpretation skills; and is also sensitive to other ultrasonic sources such as process flows and background noise. Therefore, adequate skill is required so to be able to separate the sand impacts and material degradation signals from background noise and other process interferences.

1.2 Aim and Objectives of Study

This PhD study was aimed at applying acoustic emission (AE) technique coupled with electrochemical (Linear Polarisation Resistance (LPR) and AC Impedance) methods in a Submerged Impinging Jet (SIJ) rig to investigate and characterise erosion-corrosion damage in a saturated CO_2 environment for oil and gas pipeline materials (X65).

In order to achieve this aim, the study designed, calibrated and implemented an AE set-up with electrochemical instruments in an existing SIJ rig. The PhD study objectives were:

- To validate the relationship between AE energy and kinetic energy of impinging solid particles.

- To develop a correlation between AE energy and mass loss rate due to pure erosion for different flow velocities (7, 10 m/s and 15 m/s) and sand concentrations (50, 200, 500 mg/L) at temperature of 50^oC.

- To quantify the number of sand impacts per time and the associated impact energy for different flow velocities (7, 10 m/s and 15 m/s) and sand concentrations (50, 200, 500 mg/L) at temperature of 50^oC.

- To develop a method to differentiate the mechanisms of the material damage with and without sand using the frequency spectra of generated AE signal waveforms.

- To establish a correlation between AE energy and polarisation resistance from simultaneous electrochemical measurements for CO_2 flow-induced corrosion, and erosion-corrosion for different flow velocities (7, 10 m/s and 15 m/s) at temperature of 50^oC.

- To develop a correlation between AE energy and mass loss rate due to erosion-corrosion for different flow velocities (7, 10 m/s and 15 m/s) at temperature of 50^oC.

- To perform transient technique evaluations involving electrochemical impedance spectroscopy (EIS) simultaneously with AE measurement, correlate charge-transfer resistance with AE energy and quantify the erosion-corrosion damage and its components.

1.3 Statement of Novelty and Scientific Contribution

This work contributes knowledge to real-time and on-line assessment of erosion and corrosion as a damage process in solid-containing flows. To date, this study is unique and offers a significant contribution to the existing body of knowledge on AE and electrochemistry. For the first time in University of Leeds, this study designed, procured and implemented AE set-up coupled with electrochemical monitoring in a Submerged Impinging Jet (SIJ) rig for erosion-corrosion assessment of pipeline materials.

The investigations performed in the course of the project are unique because they revealed that the effect of the mechanical damage due to sand impact which is not sensed by *in-situ* corrosion measurement using LPR or EIS is captured by the AE method. Being a measure of the energetic flux of impacting particles, the AE energy can give an insight of the mechanical damage contribution while *in-situ* electrochemical monitoring can provide information regarding the chemical dissolution or electrochemical reactions of the materials, thus the overall erosion-corrosion damage and its components can be accurately determined.

The combination of these two techniques can help in *in-situ* monitoring of both the electrochemical and mechanical damage contributions in oil and gas pipeline in service for effective integrity monitoring and proper maintenance planning of oil and gas pipelines.

1.4 Thesis Outline

This report is made up of eleven chapters.

Chapter one gives the introduction in form of the motivation, aim and objectives of the PhD study, and outline of the thesis with explanation of novelty and scientific contribution of the project to knowledge.

Chapter two treats background theory in form of the history and meaning of corrosion with emphasis on aqueous corrosion in terms of meaning, governing mechanisms, modelling (thermodynamics and kinetics), measurement methods and different forms of attack.

Chapter three deals with literature review covering previous research activities on the mechanisms, controlling factors, mitigation and modelling of CO_2 corrosion and pure erosion and erosion-corrosion.

Chapter four presents a detailed review on AE technique with emphasis on its meaning, signal processing analysis and application in monitoring and predicting corrosion, erosion and erosion-corrosion.

Chapter five considers the experimental design, materials, calibration and procedures while chapter six offers the results and discussion of the erosive wear investigation using time series and frequency spectra of measured AE signals.

Chapter seven submits the results and discussion on the determination of particle impacts and impact energy using acoustic emission signals and computational fluid dynamics (CFD) with particle tracking.

Chapter eight gives a detailed analysis of the results and discussion of investigation of CO_2 flow-induced corrosion and erosion-corrosion using the combination of acoustic emission and linear polarisation resistance measurements.

The transient technique evaluations involving simultaneous electrochemical impedance spectroscopy (EIS) and acoustic emission of the erosion-corrosion damage assessment and its components were presented and discussed in chapter nine.

Chapter ten provides an overview and discussion that links all the chapters together whilst chapter eleven summarises the PhD thesis in form of main conclusions as well as suggested future work.

Chapter 2 Background Theory

This chapter gives the background theory in form of the history and background of corrosion with emphasis on aqueous corrosion in terms of meaning, governing mechanisms, modelling (thermodynamics and kinetics), measurement methods and forms of attack common to oil and gas production facilities.

2.1 Corrosion

Corrosion can be defined as the degradation of a metal by chemical or electrochemical reaction with the environment [50]. The study of corrosion can be traced back to the classical essays of Robert Boyle (1627-1691) titled "Mechanical Origin of Corrosiveness" [51] and the work of Michael Faraday (1791-1867) [51], who made a major and important contribution by establishing a quantitative relationship between chemical reaction and electric current in what we call today as Faraday's first and second laws. These laws form the basis for the calculation of corrosion rates of metals. Following the work of Faraday, many electrochemists have contributed to the build-up of knowledge concerning the electrochemical basis of corrosion. An earlier group, whose contributions were mostly made before 1950 includes De La Rive, Evans, Hoar, Tomaschov, Uhlig, Wagner, Kolotyrkin and Pourbaix. A later group, whose contributions were basically investigation of the electrochemical kinetics of corrosion reactions, include Vetter, Heusler, Kruger, Sato, Drazic, Arvia, Lorenz and Mansfeld. A detailed discussion on the meaning and history of corrosion can be found in references [50, 51].

From the definition, it is evident that corrosion occurs because of the interaction between materials and their environment. The environment may be either dry or wet. Dry corrosion occurs at extreme high temperature systems such as in power generation (nuclear and fossil fuel), aerospace and gas turbines, heat treatment plants, [50] etc. Wet environment leads to aqueous corrosion which is an electrochemical

process at lower temperatures and it is the prevalent corrosion attack encountered in oil and gas industry.

2.2 Governing Mechanisms of Aqueous Corrosion

Aqueous corrosion is an electrochemical process because it is a chemical reaction that involves generation and transfer of electrons to electrochemically active species (EAS) dissolved in the electrolyte [52]. A detailed discussion on aqueous corrosion and its electrochemistry can be found in the work of Shreir *et al* [50], Ahmad [51], Tait [52] and Richardson [53].

From the literature read, it is well understood that a corrosion cell comprising of anode (for oxidation half reaction); cathode (for reduction half reaction); electrolyte (e.g. water or aqueous solution containing dissolved ions) and electrochemical active species (e.g. O_2, CO_2, H_2S, etc) is required for aqueous corrosion to occur. The schematic illustration of a corrosion cell is shown in Figure 2.1.
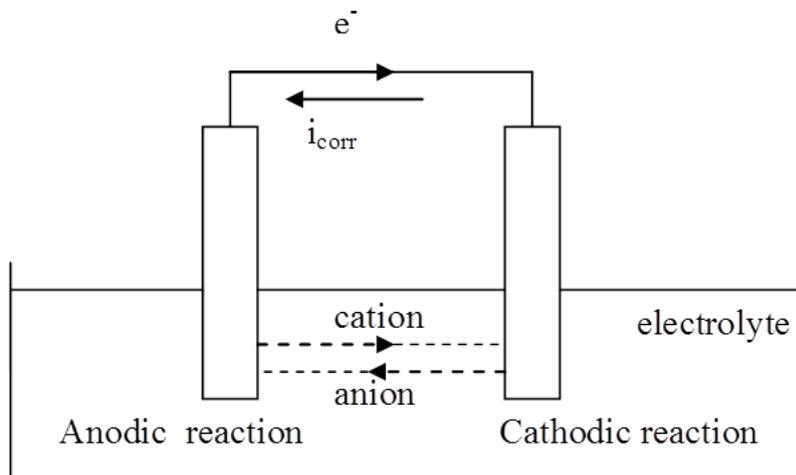
Figure 2.1: Schematic illustration of the components of a corrosion cell [43].

The basic electrochemistry involved in the corrosion can be summarised using the corrosion of carbon steel in acidic environment as follows [52]:

Anodic oxidation half reaction: $Fe^o \rightarrow Fe^{2+} + 2e^-$ (2.1a)

Cathodic reduction half reaction: $\qquad 2H^+ + 2e^- \rightarrow H_2$ $\hspace{3cm}$ (2.1b)

Overall reaction $\hspace{3cm} Fe^o + 2H^+ \rightarrow Fe^{2+} + H_2$ $\hspace{2.5cm}$ (2.1c)
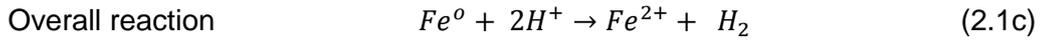
In anodic oxidation reaction, iron atoms (Fe) are oxidized to iron ion (Fe^{2+}) leading to generation of electrons and dissolution of iron into the solution while in the cathodic reaction, the hydrogen ion (H^+) from the acidic electrolyte consumes the electrons generated in the anode, thus leading to the evolution of hydrogen gas in the cathode. The two half reactions combine to form the overall corrosion reaction. After the reaction, the species are transferred from the electrode (metal surface) to the bulk electrolyte through diffusion, convection and migration [52].

In oxygen (aerated) environment, the two electrons generated at the anode are consumed in the environment as follows in acid solution:

$$4H^+ + O_2 + 2e^- \rightarrow 2H_2O \hspace{4cm} (2.2)$$

and in neutral or basic solution:

$$O_2 + 2H_2O + 4e^- \rightarrow 4OH^- \hspace{4cm} (2.3)$$

The summary of the oxygen corrosion reaction is given as:

$$2Fe + 2H_2O + O_2 \rightarrow 2Fe^{2+} + 4OH^- \rightarrow 2Fe[OH]_2 \hspace{2cm} (2.4)$$

$$2Fe[OH]_2 + H_2O + \frac{1}{2}O_2 \rightarrow 2Fe(OH)_3 \hspace{3cm} (2.5)$$

The term $Fe[OH]_2$ is iron oxide which can be oxidized to form the red-brown $Fe(OH)_3$ commonly known as rust [54].

Aqueous corrosion reaction mechanisms have been studied in the past using two different approaches, viz: thermodynamic and kinetic considerations.

2.3 Corrosion Thermodynamics

For metals to corrode, there exists an energy called Gibbs free energy $(-\Delta G^o)$ which is responsible for powering the corrosion reaction when the metal is placed in an aqueous environment. This energy results from the process of converting ore to metal. The more negative the value of $-\Delta G$, the greater the tendency for corrosion reaction to occur. When it is zero, the system is at equilibrium and when it is positive, the metal is stable and will not react spontaneously.

In an attempt to estimate the work done in corrosion process, Michael Faraday expressed the Gibbs free energy change of the corrosion process in terms of the potential difference and the charge transported as follows [51]:

$$\Delta G = (-nF)E \tag{2.6}$$

where, n is the number of electrons involved in the reaction, F is the Faraday's constant, which is the electrical charge carried by a mole of electrons (96,485 C) and E is the driving force or potential difference for the reaction to take place. The negative sign is used for cathodic reactions and a positive sign is given to indicate anodic reactions.

At standard conditions, temperature 273.15 K and one atmosphere of pressure;

$$\Delta G^o = (-nF)E^o \tag{2.7}$$

Standard values of ΔG^o for metals can be found in literature [50, 51] and E^o is the equilibrium electrode potential for standard condition. Though, corrosion reactions depend on temperature because the ΔG of the reacting species depend on temperature. Hence, half-cell potential changes with concentration of the ions present in the reaction to give the value of ΔG as follows [50]:

$$\Delta G = \Delta G^o + RT \, ln \left[\frac{[product]}{[reactant]} \right] \tag{2.8}$$

Substituting the values of ΔG and ΔG^o in Equations 2.6 and 2.7 into Equation 2.8 yields Nernst equation [51]:

$$E = E^o - \left(\frac{RT}{nF}\right) \ln \left[\frac{[products]}{[reactants]}\right] \tag{2.9}$$

Applying the equation for anodic and cathodic reaction of iron in acid environment,

$$Fe + 2H^+ \Leftrightarrow Fe^{2+} + H_2(g) \tag{2.10}$$

Gives Nernst equation of the form,

$$E = E^0 - \left(\frac{RT}{nF}\right) \ln \left\{\frac{([Fe^{2+}][H_2])}{([Fe][H^+]^2)}\right\} \tag{2.11}$$

where, E is the equilibrium electrode potential (V) for non-standard conditions for the reaction, E^0 is the equilibrium electrode potential for standard condition for the reaction, $[Fe^{2+}]$ is iron concentration, H_2 is the pressure of hydrogen gas, $[H^+]$ is the activity of dissolved hydrogen ion, R is the ideal gas constant and T temperature in Kelvin.

From the foregoing, the possibility of a metal to corrode in a certain environment (pH, O_2 concentration, etc) is determined by its reversible thermodynamic potential, whether it is more negative than that of the corresponding cathodic partner reactions.

This basic thermodynamic consideration was used by Marcel Pourbaix (1904-1998) as basis of equilibrium corrosion diagrams in which thermodynamic reversible electrode potential of metals and that of the appropriate cathodic partner reaction are plotted as a function of pH [55] as illustrated in Figure 2.2 for iron in water at 25^oC.
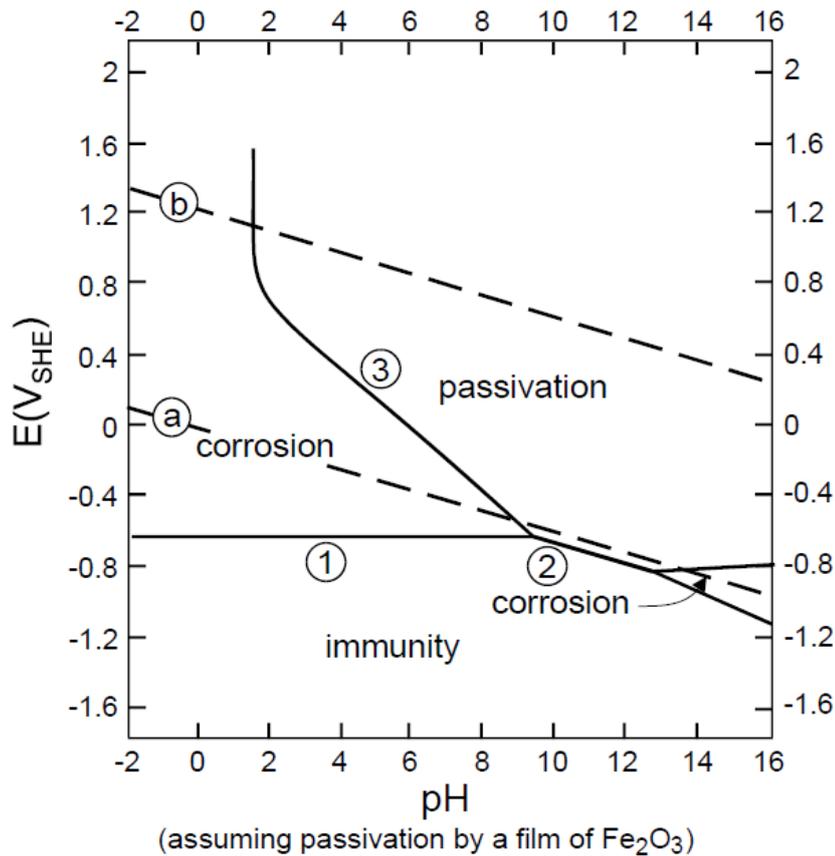
Figure 2.2: Simplified Pourbaix diagram for iron in water at 25°C [55].

Pourbaix diagrams give first approximation guidance towards corrosion safety, but they must be applied with intelligence and knowledge. This is because they only signify when corrosion is thermodynamic possible and do not give indication of practical corrosion rate. Hence, a more realistic approach can be made if the kinetic rate constants for the anodic dissolution reactions are known.

2.4 Corrosion Kinetics

Corrosion reactions can be considered as heterogeneous processes because they involve the transfer of charge at an electrode/solution interface. The kinetics of heterogeneous reactions are normally determined by a sequence of steps involving both transport through the solution (and sometimes the electrode) phase and the transfer of charge at the interface [56].

For example, consider the following simple electrochemical reaction:

$$O + ne \rightleftharpoons R \qquad\qquad (2.12)$$

There are at least five separate steps in the conversion of O:

1. Transport of O from the bulk solution to the interface,

2. Adsorption of O unto the surface,

3. Charge transfer at the electrode to form R,

4. Desorption of R from the surface, and

5. Transportation of R from the interface into the bulk of the solution.

Steps 2 to 4 are commonly referred to as the 'activation' process whereas steps 1 and 5 are known as mass transport processes [56]. Since these processes occur sequentially, then the rates of the overall reaction is equal to the rates of the individual steps (note that this does not mean equal rate constants).

It is important to note that the rates of the individual processes are time dependent, and the analysis of this time dependence forms the basis for determination of corrosion rate.

2.4.1 Mass Transport (Diffusion Controlled Mechanism)

If it is assumed that mass transport occurs only by diffusion, then the rates of transport of O to the interface and conversion of R from the interface to the bulk solution depend upon the concentration gradients at the interface in accordance with Fick's first law [59];

$$\frac{-i}{nFA} = J_R = -D_O \left(\frac{\partial C_O}{\partial x}\right)_{x=0} \qquad\qquad (2.13)$$

$$\frac{i}{nFA} = J_R = -D_R \left(\frac{\partial C_R}{\partial x}\right)_{x=0} \qquad\qquad (2.14)$$

where J is the flux in moles per unit time per unit area ($mol\,sec^{-1}\,m^{-2}$) normal to the surface, A the area of the surface, and D the diffusion coefficient in units of $m^2 sec^{-1}$.

The direction of positive flux for O is taken to be from the bulk solution to the interface, whereas that for R is considered to be from the interface into the bulk solution, thus the rate of the reaction at the surface is given by [56];

$$\frac{i}{nFA} = k_f C_O(x = 0) \qquad\qquad (2.15)$$

where k_f is the potential dependent rate constant and $C_O(x = 0)$ the concentration of O at the interface. Since the rate constant k_f responds instantaneously to potential, whereas concentration does not, then the rate at $t = 0$ is given by [56];

$$\left(\frac{i}{nFA}\right)_{t=0} = k_f C_O^b \qquad\qquad (2.16)$$

where C_O^b is the concentration of O in the bulk solution. Therefore, if the rate at $t = 0$ is known, then the rate constant k_f can be determined and can be linked with hydrodynamic parameters (such as Schmidt, Reynolds and Sherwood numbers). The interface kinetics is basically governed by interaction of charges between the metal and the solution [56].

2.4.2 Electrical Double Layer (EDL)

At the metal/solution interface, a charge separation between the metal surface and the solution occurs which is known as the electrical double layer (EDL) [56]. The double layer (illustrated in Figure 2.3) exerts a strong influence upon electrode kinetics. The EDL is divided into three regions. The innermost region known as the Inner Helmoltz Plane (IHP) i.e. adjacent to the metal, which contains specifically adsorbed ions (and water dipoles). Outside this layer, there exists an additional layer of non-adsorbed hydrated ions whose centers define the Outer Helmholtz Plane (OHP). Beyond the OHP is the 'diffuse layer', where the population of ions of given charge at any point from the surface is determined by the opposing effects of the electric field and thermal agitation [56].
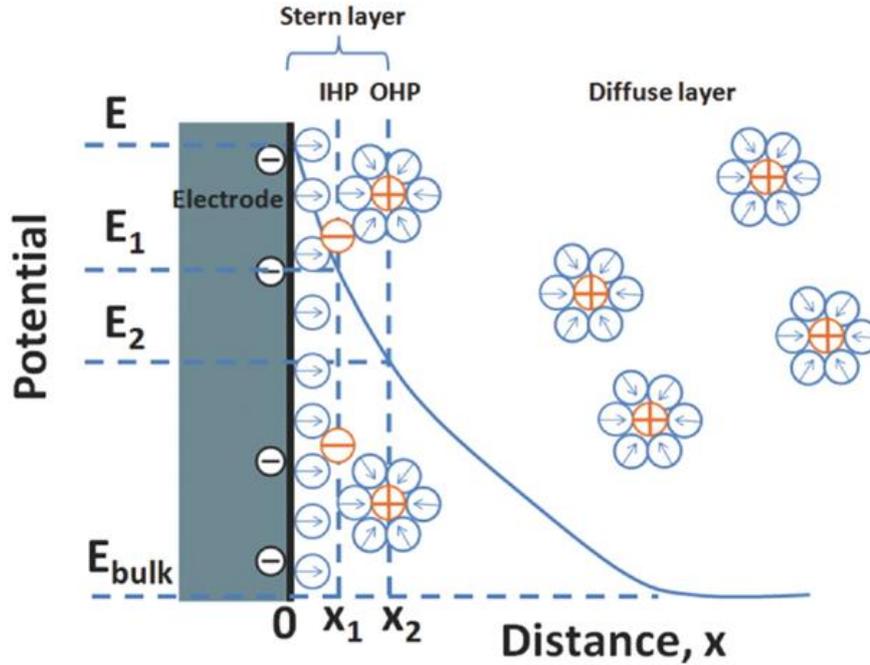
Figure 2.3: Stern-Grahame model for electrical double layer [56].

The potential drop is approximately linear with distance across the metal-IHP and IHP-OHP regions and in the diffuse layer the potential drop approximately decays exponentially with distance. A detailed discussion on the EDL potential has been given by Conway [57]. The total potential drop across the interface can be expressed as [56]:

$$\Delta_b^m E = (E_m - E_1) + (E_1 - E_2) + (E_2 - E_b) \tag{2.17}$$

where E_m is the Galvani (inner) potential of the metal phase, E_i the Volta potential at point i in solution and E_b the potential in the bulk solution.

Differentiation of Equation (2.17) with respect to the charge (q_m), and taking note of the definition of differential capacitance $C = dq/dE$ gives the expression for the overall double-layer capacitance in terms of the contributions from the three regions [56];

$$\frac{1}{C_{dl}} = \frac{1}{C_{IHP}} + \frac{1}{C_{OHP}} + \frac{1}{C_{diff}} \tag{2.18}$$

Equation 2.18 is very important because it suggests that an electrical analogy of the double layer is the series combination of three capacitors, and that the overall

capacitance of the double layer is determined basically by the smallest of the three capacitances of the layers. This analogy is useful for the analysis of the response of an electrode to various corrosion measurements, particularly to AC measurement [56].

2.4.3 Charge Transfer (Activation Controlled Mechanism)

MacDonald [56] and Conway [57] have discussed the influence of double layer upon the kinetics of charge transfer. Their analyses were based on 'activated complex theory' [56] where the forward and reverse rate constants for a simple charge transfer process are expressed as follows [57];

$$k_f = k_f^0 \exp(-\beta nFE/RT) \tag{2.19a}$$

$$k_b = k_b^0 \exp[(1-\beta)nFE/RT] \tag{2.19b}$$

where E is the electrode potential with respect to some reference electrode, and β the cathodic transfer coefficient. k_f^0 and k_b^0 are constants which do not depend on E directly but are functions of the standard Gibbs energies of activation and the electrical potentials at the initial states which is assumed to reside at the inner Helmholtz plane.

The observed current flowing through an external circuit is equal to the difference between the partial currents for the forward and reverse processes [56],

$$i = i_f - i_b \tag{2.20}$$

which, upon substitution of Equation 2.15 gives

$$i = nFA[k_f C_O(x=0) - k_b C_R(x=0)] \tag{2.21}$$

Substitution of Equations 2.19a and 2.19b for k_f and k_b, respectively therefore yields,

$$i = nFA\{C_O(x=0)k_f^0 \exp(-\beta nFE/RT) - C_R(x=0)k_b^0 \exp[(1-\beta)nFE/RT]\} \tag{2.22}$$

At equilibrium ($E = E_e$), the total current is zero, and hence no concentration gradients exist at the interface.

Therefore,

$$C_O^b k_f^0 \exp\left(-\frac{\beta nFE_e}{RT}\right) = C_R^b k_b^0 \exp\left[\frac{(1-\beta)nFE_e}{RT}\right] \quad (2.23)$$

$$= \frac{i_0}{nFA} \quad (2.24)$$

where i_0 is the exchange current. Eliminating k_f^0 and k_b^0 from Equation 2.22 using Equations 2.23 and 2.24 gives;

$$i = i_0\{[C_O(x=0)/C_O^b]\exp(-\beta nF\eta/RT) \; -[C_R(x=0)/C_R^b\exp[(1-\beta)nF\eta/RT]\} \quad (2.25)$$

where η is the overpotential, $\eta = E - E_e$. Equation 2.25 is very important because it relates the current to both the surface concentrations and the overpotential. If the rate of the reaction is so small that no appreciable concentration gradients exist at the surface, then $C_O(x=0) \approx C_O^b$ and $C_R(x=0) \approx C_R^b$. The current for a completely activation-controlled process from equation 2.25 becomes:

$$i = i_0\{\exp(-\beta nF\eta/RT) \; - \exp[(1-\beta)nF\eta/RT]\} \quad (2.26)$$

This expression is called Butler-Volmer equation, with $\exp(-\beta nF\eta/RT)$ and $\exp[(1-\beta)nF\eta/RT]$ as the anodic and cathodic terms respectively. The solution of this equation gives electrochemical corrosion curves simplified as Evans diagram and illustrated in Figure 2.4.
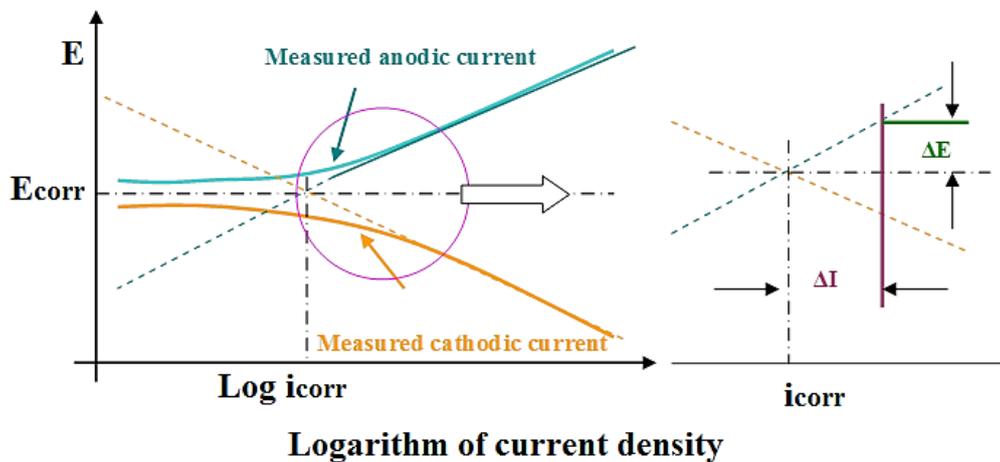
Figure 2.4: Electrochemical corrosion curves [43].

The curves can be interpolated to obtain the corrosion current (i_{corr}) which is used to compute the metal degradation rate by applying Faraday's Law.

2.4.3.1 Faraday's Law and Corrosion Rate

The amount of metal lost at the anode or deposited at the cathode is a function of the atomic weight of the metal, the number of charges transferred, and the corrosion current (I_{corr}). This expression which was established by Michael Faraday in 1833 while working as Sir Humphry Davy's assistant at the Royal Institute London is as follows [55];

$$W_t = \frac{M}{nF} t I_{corr}$$
(2.27)

where W_t is total weight loss at anode or weight of material produced at the cathode (g), n number of charges transferred in the oxidation or reduction reaction, I_{corr} corrosion current (A), F Faraday's constant of approximately 96,500 coulombs per equivalent weight of material ($\frac{M}{n}$), M the atomic weight of the metal which is corroding or the substance being produced at the cathode (g), t the total time in which the corrosion cell has operate (s).

If both sides of Equation 2.27 is multiplied by the term $\left(\frac{1}{A.t}\right)$, where A is the surface area of the anode or cathode (cm^2) and t is time (s), Equation (2.28) results:

$$\frac{W_t}{A.t} = \frac{M}{nF} \cdot \frac{I_{corr}}{A}$$
(2.28)

But $\frac{I_{corr}}{A} = i_{corr}$, the corrosion current density, then Equation 2.28 becomes [55]:

$$\frac{W_t}{A.t} = \frac{M}{nF} i_{corr}$$
(2.29)

Therefore, the weight loss per unit time per unit area is directly proportional to corrosion current density. Dividing Equation 2.29 by density (ρ) of the material (g/cm^3), the corrosion penetration rate (cm/s) can be deduced as follows [55],

$$r_{corr} = \frac{M}{nF} \cdot \frac{i_{corr}}{\rho} \tag{2.30}$$

Hence, the penetration rate for iron, based on $1\ A/m^2$ current density using the values of $(M = 55.85g, n = 2, \rho = 7.87g/cm^3, F = 96,500\ C, and\ i_{corr} = 10^{-4}A/cm^2)$is: $r_{corr} = 3.68\ x\ 10^{-9}\ \frac{cm}{s}.$

Then, converting the units to the common form of corrosion rate ($mm/year$), by multiplying the penetration rate by the number of seconds per year, and by the number of mm per cm gives:

$$r_{corr} = 3.68x10^{-9}\frac{cm}{s}x3.15x10^7\frac{s}{yr}x10\frac{mm}{cm} = 1.16\frac{mm}{yr} \tag{2.31}$$

Therefore corrosion rate ($mm/year$) of iron for corrosion current density $10^{-4}A/cm^2$ is 1.16 mm/year. Note that $0.025\ mm/year = 0.001\ inch/year$ [55].

2.5 Electrochemical Techniques for Corrosion Measurement

The measurement methods with typical experimental set-up having three-electrode cell shown in Figure 2.5 (a) can be grouped into direct current (DC) measurement methods and alternating current (AC) measurement method and each of the methods depends on the applied potential spectrum [52].

The DC methods are summarised in Figure 2.5 (b) and in Table 2.1 with Electrochemical Impedance Spectroscopy (EIS), an AC measurement method and the working principle of the three-electrode cell is described in the next paragraphs.

Table 2.1: Electrochemical corrosion measurement techniques [52]

Corrosion Measurement Method	Potential Spectrum Applied (mV)
Linear Polarisation Resistance (LPR)	± 50 from OCP
Tafel Plot (TP)	± 250 from OCP
Potentiodynamic Scanning (PDS)	Starts from -250 from OCP and ends at +1000 from OCP
Cyclic Polarisation (CP)	Combines PDS spectrum and reverse scan potentials initiated from end of PDS back to OCP
Electrochemical Impedance Spectroscopy (EIS) or AC Impedance	AC with LPR spectrum
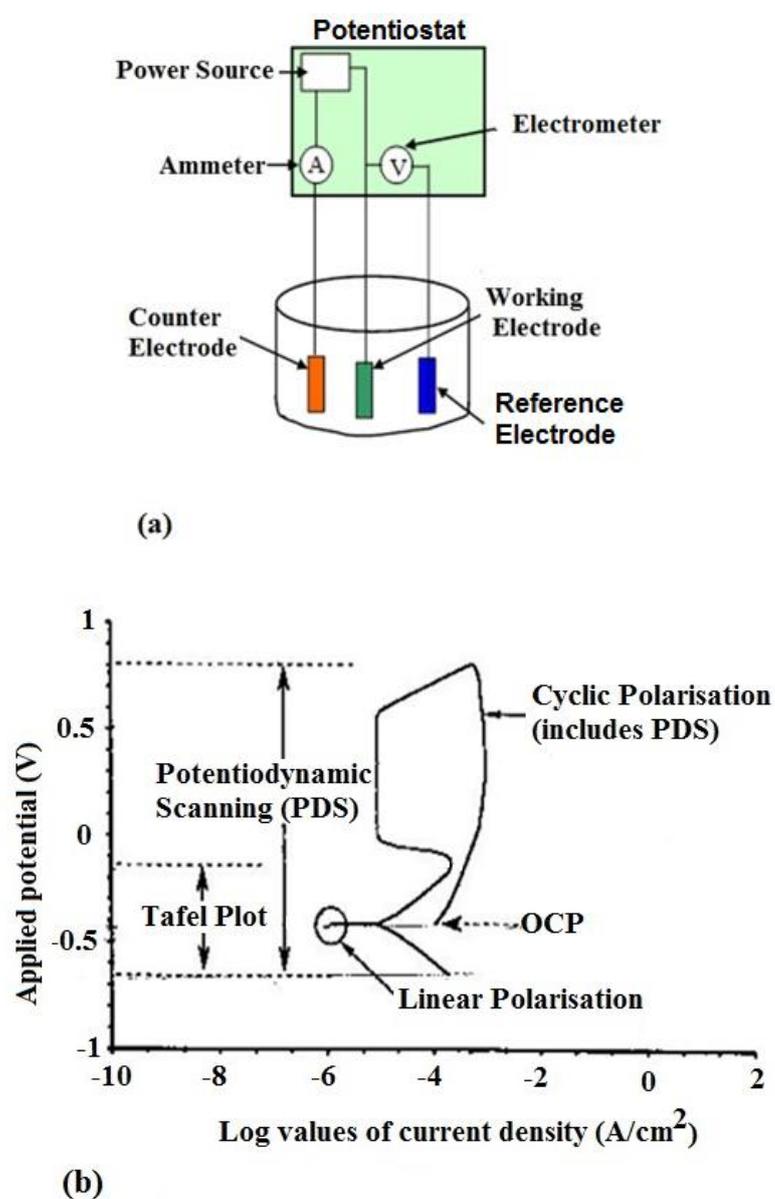
Figure 2.5: (a) Set-up for corrosion test and (b) summary of DC methods.

2.5.1 Principles of Three-Electrode Cell

In the three-electrode cell shown in Figure 2.5a, a computer-controlled potentiostat (with ammeter, electrometer and power source) works with three electrodes immersed in a conductive electrolyte. These electrodes are the working electrode (a sample of the corroding material being tested), the reference electrode (an electrode with constant and known electrochemical potential which is used as a point of reference in the cell for potential control and measurement), and the counter electrode (a current-carrying electrode that completes the cell circuit). The corrosion test using this cell entails polarisation which essentially involves applying potential or current changes on the working electrode while monitoring the resulting response in current or potential. For this to happen, current must be simultaneously withdrawn from the working electrode when current is supplied by the potentiostat to the counter electrode (and vice versa) in order to maintain electronic equipment and electrode electrical neutrality. No current flows between the potentiostat and reference electrode so it remains at its open circuit potential (OCP) and gives a 'fixed' reference point for corrosion measurement [52].

The working electrode polarisation is controlled by the potentiostat supplying electrons to either the counter or working electrodes. Ions respond to the electrode polarisation by moving between the counter and working electrodes in order to maintain electrical neutrality of the electrodes and electrolytes as shown in Figure 2.6 with reference electrode removed for clarity. Electrochemical active species (EAS) also move to the counter electrode and react with electrons supplied by the potentiostat [52].

The potentiostat supplies electrons to the counter electrode, causing positive ions (cations) to move toward the counter electrode. The potentiostat withdraws electron from the working electrode and negative ions (anions) move toward the working electrode. This may be achieved by using either a direct current (DC) or an alternating current (AC) power source.
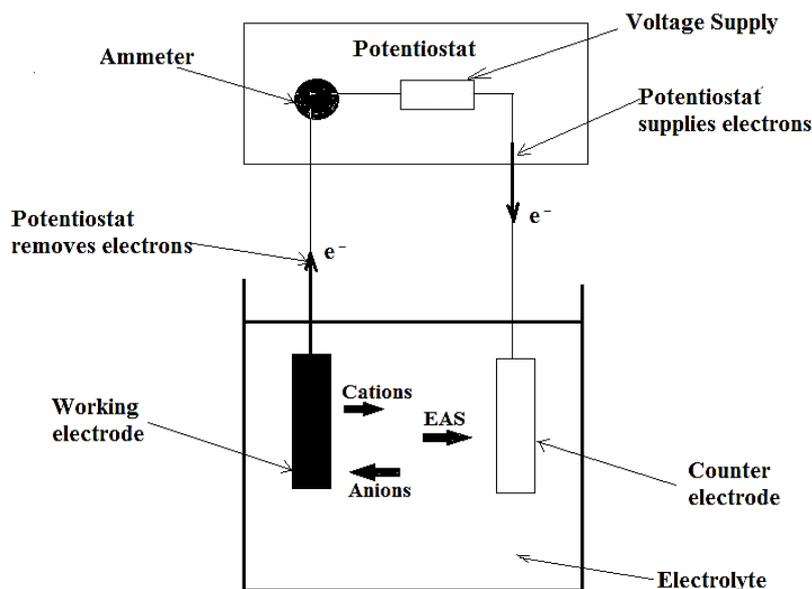
Figure 2.6: Schematic illustration of current flow during polarisation [52].

The DC polarisation involves changing the potential of the working electrode and measuring the current that is produced as a function of time or potential. For anodic polarisation, the potential is changed in more positive direction thereby causing the working electrode to become the anode and forcing the electrons to be withdrawn from the sample being tested. For cathodic polarisation, the potential is changed in more negative direction causing the working electrode to become cathodic (negative) and electrons are added to the metal. In cyclic polarisation, both anodic and cathodic polarisations are performed in cyclic manner [51].

Based on these principles, the DC corrosion tests can be classified as controlled potential (i.e. potentiostatic: Linear Polarisation Resistance (LPR), Tafel Plot (TP) and Potentiodynamic: Potentiodynamic Scanning (PDS) and Cyclic Polarisation (CP)) or controlled current (i.e. galvanostatic). For a potentiostatic procedure e.g. LPR which was applied in this study, the computer-controlled potentiostat automatically adjusts the applied polarizing potential between a working electrode (sample) and a reference electrode at a desired recommended value to measure the current density on the counter electrode. The corrosion resistance or polarisation resistance (R_p) is then

deduced from the potential and current density plot (i.e. the slope of the graph ($R_p = \frac{\Delta E}{\Delta i}$) and used to compute corrosion current density using Stern-Geary equation given by [51, 52].

$$i_{corr} = \frac{1}{2.303 R_p} \left[\frac{\beta_a \cdot \beta_c}{\beta_a + \beta_c} \right] \tag{2.32}$$

where, i_{corr} is the corrosion current density (A/cm^2), R_p is the corrosion resistance $(\Omega \cdot cm^2)$, β_a and β_c are constants called anodic and cathodic slopes respectively expressed in V/decade of corrosion current. The i_{corr} is then used to calculate the corrosion rate by applying Equations 2.30 and 2.31.

The procedure is the same for all the DC methods; the difference is in the applied potential range as illustrated in Table 2.1. The curve types of PDS and CP can be generated with up to approximately 1250 to 2250 mV potential ranges [52] and it provides additional information on corrosion kinetics and localised corrosion (e.g. pitting in stainless steel materials).

2.5.2 Uncertainties in Corrosion Measurement

Uncertainties or errors in measurement can be minimised by taking data when the test electrode is at steady state, correcting uncompensated solution resistance, using appropriate scan rate to collect data, choosing correct test electrode area, counter electrode area, and test electrode geometry [52]. Others include ensuring appropriate electrolyte chemical composition, temperature and understanding corrosion rate behaviour of the test electrode. Solution resistance uncertainty can be eliminated by application of AC impedance which is reviewed in the next paragraphs.

2.6 Alternating Current (AC) Corrosion Measurement

The alternating current (AC) corrosion measurement, known as AC impedance or electrochemical impedance spectroscopy (EIS) technique is performed over a range of low magnitude polarising voltages in the same way as LPR. It involves the application

of a small-amplitude sinusoidal potential perturbation on the sample at a number of discrete frequencies (ω). The resulting current waveform at each applied frequency will display a sinusoidal response that is out of phase with the applied potential thereby yielding values of resistance and capacitance which can give information on the corrosion behaviour and rates, and also an idea of the corrosion rate-controlling mechanisms at the material-electrolyte interface (especially in the presence of an adsorbed film or material coating) [43]. AC voltages have variable magnitudes with both anodic and cathodic polarity in each polarisation cycle. The applied voltage amplitude can range from 5 to 20 mV centred on the free corrosion potential with resulting frequencies for the impedance measurements from 100 kilohertz to a few millihertz [43].

The measurement is possible because an electrical double layer (EDL) (a charge separation between the metal surface and the solution) can have electrical properties similar to those for a simple electrical circuit composed of resistors and a capacitor as illustrated in Figure 2.7. Impedance is the AC analogue of DC resistance. It is a term used to describe the resistance to the flow of electrons in AC circuits with capacitors and inductors. An EDL capacitive reactance (C_{edl}) is similar to the capacitor capacitance, which is determined by the type of metal with its associated electrolyte composition. The charge-transfer resistance (R_{ct}) is similar to corrosion resistance, which resists the transfer of excess electrons to electrochemically active species whilst R_s is the solution resistance.
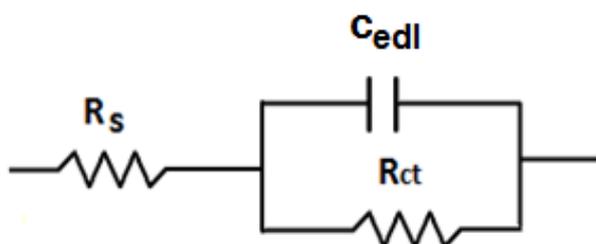
Figure 2.7: Simple electrical circuit having electrical properties similar to an EDL [43].

A capacitor or inductor takes time to reach full charge i.e. relaxation, and this charging period presents a shift between current and voltage amplitude curves as shown in Figure 2.8. This shift (or phase angle) and its magnitude are different for each polarising voltage frequency and tend to be plotted as positive quantities for EIS data irrespective of the fact that their values are negative [43].
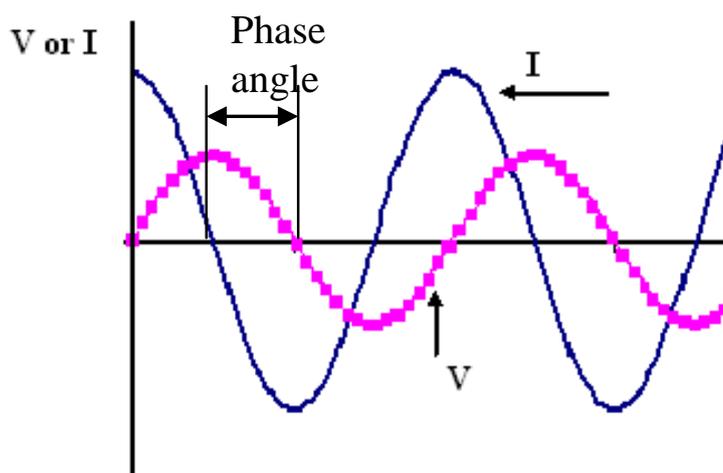
Figure 2.8: AC voltage and current response [43].

AC (and DC) current and voltage are vectors and consequently so is impedance. An impedance vector can be resolved into components as shown in Figure 2.9, where the impedance is a solid arrow and the components are dashed arrows.
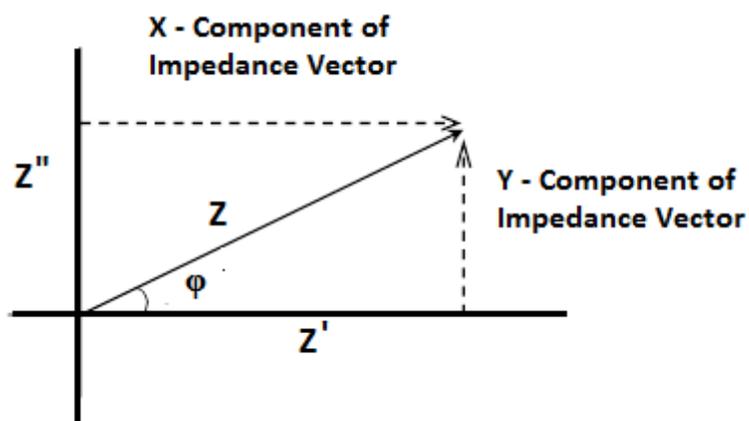
Figure 2.9: An impedance vector resolved into X-Y components [43].

Hence, the total impedance Z(ω) of the electrochemical interface can be written as:

$$Z(\omega) = \frac{E}{I} = Z' + jZ'' \qquad (2.33)$$

where $\omega = 2\pi f$, the angular frequency, E is the voltage (V), I is the current (A) Z' is real impedance magnitudes, Z'' is imaginary impedance magnitudes and $j = \sqrt{-1}$.

For a simple circuit in Figure 2.7 [43],

$$Re(Z) = Z'(\omega) = R_s + \frac{R_{ct}}{1+(\omega R_{ct} C_{dl})^2} \qquad (2.34)$$

$$Im(Z) = Z''(\omega) = \frac{j[-\omega R_{ct}^2 C_{dl}]}{1+(\omega R_{ct} C_{dl})^2} \qquad (2.35)$$

$$Mag(Z) = |Z| = \sqrt{(Z'^2 + Z''^2)} \qquad (2.36)$$

and phase angle,

$$\varphi = \tan^{-1}\left(\frac{Z''}{Z'}\right) \qquad (2.37)$$

From the above, it is evident that each polarising voltage frequency gives a different magnitude for phase angle, total impedance and the component vectors. Unlike DC polarisations, which cause ions to move in one direction for each DC magnitude and polarity, AC voltages cause ions to move back and forth between counter and working electrodes in response to the changes in polarity during an AC cycle. Hence, electron transfer also moves to and from the working electrode and electrochemically active species during polarisation.

When polarising the sample by applying an AC voltage, the EDL is forced to try and change its chemical composition as fast as the polarising voltage frequency changes. The EDL takes time to change to a composition that corresponds to a given polarising voltage magnitude [43]. A range of frequencies exist where the time it takes for a full polarisation cycle to be completed is similar to the time taken for the EDL composition to change. It is reasonable to assume that the EDL time constant will be part of this

frequency range and essentially determine its location. The response of the EDL to these frequency changes may be different to frequency ranges outside of this region.

It is important to note that the EDL is not the only source of time constants and a given electrode can possess much more than one. Inhibitor films or corrosion products such as iron carbonate ($FeCO_3$) can have capacitive reactance and resistance properties [43]. Water and ions are capable of moving through porous films in response to AC polarisation and the movement of these species is hindered by the morphology of the film which produces a pore resistance.

The equivalent circuit for a corroding, coated metal which would produce two time constants is illustrated in Figure 2.10. The circuit for metallic corrosion is nested inside the coating circuit. Nested circuits are used as opposed to series circuits to indicate that pores in the coating, or regions that are not protected by the coating can cause metallic corrosion as these are areas where the electrolyte has direct access to the metal surface.
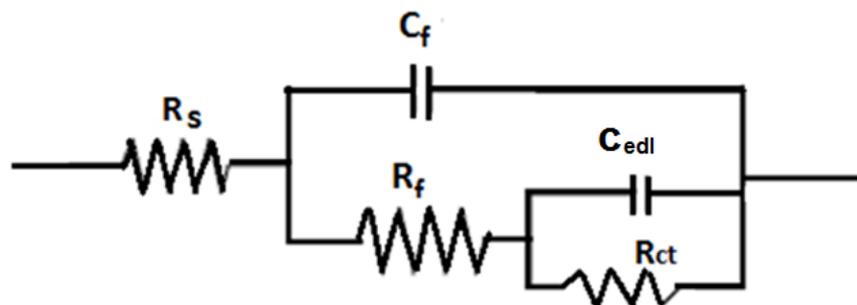
Figure 2.10: Equivalent circuit with two time constants used to model a corroding, coated metal. C_{edl} is the EDL capacitance. R_{ct} is the charge-transfer resistance, C_f is the capacitance of the film, R_f is the resistance of the film and R_s is the solution resistance [43].

2.7 Forms of Aqueous Corrosion Attack

If the ratio of corrosion attack depth to its width is much less than 1, it is termed general corrosion. However, when the depth of the corrosion attack exceeds the width, it is termed localised corrosion. When the ratio gets much greater than 1, then it is defined as pitting corrosion. Other forms of localised corrosion can be galvanic corrosion, flow-induced corrosion, mesa attack, etc. If the attack is as a result of stress, it is termed stress corrosion e.g. hydrogen damage, hydrogen induced cracking, stepwise cracking, stress orientated hydrogen cracking and sulphide cracking). Other types of corrosion attack includes, fretting (induced in between contacts with loads), cavitation corrosion (bubble collapse), microbial induced corrosion (MIC), corrosion under insulation (CUI) and erosion-corrosion (solid particle impingement) [50]. Detailed information on these forms of aqueous corrosion attack with their distinguishing features can be located in reference [50, 51], but a review of uniform corrosion, pitting, galvanic corrosion, flow-induced corrosion and erosion-corrosion commonly encountered in oil and gas production pipelines is presented in the next paragraphs.

2.7.1 Uniform Corrosion

Uniform corrosion is defined as corrosion which causes a uniform loss of wall thickness which is observed over the entire surface area of the metal exposed to the same conditions as illustrated in Figure 2.11. Wall thickness measurements and corrosion rates measured from weight loss coupons, linear polarisation resistance (LPR) or electrical resistance (ER) probes can be used to monitor the extent of the internal damage caused by uniform corrosion where corrosion occurs uniformly over the entire surface of the metal component.

It can be practically controlled by cathodic protection, use of coatings or paints, or simply by specifying a corrosion allowance (CA). In other situations, uniform corrosion gives colour and appeal to a surface. Two cases in this respect are the patina created

by naturally tarnishing of copper roofs and the rust hues produced on weathering steels and in these cases the general corrosion rate is high then decreases [58].
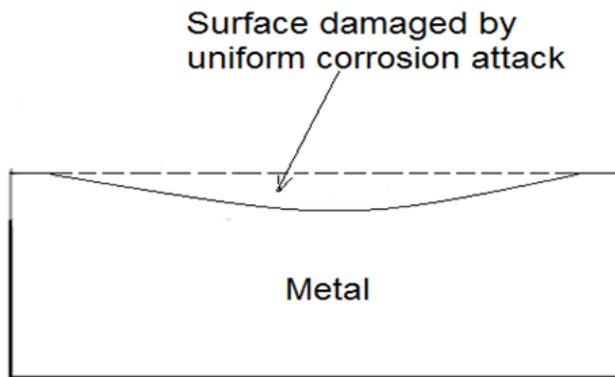
Figure 2.11: Illustration of general corrosion.

2.7.2 Pitting Corrosion

Pitting is an extremely localised form of attack where the wall loss is confined to a very small area of the surface. The conditions within the pit can quickly become increasingly aggressive causing corrosion pits to rapidly advance through the wall thickness whilst the vast majority of the pipe or vessel wall remains unaffected. This can lead to very rapid failures as the pit quickly penetrates the wall. This form of attack is one of the main forms of corrosion observed in corrosion resistant alloys, however it is also found with corrosion of carbon steels. Common pit shapes can be divided in two types: through pits and tunneling pits as shown in Figure 2.12. Pitting attack can occur as discrete localised corrosion or can be extensive over an entire surface (wide, shallow pits) and present as a more uniform attack [51].
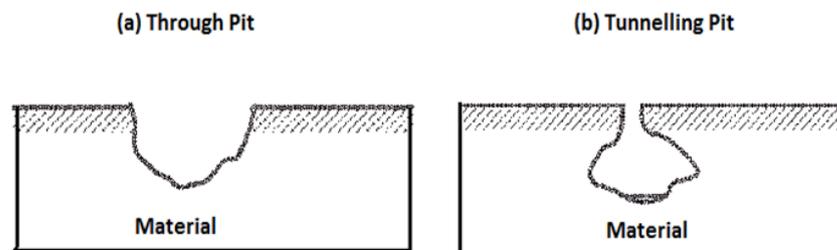
Figure 2.12: Two types of pitting corrosion attack (a) through pit and (b) tunnelling pit [58].

2.7.3 Galvanic Corrosion

Galvanic corrosion occurs at the junction of two dissimilar metals which are in electrical contact with each other as shown in Figure 2.13. According to their relative positions within the galvanic series one metal will be protected from corrosion at the expense of the other. Depending on the relative surface areas of each metal this form of corrosion can proceed extremely quickly. If the cathodic metal is much larger than the anodic metal surface then the observed corrosion rates can be extremely high as a large cathodic area is driving corrosion at a relatively small anodic point. A typical example is found in preferential weld corrosion (PWC).
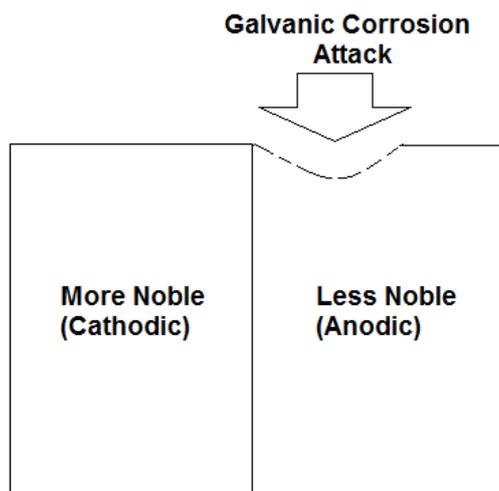
Figure 2.13: Illustration of galvanic corrosion.

To prevent corrosion attack of the weld metal the addition of more noble elements (such as Ni, Cu, Cr, Mo) has been proposed in order to make the weld more cathodic [59]. Also, knowledge of the galvanic series of metals/alloys (Figure 2.14) and standard emf series of metals (Table 2.2) are important in preventing PWC and other galvanic corrosion attack.

This is because the galvanic series allows one to determine which metal or alloy in a galvanic couple is more active. Metals that are more anodic in a given galvanic cell are prone to corrode by metal dissolution or oxidation. The more cathodic material is more corrosion resistant (i.e., more noble). However, it is important to note that metals

behave differently in different environments. The relative positions of metals and alloys in the galvanic series can vary significantly from one environment to another. The position of alloys in the galvanic series for seawater is not necessarily valid in non-saline solutions. For example, aluminium is anodic to zinc in an aqueous 1 M sodium chromate (Na_2CrO_4) solution and cathodic to iron in an aqueous 1 M sodium sulphate (Na_2SO_4) solution [60, 61].
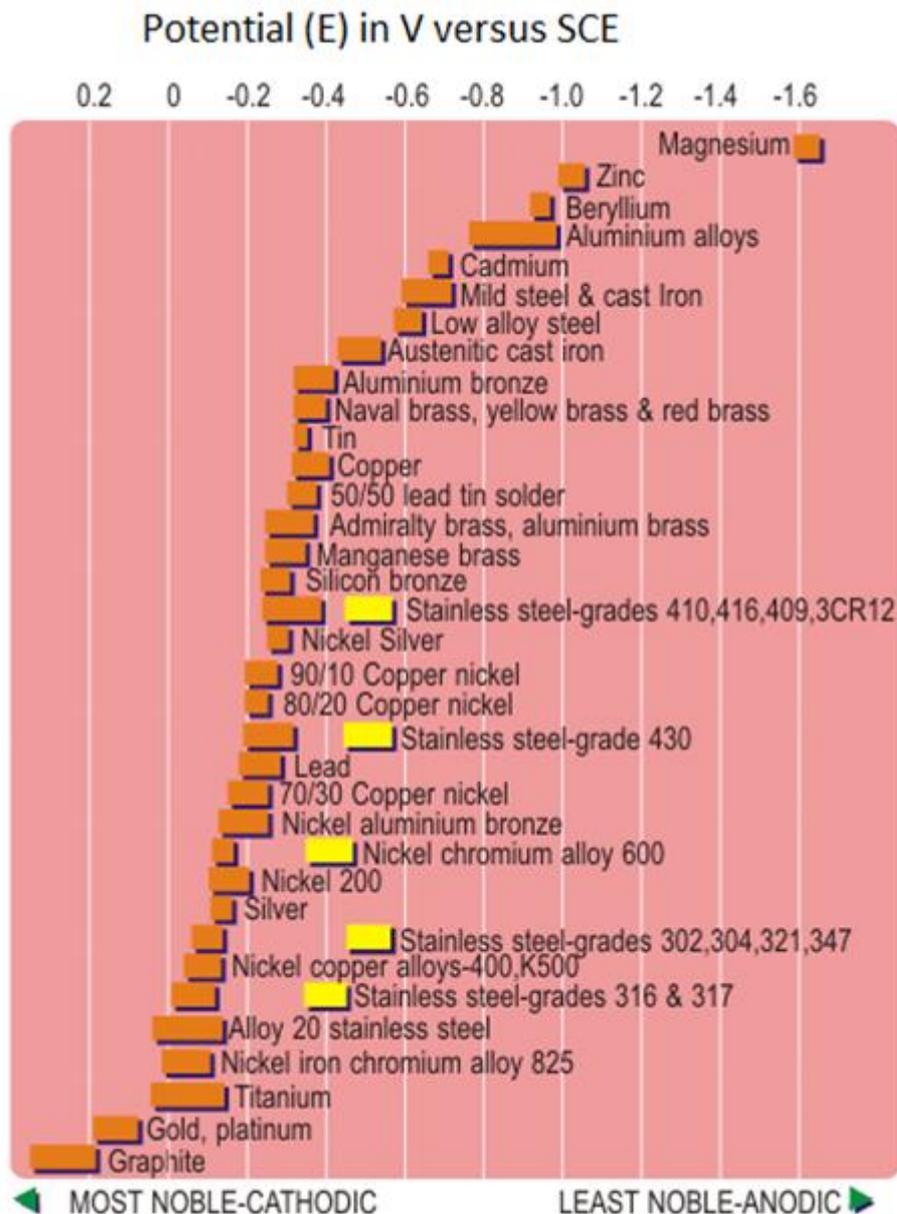
Figure 2.14: Galvanic series of metals and alloys according to ASTM 982-98.

Table 2.2: Standard emf series of metals [58]

Metal-metal ion equilibrium	Electrode potential versus SHE
Noble or cathodic	
Au-Au^{3+}	1.498
Pt-Pt^{2+}	1.200
Pd-Pd^{2+}	0.987
Ag-Ag^{+}	0.799
Hg-Hg^{2+}	0.788
Cu-Cu^{2+}	0.337
H$_2$-H^{+}	0.000
Pb-Pb^{2+}	-0.126
Sn-Sn^{2+}	-0.136
Ni-Ni^{2+}	-0.250
Co-Co^{2+}	-0.277
Cd-Cd^{2+}	-0.403
Fe-Fe^{2+}	-0.440
Cr-Cr^{2+}	-0.744
Zn-Zn^{2+}	-0.763
Ti-Ti^{3+}	-1.210
Ti-Ti^{2+}	-1.630
Al-Al^{2+}	-1.662
Mg-Mg^{2+}	-2.363
Na-Na^{+}	-2.714
K-K^{+}	-2.925
Active or Anodic	

The behaviour of the different metals and alloys can be deduced from emf series on Table 2.2 above. This is a table that lists in order the standard electrode potentials of specified electrochemical reactions. The potentials are measured against a standard hydrogen reference electrode when the metal is immersed in a solution of its own ions at unit activity. Similar to the galvanic series, it is a list of pure metals arranged according to their relative potentials in a given environment. Generally, the relative positions of metals and alloys in both emf and galvanic series are the same. An exception is the position of cadmium with respect to iron and its alloys. In the emf series, cadmium is cathodic to iron, but in the galvanic series (at least in seawater), cadmium is anodic to iron. Thus, if only the emf series were used to predict the behaviour of a ferrous metal system, cadmium would not be chosen as a sacrificial protective coating, yet this is the principal use for cadmium plating on steel.

2.7.4 Flow-Induced Corrosion and Erosion-Corrosion

Flow-induced corrosion (without sand) or erosion-corrosion (with sand) is a faster form of corrosion attack than would otherwise be expected in a given environment due to high flow conditions or localised turbulence. The increased corrosion damage is caused by the high shear stresses stripping away protective corrosion product films and increasing the transport of the corrodent in the system to the metal surface. This form of corrosion is often observed in copper structures but can affect any material susceptible to corrosion. It can be prevented by the use of more resistant alloys, surface engineering, changes in design, changes in environment, cathodic protection, removal of suspended solids, and reduction in temperature.

2.8 Summary

Corrosion has been defined as metal degradation due to its reaction with the environment. It can be either dry or wet. Dry corrosion occurs at extreme high temperature while wet or aqueous corrosion occurs at lower temperature in the presence of aqueous solution. Two approaches used in investigating aqueous corrosion were identified. One is corrosion thermodynamics through Nernst Equation and/or Pourbaix diagram and two is corrosion kinetics which may be activation controlled and/or diffusion controlled.

It has also been shown that corrosion rates can be determined through electrochemical test methods such as DC method e.g. LPR, TP, PD and Cyclic Polarization (CP)) and AC method (Electrochemical Impedance Spectroscopy (EIS) also known as AC Impedance). The forms of attack of aqueous corrosion include uniform corrosion, localized (pitting, flow-induced, galvanic) corrosion, and erosion-corrosion were also explained. The interest in this study is aqueous corrosion in dynamic CO_2 environment, hence the next chapter deals with literature review covering previous research activities on the mechanisms, controlling factors, mitigation and modelling of CO_2 corrosion and pure erosion and erosion-corrosion.

Chapter 3 Literature Review I

This chapter reviews the literature aspect involving previous research activities on CO_2 corrosion (in terms of meaning, mechanisms, controlling factors, mitigation and models); sand erosion (in form of meaning, mechanisms and prediction) and CO_2 erosion-corrosion (with regards to its meaning, controlling factors, mechanisms, prediction and mitigation).

3.1 CO_2 Corrosion

CO_2 corrosion, also known as sweet corrosion, constitutes the major form of corrosion attack in oil and gas pipelines [8, 9]. It occurs because of CO_2 co-produced with hydrocarbon or from CO_2 injection system used in secondary (enhanced) oil recovery process. CO_2 dissolves in water to form carbonic acid which is highly corrosive to carbon steel used in oil and gas production. Sweet corrosion manifests as either uniform corrosion (less severe) or localised (pitting, mesa-attack, flow-induced) corrosion which is very severe and most dangerous [19]. Knowledge of the mechanisms and mode of attack is necessary so as to be able to understand the attack and predict material performances more accurately thus operating safely and avoiding unplanned production downtimes.

As a result, many researchers [2, 3, 4, 8-30] have worked extensively to establish the mechanisms, controlling factors, mitigation and predictive models of CO_2 corrosion. The knowledge gained here is summarised under mechanisms, controlling factors, mitigation and predictive models of CO_2 corrosion.

3.1.1 Mechanisms

Different researchers have proposed different mechanisms of CO_2 corrosion. Some suggested that the carbonic acid undergo direct reduction at the steel surface [2] while many proposed that the carbonic acid which is a weak acid partially dissociates to electrochemical species (H_2CO_3, H^+, HCO_3^-) that undergo chemical reactions with iron

to produce the corrosion products [57, 58]. All of them point to the fact that the mechanisms involve anodic dissolution of iron and cathodic release of hydrogen gas. A comprehensive review of the mechanism of CO_2 corrosion with different arguments on the rate determining step (RDS) can be located in the work of Kermani and Morshed [9].

A summary of the mechanism is presented here following the work of Dayalan *et al* [3].

3.1.1.1 Carbonic Acid Formation and Dissociation

CO_2 is soluble in water and dissolves in it to form carbonic acid (H_2CO_3), a weak acid compared to mineral acids, since it does not fully dissociate.

$$CO_2(g) \rightarrow CO_2\ (aq) \tag{3.1}$$

$$CO_2(g) + H_2O(l) = H_2CO_3(aq) \tag{3.2}$$

H_2CO_3 is diprotic and partially dissociates in two steps to form bicarbonate and carbonate ions [3]

$$H_2CO_3 = H^+ + HCO_3^- \tag{3.3}$$

$$HCO_3^- = H^+ + CO_3^{2-} \tag{3.4}$$

The homogenous dissociation reactions (3.3) and (3.4) proceed much faster than other simultaneous processes in the system. Both the CO_2 dissolution (3.1) and the CO_2 hydration (3.2) reactions have been known to be much slower [30].

3.1.1.2 Species Transfer to the Steel Surface

The species are transported to the steel surface for the corrosion reactions

$$H_2CO_3\ (bulk\ electrolyte)\ \rightarrow\ H_2CO_3\ (steel\ surface) \tag{3.5}$$

$$HCO_3^-(bulk\ electrolyte)\ \rightarrow\ HCO_3^-\ (steel\ surface) \tag{3.6}$$

$$H^+(bulk\ electrolyte)\ \rightarrow\ H^+(steel\ surface) \tag{3.7}$$
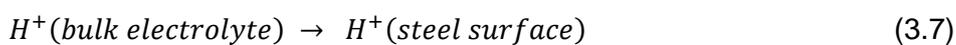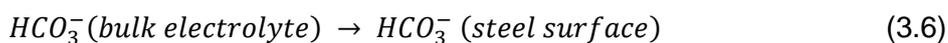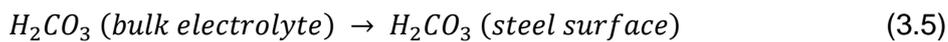
3.1.1.3 Cathodic Reduction and Anodic Oxidation

Cathodic:

$$2H_2CO_3 + 2e^- = H_2 + 2HCO_3^- \tag{3.8}$$

$$2HCO_3^- + 2e^- = H_2 + 2CO_3^{2-} \tag{3.9}$$

$$2H^+ + 2e^- = H_2 \tag{3.10}$$

The evolution of hydrogen in reaction (3.10) is believed to be one of the main cathodic reactions. This reaction is limited by the rate at which H$^+$ can be transported from the bulk solution to the steel surface [30].

Anodic:

The anodic dissolution of iron in acid solution is as follows:

$$Fe = Fe^{2+} + 2e \tag{3.11}$$

This anodic reaction has been investigated by researchers [62, 63, 64], with several multi-step mechanisms being used to explain experimental results. Most of the investigations seem to agree with the mechanism proposed by Bockris et al. [65], which represents the behaviour of the metal in strong acidic conditions.

3.1.1.4 Corrosion Product Transfer to the Bulk Electrolyte Solution

$$CO_3^{2-} \ (steel\ surface) \rightarrow CO_3^{2-} \ (bulk\ electrolyte) \tag{3.12}$$

$$Fe^{2+} \ (steel\ surface) \rightarrow Fe^{2+} \ (bulk\ electrolyte) \tag{3.13}$$
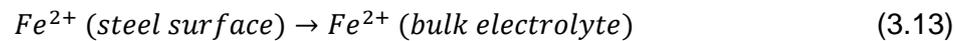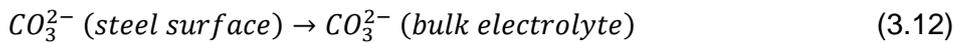
An important aspect of the mechanism is iron carbonate (FeCO$_3$) film or scale formation and it is observed that higher temperatures (> 70°C) promote its formation [9] on the corroding surface. The scales or films can be protective at high temperature or non-protective depending on the conditions which they are formed. When FeCO$_3$ precipitates at the steel surface, it can retard corrosion process by creating a diffusion barrier for the species involved in the corrosion process and/or covering (inhibiting) a

portion of the steel surface [9]. A detailed discussion on CO_2 corrosion mechanisms involving protective film formation is contained in the work of Dayalan *et al* [4].

The films form when the concentrations of Fe^{2+} and CO_3^{2-} ions exceed the solubility limit [66].

$$Fe^{2+} + CO_3^{2-} \rightarrow FeCO_{3(s)} \tag{3.14}$$
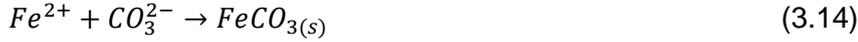
The tendency of the iron carbonate film to form or the scaling tendency (ST) can be defined as the ratio of the precipitation rate (PR) to corrosion rate (CR) and expressed as follow [66]:

$$ST = \frac{PR}{CR} \tag{3.15}$$

where, precipitation rate is a function of $FeCO_3$ supersaturation SS, the solubility K_{sp}, the temperature through Arrhenius Law ($k_r = e^{A - \frac{B}{RT}}$) and surface area-to-volume ratio $\frac{A}{V}$ which is given as [66]:

$$PR = k_r \frac{A}{V} K_{sp}(SS - 1)(1 - SS^1) \tag{3.16}$$

and, supersaturation is defined as ratio the products of the species concentrations ($Fe^{2+} CO_3^{2-}$) to the solubility limit (K_{sp}) [66]:

$$SS = \frac{Fe^{2+} CO_3^{2-}}{K_{sp}} \tag{3.17}$$

Hence, it can be seen that higher supersaturation gives higher precipitation which in turn produces lower corrosion rates and Kermani and Morshed [9] have observed that higher pH values and higher temperatures favour higher supersaturation and precipitation.

3.1.2 Controlling Factors

In addition to the $FeCO_3$ film mentioned above, many researchers [2, 3, 4, 8-30] have observed that there are many factors that affect sweet corrosion. These factors have been reviewed in detail by Kermani and Morshed [9]. They include environmental

factors (solution chemistry/super-saturation, CO_2 partial pressure, temperature, *in-situ* pH, effect of H_2S, effect of acetic acid); physical factors (water wetting, effect of wax, effect of crude oil, flow and erosion); and metallurgical factors (steel composition, heat treatment and steel microstructure).

3.1.3 Mitigation

 CO_2 corrosion in oil and gas production can be mitigated by using corrosion inhibitors, lowering CO_2 partial pressure or modifying chemistry of the environment e.g. increase pH, changing operational parameters e.g. flow, temperature, etc, using internal surface resistant coating e.g. fusion bonded epoxy, phenolic-modified epoxy; and using more corrosion-resistant materials e.g. 13% Cr steel or duplex steel either in the solid form or as cladding on carbon steel [9].

3.1.4 Models

 The earliest and simplest predictive model was developed in late 1950s by American Petroleum Institute (API) which was in form of 'Rule of Thumb' requirement based on CO_2 partial pressure for carbon and low-alloy steels [9]. It predicted qualitative severity rather than quantitative corrosion rates in mm per year. The 'Rule of Thumb' model is summarized in Table 3.1 in the next paragraph.

Table 3.1: API rule of thumb CO_2 corrosion model [9]

S/N	CO$_2$ Partial Pressure p_{CO_2} (bar)	Level of Corrosion
1.	$p_{CO_2} < 0.5$	Corrosion unlikely
2.	$0.5 < p_{CO_2} < 2$	Possible Corrosion
3.	$p_{CO_2} > 2$	Corrosion likely

Later in 1975, a quantitative model was developed by de Waard and Milliam [2] which replaced the qualitative 'API rule of thumb'. This development led to several researches that have developed several models today which will be summarized under empirical [13-17], semi-empirical [18-22] and mechanistic [3, 4, 23-30, 62, 67] models.

3.1.5 Empirical Models

These models are data driven and rely mostly on measured corrosion rates [49]. Variables and parameters are fitted directly to corrosion rate data and the calculated corrosion rate is an interpolation of the experimental data.

Examples of CO_2 corrosion empirical models include LIPUCOR [13], NORSOK [14], SWEETCOR [15], CORPOS [16] and CBR-TS [17] which are summarised in Appendix 1 based on their input parameters. Here, NORSOK model [14, 49, 68] is used to illustrate the mathematical equation of an empirical model. The model was developed by the Institute for Energy Technology (IFE), Norway using large amount of flow loop experimental data. A comprehensive discussion on the model can be located in reference [68] with governing equation given by [49]:

$$CR_{NOR} = K_t f_{CO_2}^{0.62} \left(\frac{\tau_w}{19}\right)^{0.146+0.0324 log\left(f_{CO_2}\right)} f(pH)_t \qquad (3.18)$$

where, CR_{NOR} is the NORSOK model corrosion rate in mm/year, K_t is temperature dependent constant, f_{CO_2} is the fugacity of CO_2, τ_w is the wall shear stress in Pascal (Pa), and $f(pH)_t$ is a complex function of pH and temperature, t in ^{o}C.

3.1.5.1 Semi-Empirical Models

The CO_2 corrosion semi-empirical models are similar to empirical model which rely on parameters fitted to corrosion rate but physical and chemical processes are represented in semi-empirical equations with some unknown parameters which must be fitted to measure corrosion rate [49]. Just like empirical models, extrapolation and experimental data requirements are the major setbacks of semi-empirical models [49].

A good example of semi-empirical CO_2 corrosion model is the popular de Waard and Milliams (DM) Model [2] developed in 1975 from their corrosion experiments which they performed using stirred beakers and determined corrosion rates by means of weight loss coupons and polarization resistance measurements. Their corrosion rate is given as follows [2]:

$$log(CR) = 5.8 - \frac{1,710}{T} + 0.67log(f_{CO_2}) \tag{3.19}$$

where, CR is the corrosion rate in mm/year, T is temperature in Kelvin (K) and f_{CO_2} is the fugacity of CO_2 in bar. The result of the model was in form of CO_2 corrosion nomogram shown Figure 3.1.

The de Waard and Milliams (DM) Model [2] was modified in 1993 to cater for the effect of protective film of $FeCO_3$ on the corrosion rate at higher temperatures [11] and in 1995 to account for flow independent kinetics (V_r) and the flow dependent mass transfer (V_m) of CO_2 using a simple resistance model as follows [12];

$$\frac{1}{V_{corr}} = \frac{1}{V_r} + \frac{1}{V_m} \tag{3.20}$$

Other selected semi-empirical models are summarised in Appendix 2 based on their input parameters.
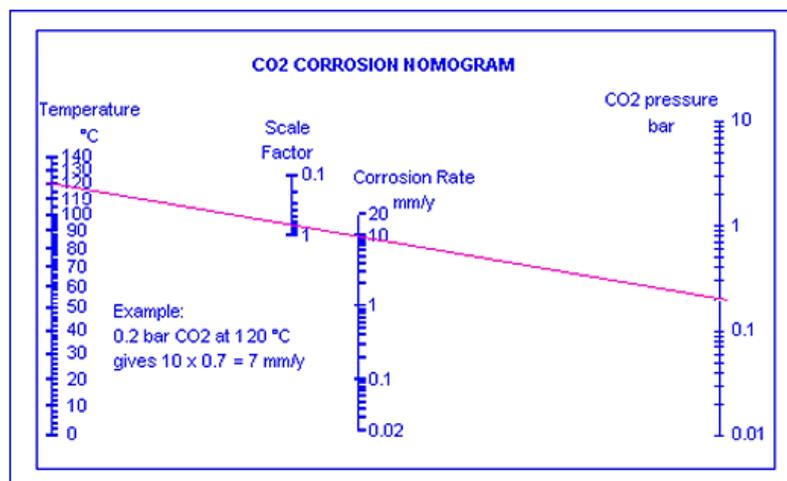
Figure 3.1: CO$_2$ corrosion nomogram [43].

3.1.5.2 Mechanistic Models

 Mechanistic CO_2 corrosion models, unlike empirical and semi-empirical do not rely on measured experimental corrosion rate data [49]. Rather, calculations are predictive with variables extrapolated within the limits of theories, and may be extended to new systems. Its major challenge is that it does not guarantee that the models represent

measured corrosion rate data unless it is validated with experimental data [49]. But its merit is that it provides greater insight into the critical variables driving the overall corrosion mechanism [49] and therefore suggests strategies for minimizing the CO_2 corrosion risk during design and operation. Examples of mechanistic models include Tulsa [3], HYDROCOR [23], KSC [24], Ohio [25], OLI [26], DREAM [27], MULTICORP [28], WWCORP [29] and FREECORP [30]. These models are summarised in Appendix 3 based on their input parameters.

Nesic *et al* model [24, 62, 63] is a mechanistic electrochemical model of CO_2 corrosion that combines two cathodic reactions (the reduction of hydrogen ions H^+, and carbonic acid H_2CO_3) with single anodic reaction, the dissolution of iron. The corrosion potential and current densities are determined by applying the equality [63]:

$$\sum i_c = i_a \tag{3.21}$$

Individual current densities for activation (from Butler-Volmer equation) and diffusion (from flow condition – mass transfer and Sherwood number) for the cathodic reactions are calculated, summed together ($i_{H^+} + i_{H_2CO_3}$) and equated to anodic corrosion current density (i_{Fe}). Once the corrosion current density (i_{Fe}) of the anodic reaction is calculated, it can then be used to determine the corrosion rate (CR (mm/year) as follows:

$$CR = \frac{i_{Fe}M_{w,Fe}}{\rho_{Fe}nF} \tag{3.22}$$

Other CO_2 corrosion models include neural network models [69].

From the foregoing, it is known that the presence of dissolved CO_2 makes the environment corrosive to steel materials and the moving corrosive liquid over the steel surfaces may enhance the corrosion rate. This is because the flow can possibly increase the corrosion rate by increasing the mass transport of reactants and products of corrosion. It can also create shear stress and pressure fluctuations on the surface

thereby challenging the protectiveness of the surface films and ultimately causing wear [70, 71].

It leads to flow-induced CO_2 corrosion which can be defined as the CO_2 corrosion resulting from the effect of turbulence due to moving fluid that does not contain solid particles in sufficient concentration and/or size to impinge on the metal surface [72].

It was established by Efird [73] that the violent, rapidly fluctuating nature of turbulent flow in the viscous region and diffusion boundary layer, and its interactions with the solid surface, is the major reason that mass transfer and wall shear stress are the basic hydrodynamic factors that define the effect of flow on corrosion.

Generally, the corrosion rate in flow-induced corrosion is limited by the mass flow N of one or more components according to the equation [71]:

$$N = -D\nabla c + \vec{v}c \qquad (3.23)$$

where, $-D\nabla c$ is the contribution due to diffusion in the concentration gradient and $\vec{v}c$ is the contribution due to convective diffusion in the moving fluid.

A known solution to this equation for simple flow patterns is expressed in form of dimensionless power laws as follows [71]:

$$Sh = a.Re^b.Sc^c \qquad (3.24)$$

where, Sh is standardised material transport called Sherwood number, Re is the state of flow called Reynolds number, Sc is the Schmidt number which relates the thickness of the hydrodynamic layer and mass transfer boundary layer, a, b and c are constants that depend on material geometry and flow pattern. A detailed discussion on mechanisms of flow-induced CO_2 corrosion has been documented by Efird [73, 74], and Schmitt and Bakalli [75].

In 1993, Efird *et al.* [74] performed flow-induced CO_2 corrosion experiments with three different systems, viz: pipe flow loops (25.4 mm and 12.7 mm pipe diameter), rotating cylinder electrode and jet impingement methods and developed a relationship between corrosion rate and wall shear stress as follows [74]:

$$CR = a\tau_w^b \qquad (3.25)$$

where, CR is the corrosion rate in mm/year, τ_w is the wall shear stress in N/m^2, a and b are constants. They proposed that this equation is only valid for brine but the values of a and b can have different values to extend it to other systems. They stressed that the value of a varies with the temperature, CO_2 partial pressure and the type of flow. They also discovered that data from the pipe flow experiment correlated better with the jet impingement method, whereas the results from rotating cylinders did not adequately predict the corrosion rates. The summary of their results is shown in Figure 3.2 in the next paragraph.
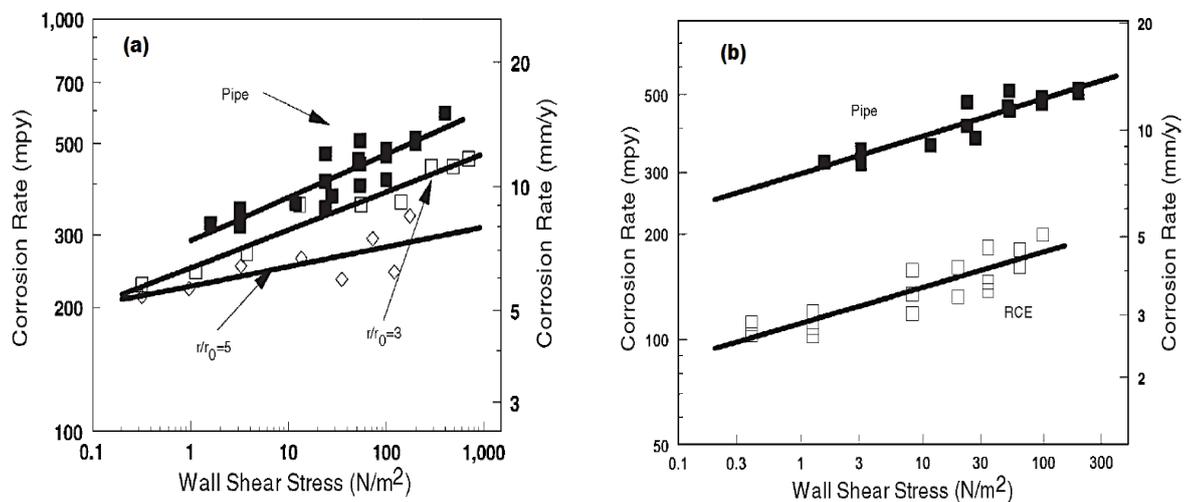
Figure 3.2: Corrosion rate of carbon steel as a function of wall shear stress value for (a) pipe flow and jet impingement rings at r/r$_0$=3 and r/r$_0$=5, and (b) RCE and pipe flow [74].

From 1994 to 1996, Jepson et al. [76] conducted corrosion experiments in a flow loop, at CO_2 partial pressures of up to 0.79 MPa, temperature of 40 to 90°C with oil of different viscosities and water cuts.

They observed that the corrosion rate increased with increase in temperature over their entire range of study for low viscosity, and they further noticed that levels of high shear and turbulence at the bottom of the pipe removed the protective films of corrosion products formed on the pipe wall resulting to high corrosion rate.

On the other hand, the corrosion rate decreased with an increase in oil composition from 0 to 60% and reduced to negligible values for a composition of 80% due to the transition from water continuous phase to oil continuous phase. From their experimental data, they proposed a predictive model which indicates that corrosion rates depend on temperature, CO_2 partial pressure, pressure gradient across the slug and water cut as follows [76]:

$$CR = k p_{CO_2}^c \tau_w^b \qquad (3.26)$$

where, CR is the corrosion rate in mm/year, p_{CO_2} is carbon dioxide partial pressure in MPa, τ_w is the wall shear stress in N/m^2 b and c are constants exponents with values 0.1 and 0.83 respectively and k is constant (mm/year)(MPa)$^{-0.83}$(N/m^2)$^{-0.1}$.

The summary of their major findings is illustrated in Figures 3.3 to 3.6.

They maintained that their model is valid for full pipe flow of low viscosity oils with water cut of up to 60%, CO_2 partial pressures up to 0.79 MPa and temperatures up to 90°C.
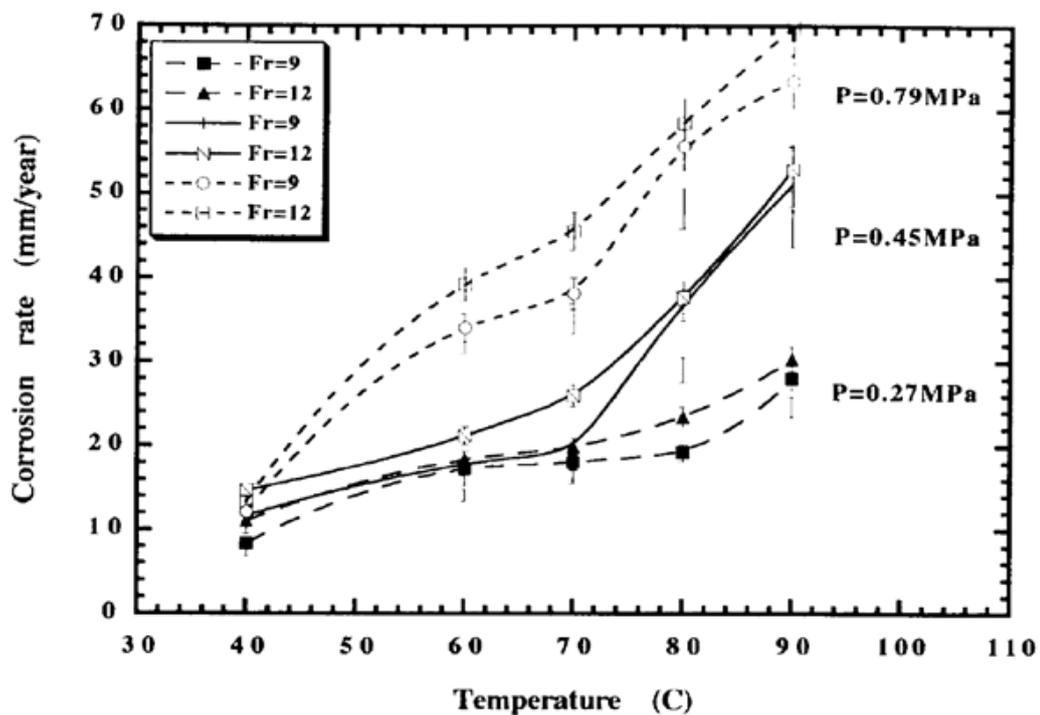
Figure 3.3: Corrosion rate vs. temperature for brine [76].
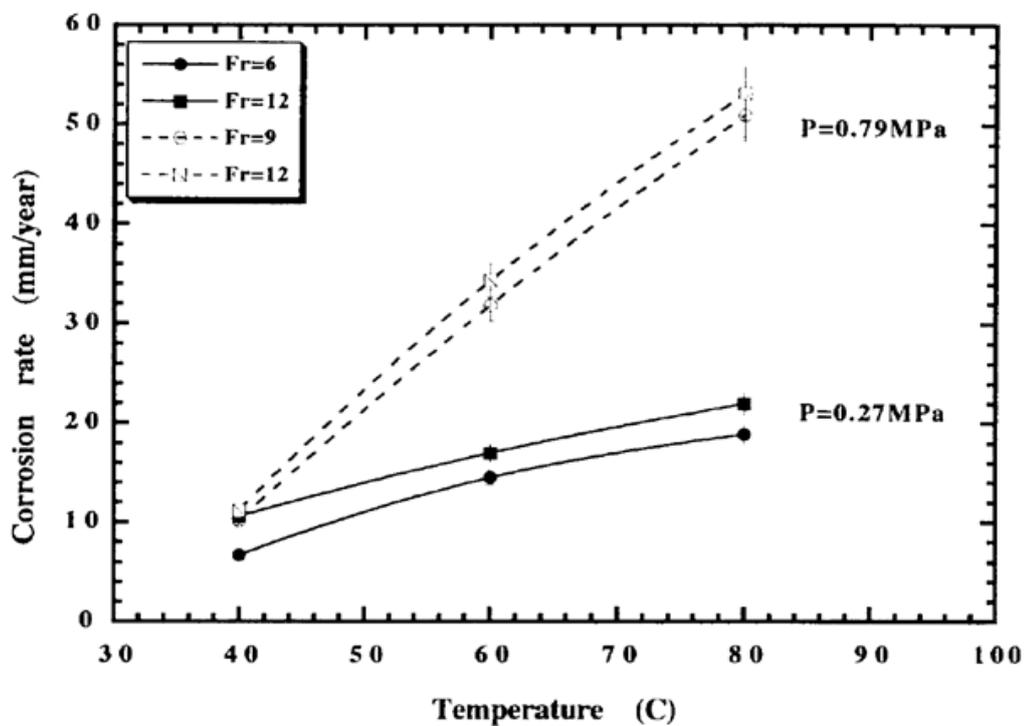
Figure 3.4: Corrosion rate vs. temperature for 80% water cut [76].
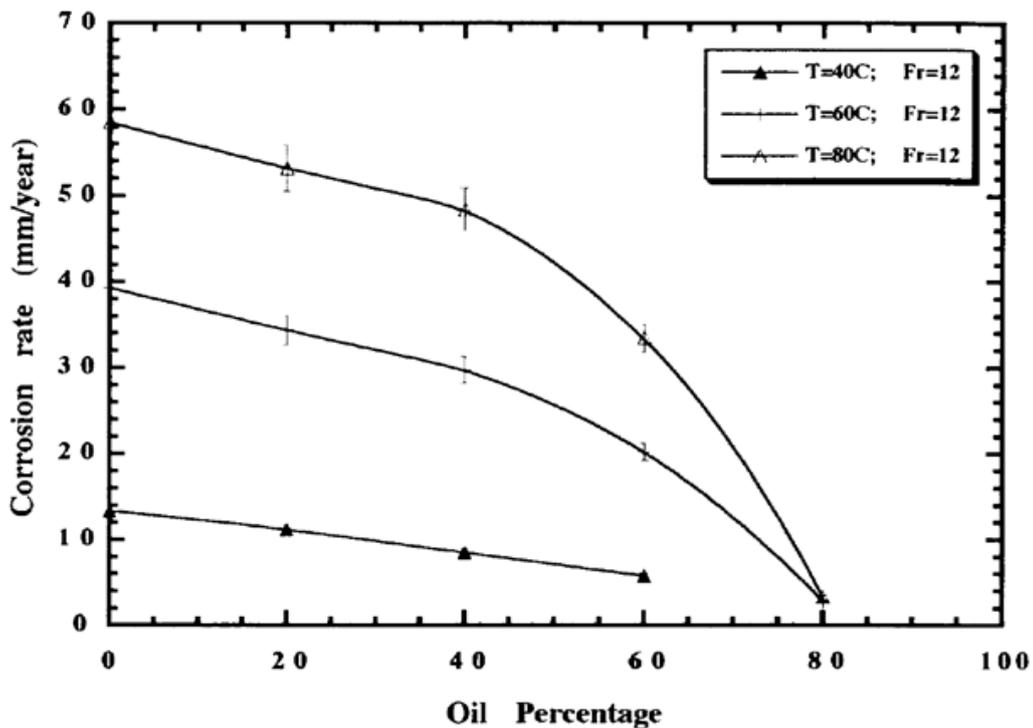
Figure 3.5: Corrosion rate vs. oil composition at CO_2 partial pressure of 0.79 MPa and Froude number of 12 [76].
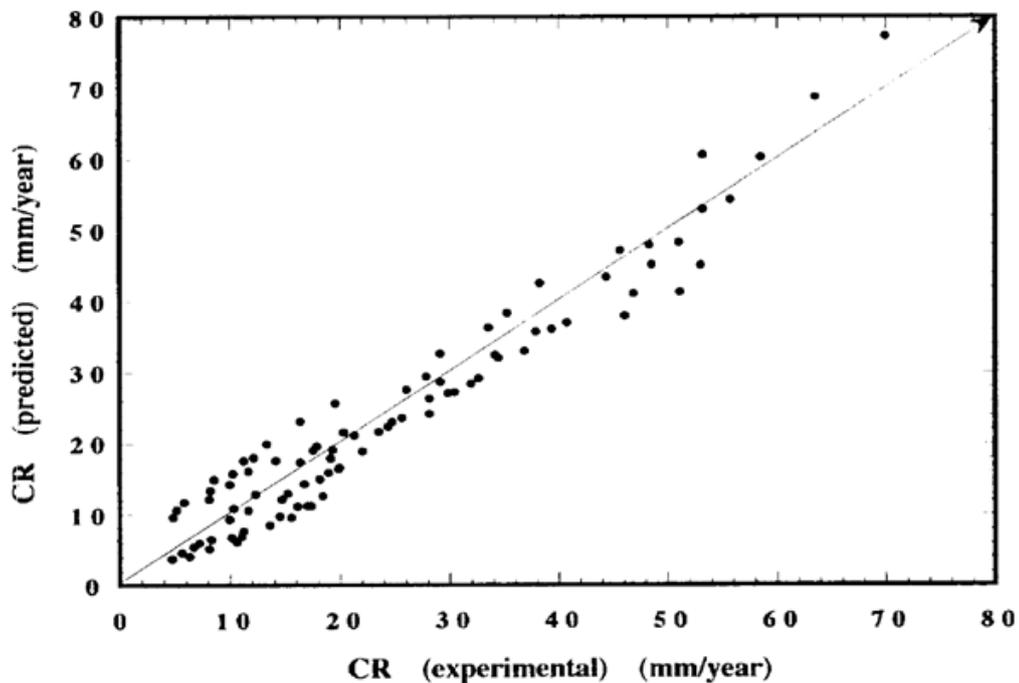
Figure 3.6: Predicted corrosion rate vs. experimental values [76].

Further understanding of flow-induced CO_2 corrosion can be acquired from the works of Dugstad group [18], Nesic group [70], and Hara group [77] for flow loop systems; and Efird group [73, 74, 78], Schmitt group [75] and Neville group [79] for jet impingement set-up. A review of the findings of Dugstad, Nesic, Hara and Neville groups are presented in the next paragraphs.

Using a flow loop, Dugstad group [18] performed corrosion studies involving effect of flow regimes, temperature, CO_2 partial pressure, Cl^- and pH on localised corrosion and formation of corrosion product films along the top and the bottom of the pipe under stratified and annular flow conditions. They observed that localised corrosion is found only at high temperature (90°C) in both Cl^- containing and Cl^- free solutions (with different pitting density). That it also occurs at lower pH (4.5-6.0) while at pH 6.2 very protective films form and no localised corrosion is identified. They maintained that CO_2 partial pressure affects film formation and thus the localised corrosion when a partially protective film is formed and also that corrosion behaviour at the top approached that of the bottom when annular flow is maintained.

Similarly, the Nesic group [70] investigated the influence of velocity (0.2m/s, 1 m/s, and 2 m/s) and CO_2 partial pressure (3, 10 and 20 bar) at pH 5 and 60°C on corrosion rate of X-65 carbon steel in a single-phase flow using a 0.16m I.D inclinable stainless steel high pressure flow loop. They discovered that flow did not affect the anodic reaction at these three CO_2 partial pressures as it was under charge transfer control. They also observed that the cathodic limiting current density became less flow-sensitive with the increase in CO_2 partial pressure although its value increased with the increase in CO_2 partial pressure; this was probably because at such high CO_2 partial pressures, the cathodic limiting current density came largely from the slow chemical reaction of the hydration of dissolved CO_2 into carbonic acid. Recently, they extended their studies to different pH's (3 to 5), temperatures (25 to 50°C), near critical and supercritical CO_2 partial pressures and at equivalent fluid velocities from 0 to 1.5 m/s [70], and they

noticed that the increase in CO_2 partial pressure reduced the flow-sensitivity of CO_2 corrosion rate most probably due to the increase in carbonic acid concentration whose reduction is limited by hydration of dissolved CO_2. Under their test conditions, only iron carbide seems to have formed, and it did not provide sufficient corrosion protection. The flow-sensitivity of CO_2 corrosion was not clearly observed even at a low pH (pH 3). This is opposite to what has normally been observed at a low CO_2 partial pressure and even at a relatively high CO_2 partial pressure, anodic reaction seems not to have been flow-sensitive probably because it was under charge-transfer control.

The summary of their results is illustrated in Figures 3.7 to 3.10.
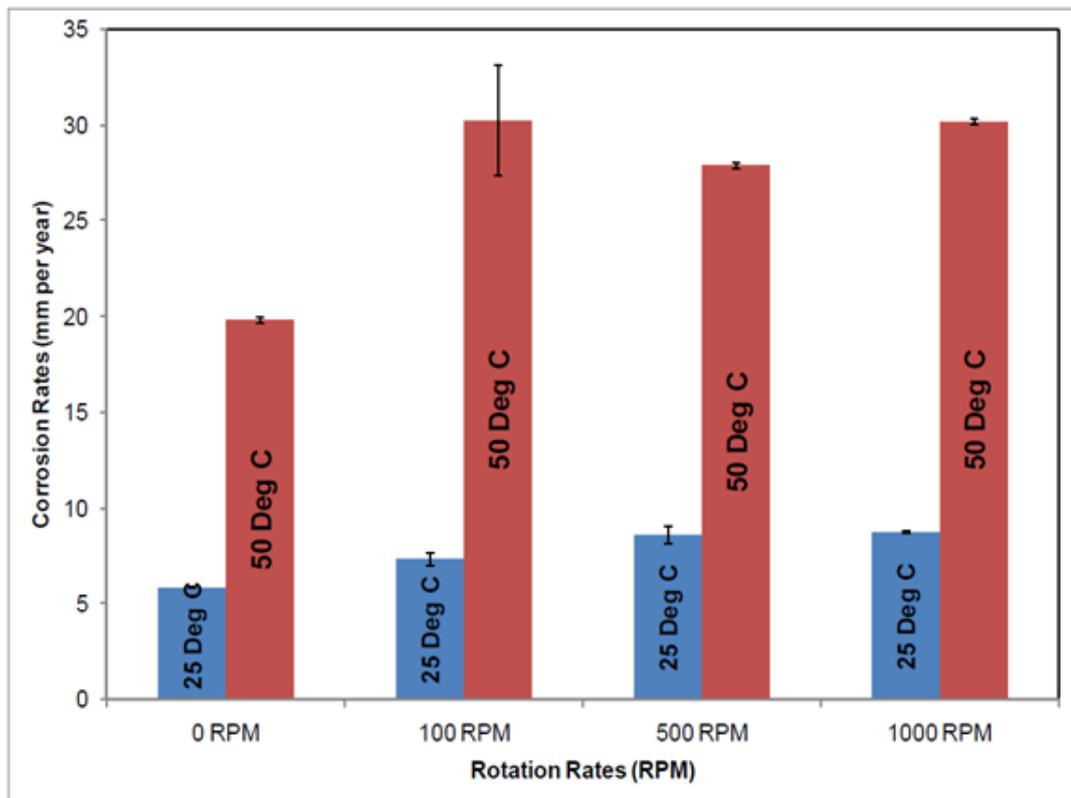
Figure 3.7: Variation of corrosion rate with flow velocity flow velocity and pCO$_2$ = 10 bar at 25°C and 50°C and pH 3 [70].
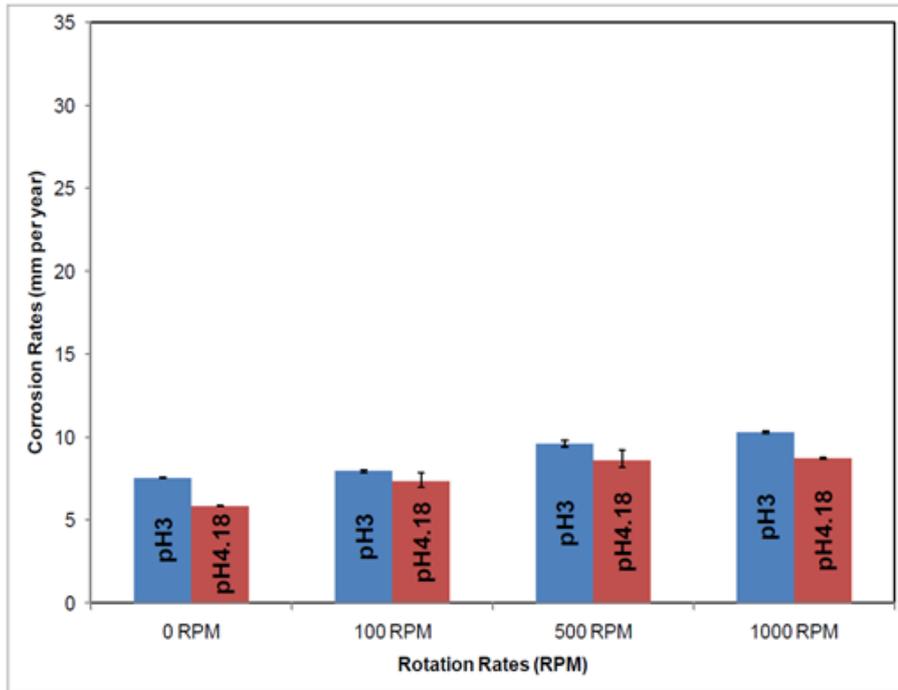
Figure 3.8: Variation of corrosion rate with flow velocity for pH 3 and 4.14 at pCO$_2$ = 10 bar [70].
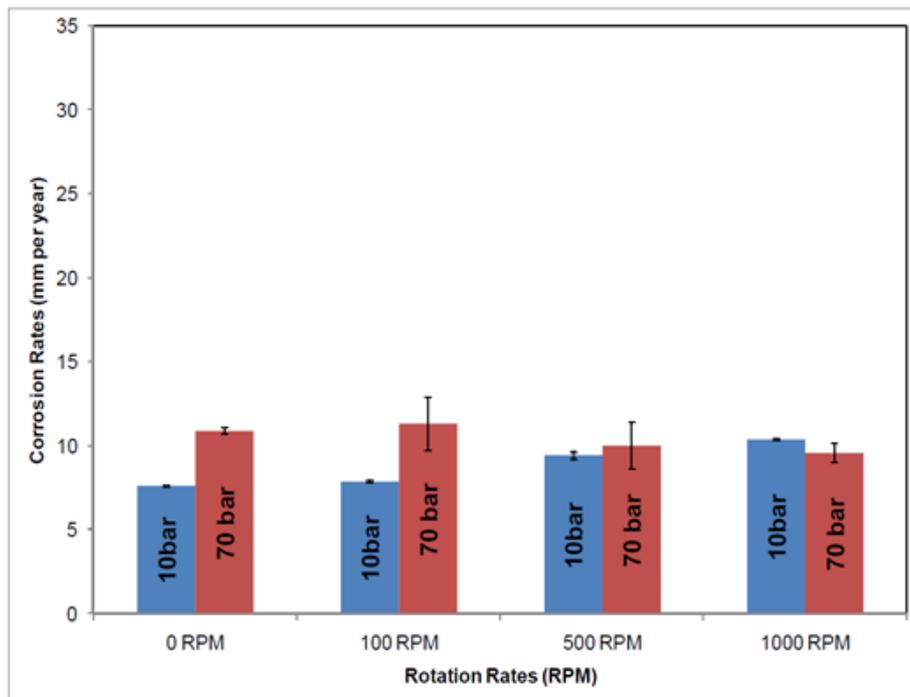
Figure 3.9: Variation of corrosion rate with flow velocity and pCO$_2$ = 10 and 70 bar at 25°C [70].
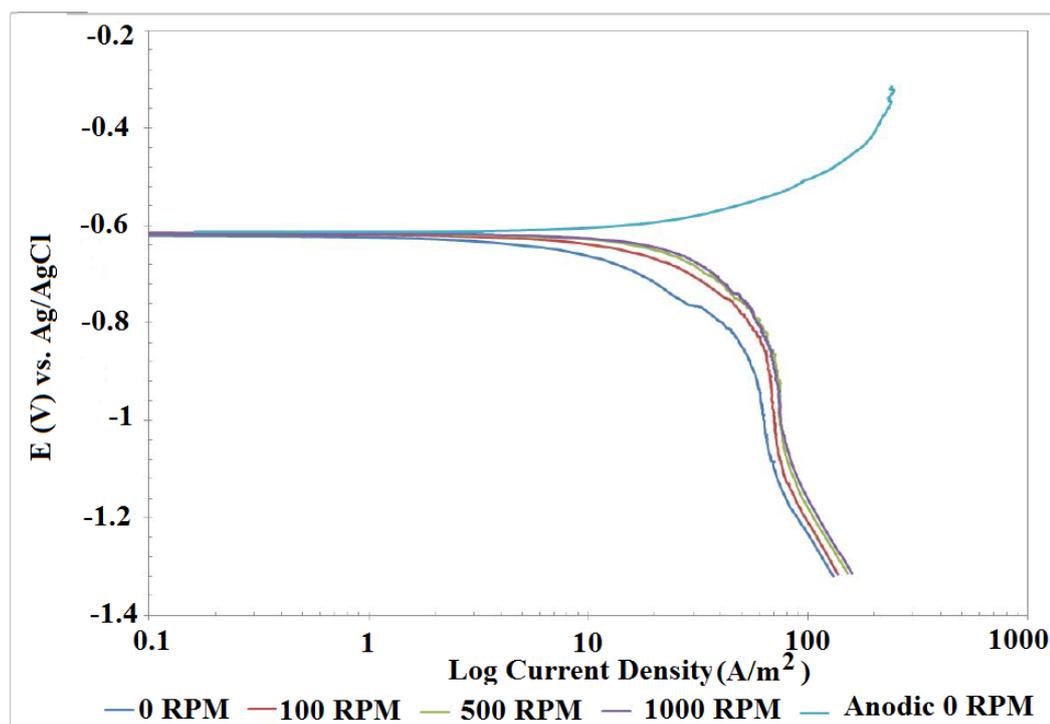
Figure 3.10: Cathodic polarisation curves at pH 3, 25°C and pCO$_2$ = 10 bar [70].

Furthermore, the Hara group [77] investigated the effect of flow on carbon steel (N80), low alloy steel and stainless steels (13%Cr) in a flow loop tester: an autoclave equipped with solution circulation and an external test section. Static experiments were run in the autoclave while flow experiments were run in the external test section. Their tests were performed in non-film forming conditions at various CO_2 partial pressures (4 to 40 bar), temperatures (45 to 180°C), and velocities (2 m/s to 17 m/s) for duration of 96 hours. Corrosion rate was determined from weight loss. Their results suggested that the corrosion rate was under mass transfer control. They further observed that the corrosion rates of the carbon steel and low alloy carbon steel increased with increase in flow velocity and temperature whilst for stainless steel, at 120°C, the corrosion rate was independent of flow velocity up to the highest value of 17 m/s but at both 150 and 180°C, the corrosion rate was independent of flow velocity up to 8 m/s, beyond which it increased with increasing flow velocity as shown in Figure 3.11.
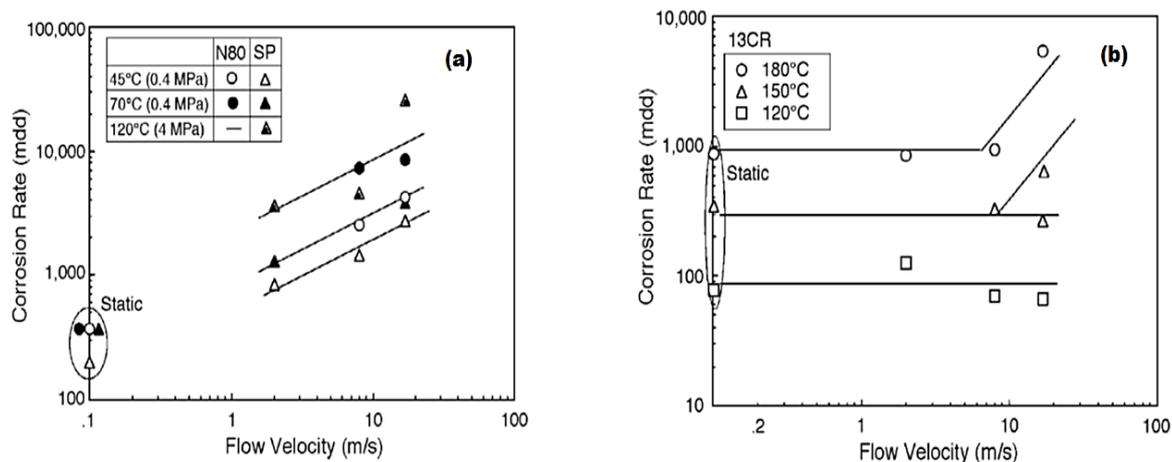
Figure 3.11: Effect of flow velocity and temperature on corrosion rate for (a) carbon steel and low alloy steel and (b) stainless steel (13%Cr) [77].

Their work is considered important as the analysis relates the corrosion rate and the hydrodynamic parameters. The analysis, however, only considered the reduction of proton and neglected the contribution of carbonic acid reduction to the total cathodic current density, yet the Sh number calculated from weight loss must have incorporated the direct reduction of carbonic acid. Without electrochemical measurements, particularly from potentiodynamic sweeps, it may be difficult to conclude that the corrosion rate came mainly from proton reduction; the order of magnitude of the change in corrosion rate due to the change in proton concentration alone is much larger when carbonic acid reduction is also considered [77]. At 40 bar, the effect of flow was observed most probably because the test pH was at the pH value of 3.47 [77]. At this pH, the proton concentration was relatively high. Moreover, the effect of flow at 40 bars was restricted to 120°C where diffusion coefficient is relatively high.

Using the submerged impinging jet rig, the Neville group [79] assessed the flow-induced corrosion of carbon steel pipework in oil and gas production and suggested that the weld material revealed a significantly lower degradation rate compared to both the HAZ and parent metal a reversal of behaviour seen in static conditions in which the weld material had the highest corrosion rate. It is possible that the higher hardness of the weld material in comparison to the HAZ and parent metal may have assisted in

resisting the deformation and removal of material due to the shear on the specimen surface.

The summary of their results is shown in Figure 3.12.
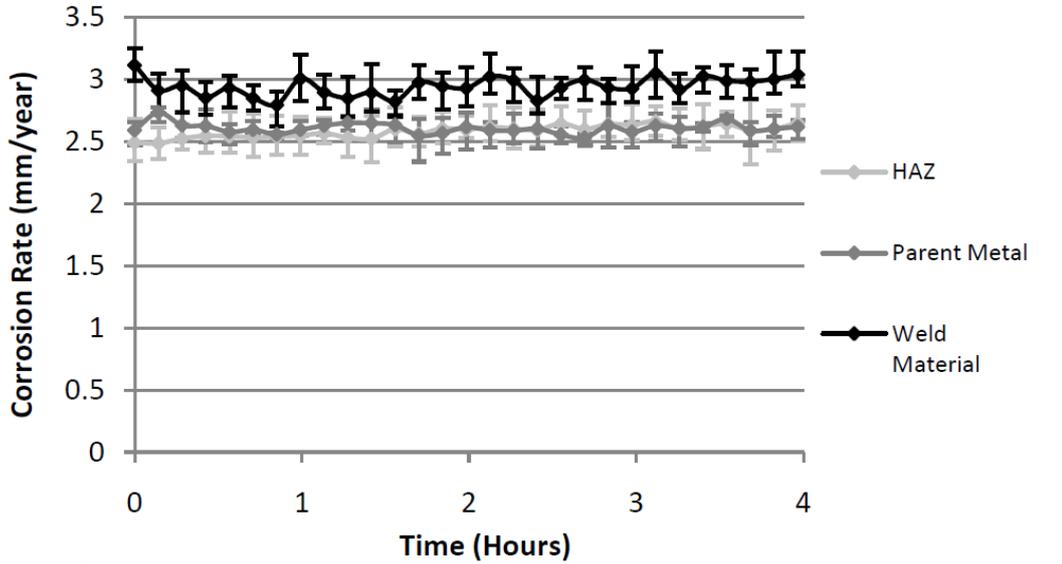
(a)
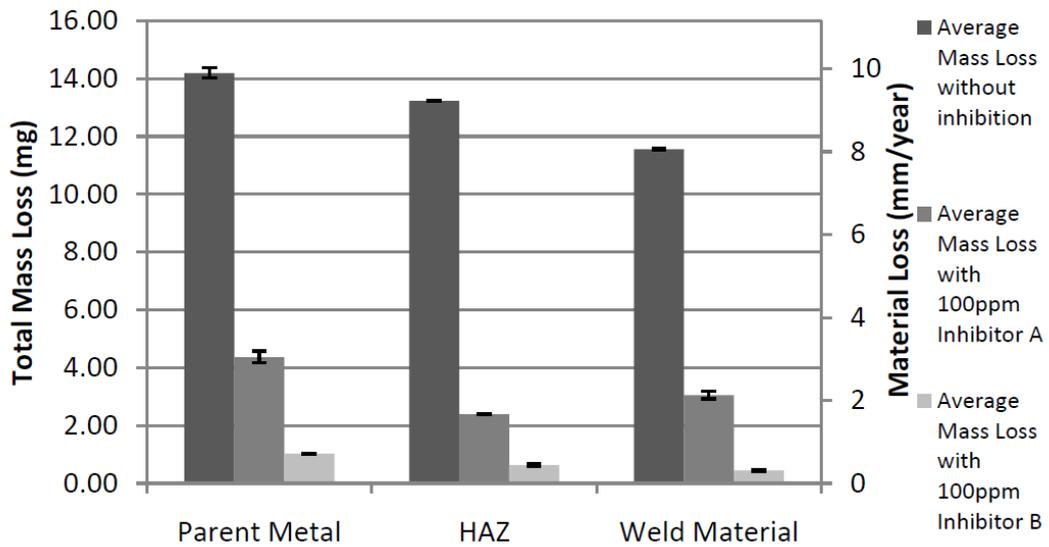
(b)

Figure 3.12: The degradation rate of the parent metal, heat affected zone (HAZ) and weld material in (a) static and (b) flow conditions [79].

3.2 Erosion

Erosion can be defined as a mechanical removal of material from metal surfaces, and is quite different from corrosion which is removal by chemical or electrochemical reaction [31, 32]. Erosion process could be dry or aqueous erosion [44], only aqueous erosion is of interest in this study. Aqueous erosion may involve material removal by cavitation (bubble collapse), liquid or solid particle impingement [32]. Here, we consider liquid and/or solid particle (sand) erosion, and it is important to note that the material removal is usually at extreme when sand is present in the produced fluid and this phenomenon is a great problem in oil and gas production.

Martin [80] observed that increased erosion problems in oil and gas production will keep on increasing due to increased water-cuts which put pressure on total fluid production rates to maintain oil production; increased use of multiphase flow in the transport of production fluids; increased sand and other solid particles production due to increased use of proppant and reservoir fracturing techniques; dissolution of cementing materials and loss of capillary pressure after water-cut. If not checked, the sand can cause damage and eventual failure of sub-surface equipment and surface facilities through erosion.

3.2.1 Mechanism

The mechanism of sand erosion has been described in different ways. Details of the mechanism are discussed in details in references [33, 34, 81-85]. Here, attempt is made to summarise the key contributions. One way is that of Martin [80] who described the mechanism of erosion of most ductile materials as ductile ploughing of the surface by impacting sand particles and that the material lost per impact is greatest at angles of impact between 15° and 60°. Two is Jordan [33], who proposed that the erosion mechanism and rate of material removal is governed by angle of impact, particle impact velocity and metal mechanical properties - ductility (involves scrapping or cutting) and brittleness (involves cracking and chipping). Three was given by Bitter [81,

82] who identified two heavy erosion attacks in a fluid-bed transport lines for solids. One by repeated deformation during collision resulting to breaking loose of piece of materials and the other caused by the cutting action of the free-moving particle. He maintained that the cutting exists if particles strike a body at an acute angle, thereby scratching out some material from the surface. This scratching is highly influenced by velocity and the impact angle of the eroding particles. The velocity and the impact angle were observed by Hutchings [83, 84] to be influenced by the fluid local hydrodynamics with forces such as drag force, buoyant force and the weight acting on the particle within a confined geometry. A change in the force balance due to change in local fluid flow can cause particles to cross fluid streamlines leading to impingement and subsequent loss of material [83] as illustrated in Figure 3.13.
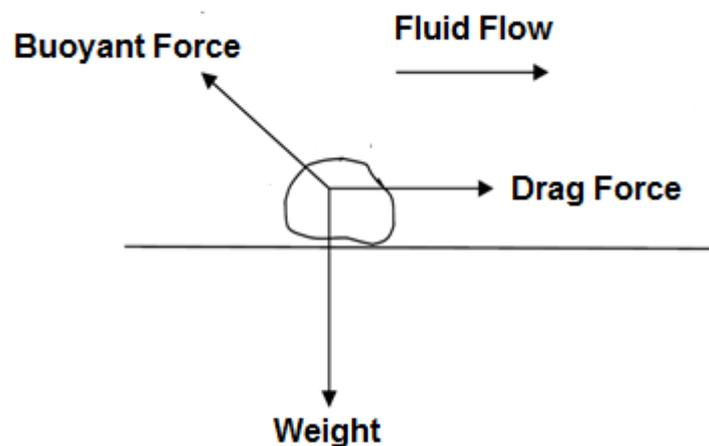
Figure 3.13: Schematic illustration of the major forces acting on a solid particle within a flowing fluid [83]

Based on the micro-machining erosion mechanisms, Hutchings [83] proposed that ductile materials tend to suffer most severe erosion at impact angles of 30° while brittle materials often suffer peak erosion for normal incidence as shown in Figure 3.14 (a), whereas Levy and Yau [85] proposed a micro-extrusion erosion mechanism and reported maximum erosion rate at impact angle of 90° in a jet impingement system for steels with secondary peak erosion occurring at impingement angle of $40\text{-}60^{o}$ in some alloys as shown in Figure 3.14 (b).
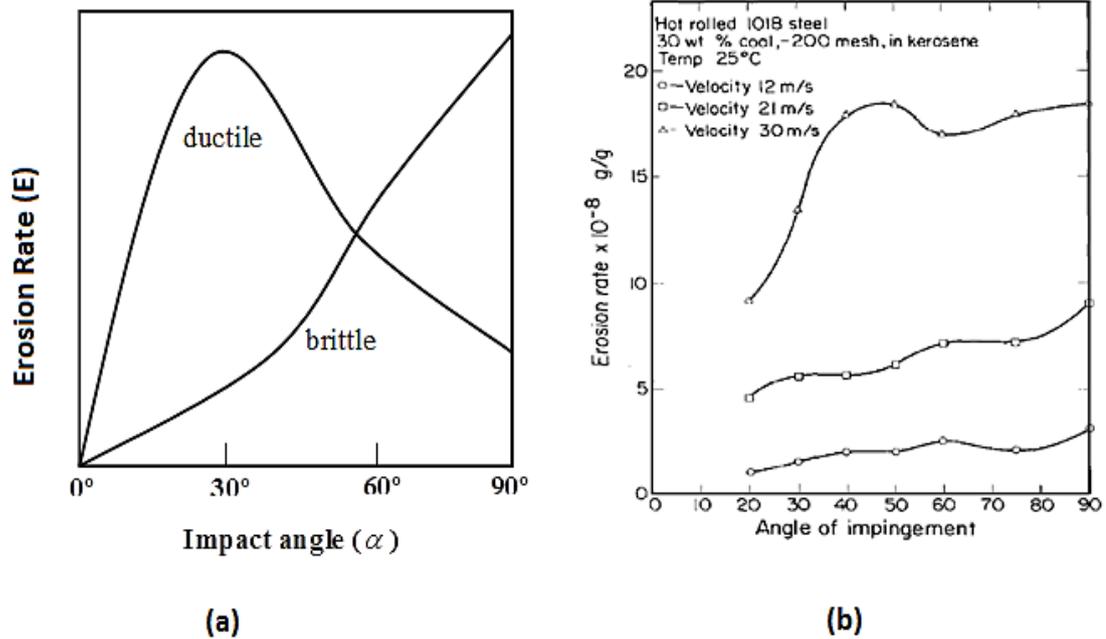
Figure 3.14: Effect of impact angle on erosion (a) Hutchings [83], (b) Levy and Yau [86].

Sand control measures such as gravel packing, sand consolidation and controlled production have problem with practicality and success [87]. As a result, some prediction methods have been developed over the years to predict erosion and are reviewed in the next paragraphs.

3.2.2 Prediction

Erosion prediction methods include empirical methods [31-34, 80-86, 88-91], experimental methods [92, 93] and computational methods [47, 94-96]. Computational methods involves modelling with Computational Fluid Dynamics (CFD) and particle tracking technique [47, 96]; experimental methods include jet impingement [94, 97], coriolis and pot testers [93], pipe flow loop [98]; and empirical methods could be seen to be composed of erosion models with some parameters established from experiments. These models have been reviewed in detail by Meng and Ludema [34]. An attempt is made here to summarise selected major models.

3.2.3 Erosion Models

The review of the selected erosion models is presented in the next paragraphs.

3.2.3.1 API RP 14E Erosion Model

This model provides a guideline erosion velocity below which a tolerable amount of erosion occurs and expressed as [32]:

$$V_e = \frac{C}{\sqrt{\rho_m}}$$ (3.27)

where, V_e is in m/s, C is an empirical constant and ρ_m is the gas/liquid mixture in kg/m³.

It has been argued that the equation is only correct for erosion resulting from liquid impingement and will be appropriate for a non-corrosive and sand-free environment. However, the equation can be modified and used in corrosive environment, for example, Martin [80] reported that BP-Amoco uses the value of C = 100 and C = 125 for continuous and intermittent flow respectively, and also the values of C=135, 300, 350 for carbon steel, 13% Cr steel and duplex stainless respectively in a corrosive environment.

3.2.3.2 Finnie's Model

Based on his proposed erosion mechanism in 1960, Finnie [99] suggested that the volume of material removed Q, by single abrasive particle of mass m, having a velocity V and striking the surface at an angle θ can be calculated by applying the following equations [99]:

$$Q = \frac{mV^2}{PD_rF_R}f(\theta)$$ (3.28a)

$$f(\theta) = \begin{cases} \sin(2\theta) - 4sin^2\theta & for\ \theta \leq 14.04^o \\ \frac{1}{4}cos^2\theta & for\ \theta > 14.04^o \end{cases}$$ (3.28b)

where, F_R is the ratio of vertical force to the horizontal force component assumed to be 2 for angular abrasive particle, D_r is the ratio of contact to depth of cut assumed to be 2 and P the eroding flow stress (plastic flow stress) of substrate related to hardness in Pascal assumed to be 0.1. It was observed that this model predicts erosion of steel adequately at low angles (14 to 20°) of impacting particles and immensely

underestimate erosion for angles above 40°, and predicts zero erosion at normal angle of incidence i.e. angle 90°.

3.2.3.3 Bitter's Model

In 1963, Bitter [81, 82] modified Finnie's Model by considering both ductile and brittle materials which is presented as follows [81, 82]:

$$Q_D = \left(\frac{0.5m}{\epsilon}\right)\left(V\sin\theta - V_y\right)^2 \tag{3.29a}$$

$$Q_{C1} = \frac{2mC(V\sin\theta - V_y)^2}{\sqrt{V\sin\theta}}\left(V\cos\theta - \frac{C(V\sin\theta - V_y)}{\sqrt{V\sin\theta}}\phi\right), \ for \ \theta \leq \theta_0 \tag{3.29b}$$

$$Q_{C2} = \frac{0.5m}{\phi}\left(V^2\cos^2\theta - K\left(V\sin\theta - V_y\right)^{3/2}\right), \ for \ \theta \geq \theta_0 \tag{3.29c}$$

The total erosion of material at any given point is expressed as [81, 82]:

$$Q_T = Q_D + Q_{C1} \tag{3.30a}$$

or,

$$Q_T = Q_D + Q_{C2} \tag{3.30b}$$

where, Q_T is the total material volume loss, Q_D is deformation wear with Q_{C1}, Q_{C2} as cutting wears, m is the total mass of the impinging particles, V is the particle velocity, θ is the impact angle, ϵ is the energy needed to remove a unit volume of material from the body by deformation wear (i.e. deformation wear factor), ϕ is the energy required to scratch out a unit volume from the material, θ_0 is the impact angle at which the horizontal velocity component has just become zero when the particle leaves the body, V_y is the maximum particle velocity at which the collision is purely elastic, expressed as [81, 82]:

$$V_y = \frac{\pi^2}{2\sqrt{10}}\cdot y^{5/2}\cdot\left(\frac{1}{d_1}\right)^{1/2}\cdot\left[\left(\frac{1-q_1^2}{E_1}\right) + \left(\frac{1-q_2^2}{E_2}\right)\right]^2 \tag{3.31a}$$

The values of the constants C and K are given as follows [81, 82]:

$$C = \frac{0.288}{y}\left(\frac{d_1}{y}\right)^{1/4} \tag{3.31b}$$

$$K = 0.82y^2 \left(\frac{d_1}{y}\right)^{1/4} \left[\left(\frac{1-q_1{}^2}{E_1}\right) + \left(\frac{1-q_2{}^2}{E_2}\right)\right] \qquad (3.31c)$$

where, d_1, y, q and E are the density, elastic load limit, Poison's ratio and Young's Modulus respectively with subscript 1 and 2 for the particle and target material respectively.

3.2.3.4 Neilson and Gilchrist Model

In 1968, Neilson and Gilchrist [100] performed erosion experiments on aluminium and proposed their model based on Bitter's Model as follows [100]:

$$\dot{Q} = \begin{cases} \frac{1}{2}\left[\left(\frac{V^2cos^2\theta - V_P^2}{\phi}\right) + \left(\frac{Vsin\theta - V_y}{\epsilon}\right)\right] & for\ \theta < \theta_0 \\ \frac{1}{2}\left[\left(\frac{V^2cos^2\theta}{\phi}\right) + \left(\frac{Vsin\theta - V_y}{\epsilon}\right)\right] & for\ \theta > \theta_0 \end{cases} \qquad (3.32)$$

where, $\dot{Q}$ is the erosion rate (kg. of material per kg. of particle), V is the velocity of the particle (m/s), V_p is residual parallel component of particle velocity (m/s), V_y is particle velocity component normal to the surface below which there is no erosion (m/s), ϕ is the energy required to cut and remove unit mass of material (J/kg), ϵ is the energy required to deform and remove unit mass of material (J/kg), θ is angle of impact and θ_0 is the angle of impact when $V_p = 0$.

The first and second parts of each of the equations account for cutting wear and deformation wear respectively.

3.2.3.5 Tilly's Model

In 1973, Tilly [85] conducted an experiment and concluded from his photographic and metallographic observations that erosion in a ductile material involves two stages summarised as follows [85]:

$$\dot{Q}_1 = \frac{V^2}{\phi}\left[1 - \left(\left(\frac{D_C}{D}\right)^{\frac{3}{2}}\left(\frac{V_C}{V}\right)\right)\right]^2 \qquad (3.33a)$$

$$\dot{Q}_2 = \frac{V^2}{\Omega}.F \qquad (3.33b)$$

where, $\dot{Q}_1$ and $\dot{Q}_2$ are the first and second erosion rates respectively expressed each as mass of material removed per unit mass of particle, ϕ is the energy required to remove unit mass of material by the first erosion process and Ω is the second erosion factor, V is the particle velocity, D is the particle diameter, and D_C and V_C are the threshold particle diameter and velocity to cause any erosion respectively and F is the degree of fragmentation expressed as follows [99]:

$$F = \frac{m_0 - m}{m_0} \qquad (3.33c)$$

where, m_0 is the proportion of the particle sample mass within specified range before testing and m is the proportion after. If all of the particles are broken into smaller sizes, then $F = 1$.

It is observed that Tilly [85] two stage ductile erosion model can be useful for erosion at high velocity and relatively large particle sizes because Tilly's experiments covered particles size range of $350 - 500 \, \mu m$ and $500 - 850 \, \mu m$ at a velocity of approximately 200 m/s.

3.2.3.6 Hutchings' Model

Based on his research, Hutchings [101] presented a model in 1981 as follows [101]:

$$\dot{Q} = 0.033 \frac{\alpha \rho_t \sigma^{1/2} V^3}{\Omega_C^2 H_t^{3/2}} \qquad (3.34)$$

where, $\dot{Q}$ is the erosion rate (mass loss per unit mass of impinging particles), α is the fraction of the volume of particle indentation on the target material (α depends on the indentation geometry, impact velocity and target material), V is the impact velocity, ρ_t is the density of the target material, Ω_C is erosion ductility measured experimentally together with α as $\frac{\alpha}{\Omega_C^2}$ and H_t is the dynamic hardness of the target material.

According to Hutchings [83, 101], there are three types of ductile erosion mechanisms by which material could be removed when spherical or rounded surfaces of irregular erosive particles strike the surface at low angle of impact. These mechanisms include

ploughing (high impact velocity at low impact angle); cutting deformation I (when angular particle impacts at high rake angle), cutting deformation II (when angular particle impacts at low rake angle) and an indentation (when a spherical particle impact at 90° impact angle).

3.2.3.7 Sundararajan Model

This development was presented in 1991 by Sundararajan [102] who applied the concept of localisation of plastic deformation leading to lip formation and the generalised energy absorption relations to generate erosion equations considered to be valid for all impact angles and all shapes of eroding particles and expressed as follows [102]:

$$\dot{Q}_D = \frac{0.05}{(T_m - 436)^{3/4}} \cdot \frac{2^{n_c} f_t V^2 \sin^2\theta (1 - e^2)}{n_c C_p} \tag{3.35a}$$

$$\dot{Q}_C = \frac{0.05}{(T_m - 436)^{3/4}} \cdot \frac{(n_c + 1)(\mu/\mu_c)(2 - \mu/\mu_c)V^2 \cos^2\theta}{2^{(2-n_c)}(1+\lambda)n_c C_p} \tag{3.35b}$$

$$\dot{Q}_T = \dot{Q}_D + \dot{Q}_C \tag{3.35c}$$

$$\mu_c = \frac{1}{(1+\lambda)(1+e)\tan\theta} \tag{3.35d}$$

$$e = \frac{1.36 H_s^{5/8}}{E_e^{1/2} \rho_1^{1/8} V^{1/4}} \tag{3.35e}$$

$$E_e = \frac{E_2 E_1}{[E_1(1-v_2^2) + E_2(1-v_1^2)]} \tag{3.35f}$$

where, $\dot{Q}_D$ is the erosion rate due to deformation (mass loss due to deformation per unit mass of impinging particles), $\dot{Q}_C$ is the erosion rate due to cutting (mass loss due to cutting per unit mass of impinging particles), $\dot{Q}_T$ is the total erosion rate, T_m is melting temperature point of the metal (K), n_c is strain hardening coefficient (0.3), f_t is numerical constant (0.025), ρ_1 is density of the particle (2650 kg/m³), V is velocity of particle (m/s), C_p is the specific heat capacity (J/kg.K), e is coefficient of restitution, μ is

coefficient of friction, μ_c is the critical coefficient of friction at the contact surface between the particle and the eroding material i.e. the maximum value of μ. H_s is Hardness of the particle (Pa), E_e is reduced Young's modulus of elasticity (modulus of collision) (Pa), E_1 and E_2 are the Young modulus of the particle and target materials respectively; and ν_1 and ν_2 are the Poison's ratio of the particle and target materials respectively.

3.2.3.8 McLaury and Shirazi Models

A remarkable advancement in erosion rate calculation was made in 1999 by McLaury and Shirazi [88, 91] who developed two erosion models, one for single-phase flow and the other for a multiphase flow.

a. Single-Phase Flow Model: The model is given as follows [88, 91]:

$$h = F_M F_S F_P F_{r/D} \frac{W V_L^{1.73}}{D^2}$$

(3.36)

where, h is the penetration rate in m/s, F_M, F_S, F_P, and $F_{r/D}$ are empirical constants that account for material hardness, sand sharpness factor, factor for steel and penetration factor for elbow radius respectively; W is the sand production rate in kg/s, V_L is the particle impact velocity m/s and D is the ratio of pipe diameter in inches to one inch pipe.

b. Multiphase Flow Model: They derived the multiphase flow model by modifying the fluid properties and average flow velocity [88, 91]:

$$\rho_m = \frac{Q_L \rho_L + Q_G \rho_G}{Q_L + Q_G} = \frac{V_{SL} \rho_L + V_{SG} \rho_G}{V_{SL} + V_{SG}}$$

(3.37a)

$$\mu_m = \frac{Q_L \mu_L + Q_G \mu_G}{Q_L + Q_G} = \frac{V_{SL} \mu_L + V_{SG} \mu_G}{V_{SL} + V_{SG}}$$

(3.37b)

where, ρ_m and μ_m are the mixture density and viscosity, Q_L, is the volume flow rate of liquid in m^3/s, Q_G, the volume flow rate of gas in m^3/s, V_{SL}, and V_{SG} are the superficial liquid and gas velocity in m/s respectively.

3.2.3.9 Zhang et *al.* Model

Based on the available empirical data and the general erosion equation, Zhang *et al.* [103] developed a model for the prediction of erosion rate in oil and gas production for carbon steels, this model is given as follows [103]:

$$E_r = A(HB)^{-0.59}F_s V_P^{1.73} f(\theta) \tag{3.38}$$

where, E_r is a dimensionless erosion ratio which is the mass loss of wall material divided by the mass of particles, A is a material dependent constant, HB is Brinell hardness, F_s is the particle sharpness factor, V_p is the particle impact velocity which depends on many parameters such as flow pattern, fluid rates and properties, sand rate/size and geometry type and size. $f(\theta)$ is the impingement angular dependence defined as follows [103]:

$$f(\theta) = a\theta^2 + b\theta \ , \qquad\qquad \text{for } \theta \leq 15^o \tag{3.39a}$$

$$f(\theta) = x cos\theta^2 sin\theta + y sin\theta^2 + z, \qquad \text{for } 90^o > \theta > 15^o \tag{3.39b}$$

where, a, b, x, y and z are empirical constants to be determined experimentally.

3.2.4 Computational Techniques in Erosion Rate Prediction

From the review of erosion models, it is evident that the erosion of a surface by abrasive particles in an inert fluid depends on the number of particles striking the surface, their velocity and their direction relative to the surface. These quantities are largely determined by flow conditions. Clark [104-106] suggested that if an understanding of erosion rates is desired, it is necessary to know the number of particles striking a unit area, the velocity of the particles and their impact angle. It is believed that particle impact dynamics must be analytically modelled to be able to fully understand erosion behaviour. A more comprehensive method to model erosion and to determine the parameters mentioned above can be achieved using computational techniques such as Computational Fluid Dynamics (CFD).

This technique is made up of flow modelling, particle tracking and erosion equations. Studies by Wang *et al.* [47], Huser and Kvernvold [95] and Chen *et al.* [107, 108], are good examples of application of CFD in the prediction of erosion rate within geometries such as elbow and plugged tees, two sections of pipelines that suffer higher attack in erosion environments. A flow model is used to determine the flow field for a given geometry and particle tracking is used to determine the trajectories in the flow. Impact data such as particle impact speed, angle and locations are used along with empirical equations to predict erosion rates. However, this technique requires highly specialised skills in CFD as well as a huge computing time and memory [109]. Typical illustration of particle tracking is shown in Figure 3.15.

Recent investigations by Gnanavelu *et al.* [94, 110] applied an approach which is different from that of Chen *et al.* [107, 108] by combining submerged impinging jet experiments with CFD. They initially created a universal wear map for stainless steel materials. The local wear rate from the surface profile is interpreted using a CFD simulation of the test, which produces a map giving local wear rates as a function of particle impact angle and velocity. A CFD simulation is then calculated for a series of different erosion configurations to provide particle impact data at each point on the surface. The wear maps from the jet impingement tests are then used to calculate the local wear rates.
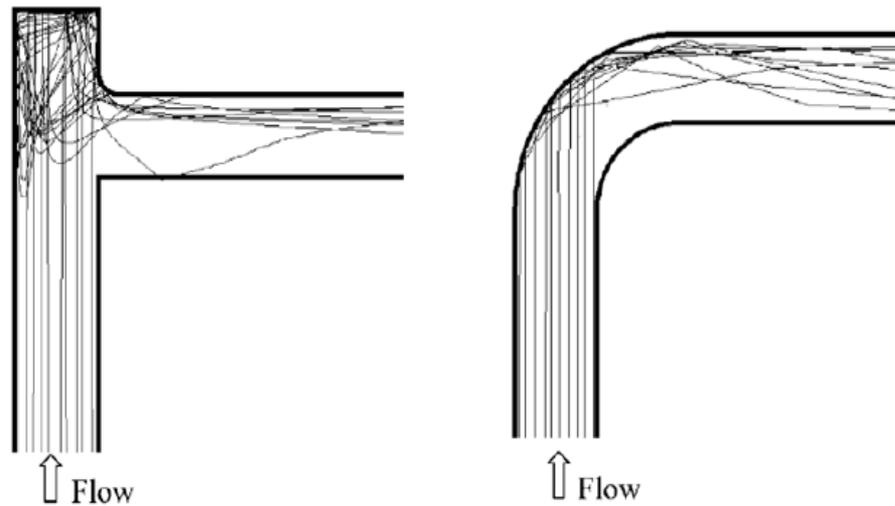
Figure 3.15: An illustration of predicted particle impact trajectories in a plugged tee and elbow [108].

3.3 CO$_2$ Erosion-Corrosion

3.3.1 Meaning

When erosion and corrosion act together in a CO$_2$ aqueous environment, a co-joint action known as CO$_2$ erosion-corrosion occurs [41, 42]. The corrosion is accelerated in the base metal by the removal of the surface protective films allowing corrosion to occur at more rapid initial rates [111]. The combined effects of mechanical forces (i.e. plastic deformation or cutting in the surface layer due to solid particles impingement) and electrochemical or chemical reactions (i.e. dissolution of metallic ions) during erosion-corrosion usually result in more total material loss in corrosive fluids than the sum of the losses caused by pure erosion and pure corrosion [35, 36, 38-43, 48].

The total material loss rate (TML) of the erosion-corrosion process can be expressed as [38-43, 46]:

$$TML = E + dE_C + C + dC_E \qquad (3.40)$$

where, $(E + dE_C)$ and $(C + dC_E)$ are the material loss rate caused by erosion and corrosion respectively when the material is eroded in CO_2 environment with sand, E is the pure erosion rate, C is the pure corrosion rate, dE_C is the additional erosion rate caused by the corrosion-enhanced erosion and dC_E extra corrosion rate due to the erosion-enhanced corrosion.

The synergism (W_S) is the additional contribution of each component of erosion and corrosion, and is given by [41-43, 46]:

$$W_S = dE_C + dC_E \qquad\qquad (3.41)$$

Observations made from the work of different researchers [35-48, 87, 112-123] reveal that the complexity in erosion-corrosion process arises from the various factors affecting the process which include the synergism, mechanical properties of materials, operating conditions such as impact angles, hydrodynamic effects, temperature, corrosivity of the environment, and concentration and characteristics of the eroding solid particles. Detailed discussion on these factors can be located in references [114-119] but the salient points are reviewed in the next paragraphs.

3.3.2 Factors Affecting Erosion-Corrosion

3.3.2.1 Synergistic Effect

3.3.2.1.1 Erosion-Enhanced Corrosion Loss

In passive (i.e. self-healing) materials, two explanations have been given by Zheng *et al.* [113] for the enhanced effect of erosion on corrosion. One is that the disturbance of solid particles in flow field can enhance the transport process of both reactants and corrosion products, and then promote the corrosion process. The second is that the solid particle impingement can remove the corrosion product or protective passive film (as shown in Figure 3.16), thus leading to fresh metal surface being exposed to corrosive environment and causing severe damage due to corrosion. These explanations are in line with the work of Dave *et al.* [37] who observed that the

repassivation process roughens the metal surface which in turn increases the erosion rate (because the erosion damage is very sensitive to impact angle of the solid particles), thereby exposing more fresh surfaces to more corrosion attack.

However, Guo *et al.* [117] in their study suggested that when the velocity is sufficiently high, mass transfer is not the rate determining step which indicates that the system is controlled by active dissolution. This means that for active materials, even though the disturbance of sand accelerates the mass transport at the interface, it still cannot affect the corrosion rate. They further maintained that the corrosion products formed in active dissolution system could be loose, non-protective and even soluble so that the removal of the corrosion products by the impingement of solid particles cannot largely affect the dissolution rate. Hence, active metals or alloys are less sensitive to erosion-enhanced corrosion than passive metals or alloys [117].

(a) Undamaged film   (b) Damaged film
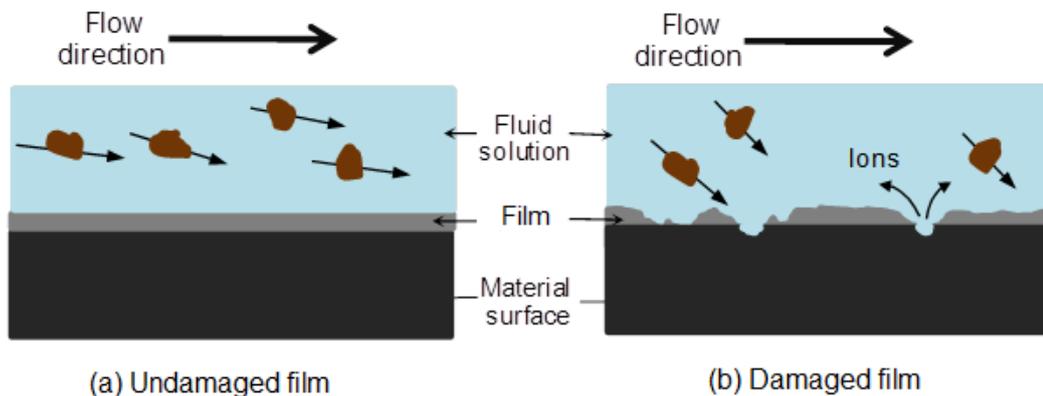
Figure 3.16: Illustration of (a) undamaged corrosion product film preventing corrosion loss and (b) enhancement of corrosion loss due to particle impacts removing the corrosion product film [110].

3.3.2.1.2 Corrosion-Enhanced Erosion Loss

This happens due to 'chemo-mechanical effect' [118] of the erosion-corrosion process. Li *et al.* [119] observed that corrosion affects erosion rate through detachment of flakes formed by repeated solid particles impingement. Reyes and Neville [120] proposed that the preferential dissolution of a matrix would lead to easy removal of the hard particles

in micro-structure which results to acceleration of erosion. However, this is only valid for materials strengthened with hard precipitates and cannot be applied in materials comprising mainly a single phased structure. Matsumura *et al.* [121] recommended that the impingement of the particles would damage the passive film and enhance the dissolution of the work-hardened layer, which degrades the erosion resistance of material. Recently, Lu *et al.* [48] pointed out that since erosion rate increases with decreasing hardness, the hardness-degradation caused by the anodic dissolution (enhancing mobility in the surface layer) is an important mechanism of corrosion-enhanced erosion loss.

3.3.2.2 Mechanical Properties of Material Effect

Material properties such as hardness, density, Young's modulus, fracture toughness, critical plastic strain, depth of deformation, etc can influence erosion rate which will in principle affect erosion-corrosion rate. Among these properties, hardness (resistance to scratching, wear and penetration [115]) has been considered to be a good method of ranking erosion-corrosion. However, in engineering practice, there are varying opinions on this. For example, Barker and Ball [122] discovered that metastable austenite steels with bulk hardness values three times lower than various martensitic steels showed a better erosion-corrosion resistance in brine. As a result, some researchers [123, 124] have argued that the ability of a material to accommodate repetitive deformation gives a better indication of erosion-corrosion resistance. They maintained that materials with high work or strain hardening ability can attain ultimate hardness while plastically accommodating the stress imposed by particle impacts and resisting micro fracture of flakes, thus leading to minimized erosion-corrosion damage in a particular corrosive environment.

Depending on the angle of impingement of particles, Hutchings [83] proposed that brittleness or ductility of materials can also be an important parameter in erosion. He stressed that at low impact angle (up to 30° measured from the plane of the surface)

the erosion component of the total erosion-corrosion rate will be larger for a ductile material but at higher impact angle (up to 90°) the erosion component of a brittle material would be high.

Microstructure and alloy compositions of materials can also affect its erosion-corrosion behaviour. Heitz [125] proposed that iron-chromium alloy is appropriate in mitigating erosion-corrosion if the carbide distribution in the matrix is well arranged. The distribution of the carbide is very important so as to avoid carbide dissolution leading to pitting and/or localized flow effects due to changing surface structure. Wang *et al.* [126] pointed out that an increase in carbon content of white cast iron deteriorates its corrosion resistance but that addition of chromium and tungsten enhances the corrosion resistance during erosion-corrosion with greatest erosion resistance established at 2-2.5% carbon. The work of Hu and Neville [97] is in line with the previous works of Blatt *et al.* [127], Umemura [128] and Madsen [129] suggesting that at certain operating conditions erosion-corrosion weight loss of carbon steel is greater than that of stainless steel. All studies point to the significance of corrosion-related effects dominance in the erosion-corrosion process. Hence, the corrosion-related effects must be taken into consideration when designing or predicting the pipeline loss due to erosion-corrosion damage.

3.3.2.3 Operating Condition Effects

3.3.2.3.1 Angle of Impact Effect

Erosion is very sensitive to angle of impact and varying the angle of impact influences erosion component thereby affecting the total material loss due to erosion-corrosion. Burstein and Sasaki [130] in their analysis, indicated that the maximum peaks of both pure erosion and erosion-corrosion rates occur at oblique angles between 10° and 20° and that erosion-corrosion rate is higher than the erosion rate alone at all angles studied.

3.3.2.3.2 Hydrodynamic Effect

Flow turbulence, shear stress and mass transfer are the hydrodynamic factors that can affect erosion-corrosion process. Schmitt and Bakalli [75] proposed that flow effects result from enhanced mass transfer and diffusion of the corrosive species in the boundary layer of the liquid at the electrolyte and electrode interface. They maintained that if the passive film or scale is not destroyed at the steel surface, the molecular diffusion becomes the rate determining step of the corrosion rate but when the scale is destroyed as in erosion-corrosion, the corrosion rate increases abruptly and becomes mass transport controlled according to boundary condition of scale-free system, i.e. the corrosion rate at the scale-free surface is flow dependent, governed by Reynolds number (Re) and Schmidt number (Sc) as follows [75]:

$$Sc = \frac{v}{D} = \left(\frac{u_0 l}{D}\right) / \left(\frac{u_0 l}{v}\right) = \frac{Pe}{Re} \qquad (3.42)$$

where, Pe is the Peclet number given as the ratio between the convection ($u_0 l$) and the diffusion coefficient D, and Re is the Reynolds number given as the ratio of the convection ($u_0 l$) and the kinematic viscosity v.

For turbulent flows, a governing equation exists for mass transport correlations at different flow patterns as a function of dimensionless parameters Re, Sc and Sh (Sherwood number) as follows [75]:

$$Sh = a. Sc^b Re^c = \frac{k.l}{D} \qquad (3.43)$$

where, $k = D/d_N$, the mass transfer coefficient (m/s) and l is the characteristic length (m), a, b and c are constants which depend on the flow patterns at different flow devices and have standard values.

However, Heitz [125] and Poulson [131] argued that when corrosion scale or a passive film forms, the corrosion reactions in the flowing slurries are not always governed by mass transfer process because the experimental values of the Reynold's number and Schmidt's number exponents do not agree with computed values. They stressed that if

the scale or passive film is eroded, the damage resulting from erosion-corrosion depends not only on the hydrodynamic effect and corrosivity of the slurries but also on the mechanical properties and electrochemical features of the passive films and/or surface layer.

It is generally observed that the flow velocity increases the fluid turbulence; the energy and erosive ability of impinging particles as well as enhancing wall shear stress and mass transfer coefficient of the corrosive species as demonstrated in the work of Hu and Neville [97] who proposed that the flow velocity shows more effect on the total material loss for carbon steel X65 than duplex stainless steel 22%Cr in CO_2 saturated brine.

3.3.2.3.3 Temperature Change Effect

There are two major ways a change in temperature can affect erosion-corrosion process. One is by enhancing corrosion kinetics and charge transfer as suggested by Hu and Neville [97] that there is a significant dependence of X65 carbon steel on temperature due to enhanced corrosion charge transfer as temperature increases, whereas 22Cr% duplex stainless steel shows very little temperature dependence suggesting less corrosion dominance. Two is by affecting the density and viscosity of fluid. As temperature of the fluid increases, the density and viscosity of the slurries decreases leading to high turbulence intensity, higher particle velocity (due to decrease in viscous drag acting on the particles) and higher erosion component [115].

3.3.2.3.4 Solution Corrosivity Effect

An increase in the corrosivity of the environment can have a significant effect on the erosion-corrosion process by increasing the corrosion component which in turn will enhance the erosion component. As evident in CO_2 corrosion [9], increasing the partial pressure of CO_2 or decreasing pH of the solution increases the corrosion rate and this

may also be applicable to erosion-corrosion process as the corrosion component will enhance erosion rate by accelerating material dissolution.

3.3.2.4 Concentration and Characteristics of the Eroding Solid Particles Effect

3.3.2.4.1 Particle Size Effect

It is expected that an increase in particle size leads to increase in the erosion-corrosion process by increasing the erosion component to certain level [115], this happens when the kinetic energy of the impacting particles is high enough to cause plastic deformation of the target material. It has also been reported [115] that larger particles have less dependence on impact angles, meaning that with increasing size, the geometry and type of target will be less relevant. In addition, Levy and Hickey [124] studied the effect of particle size on steel materials (A53 and 304SS) and discovered that larger particles eroded the steel materials more than the finer particles only at high velocities and that at 3.5 m/s both particle sizes cause almost the same amount of erosion.

3.3.2.4.2 Particle Loading Effect

Generally, it is expected that increasing particle loading will increase erosion-corrosion damage of materials by increasing the erosion component. Hu and Neville [97] specifically proposed that the sand loading effects for two different steel materials are quite different, that X65 carbon steel shows a linear increase in the material loss with increase in solid loading while an exponential relationship is observed for the 22%Cr duplex stainless steel. However, this trend has been reported to be valid for low particle loading [115]. This is because erosion efficiency (ratio of wear to particle loading) decreases with increase in particle loading according to a power law of the particle volume fraction with an exponent of approximately 0.33, and above a loading of approximately 13%, the erosion efficiency becomes constant as a result of particle-particle interaction [115].

3.3.2.4.3   Particle Hardness

As long as the hardness of erodent particle is greater than that of target material, the erodent will cause greater wear on the target material. Tsai *et al.* [132] studied the erosion behaviour of three steel alloys with silicon carbide (SiC) and coal particles under erosion slurry, and observed that SiC produced erosion rates 40 to 100 times larger than equivalent coal particles. Harder particles will increase erosion-corrosion damage through the erosion component. This is in line with the work of Pitt and Chang [133] who studied the effect of hard particles on erosion-corrosion of high chromium cast iron and high carbon steel with quartz and chalcopyrite. They proposed that the erosion rate was lower for the softer chalcopyrite than the quartz, and that the chalcopyrite did not damage the corrosion scale much as the quartz leading to reduced corrosion rate with the chalcopyrite.

3.3.2.4.4   Particle Angularity

It has been reported [115] that angular particle will cause more erosion than smooth particle thereby increasing the erosion-corrosion rate through the erosion component. This assertion is supported by the work of Postlethwaite and Nesic [134] who proposed that angular sand particles gave much more erosion rates than smooth glass beads of the same size. It is also important to note that prolonged use of angular particles can make them smooth and less erosive. Particle smoothing and degradation due to prolong use have been reported by Zu *et al.* [135] and Hu [52].

3.3.3 Mechanisms of Erosion-Corrosion

Erosion-corrosion damage is well known to oilfield engineers as the major cause of failures of pipeline components such as surface and sub-surface safety valves, chokes, flanges, tee and elbow joints, etc. This happens due to poor understanding of the mechanisms of erosion-corrosion, and the failures can pose serious safety threat to the operations and a risk to the environment. Hence, it is necessary to adequately

understand the mechanisms of sand erosion in corrosive environment for effective, efficient and reliable service life prediction of important pipeline components.

In CO_2 environment, depending on the conditions, the erosion-corrosion damage starts with the removal of the iron carbonate ($FeCO_3$) protective scales or films by the impingement of sand particles, the scales break way thereby allowing the corrosive environment to react with the bare steel surface [115] as illustrated in Figure 3.17 with different attack angles [130]. For this to happen, a critical flow velocity (i.e. breakaway velocity) or shear stress [136] must be exceeded in the fluid flow. If the scale breakaway is localised, a severe corrosion may take place characterised by shallow round or horse-shoe shaped pits. On the other hand, if the breakaway is more general, then a uniform material loss will be observed depending on the orientation and distribution of the impacting particles [136]. Detailed discussion of this mechanism can be located in references [115, 136].
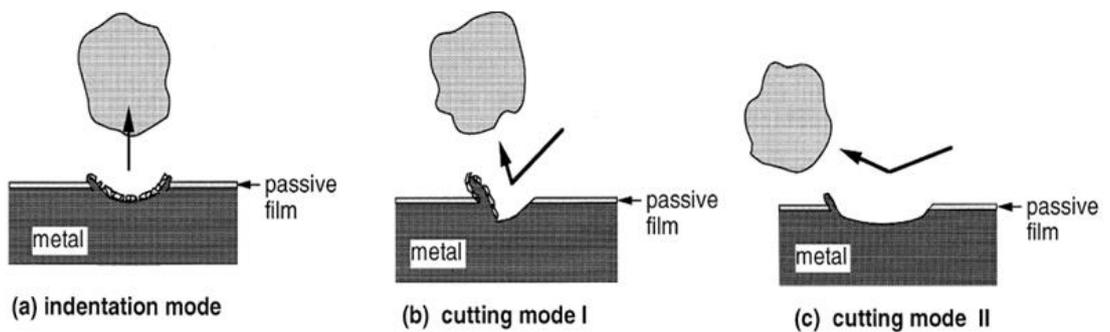
Figure 3.17: Illustration of erosion-corrosion process [130].

Evans [137] gave a general and simplified mechanism of erosion-corrosion as illustrated in Figure 3.18 (a-c). When a continuous film is formed in the corrosion process, the material loss rate will be as illustrated in Figure 3.18 (a), but for a repeated number of particles impact on the film, causing it to breakaway and exposing the metal surface, the material loss rate is as shown in Figure 3.18 (b) because the corrosion resumed rapidly with initial rates at points P_1, P_2 and P_3. However, if the frequency of particle impact is increased, the mechanism may take the form of Figure 3.18 (c)

because each particle causes damage to the film and the graph tends to linear with a slope approaching to the first curve in Figure 3.18 (a).
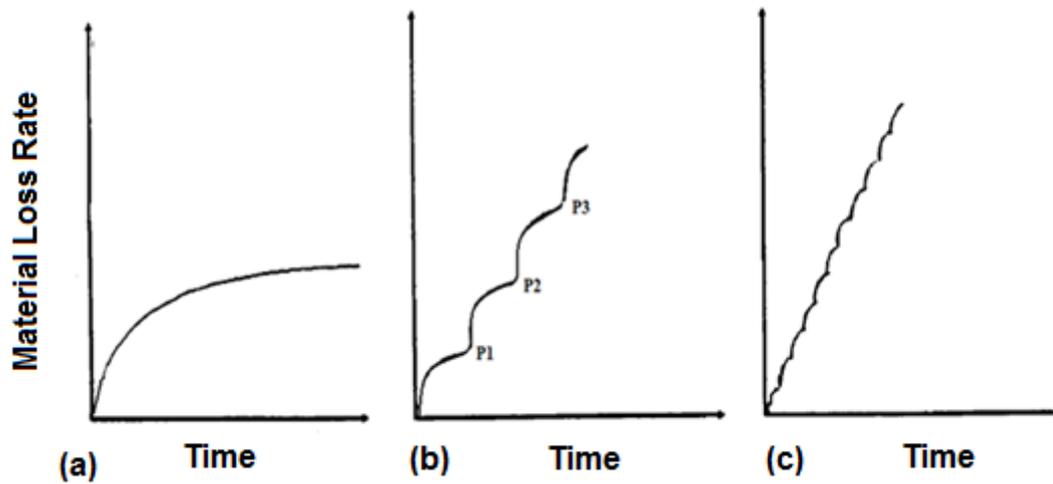
Figure 3.18: Illustration of erosion-corrosion mechanism [136].

In view of the above, attempts have been made by different researchers world-wide to investigate erosion-corrosion process with the aim of establishing predictive and monitoring tool for design, material selection and maintenance planning purposes. These attempts are grouped under prediction methods and summarised in the next paragraphs with particular focus on erosion-corrosion in CO_2 environment which is the main focus of this study.

3.3.4 Prediction of Erosion-Corrosion

The different methods have been successfully applied in erosion-corrosion predictions. These include computational [39, 45, 138-142], empirical [41, 48,] and experimental [136] methods.

3.3.4.1 Computational Method

This involves the use of CFD (for turbulent or continuous flow modelling); particle tracking (for erosion modelling) and mass transfer coefficient prediction (for corrosion modelling) [152]. Particle properties are predicted by particle tracking and used to calculate erosion rates with appropriate erosion model [34], near-wall mass transfer

coefficients are predicted and converted to corrosion rates [138] and the sum of the erosion and corrosion rates yields the material loss rate due to erosion-corrosion in the geometry under study. Therefore, the erosion mechanism needs to be linked with electrochemical information related to the corrosion of the material in its environment in order to fully represent the effects encountered in an erosion-corrosion regime.

It is important to note that CFD has developed into one of the more promising approaches for the analysis and solution of a wide range of flow problems. CFD codes are capable of solving the full set of fluid mechanics balancing equations (usually in Navier-Stokes formulation for momentum balance). Turbulence can also be accounted for using a variety of models. In particular, the FLUENT code solves the balance equations through domain discretisation, using a control volume approach to convert partial differential equations into algebraic equations, which are solved numerically. The FLUENT solution procedure involves integrating the balance equations over the control volume to obtain discrete equations. FLUENT is also capable of simulating complex flows in two and three-dimensions, also accounting for turbulence.

Recently, the Stack group [45] combined various models of solid particle erosion with those for aqueous corrosion. These models were then incorporated into a simulated flowing environment using CFD techniques to predict the erosion-corrosion behaviour of pure metals. The technique provides a means of mapping the level of degradation of components undergoing erosion-corrosion and enables the superimposition of erosion-corrosion maps onto real surfaces. The results presented a new technique for mapping erosion-corrosion regimes onto real pipes. The erosion-corrosion boundaries were defined using ratios of corrosion damage to erosion damage. Predictions from the model were mapped onto a pipe elbow and indicated that there were significant differences between erosion-corrosion regimes, with dissolution and dissolution-erosion being the dominant mechanisms for pure iron. The methodology also allowed

wastage maps to be generated to indicate regions that were most susceptible to degradation.

3.3.4.2 Empirical Method

Here, data generated from experiments is used to formulate equations for the prediction of erosion-corrosion damage. Hu *et al.* [41], Stack and co-workers [44], Lu and co-workers [46, 48], and others [143] have presented different empirical erosion-corrosion models in aqueous environment. A comprehensive review of tribo-corrosion (dry and aqueous) models can be located in the work of Stack *et al.* [44], and Wood [143]. All these researchers agree that erosion-corrosion is a tribo-corrosion process and that the total material loss is the sum of corrosion, erosion and their synergism. Most of the aqueous tribo-corrosion empirical formulations are concerned with aerated aqueous corrosion except Hu *et al.* [41] and Shadley *et al.* [1, 35].

Hu *et al.* [41] used their experimental results to present an empirical CO_2 erosion-corrosion model for oil and gas pipeline materials (X65 carbon steel) using linear regression analysis. The empirical model is given as follows [41]:

$$W_T = S^\alpha e^{(\beta V + \gamma T)} \tag{3.44}$$

where, S is the sand loading (mg/L), V is the flow velocity (m/s) and T is temperature ($°C$). α, β and γ are constants derived from linear regression analysis.

From 1996 to 1998, Shadley *et al.* [1, 35] at the University of Tulsa set out to characterise erosion-corrosion behaviour of a carbon steel elbow over a range of environmental conditions through the use of an empirical model. They applied the results of the study, long with published erosion and corrosion models, to predict erosion-corrosion penetration rates for a carbon steel elbow. Shadley *et al.* [1, 35] made strong reference to the 'threshold velocity' and believe that the first step in predicting erosion-corrosion penetration rates is to compute the threshold velocity, because below this velocity the protective $FeCO_3$ scale remains intact, and above the velocity, the scale breaks down.

Shadley *et al.* [1, 35] examined thirteen sets of environmental conditions in flow loop tests. For each set of conditions, erosion parameters (sand size, sand concentration and flow velocity) were varied. If scale formed everywhere in the elbow, then the erosivity of the next test was increased. If pitting or uniform corrosion was observed, the erosion severity was reduced. The objective was to determine the erosion-corrosion resistance i.e. define the highest erosion rate that the system could tolerate without eroding the protective scale. The erosion-corrosion resistance was then calculated from the parameters using published prediction models. This enabled the threshold velocity to be calculated. Once the threshold velocity was identified, erosion and corrosion rates corresponding to selected flow velocities could be estimated [1]. Three types of behaviour were identified from the flow loop tests performed on the carbon steel elbow. At low velocities, a protective iron carbonate film was formed over all surfaces of the elbow, and corrosion rates were very low. At high velocities, the impingement of sand particles prevented the formation of a protective film anywhere on the surface. Accordingly, corrosion rates were recorded as extremely high and uniform over the entire elbow. At intermediate velocities, a protective film was formed over the surface, except at localised regions, promoting pitting and high wall penetration rates.

3.3.4.3 Experimental Methods

These methods in the literature include the following:

i. Rotating cylinder electrode (RCE) [136, 144];

ii. Rotating disc [73, 136];

iii. Rotating cage [73, 136];

iv. Flow loop [35-38, 40, 136] and

v. Jet impingement [41-43, 73, 78, 79, 136].

The governing equations of these methods are summarized in Appendix 4.

It is important to note that electrochemical tests (e.g. LPR) can be attached to any of the above methods to obtain corrosion results, and weight loss (gravimetric) techniques are used to obtain total mass loss due to erosion-corrosion. Also, surface analysis techniques such as scanning electron microscopy (SEM), energy-dispersive X-ray (EDX) spectroscopy, secondary ion mass spectroscopy, atomic force microscope (AFM), profilometry, etc are also used in erosion-corrosion studies.

Jet impingement (submerged) method at 90° impingement angle couple with acoustic emission (AE) and electrochemical techniques is chosen and implemented for this study. Detailed discussion on jet impingement method can be found in references [41-43, 73, 78, 79, 136]. It is selected because of the well-defined hydrodynamic features of a jet impinging on a flat plate as shown in Figure 3.19 and corrosion data from the wall jet region correlate well with pipe flow [74].

Its main advantages are that equation of wall shear stress is well established, very high wall shear stress (>1000 Pa) can be obtained, electrochemical tests and multi-phase operations can be applied [136]. However, it requires pumps, valves and flow control equipment which need to be properly calibrated to obtain accurate results. Also, proper and adequate test cell design and sensing element position are required to obtain valid results [78].
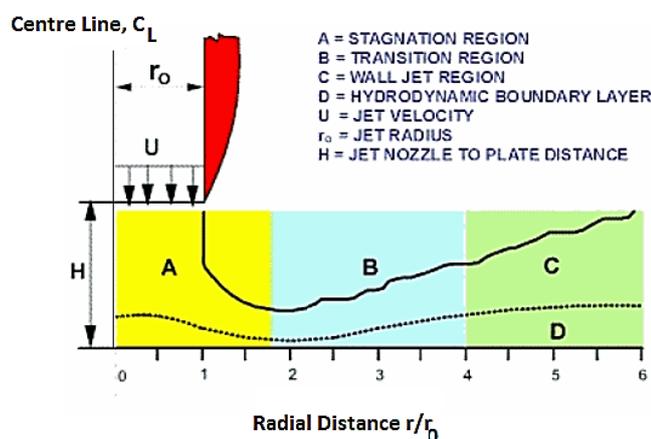
Figure 3.19: Hydrodynamic features of a jet impingement on a flat plate [78]

The submerged jet impingement method has been successfully applied in the various investigations done by Neville *et al.* [41-43, 52, 79, 97] and the University of Alberta group [47, 48]. They all agree that the total mass loss due to erosion-corrosion is greater than pure erosion or pure corrosion acting alone; also there is a synergy between them (i.e. corrosion-enhancing erosion and erosion-enhancing corrosion).

In an attempt to understand the mechanism of the CO_2 erosion-corrosion processes using experimental methods, and predict specifically carbon steel material performance accurately, researchers have performed several investigations of erosion-corrosion degradation of carbon steel material in CO_2 environment. Shadley *et al.* [35] performed an investigation with a carbon steel elbow and sand entrained in flow loop for 96 hours. They observed that at low flow velocities corrosion rates were low due to presence of protective iron carbonate (FCO_3) films, at high flow velocities, sand impingement at the elbow prevented the protective films from forming and corrosion rates were high and at intermediate velocities, protective films formed all over the elbow surface except at localised points which had deep pits and high penetration rates due to sand impacts.

 Addis *et al.* [40] conducted a similar test for non-protective film forming conditions and discovered that there was no synergistic effect between erosion and corrosion, and that for an unprotected base metal the rate of metal loss is equal to the sum of erosion loss and corrosion loss. They maintained that higher salt (NaCl) concentration led to a lower corrosion rate and erosion rate which they attributed to changes in density and viscosity of the fluid which affect the mass transfer reactions.

Using a submerged impinging jet rig, Hu and Neville [42] carried out a similar test on X65 carbon steel for different temperatures, sand concentrations and flow velocities. Their observation was in line with Malka's [98] that the effect of corrosion in enhancing erosion is significant especially at high temperature, and that the mechanical removal of material enhancement by corrosion may be due to the roughening effect which degrades the exposed surface. They further established critical values of sand loading

(30 mg/L) and flow velocity (6 m/s) which move the damage mechanism from flow-induced corrosion regime to erosion-corrosion regime signifying that impact intensity on the material is a key factor in material degradation of X65 carbon steel in CO_2 erosion-corrosion environment.

3.3.5 Mitigation of Erosion-Corrosion

The major strategies of mitigating erosion-corrosion in oil and gas production include installation of down-hole sand exclusion systems (gravel packs/screen and sand consolidation); reduction of flow velocities and management of the sand production by designing the facilities to handle sand if co-produced with hydrocarbon and production fluids [145]. The last option is always adopted since companies will like to optimise production rate.

This can be achieved by material selection of either carbon steel with chemical inhibition [43, 146] or corrosion resistant alloys (CRA) for specific erosive and/or corrosive environment [52]. The former is commonly applied because carbon steel is cheap, readily available and can be easily fabricated. Extensive work and documentation on erosion-corrosion mitigation with chemicals can be located in reference [43] while the behaviour of corrosion resistance alloys to erosion-corrosion is fully documented in reference [52]. A brief review of inhibition with chemical is presented in the next paragraphs.

The process of corrosion inhibition by chemicals involves physisorption or chemisorption of the inhibitors on the metal surface and subsequent interference with cathodic and/or anodic reactions [43, 147] as illustrated in Figure 3.20. It is made up of polar head groups that interact with the metal surface and hydrocarbon tails which repel water. The polar head groups are established by electrostatic attraction between the repelling inhibitor head and the metal surface. However, Schmitt and Bakalli [75] proposed that chemical inhibitor can mitigate corrosion attack of scale-covered metal surfaces in flow systems by drag reducing process. They argued that it is the reduction

of the transmittance of hydrodynamic forces onto the scale by drag reducing effects of the inhibitors that reduces corrosion rate.

The ability of a corrosion inhibitor to mitigate corrosion is expressed in terms of inhibition efficiency (E) as follows [43]:

$$E = \left(\frac{ML_B - ML_I}{ML_B}\right) \times 100 \qquad (2.91)$$

where ML_I and ML_B are mass losses with and without inhibitor respectively.
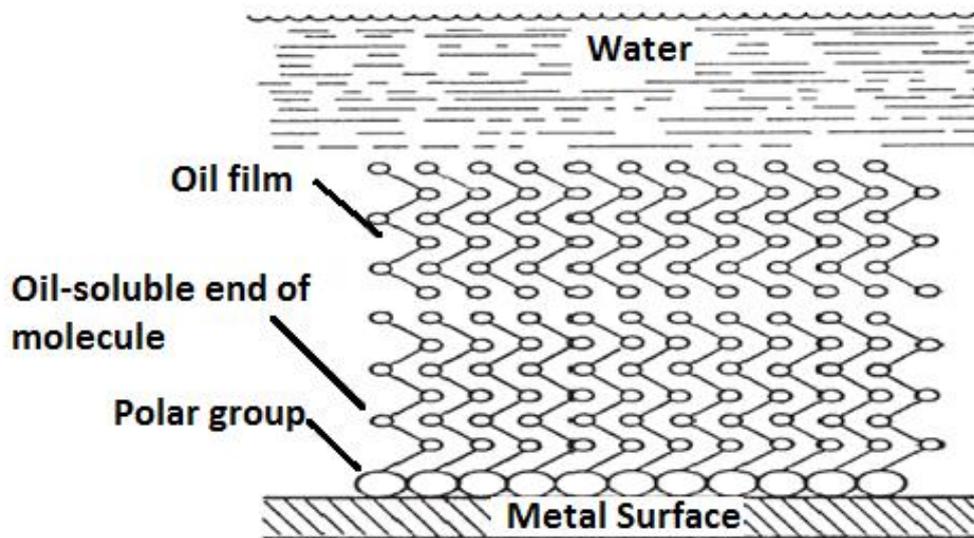
Figure 3.20: Illustration of basic principles of inhibitor film-forming [147].

Investigations by Dave *et al.* [37] suggested that an amidoamine fatty acid inhibitor was able to significantly reduce the corrosion component of material loss in erosion-corrosion environments at 50°C, 13 m/s and 1 wt.% sand. However, the presence of sand disrupted the inhibitor film and increased the rate of dissolution of the carbon steel as shown in Figure 5.8. Although sand presence did increase the corrosion rate in the system, increasing inhibitor concentration reduced the effect of film disruption and improved the level of corrosion protection. Despite this increase in overall efficiency, the inhibitor failed to reduce the level of erosion damage on the surface. In inhibited

erosion-corrosion systems where sand concentration is high, the metal loss rates could be higher than the target ranges due to the mechanical damage component alone.

Several authors have also proposed that chemical inhibition can significantly reduce the corrosion component of damage in erosion-corrosion environments, but fails to offer little or no resistance to pure erosion [148, 149]. With the increasing trend of oil and gas companies operating with small levels of sand in CO_2 systems, there is an ever increasing demand for corrosion inhibitors in erosion-corrosion environments which can reduce the mechanical damage as well as the dissolution of the material. Indeed, there are aspects of the literature suggesting there is potential for inhibitors to meet this requirement, especially in environments where $FeCO_3$ formation occurs. Jasinski [150] found that an amine based corrosion inhibitor was able to transform the morphology of the corrosion product scale that forms in CO_2 conditions, making the scale a lot more compact. Shadley et al. [35] speculated that the denser scales formed under the presence of inhibitors in environment such as these may possess more erosion resistant properties than ones formed without inhibitor, suggesting inhibitors may be capable of reducing the erosion component associated with erosion-corrosion processes.

In University of Leeds, studies by Wang *et al.* [43] and Akbar *et al.* [151, 152] suggested that the application of high shear CO_2 corrosion inhibitors may help to reduce the erosion component as well as the synergy which exists between erosion and corrosion. Barker *et al.* [153] have extended this investigation to inhibition of CO_2 flow-induced corrosion and erosion-corrosion of carbon steel parent metal of pipe work in comparison to the heat-affected zone (HAZ) and the nickel-molybdenum weld material.

3.4 Summary

CO_2 erosion-corrosion has been defined as the co-joint action of mechanical erosion and electrochemical corrosion in CO_2 aqueous environment and its effect is higher than each of them acting alone due to the synergism. It is a complex material degradation process because of the several factors affecting the process which include synergism, mechanical properties of the material, operating conditions (angle of impact, hydrodynamic, temperature, solution corrosiveness, etc), and concentration and characteristics of the erodent (particle size, loading, hardness, angularity, etc).

As a result, different researchers have applied computational, empirical and experimental methods in order to investigate and understand this erosion-corrosion process. However, it is noticed that little or no effort has been made to apply acoustic emission (AE) technique in studying this process in CO_2 environment, hence this study adopts a submerged impingement jet (SIJ) coupled with AE and electrochemical monitoring to investigate the erosion-corrosion damage for oil and gas steel pipeline materials using circular specimens. In view of this, the next chapter explores the technology of AE technique and how it has been applied in corrosion, erosion and erosion-corrosion studies.

Chapter 4 Literature Review II: Acoustic Emission (AE)

4.1 Introduction

This chapter presents the historical background and literature review of acoustic emission technology with emphasis on its meaning, signal processing analysis and application in monitoring and predicting corrosion, erosion and erosion-corrosion. These are presented so as to adequately understand the technology, appreciate the recent investigations done in the field so that the technique can be effectively applied to investigate and characterise erosion-corrosion degradation of pipeline materials in saturated CO_2 environment.

The application of AE in predicting and monitoring of erosion-corrosion damage in oil and gas pipeline systems can be used to prevent failures, avoid production outages and reduce associated corrosion, erosion and erosion-corrosion costs. This is because of its potential and increased sensitivity in detecting the earliest stages of loss of mechanical integrity or general degradation of engineering systems [154, 155] when compared to conventional methods such as visual inspection and weight-loss coupon analysis.

If fully developed, the technique is capable of giving an on-line and real-time monitoring scheme which will help in developing predictive maintenance strategies that can detect impending failures and allow for proper planning and scheduling of pipeline replacements. In addition, buried or remote pipes can be monitored from single sensor location, thereby reducing cost and time of inspection.

However, this technique requires highly specialised sensors and signal processing skills; and also it is sensitive to other ultrasonic sources such as cavitation, turbulence, background noise, etc [154]. Therefore, effort should be made to separate the erosion-corrosion signals from background noise and other interference.

4.2 Historical Background

The occurrence of AE in materials has been noticed centuries ago. Tinsmiths have heard 'tin cry' as a result of crystal twinning in metals ever since ancient times and steel workers have long noted audible clicks caused by martensitic transformations. Mine workers know well the ominous creaking sounds heard immediately prior to a cave-in, while construction workers are familiar with the crackling sound associated with the impending failure of overloaded wooden structures. The most dramatic example of AE occurs in the field of seismology, where stress waves are used to characterise earthquakes in terms of energy release, location and depth [156].

The earliest encounter of AE in materials research was in 1923 when the French metallurgists, Portevin and LeChatelier [157] were studying the effects of large deformations on aluminium alloys. They noted that load drops which were accompanied by a Luder's line formation coincided with a specimen emitted noise. Thereafter, Joffe [158] reported hearing noises from zinc and heated rock salt. They were studying shear deformation and discovered that as shear progressed in each material with a series of small jumps a noise like the tick of a clock was heard. Each tick could be correlated to a load drop and it was found that the rate of ticking was proportional to the applied load, with thousands of ticks occurring during a single test. In 1948 Mason *et al.* [159] made a major breakthrough in AE study involving the investigation of dislocation movements induced by twinning tin. Their work is worth noting for the simple fact that it remains today as one of the earliest observations of what is perhaps a true acoustic emission waveform. Detailed discussion on the history of AE can be found in the work of Carlyle [156].

Modern AE study started with Josef Kaiser's PhD investigation [160] on tensile tests of polycrystalline zinc, steel, tin, brass, aluminum, copper and lead samples which was published in 1950. He employed transducers, amplifiers and oscilloscopes to study the faint noises on the samples. His conclusion that the emissions were produced primarily

by grain boundary sliding has since been disproven, while his observation that the emissions were of two types, a low amplitude continuous sound with high amplitude bursts superimposed, has been confirmed many times [156]. He also observed that the amplitude and frequency of the emissions were characteristic of the material and stress level. His greatest contribution was the observation that acoustic emission activity appeared to be irreversible and that when a previously loaded sample was reloaded, no emissions were generated until the stress level exceeded its previous level. This behaviour is known today as the 'Kaiser effect' [156].

Kaiser's work opened up several AE studies all over the world in the 1960s and 1970s, and many researchers made tremendous efforts to develop the AE technique. Rettig and Felsen [155] proposed that by measuring the rate of acoustic pulse emission, the cumulative count of acoustic pulse generated, and the pulse amplitudes of the acoustic emissions, correlation may be made with empirical obtained data to permit failure prediction. Dunegan [161] suggested that quantitative predictive information on structural failure can be generated from a combination of acoustic emission and linear fracture mechanics analysis. He gave experimental evidence of the correlation between acoustic emission activities and mechanical deformation process. Recently, Mba *et al.* [162-164] worked extensively on the application of AE in continuous condition monitoring of rotating machinery such as gears, bearings, shafts, etc. They observed that AE systems are the strongest and most potent tools for condition monitoring of engineering structures especially where damage detection sensitivity is a major concern. They maintained that modern AE technique can provide a flexible, portable instrumentation and cost effective systems than conventional methods.

Pioneering work on the use of the AE techniques to study corrosion was done by Okada *et al.* [165] who applied the technique to experimentally investigate stress corrosion cracking and they concluded that there exists a correlation between acoustic emission signals and crack growth due to corrosion and hydrogen embrittlement. Also,

Rettig and Felsen [155] in their experimental study confirmed the correlation between AE activity and corrosion process, and remarked that the corrosion reactions generate elastic waves which may be captured by AE sensor.

4.3 Meaning of Acoustic Emission

Acoustic emission can be defined as the characteristic noise or elastic wave emitted by a material when it is stressed [155]. The stress can be plastic deformation, phase transformation, dislocation, fracture, etc, which leads to rapid release of kinetic energy that propagates in the form of elastic waves from the source and can be detected as small displacements on the surface of the material [154]. Its frequency content is beyond the threshold of human hearing (20 kHz) and normally between 100 kHz and 1 MHz [154, 166]. They propagate on the surface of materials as surface (Rayleigh) waves and can be measured with an acoustic emission (AE) sensor. Other wave types associated with the propagation of AE include Lamb and bulk waves. Lamb waves are guided waves which propagate as plate waves along the thickness of the structure while bulk waves propagate along the bulk of the material as longitudinal or transverse waves [166]. A schematic illustration of Rayleigh and Lamb wave propagation in structures is shown in Figure 4.1.

(a) Rayleigh Wave   (b) Lamb Wave
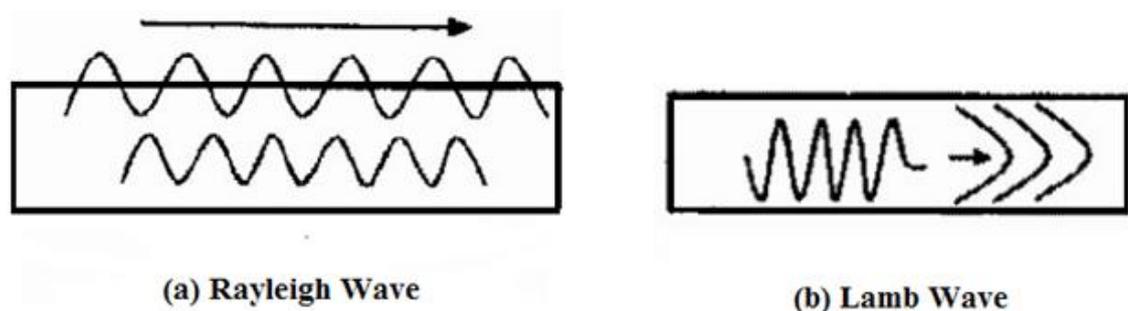
Figure 4.1: Schematic illustration of (a) Rayleigh wave and (b) Lamb wave propagation in a structure [166].

The features of a typical AE signal are illustrated in Figure 4.2. The signal types can be either burst or continuous or a combination of both. A burst signal is usually created by

a short-term event such as sudden impact or increment of a crack propagation in a brittle material with the emission burst lasting typically tens of microseconds [162]. It is characterised by the beginning and end of the signal that deviate clearly from the background noise. The continuous signal has an initial appearance similar to background noise but the average time between emissions of similar amplitude is less than the duration of the emission [162].
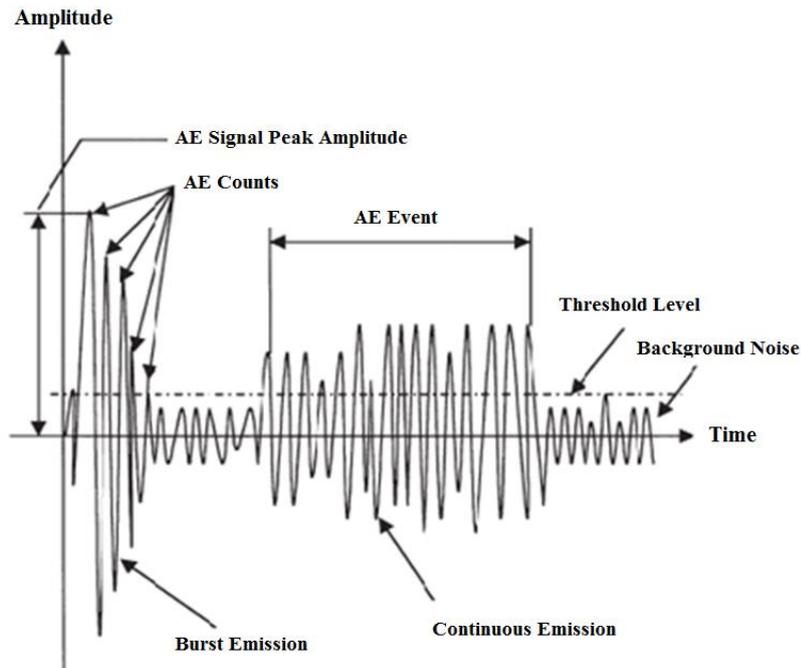
Figure 4.2: Illustration of the features of an AE signal [162].

From Figure 4.2 it can be seen that the AE signal is composed of different parameters as shown in the time-domain signal. These parameters include the following [167]:

AE Events - are the actual detected or measured signals.

AE Counts - are the number of times an acoustic emission signal exceeds a pre-set threshold voltage or amplitude (usually above the background noise level) during a test.

AE Count Rate - is the rate at which AE counts occur.

Rise Time – is the time interval between first threshold crossing and peak amplitude.

Signal Duration - is the time interval between first and last threshold crossing.

AE Peak Amplitude – is the peak voltage of the largest excursion reached by the signal waveform during an AE event.

AE Energy – is defined as the electrical energy in an AE signal and it is regarded as the energy released by an AE source. AE energy is the integral of squared or absolute amplitude over time of signal duration.

The potential sources of AE in oil and gas pipelines include uniform corrosion, localized corrosion and pitting corrosion, leakages, cavitation, turbulence, erosion, erosion-corrosion, etc [154, 155]. For example, the cathodic evolution of hydrogen (bubbles) or anodic dissolution of iron during corrosion reaction can trigger the release of AE activity which can be measured and used to determine corrosion rate. Other sources of AE include friction, mechanical impact, weld defects (lack of penetration and fusion, cracks, inclusions and porosity), crack propagation (static, fatigue, stress corrosion), etc [154]. The advantages and limitations of the AE technique in erosion-corrosion prediction and monitoring are summarised in Table 4.1.

Table 4.1: Advantages and limitations of acoustic emission technique in the prediction and monitoring of erosion-corrosion damage [154, 155, 168]

Advantages	Limitations
- It is a non-destructive technique.	- Signals capture may require high level skill for their interpretation and analysis.
- The actual energy of particles responsible for erosion-corrosion can be quantified.	- Background noise may complicate signals (though modern equipment can filter signals from noise).
- Online and real-time quantification of corrosion and erosion-corrosion rate.	- Modern data acquisition and processing equipment can be expensive.
- Long distance or remote area can be monitored from single sensor location.	
- Separation of impact of solid particles from those of bubbles and flow is possible.	
- It can be used for low to high temperature systems.	

4.4 Signal Processing and Analysis Techniques

One of the greatest challenges in the application of AE technique is signal processing, analysis and interpretation i.e. being able to process, analyse and interpret results of the measured AE signals in order to identify deviations from normal conditions.

These techniques have been discussed in detail in references [154, 155]. They include time-domain analysis (count rate - threshold crossing and event counts, and energy), frequency-domain analysis and root mean square (RMS) which were applied in this study and are discussed in the next paragraphs. The novelty of the research in this aspect is that the study was able to separate the events due to sand impact from flow and background noise in a submerged impinging jet rig and applied it to characterise sand particle impact per second and material degradation rate.

4.4.1 Time–Domain Analysis

In time-domain, the time histories (waveform) showing the measured signal amplitude and corresponding time are displayed. Signals can be analysed in this domain using count rate method [155] and energy method [154, 156, 169].

4.4.1.1 Count Rate Method

This method is also known as ring down counting [170]. It is a method whereby a threshold signal value (usually above the noise level) is specified and the number of threshold crossings per unit time is determined and recorded. The total number of counts gives a measure of the signal strength. This is illustrated in Figure 4.3. This process can also be used in counting AE events so as to determine the events occurring at a particular time [154].

4.4.1.2 Energy Method

AE energy (see Figure 4.3) is the integral of squared or absolute amplitude (A) over time of signal duration (t) and is given by [154]:

$$SE = \int_0^t A^2 (t) \mathrm{d}t \qquad\qquad (4.1)$$
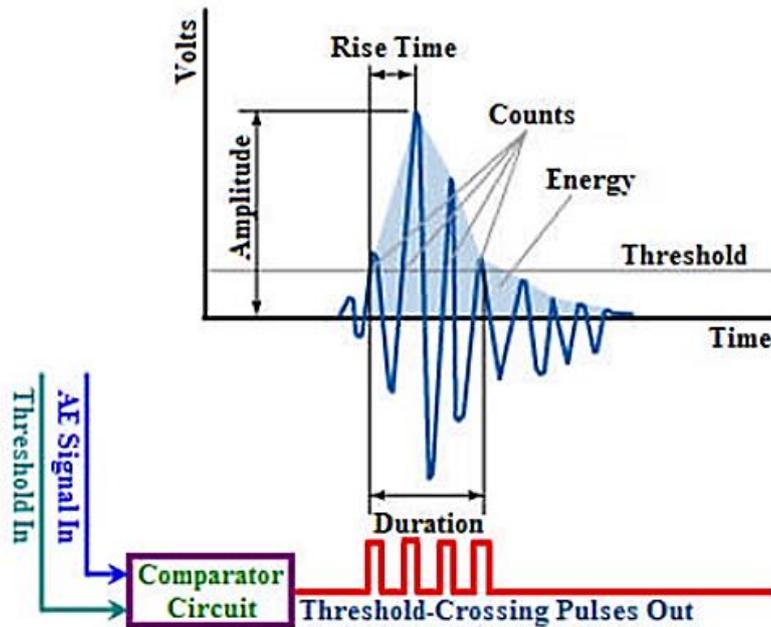
Figure 4.3: Illustration of count and energy of AE signal [154].

4.4.2 Frequency-Domain Analysis

The frequency-domain analysis is a Fourier transform technique that takes the waveform of the measured AE signal and converts it to frequency space [169]. Fast Fourier Transform (FFT) is an optimised tool for the Discrete Fourier Transform (DFT) to perform frequency analysis. It uses algorithms that have been built in some software such as MATLAB, ORIGINLAB or any other computer programming language.

The need for frequency spectrum analysis arises because the manner in which the frequency spectrum displays information will normally reveal details of an AE signal that are too difficult or complex to observe in the time domain, irrespective of the fact that the frequency spectrum of a signal has no more information in it than the time domain signal. For instance, an AE signal may appear to be one sine wave in the time domain, but the frequency spectrum may clearly reveal that the signal is composed of one large sine wave and several smaller sinusoidal components [156]. This analytical power of spectral analysis makes it an attractive technique for characterising acoustic emission signals because each source mechanism should have a characteristic frequency spectrum based upon its size and speed of operation.

4.4.3 Root Mean Square (RMS)

This is also known as Quadratic Mean (QM) [154] and in power system engineering it means the rectified, time averaged signal measured on a linear scale and reported in volts but commonly used in AE signal analysis. RMS can be calculated for individual event (X) and sample size (N) as follows [154]:

$$RMS = \sqrt{\left(\frac{X_1^2 + X_2^2 + X_3^2 \dots\dots\dots + X_N^2}{N}\right)} \qquad\qquad (4.2)$$

4.5 AE in Corrosion Prediction and Monitoring

The principle of corrosion monitoring and prediction is based on the theory that there is a redistribution of energy from chemical reactions of metallic corrosion leading to release of elastic waves (acoustic emission). Hence, any corrosion process is a potential source of acoustic emission [155].

AE signals from corrosion reactions can be detected by AE sensors, amplified, filtered, recorded and analysed using sensitive instrumentation as illustrated in Figure 4.4. A correlation of the signals with known standards such as weight loss or iron dissolution rate (through corrosion current density or potential) provides a non-destructive technique for monitoring and predicting corrosion rate. In addition, proper correlation of the mean amplitudes and count rates of the emitted AE signals can be used to determine different types of corrosion such as uniform corrosion, pitting corrosion, localised corrosion and erosion-corrosion [155, 171].
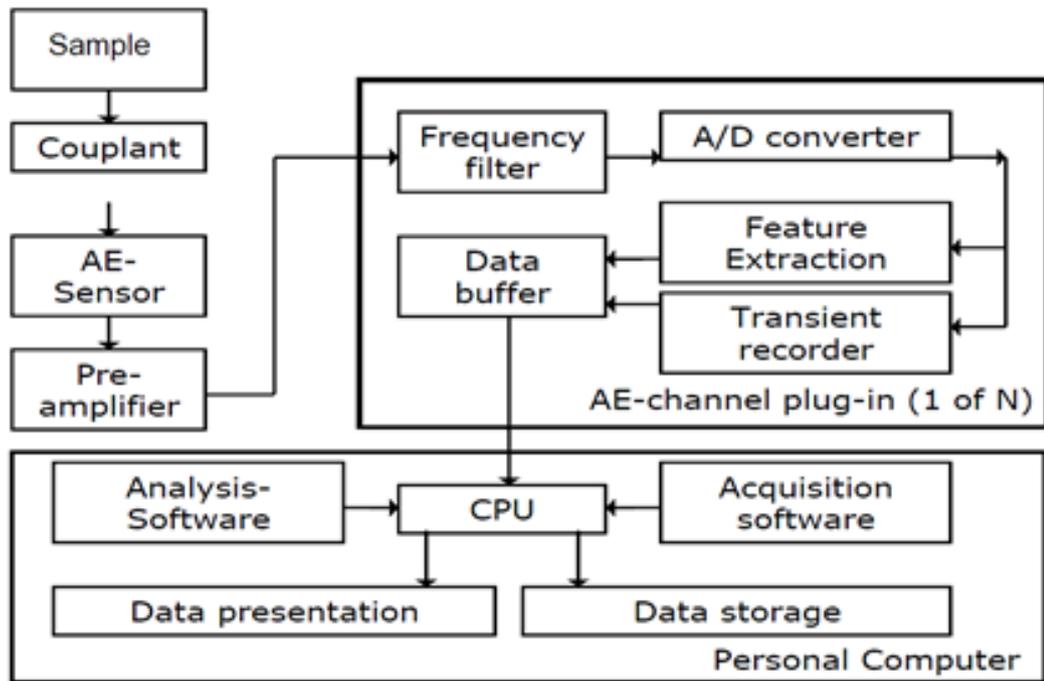
Figure 4.4: Block diagram of AE instrumentation [168].

Some researchers such as Rettig and Felsen [155], Seah *et al.* [170], and Ferrer *et al.* [172] have made attempts in the past in the application of this technique to model and characterise corrosion rate. Rettig and Felsen [155] conducted simple AE experiments using iron and aluminium joined together to determine hidden corrosion at the joints.

They observed that acoustic emissions are generated by corrosion reactions in the form of discrete pulses or bursts of acoustic emission energy which travel at the speed of sound in the material. They further immersed iron wire in 2 M HCl solution and measured the AE count rate vis-a-vis the volume of hydrogen released during the corrosion of iron. They discovered that the AE count rate is linearly proportional to the corrosion reaction process (measured by hydrogen formation) as shown in Figures 4.5a and 4.5b, an indication that the count rate can be used to determine corrosion rate.
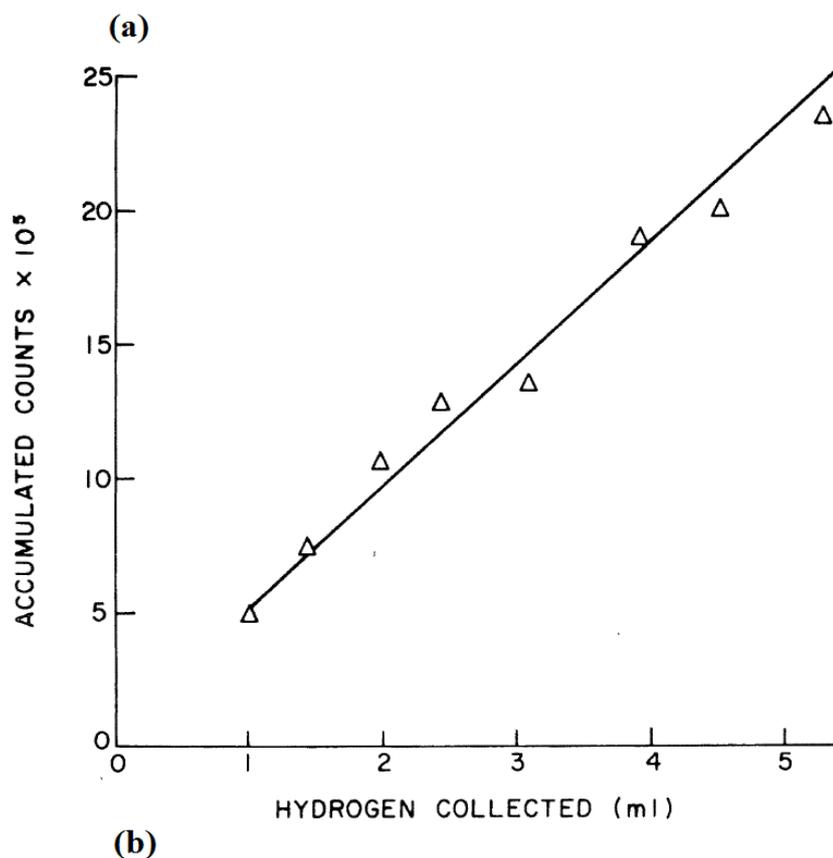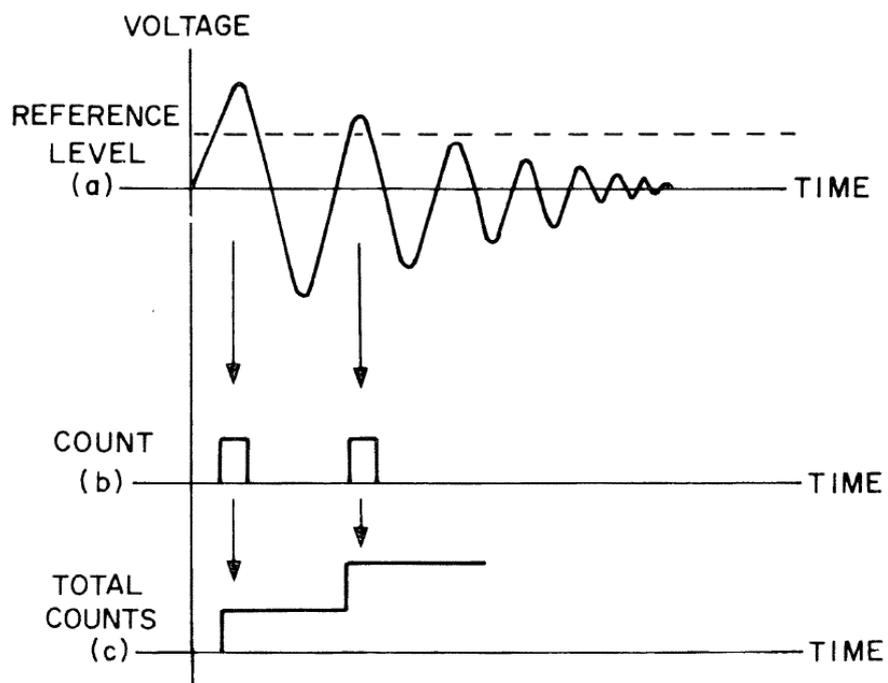
Figure 4.5: Schematic illustration of (a) AE output from the apparatus and (b) correlation of hydrogen generation with Acoustic Emission [155].

Seah *et al.* [170] performed an experiment to correlate AE with corrosion rate. They exposed a mild steel (AISI 1020) sample to a corrosive environment (diluted HCl of molarities ranging from 0.0005 to 0.01) for a test duration of 48 hours while monitoring the AE activity using sensitive AE instrumentation. They observed that as the molarity of the corrosive medium increased from zero, the corrosion rate and AE count rate increased rapidly, but finally reached a limiting value when molarity goes beyond 0.08. They proposed that there is a correlation between the corrosion rate and the count rate with both increasing with increasing molarity of the corrosive environment; the relationship between the AE count rate expressed in counts per square decimetre per day (cdd) and corrosion rate expressed in weight loss (milligrams per square decimetre per day (mdd)) is shown in Figure 4.6.
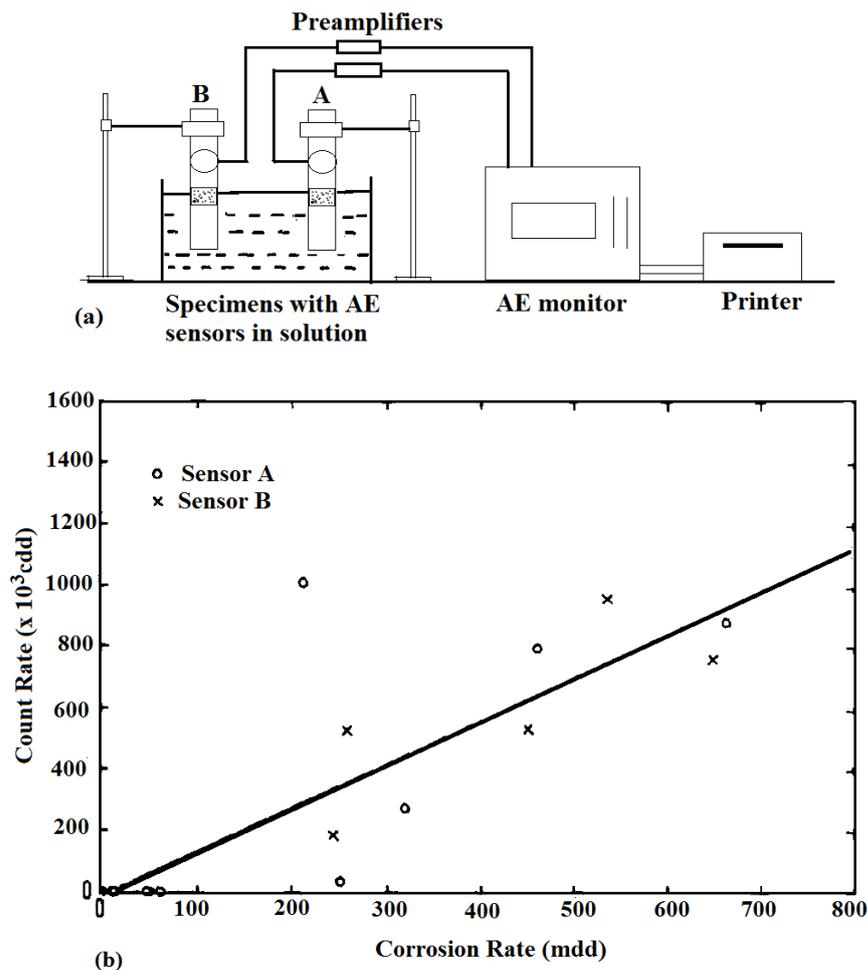
Figure 4.6: (a) Experimental set-up and (b) AE count rate vs. corrosion rate [170].

They concluded by stating that the AE signals detected were as result of the release of hydrogen bubbles during the corrosion process (though no conclusive evidence), and that the correlation between AE activities and corrosion rate is very clear, meaning that AE activity can be used to characterize corrosion rate. Based on their observed mean amplitudes and count rates of the AE signals due to corrosion as a result of different molarities of corrosive medium, it is possible to monitor and detect different types of corrosion such as uniform corrosion, pitting and intense localized corrosion.

Ferrer *et al.* [172] conducted a static corrosion experiment using carbon steel (XC18) sample exposed to 94-98% concentrated sulphuric acid with AE sensor coupled to the specimen as shown in Figure 4.7a.
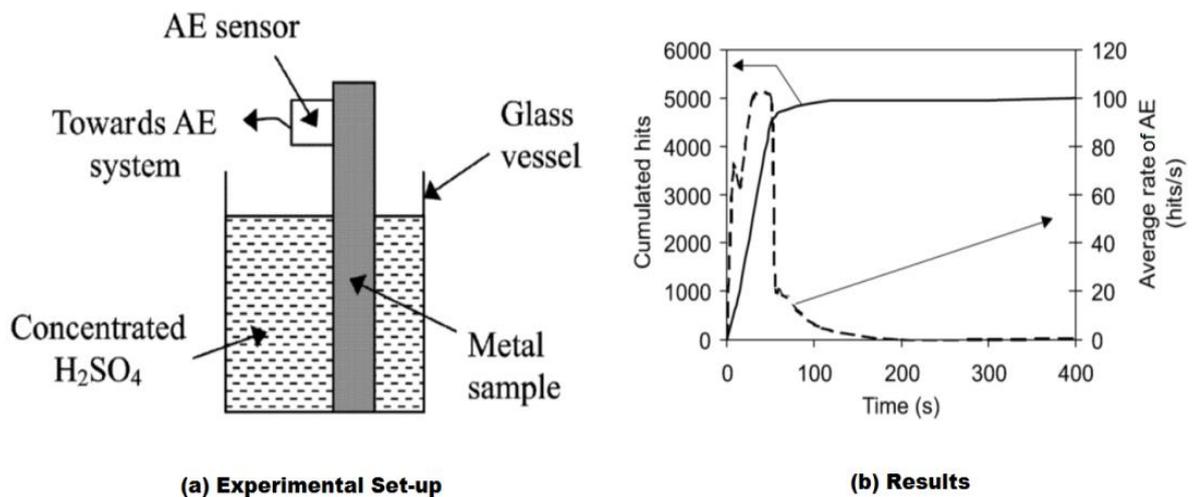
Figure 4.7: AE static corrosion test (a) experimental set-up (b) results [172].

Their results (Figure 4.7b) show an increase in AE activity with corrosion rate over a time period which reaches maximum and begins to decrease when a protective layer of iron sulphate ($FeSO_4$) starts to form on the steel surface. According to them, a protection against corrosion by stabilised protective $FeSO_4$ layer is observed when the AE activity becomes constant. The AE activity did not stop completely but reduced to one hit per ten seconds which is an indication of residual corrosion. Their conclusions conform to those of Seah *et al.* [170] that hydrogen gas evolution releases the AE signals during the corrosion process.

Recently, Prateepasen and Jirarungsatian [171] have extensively investigated the application of AE in the study of pitting corrosion on stainless steels and uniform corrosion on carbon steels. Their findings are in agreement with the works of Rettig and Felsen [155], Seah *et al.* [170], and Ferrer *et al.* [172].

4.6 AE in Erosion Prediction and Monitoring

Similarly, erosion processes in engineering materials generate acoustic emission due to the plastic deformation and/or cutting processes that accompany erosion events. The nature and features of the AE signal such as frequency, amplitude, duration, growth and decay rates are governed by the magnitude of the impact, target material geometry and properties, erodent properties and type of sensor used [173].

For example in elastic deformation, Hunter [174] in his study showed that for elastic impact of hard steel spheres with a steel target, the fraction λ of the initial kinetic energy of the sphere which is dissipated as elastic waves (acoustic emission) is given by [174].

$$\lambda \cong 1.04 \left(\frac{V}{C_o}\right)^{\frac{3}{5}} \qquad (4.4)$$

And for the impact of hard steel spheres with glass [174]:

$$\lambda \cong 1.27 \left(\frac{V}{C_o}\right)^{\frac{3}{5}} \qquad (4.5)$$

where, V is the velocity of impact and C_o is the velocity of longitudinal elastic waves along the target material.

For plastic deformation, Miller and Pursey [175] proposed that the fraction of the kinetic energy dissipated in elastic wave (acoustic emission) is in few percents and distributed among the various components of the elastic wave field with greater percentage carried as Rayleigh wave. They showed that 6.9% of the energy is radiated as

longitudinal (compressional) wave, 25.8% by transverse (shear) wave and 67.4% by surface (Rayleigh) wave.

This finding has been confirmed by Hutchings [101, 176] who derived an expression for the approximate fraction of the initial kinetic energy of a rigid spherical erodent that is dissipated in the elastic waves generated by plastic impact against a massive target. He concluded that the fraction is only a few percent (1-5%), and carried mainly by the Rayleigh wave. The balance of the energy is dissipated as plastic work in form of heat and stored energy as illustrated schematically in Figure 4.8.
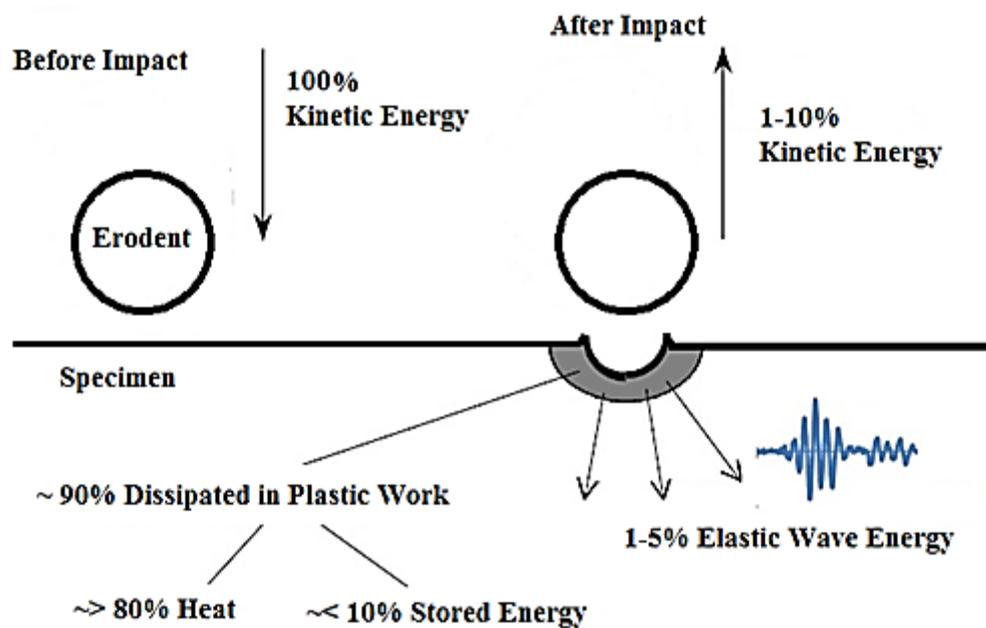
Figure 4.8: Illustration of AE release from solid particle impact [101, 176].

4.7 Mechanism of Energy Transfer

From Figure 4.8, AE is the transient elastic energy released in the material as a result of this deformation process. Therefore, AE relies on the deformation mechanisms and it has been observed by Dornfeld and Kannatey-Asibu [177] that dislocation motion is the major mechanism of plastic deformation that releases AE in most crystalline materials. Based on this, two mechanisms of elastic wave energy transfer during plastic deformation were identified to explain the causes of acoustic emission during

the process. The first is related to non-stationary dislocation motion which has been explained in details by Eshelby [178]. He suggested that the process is 'a dislocation kink vibration' and that the resisting force is an effect of acoustic radiation by the kink. He also remarked that AE involving non-stationary motion of dislocations is analogous to electromagnetic radiation of accelerated and/or decelerated charged particles which is referred to as 'bremsstrahlung acoustic radiation' [178]. The second is based on the theory of classical electromagnetic radiation generated by charged particles going through the boundary between two media of different dielectric constants. This second aspect has been discussed in detail by Trochidis and Polyzos [179] who proposed that the annihilation of dislocations rather than the non-stationary motion can be the main source of the AE during plastic deformation of metals.

However, it has been argued that since AE is also observed during deformation of non-crystalline materials, its generation cannot be ascribed alone to the dislocation motion mechanisms mentioned above. In view of this, Pollock [180] used a simple spring-mass model to propose that acoustic emissions possess kinetic energy (KE) which is drawn from the reservoir of elastic energy stored in the stressed material undergoing plastic deformation. He maintained that a process that generates AE is a process that involves a momentary instability of the system which creates a mechanical oscillation that propagates on the material. Because acoustic emission comes from a point source rather than a line or an area, the stress wave will propagate as a diverging spherical wave. Kinsler and Frey [181] gave the spherical wave equation as:

$$\frac{\partial^2 (rp)}{\partial t^2} = \frac{c^2 \partial^2 (rp)}{\partial r^2} \qquad (4.6)$$

where r is the radius, p is the pressure, c is the wave speed, and t is the time. For a diverging spherical wave having harmonic vibrations, the solution to equation 4.6 is:

$$p = \frac{A}{r} e^{(j\omega t - kr)} \qquad (4.7)$$

where A is the amplitude, j is $\sqrt{-1}$, ω is the angular frequency, and k is ω/c, the wavelength constant. Thus, a given diameter transducer sensitive to force would have an electrical output inversely proportional to its distance r from the source simply due to the spreading of the wavefront. Generally, the amplitude of the wave will not be constant as indicated in Equation 5.2, but will instead decrease according to [181]:

$$A = A_0 e^{-\alpha r} \tag{4.8}$$

where α is the attenuation coefficient. The attenuation is due to two general processes, namely absorption, wherein the acoustic wave performs work as it propagates and thus loses energy, and scattering, whereby part of the energy in the wave is reflected out of the path of propagation. The value of the attenuation coefficient is a function of the material, its homogeneity, its temperature, and the frequency content of the acoustic wave [181].

The nature of the emission can be 'continuous emission' (similar to low-amplitude background noise with steady events that overlap in time, lasting for periods of order of seconds) or 'burst emission (high-amplitude and erratic discrete events). Mathematically, continuous emission with constant amplitude, A_0, frequency, f and time, t can be expressed as [182]:

$$A(t) = A_0 \sin 2\pi f t \tag{4.9}$$

For burst-type emission with the assumption that the signal from a single event is a damped sinusoid can be written as [182]:

$$A_n = A_{on} e^{-t/\tau} \sin 2\pi f t \tag{4.10}$$

where A_n is the amplified and filtered AE signal to counter, A_{on} is the initial amplified and filtered voltage from single event to counter and τ is the decay time of the AE signal.

Depending on the nature of the source event, various percentages of the total energy released will be available as measurable acoustic emission waves which have a waveform that can be characterised in different ways. It can be longitudinal wave (if the particle displacement is parallel to the direction of wave propagation) or transverse wave (if the particle displacement is perpendicular to the direction of wave propagation). The interaction between the two waves (also known as bulk waves) by way of reflection, refraction and mode conversion [156, 166] with the boundaries give rise to guided waves such as Rayleigh (surface) waves and Lamb (plate or thickness mode) waves [156, 166].

Rayleigh waves exist at the free surface of the structure and their amplitude decay with depth while Lamb waves exist as plate waves and normally propagate along the thickness of the structure [166]. The discussion of the dynamics of these waves is beyond the scope of this work. The interest here is on detecting Rayleigh waves due to erosive source events using AE sensor attached at the back surface of the specimen and using it to characterise the erosive wear of the specimen.

During the impingement of a solid-liquid stream that creates erosive source events, the surface is displaced and this displacement is transmitted into the front face of the piezo-electric crystal of the sensor. The degree to which this displacement is converted into strain in the crystal depends on the relative movement of the back and front faces of the crystal. Slow displacement does not induce any strain whereas rapid movement produces strain [183]. At higher rapid rates, the strain produced in the crystal for given amplitude of displacement at the front face is increased with a considerable increase in the stress in the crystal.

The relationship between the stress and strain in the crystal and the resultant output voltage is quite complex and some resourceful techniques are currently being applied by AE companies [184] to get calibration for practical sensors. An investigation conducted by Hill and El-Dardiry [185] revealed that the measurement precision and

magnitude of acoustic emission signals will be affected by the type and thickness of the couplant used to couple the sensor to the specimen. They maintained that the resulting waveform has a spectrum which is the convolution of the source spectrum with the transfer functions of the specimen and sensor detecting the acoustic signal. This makes the transfer of energy from the stressed specimen into the sensor a complex process and it has not been possible to quantify the various transfer functions explicitly, thus leading to the characterisation of the waveform using AE signal processing and interpretation parameters such as threshold crossing count, event count, amplitude and energy analyses. These techniques have been discussed in detail in Section 4.4 and further understanding of them can be found in the work of Stone and Dingwall [183].

Investigations by Oltra *et al.* [186] and Ferrer *et al.* [187] have experimentally established the relationship between particle kinetic energy and acoustic emission energy during the erosion process.

Using glass beads of various diameters, 316L stainless steel and sodium sulphate (1 M Na_2SO_4) solution with pH of 7 in a jet impingement system (90° impingement angle) at 25^oC, Oltra *et al.* [186] on erosion aspect, suggested that the acoustic emission energy expressed in RMS value is linearly proportional to the square root of the kinetic energy of the eroding particles. They maintained that the mechanical wear (erosion) in absence of corrosion is also linearly related to the AE parameters after one hour of exposure time. Their results are as shown in Figures 4.9a and 4.9b.
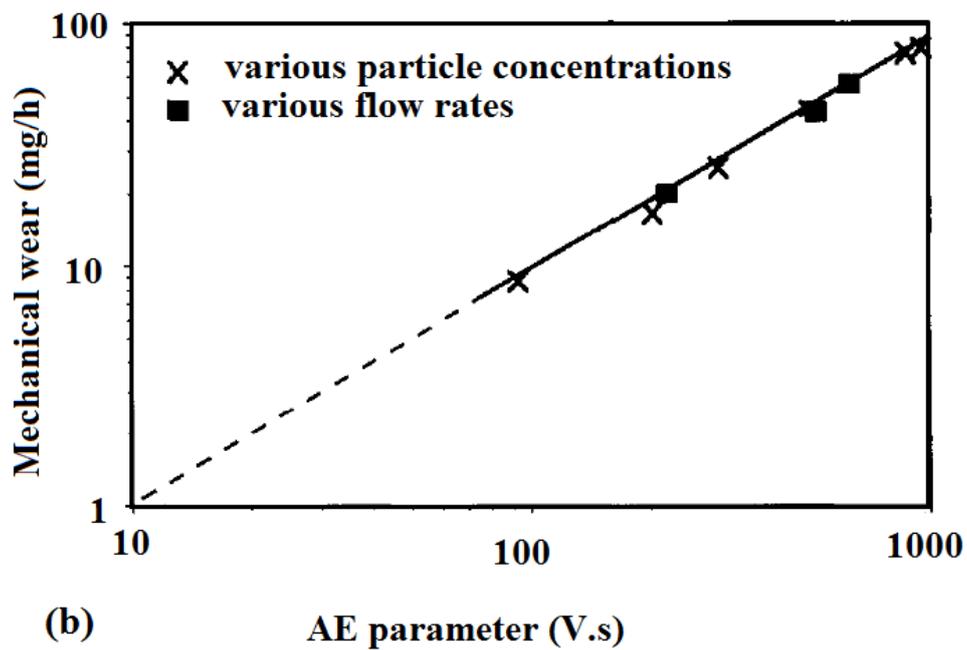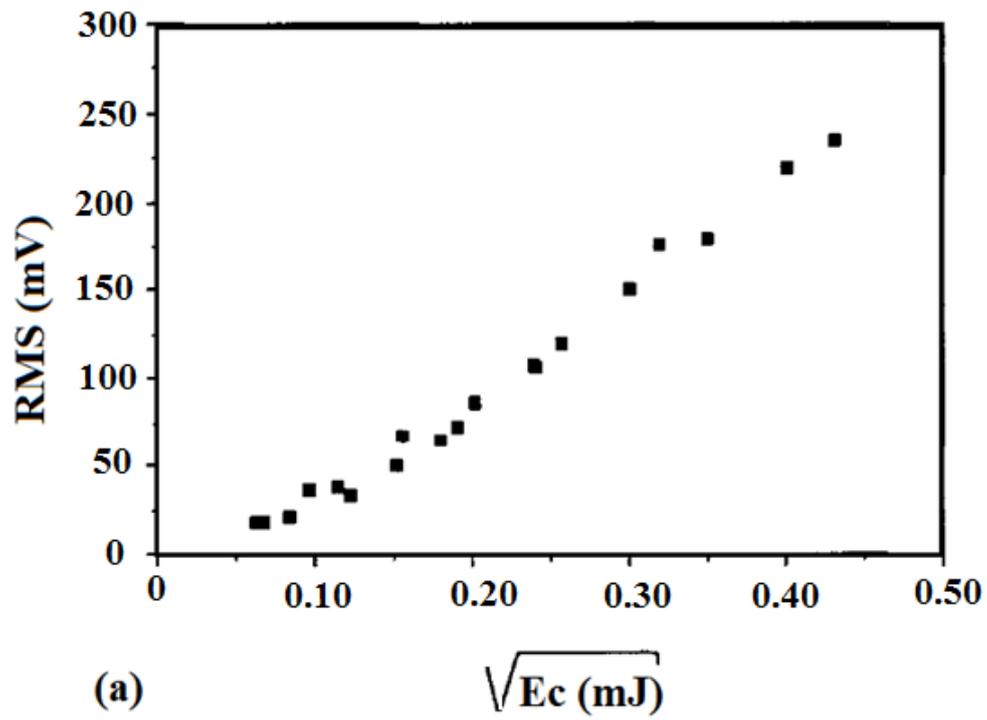
Figure 4.9: (a) AE (RMS) vs. particle K.E and (b) Erosion vs. AE (RMS) [186].

Ferrer *et al.* [187] performed a similar study for different impingement angles (30°, 45° and 90°), increasing flow velocities (between 1 and 16 m/s) and increasing particle loading (glass beads for single impact and SiC particles for multi impact - between 1

and 8 wt. %) using stainless steel (AISI 304 L) and Na_2SO_4 solution (1 wt. %) with neutral pH. They observed that the AE energy is also linearly proportional to the particle kinetic energy with 90° impingement angle having the greatest increase. They stressed that the weight loss (Δm) due to pure erosion also varies linearly with AE energy for different flow velocities, particle loading and impingement angles. Their results are summarised in Figures 4.10a and 4.10b.

(a)

(b)
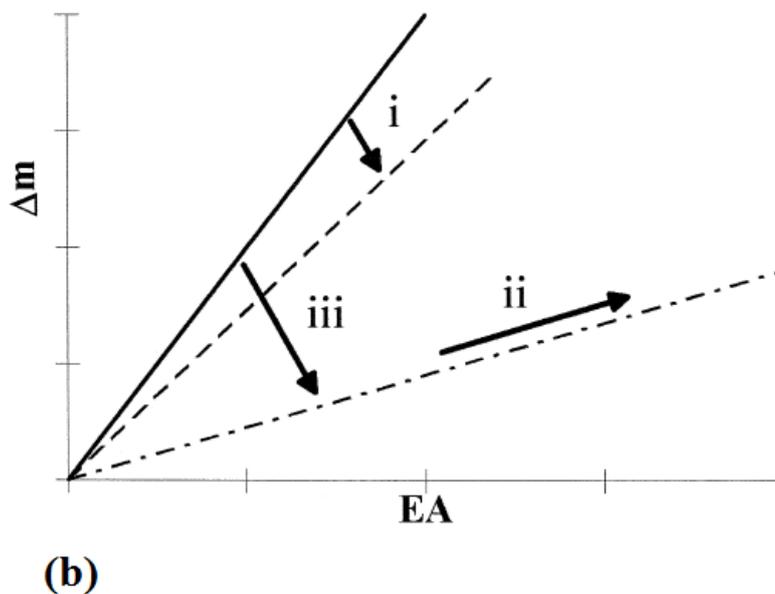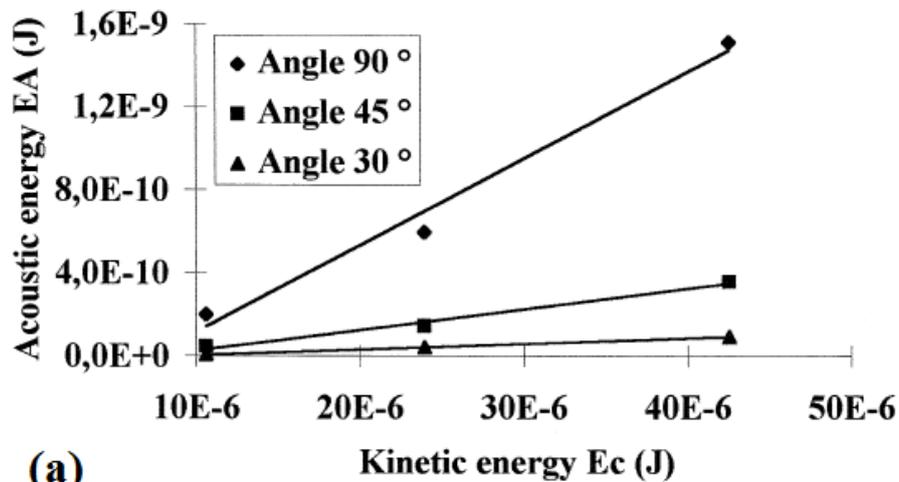
Figure 4.10: Illustration of (a) AE energy vs. particle K.E for different impingement angles and (b) Weight loss vs. AE energy for increasing flow velocities (i), increasing particle loading (ii) and increasing impingement angle (iii) [187].

Other researchers that have successfully applied AE techniques to monitor and characterise mechanical wear include Mechefske et al [167], Bonness and McBride [188], Lingard *et al.* [189], Hase *et al.* [190] and Droubi *et al.* [191] to mention but a few. A detailed review of the application of AE in the study mechanical wear processes in both dry and wet conditions can be located in the work of Droubi *et al.* [191].

4.8 AE in Erosion-Corrosion Prediction and Monitoring

Very few studies exist in the literature that adequately investigated the application of AE technique in characterising erosion-corrosion. This could be as a result of the complex nature of the erosion-corrosion process. The very few that were seen during the literature search include the work of Ferrer *et al.* [172, 173] and Oltra *et al.* [186].

 Ferrer *et al.* [172] in their dynamic erosion-corrosion test of XC18 carbon steel tubes in concentrated sulphuric acid circulated in a flow loop at temperature of $20^{o}C$ and at very low flow velocities (0.1 to 1 m/s) for a duration of two hours without solid particle loading attempted to correlate the AE activities with erosion-corrosion damage. They observed that there is an appreciable increase in AE activity (cumulated hits) with increase in flow velocity and that the injection of a corrosion inhibitor into the solution decreases AE activity to a low value, an indication that active corrosion is the AE emitting source, even at a high velocity, turbulence has little influence.

Their results (Figures 4.11a and 4.11b) were confirmed by an electrochemical corrosion test which supported the assertion that the corrosion rate increases with increase in flow velocity with 0.3 m/s as their critical velocity. They remarked that during the active-passive transition of the carbon steel, two possible sources of acoustic emission can be expected. One is the hydrogen gas release from corrosion reaction and the other is the breakdown of the $FeSO_4$ protective film by erosion process as the critical velocity is exceeded.
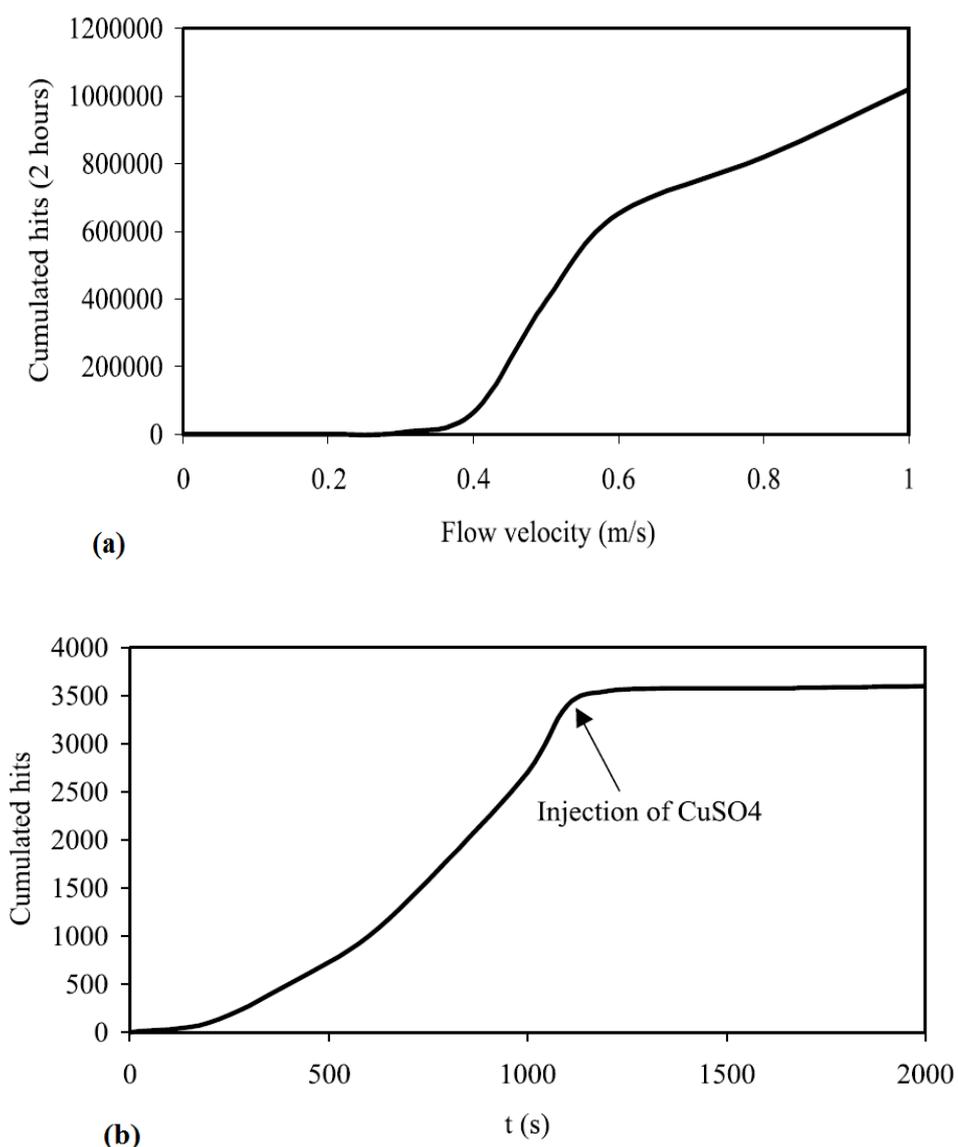
Figure 4.11: Illustration of (a) AE activity variation with flow velocity in erosion-corrosion test and (b) the effect of an inhibitor on the AE activity at 2 m/s [172].

Ferrer *et al.* [173] further applied the same AE technique coupled with electrochemical measurement, this time in a jet impingement system to investigate erosion-corrosion on AISI 304 L cylindrical sample (diameter 30 mm, thickness 3 mm and 0.5 cm^2 surface area in contact with corrosive environment made up of NaCl solution (3 wt%) acidified to pH of 1.5 with HCl). The erodent was SiC particles (125 μm grain size) with increasing loading of 1 to 8 wt% and increasing flow velocity of 4 to 10 m/s.

They established a correlation between variation of acoustic energy and corrosion potential during erosion-corrosion test which is evidenced by sudden increase of

acoustic energy with decrease in corrosion potential when solid particles are introduced in the environment as shown in Figure 4.12. The acoustic energy and corrosion potential confirm the existence of energy flux of impacting particles and corrosion reaction respectively, with a negligible bursts resulting from bubbles. Having confirmed that, they used AE parameter (Average RMS) to characterise the total weight loss due to pure erosion, pure corrosion, their synergistic effect and erosion-corrosion. They observed that the total weight loss due to all the damage processes (pure corrosion, pure erosion and erosion-corrosion) increases linearly with increase in AE activity for all the flow velocities, particle loading and impingement angles studied. They maintained that at low erosion rate, the synergistic effect increases with increase in erosion and dependent on angle of impact, while at high erosion rate the synergistic effect decreases (until it gets to a limiting value at 25% of total weight loss) whereas the erosion rate increases monotonously, and the total weight loss as well as the synergistic effect being controlled by pure erosion process whatever the angle of impact.
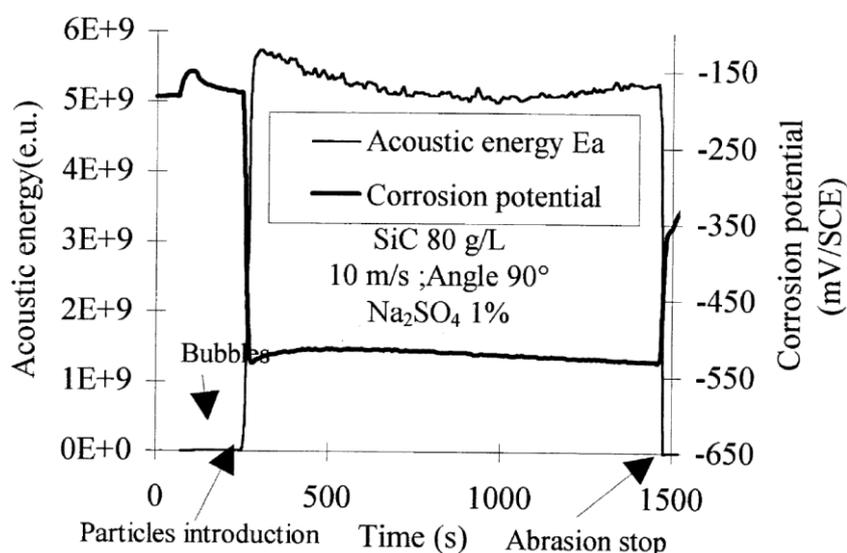
Figure 4.12: Simultaneous variation of acoustic energy and corrosion potential for high abrasion rate [173].

Oltra *et al.* [186] further conducted an erosion-corrosion study by applying the same AE technique coupled with electrochemical (current) noise using 316 stainless steel, SiC

particles (500 μm mean size), 90° impingement angle, 9 m/s flow velocity and corrosive environment (1 M H_2SO_4 solution at 25°C). Their results were in agreement with the Ferrer *et al.* [173] results in terms of correlation between AE activity with mass losses due to pure erosion, pure corrosion and their synergy. However, they noted that the mechanical and corrosive damage can be quantified by AE cumulative events but cannot be clearly related to measurements performed during individual impacts.

4.9 Summary

AE is the elastic wave emitted by a material when it is stressed. It can be detected by AE sensors, amplified, filtered, recorded and analysed using sensitive instrumentation. Signal analysis can be done either in time-domain using count rate, energy method, Root Mean Square (RMS) or in frequency-domain using Fast Fourier Transform (FFT).

It was observed that corrosion, erosion and erosion-corrosion are potential sources of acoustic emission as evidenced in the reviewed literature. Erosion-corrosion damage being an electrochemical and mechanical process, so combining electrochemical monitoring with AE can be considered a good approach to investigating the erosion-corrosion degradation processes. This is because AE can give an insight of the sand particle impacts that lead to erosion damage contribution whilst electrochemical monitoring can provide information regarding the chemical dissolution or electrochemical reactions of the materials, thus the overall erosion-corrosion damage and its components can be accurately quantified. Hence, this study adopted the combined technique to investigate and characterise erosion-corrosion degradation of X65 pipeline materials in CO_2 saturated environment using submerged impinging jet rig.

A detailed description of the methods, materials and procedures used in the investigation is contained in the next chapter.

Chapter 5 Experimental Design, Materials and Procedures

This chapter presents detailed layout of the experimental methods, materials and procedures.

5.1 Experimental Design

All the experimental tests were performed in a 50-litre capacity submerged impinging jet (SIJ) rig coupled with acoustic emission and electrochemical instruments as illustrated in Figure 5.1 The rig is a re-circulating system controlled by a centrifugal pump that enhances the mixture of fluid and sand particles. The mixture was delivered through a double nozzle system impinging onto a flat specimen at 90° impingement angle. The components of the rig and their functions are as follows:

5.1.1 Centrifugal Pump

The pump is a variable speed controlled centrifugal pump (INVENT HYDROVAR) which provides the required flow velocity, mixing and recirculation of the fluid and sand mixture in the rig.

5.1.2 Dual Nozzle System

This device provides the jet that impinges on the flat specimen surface. The nozzle diameter is 4 mm and it is placed at a fixed distance of 5 (±0.2) mm from the specimen's flat surface so as to establish the required mass transfer with well-defined hydrodynamics on the specimen's surface as illustrated in section 3.3.4.3, and also to ensure that virtually all the sand particles exiting the nozzle hit the specimen's surface.

5.1.3 Two Sample Holders

 The specimens are rigidly clamped onto the holders to keep the specimens in a firm and steady position throughout the duration of the test.

5.1.4 Reservoir/Mixing Tank

This houses the water and also helps in proper mixing of the water, salt solution and sand particles. The water and salt are properly mixed in the reservoir before the start of each test whilst sand particles mix with the mixture by the recirculation created by the pump.

5.1.5 Heating Device/Thermocouple

This provides the heating and control the experimental rig fluid temperature.

5.1.6 CO_2 Tube

This is a long glass tube that is used to introduce and/or sparge CO_2 in the test fluid.
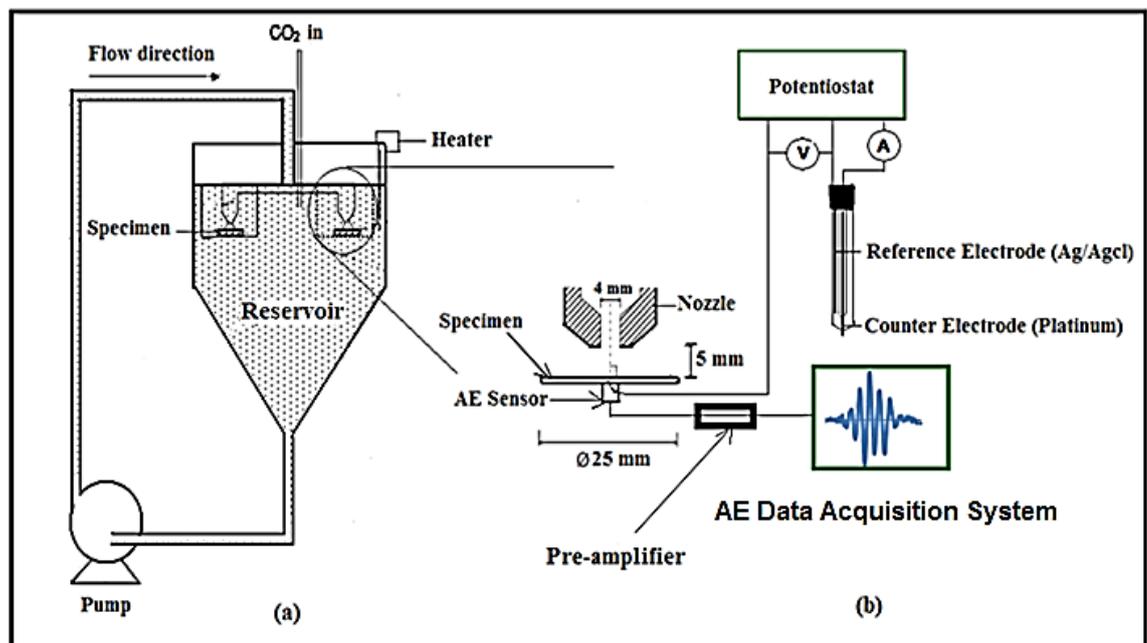
Figure 5.1: Schematic illustration of experimental rig set-up.

The SIJ system was chosen because it can reproduce a wide range of local impact conditions similar to those obtained in oil and gas pipeline systems (tees, elbows, chokes, valves, etc.). This has been confirmed by the CFD predictions of Gnanavelu *et al.* [94, 110] who observed that for a nominal impingement angle of 90°, the local angles varied approximately from 90° to 6° and for a nominal impact velocity of 5 m/s, the local impact velocity can vary between 1 and 5.5 m/s.

5.1.7 Acoustic Emission (AE) Hardware

A wideband piezoelectric ceramic AE sensor (resonant frequency of 350 kHz and frequency range of 80-900 kHz, preamplifier (34 dB gain)), a data acquisition system and software for data capturing and signal analysis were used to detect waveform and characteristic acoustic parameters. The hardware and software were supplied by Vallen [192]. AE signals were sampled at 2.5 MHz sampling rate in accordance with Nyquist criterion (or sampling theorem) and to avoid signal aliasing [156]. The signals were filtered and amplified with band filter frequency of 90-850 kHz and threshold set at 40 dB (justification of threshold setting is discussed in detail in section 5.5) for all tests. The sensor calibration (details in section 5.3.2) was performed using a pencil lead technique [184] to confirm that it conforms to manufacturer's specification and the sensor was coupled to the back of the specimen by means of vacuum grease (to avoid AE signal attenuation [156]) together with electrical contact for electrochemical measurements in a secured test cell/specimen holder (Figure 5.2).

5.1.8 Electrochemical Instruments

These devices were used for the Linear Polarization Resistance (LPR) and AC impedance measurements to obtain *in-situ* corrosion results. They are made up of a three-electrode system (with the specimen as the working electrode, platinum-rod redox electrode as the counter electrode and Ag/AgCl as the reference electrode) and potentiostat linked to a computer for data capturing. The computer-controlled potentiostat (Solartron), equipped with corrosion software (CorrWare, CorrView, ZView and ZPlot), measures and records the current passing between the working and counter electrode as the specimen is polarized. For AC impedance measurement, a small sinusoidal potential excitation (±10 mV) is applied to the system and the resulting current measured. Measurements are carried out over a wide frequency range (20 kHz to 0.1 Hz) and the impedance $(Z = \frac{V}{I})$ calculated and recorded at each frequency.

Since there is generally a phase shift present between current and potential, these ratios are by definition, complex quantities.

5.2 Materials

5.2.1 Specimen Material

The test specimen used in the experiment is X65 carbon steel with a Brinell Hardness number of 217 HB 10/3000/30 and nominal chemical composition as illustrated in Table 5.1. This material was chosen because it represents a common pipeline material used in oil and gas production, processing and refining.

Table 5.1: X65 carbon steel nominal composition (wt %) as supplied by Tata [244]

C	Si	Mn	P	S	Cr	Mo	Ni
0.120	0.180	1.270	0.008	0.002	0.110	0.170	0.070
Cu	Sn	Al	B	Nb	Ti	V	Fe
0.120	0.008	0.022	0.0005	0.054	0.001	0.057	Balance

5.2.2 Specimen Geometry and Dimensions

The specimens for this study are 25 mm diameter 10 mm thick flat circular discs with 490 mm^2 exposed area to the test solution. The main reason for choosing these specimens is that the structure of turbulence and hydrodynamic characteristics on the experimental flat specimens are well defined in jet impingement (as shown in Figure 5.2a) and similar to those obtained in oil and gas pipeline facilities in the field such as tees, elbows, chokes and flanges [78]. In addition, it has been shown by Efird *et al.* [74] that corrosion rates (computed through wall shear stress) from the wall jet region correlate well with corrosion rate in pipe flow. This is supported by the recent CFD predictions of Gnanavelu *et al.* [110] who proposed that the region has the maximum wall shear stress (as illustrated in Figure 5.2b). A test cell/specimen holder for the circular specimen was designed and fabricated as described in the next section.

(a)   (b)
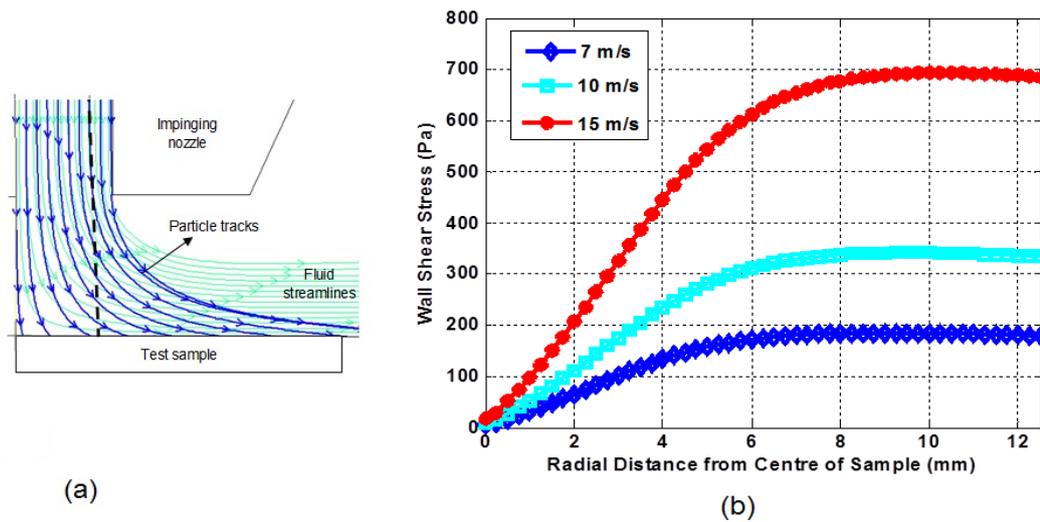
Figure 5.2: (a) Fluid streamlines with the particle tracks in the SIJ system and (b) wall shear stresses across the surface for 7, 10 and 15 m/s flow velocities [110].

5.2.3 AE Test Cell/Specimen Holder

Due to the need to securely hold the AE sensor and electrochemical measurement wire on the circular specimen, a test cell/sample holder made of non-conducting and non-corrosive nylon material that can withstand temperature of 85°C was designed and fabricated. The isometric view of the test cell/holder is shown in Figure 5.3 while the detailed engineering drawing used in the fabrication is shown in Appendix 6.
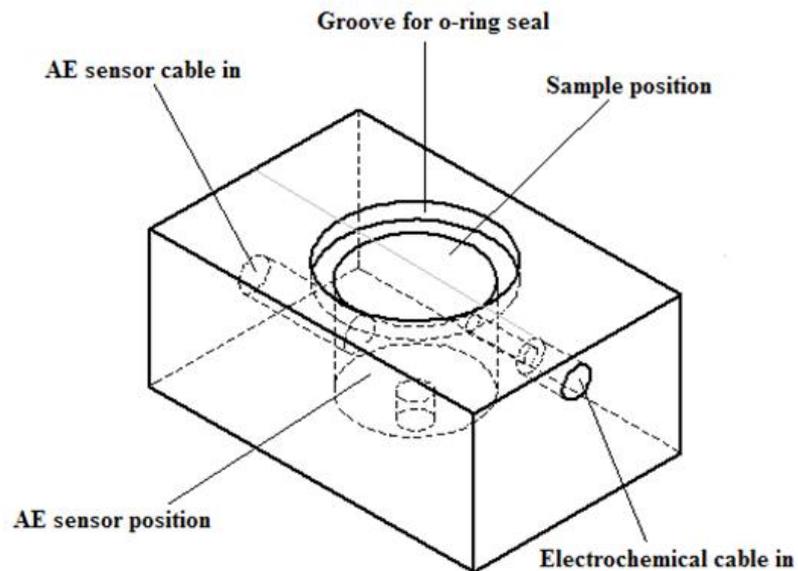
Figure 5.3: Isometric view of AE test cell/specimen holder.

5.2.4 Sand Particle Size and Shape

The sand type used in the erosion-corrosion experiments is HST 60 sand with size distribution in Figure 5.4, and size and shape shown in Figure 5.5. It can be seen from the scanning electron microscopy (SEM) image that the sand is round and almost spherical in shape with average diameter of 250 μm.
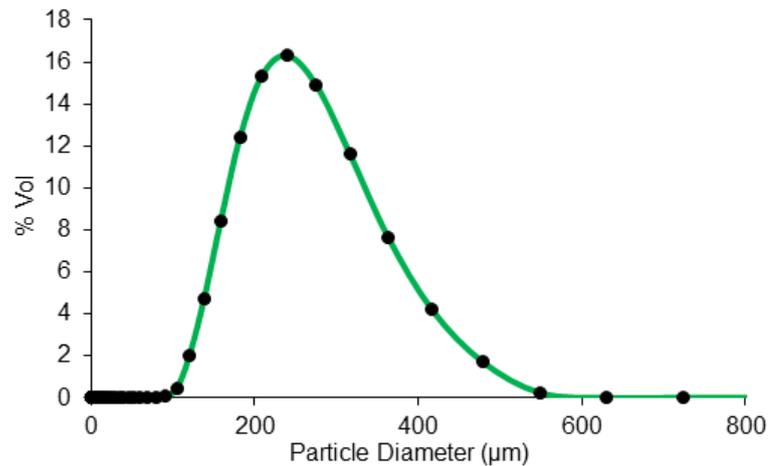
Figure 5.4: Sand particles' size distribution from sieve experiment.
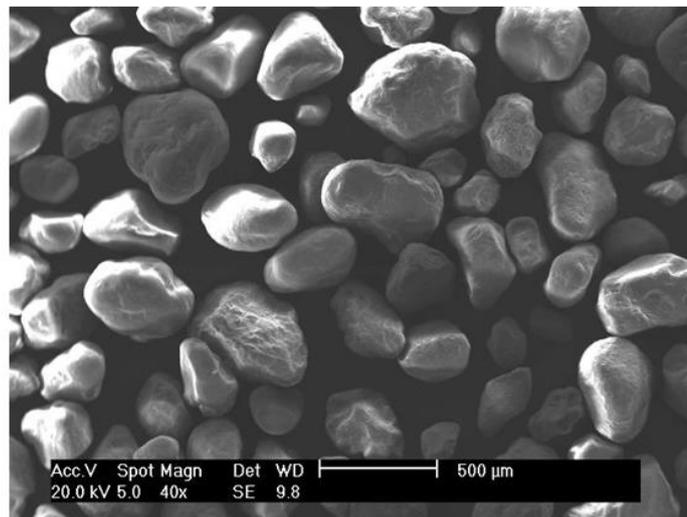
Figure 5.5: Sand particles' shape and sizes from Scanning Electron Microscopy (SEM).

It is important to note that the sand particles are always renewed after every experiment because of the breaking down of the sand particles into smaller particles

due to repeated impact. A study by Hu [58] revealed that only slight variations of size distribution and shape of the sand particles occur after 4 or 8 hours. Hence, it is expected that within the duration of 2 hours test, the shape and size distribution of the sand particles will remain unchanged.

5.3 Calibration

For accurate measurements and results, it is important to perform necessary checks and calibrations on the rig in order to ensure that all components are functional and in good condition with reliable and repeatable results before commencing experimental investigations. As a result, nozzle flow velocity, sand loading and AE sensor calibrations were carried out as reported in the next paragraphs.

5.3.1 Flow Velocity and Sand Loading Calibration

Calibration of the nozzle exit flow velocity and impinging sand loading were performed on the 50-litre capacity rig so as to ensure that similar operating conditions and erosion-corrosion results would be obtained when an experiment is repeated twice or thrice. This is essential in order to accurately reproduce the required conditions that would be encountered in the field or industrial situations which are needed for reliable correlations.

5.3.1.1 Flow Velocity Calibration

The calibrated flow velocity used in all the experiments is the nozzle exit flow velocity. This is because the impingement action is created by the recirculation of the fluid in the reservoir by the centrifugal pump and delivered through the nozzle to the specimen surface. The pump is controlled by an electric motor with frequency attenuator that helps to maintain easy control over the rotational speed of the pump and flow rates.

During the calibration, the nozzle exit flow velocity is calculated from the flow rate through manual flow measurement which was done by operating the pump at a certain frequency, and then collecting and measuring the fluid exiting the nozzle over a fixed

time interval. The volume of the fluid collected in litres (L) is converted to m^3 and then divided by time in seconds to obtain the volumetric flow rate ($Q = AV$) in m^3/s, where A is the flow area (m^2) and V is the flow velocity ($V = Q/A$) in m/s. The flow velocity (m/s) is then determined by dividing the flow rate by the nozzle area ($A = \frac{\pi D^2}{4}$) where D is the diameter of the nozzle.

Measurement of the flow rates for different pump frequencies were carried out and the corresponding nozzle exit flow velocities (calculated as described above) plotted against frequencies as shown in Figure 5.6. The plot reveals that pump frequencies of 16.0, 21.6 and 31.1 Hz give nozzle flow velocities of 7, 10 and 15 m/s respectively. The flow velocity calibration was carried out every two months to ensure repeatability and consistency of experimental results.
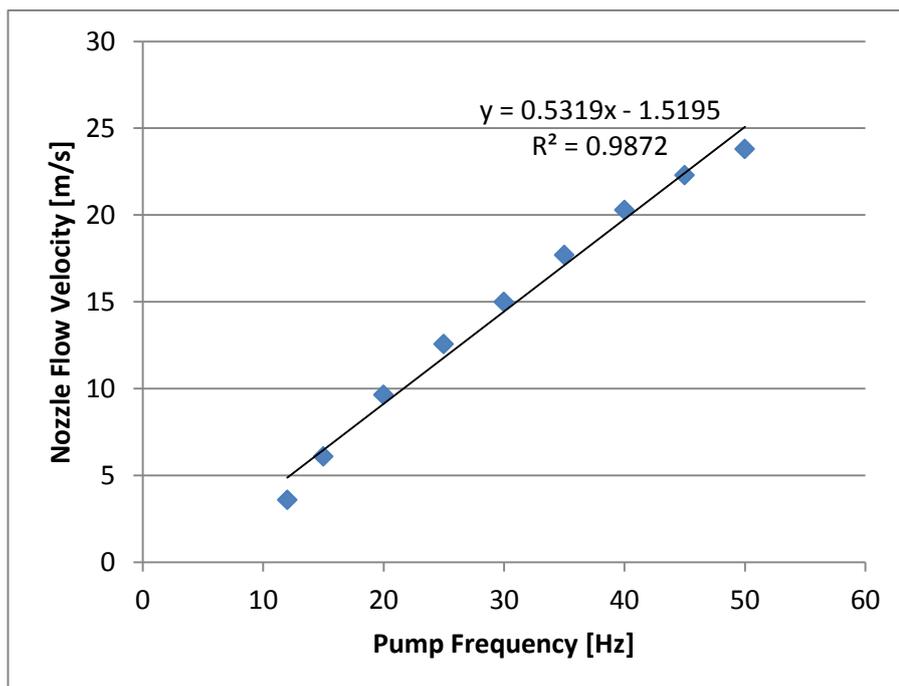
Figure 5.6: Plot of nozzle flow velocity variation with pump frequency during the flow velocity calibration.

5.3.1.2 Sand Loading Calibration

This is defined as the ratio of total weight of sand particles to the total weight of fluid solution within the reservoir. It can be expressed as weight per cent (wt%), milligram per litre (mg/L) or part per million (ppm). It is always a challenge to accurately determine the amount of sand particles impacting the test specimen's surface by the re-circulating impingement apparatus.

Gnanavelu *et al.* [110] and Wood and Wheeler [193] have observed that not all the sand particles that were added to the reservoir actually impact the surface because of inter-particle collision at the surface, sweeping action of the liquid jet away from the surface and non-uniform mixing of particles within the reservoir.

As a result, sand loading in the rig was calibrated by operating the pump at certain frequency starting with 50 Hz, then 40 Hz, 30 Hz and then adding a constant amount of sand (say 20 g) at each frequency. During each test, water samples were collected from each of the two nozzles, filtered, dried and weighed to determine the re-circulating sand concentration (ppm) exiting the nozzle. The weight of the dried sand is then divided by the volume of fluid collected in each case to establish the sand concentration. Groups of tests were performed for 7, 10 and 15 m/s nozzle flow velocities and the results plotted as shown in Figures 5.7, 5.8 and 5.9 respectively.

Using 7 m/s flow velocity as an example, putting sand loading of 84, 815, and 131,025 mg of sand into the reservoir will produce approximately 50, 200 and 500 (±5) mg/L of sand concentration exiting the nozzle respectively.

The nozzle exit sand concentration data obtained for 7, 10, 15 m/s flow velocities are verified from time to time to ensure consistency of results, and were used in all the experimental investigations of the erosion-corrosion damage.
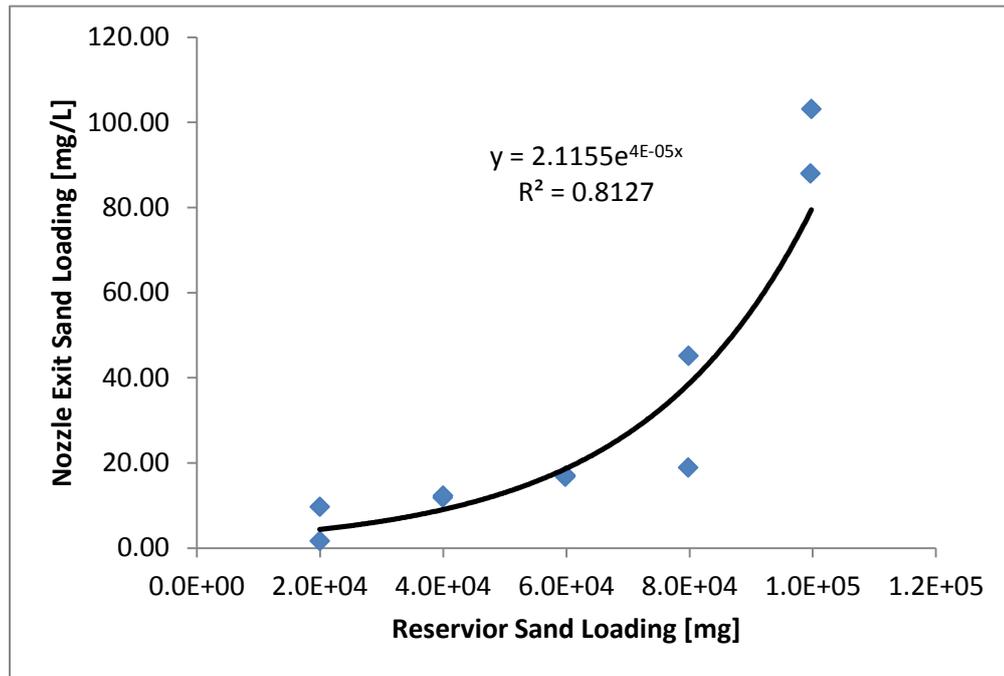
Figure 5.7: Plot of nozzle exit sand concentration variation with sand loading added to the reservoir during the sand loading calibration for 7 m/s flow velocity.
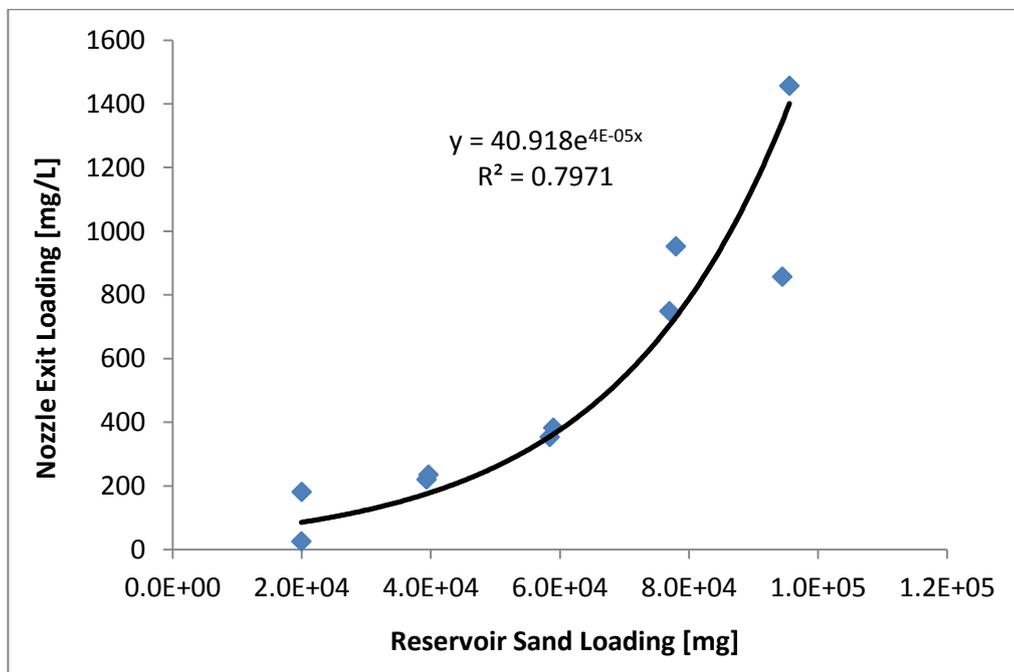
Figure 5.8: Plot of nozzle exit sand concentration variation with sand loading added to the reservoir during the sand loading calibration for 10 m/s flow velocity.
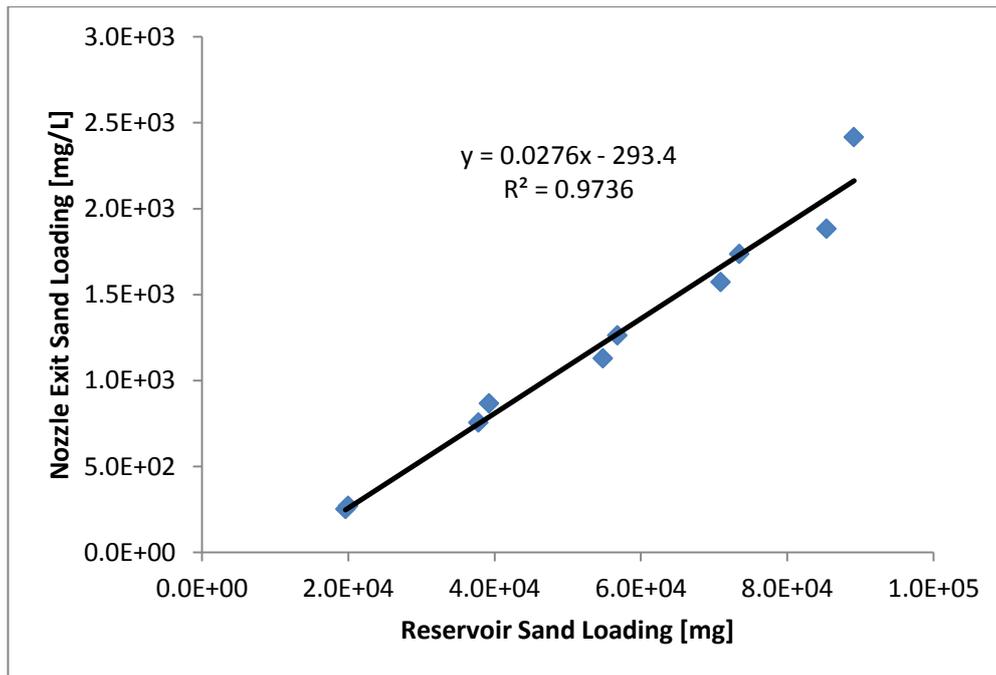
Figure 5.9: Plot of nozzle exit sand concentration variation with sand loading added to the reservoir during the sand loading calibration for 15 m/s flow velocity.

Questions may be asked regarding the variation of data for 7m/s and 10m/s flow velocities, and why their graphs are non-linear but linear for 15 m/s flow velocity sand loading calibration.

Possible explanation for this may be because sand particles (density - 2650kg/m^3) are denser than the fluid (density - 1000kg/m^3) which allows for particles to settle at the base of the reservoir and pipe fittings. All these particles should ideally be dragged by the re-circulating fluid solution promoting uniform mixing. However, particles can be trapped at various pipe bend sections, obstructions, misaligned pipe sections and the reservoir's base, thereby effectively reducing the number of particles flowing through the nozzle. This can be significant in low flow velocity and sand concentration.

At low to medium flow velocities (7 and 10 m/s) the sand concentration exiting the nozzle was very small when compared to the sand added to the reservoir. This reduction in the amount of sand exiting the nozzle can be attributed to low and non-

uniform recirculation at these flow velocities due to particles getting trapped at various pipe fittings within the loop. The flow velocity may be considered not sufficient enough to provide uniform mixing of the sand and fluid thereby giving rise to the sand concentration (circulating in the rig) becoming much lower than sand loadings (added to the rig) which gives a scattered variation and non-linear relationship as shown in Figures 5.7 and 5.8.

However, at high flow velocity of 15 m/s, uniform mixing of the sand with the fluid can be achieved which leads to appreciable quantity of sand exiting the nozzle thereby giving a linear relationship as shown in Figure 5.9.

5.3.2 Acoustic Emission (AE) Sensor Calibration

AE sensors are designed and manufactured to extract and record a set of parameters from measured AE signals. The characterisation of these signals depends on the type of sensor commercially available. Therefore, verifying AE signal parameters recorded by the AE sensor is very important. This is achieved by carrying out checks in form of calibration on the sensor and other devices to be used in the AE test.

Results of calibration are then compared with published results and manufacturer's specifications. ASTM-E976 is the standard guide for determining the reproducibility of AE sensor while ASTM-E1106 is the standard method for primary calibration of AE sensors [194].

An example of a published calibration certificate for the AE sensor used in this study is shown in Figure 5.10.
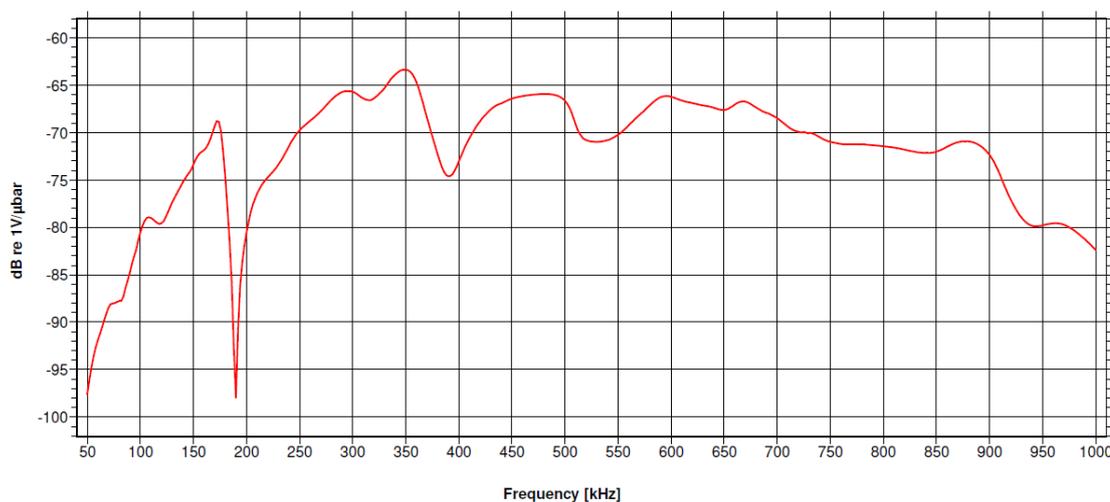
Figure 5.10: Published AE sensor (VS900-M) calibration certificate [194].

The success of any AE measurement depends on the selection of the correct sensor. This is because the sensors are the starting point in the measurement chain. They are attached behind the specimen surface to detect dynamic motion resulting from the AE events and then convert the motion to voltage-time signals that are analysed and interpreted in the measurement. The types and features of the sensor control the characteristics of the obtained signal. Hence, the repeatability and success of the measurement depends on the resulting electrical signals. Sensors are categorized based on the mechanism of their transduction [194], e.g. laser interferometer, displacement and capacitive sensors, etc. The sensors used in this study are piezoelectric sensors because they utilize piezoelectric elements for transduction. The element (made of a special ceramics called zirconate titanate (PZT) [194]) is shown in Figure 5.11. The surface of the sensor is attached to the surface of the specimen so that the dynamic surface motion propagates into the piezoelectric element which in turn generates an output voltage signals that are processed by the acquisition system. The AE devices (sensors, preamplifiers and two-channel acquisition system) were supplied by Vallen AE Company, Germany [194]. They were chosen because Ferrer *et al* [172, 173, 187] have successfully used Vallen AE devices to study abrasion-corrosion of

AISI 304L austenitic stainless steel in acidified saline solution using jet impingement apparatus.
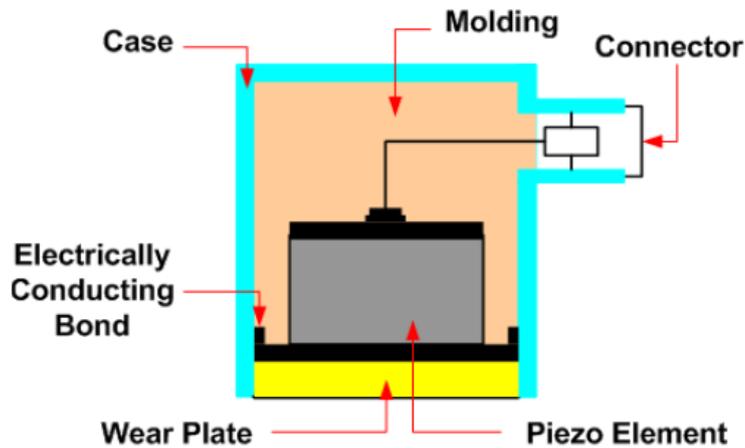
Figure 5.11: Illustration of the components of piezoelectric sensor [168].

During the calibration, the sensor was coupled to the X65 carbon steel sample by means of vacuum grease and connected through a BNC connector to the pre-amplifier which is then connected to the Vallen AMSY 6 acquisition system. The PC with the acquisition and analysis software is thereafter connected to the acquisition system through a USB 2.0 port. The set-up is schematically illustrated in Figure 5.12.
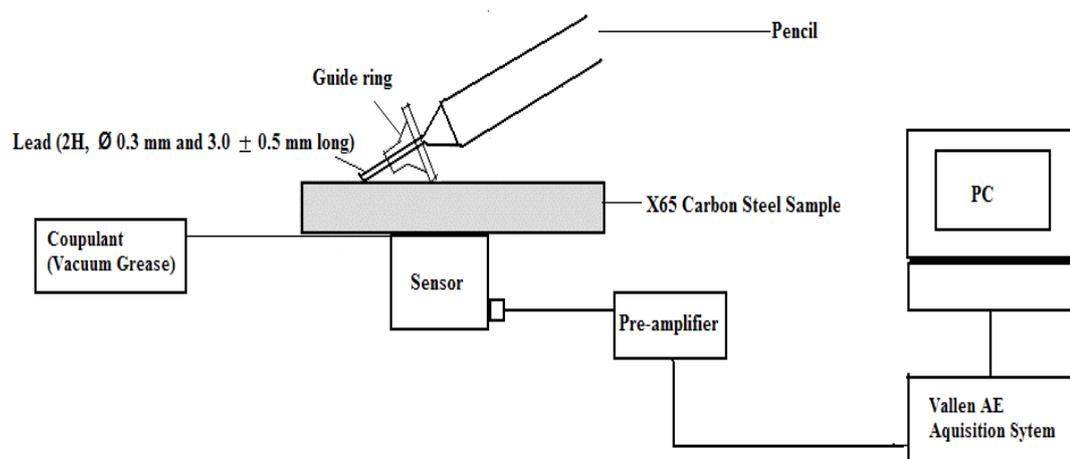
Figure 5.12: Schematic illustration of AE sensor calibration set-up.

The procedure involves pencil lead breaks. It was performed by breaking a 2H lead of 0.3 mm diameter and length of $3 \pm 0.5\ mm$ from its tip by pressing it against the surface of the sample as shown in Figure 5.12. This generated an intense AE signal that is similar to natural AE source that the sensor can detect. The generated signal was processed, analysed and compared with manufacturer's published calibration certificate which shown in Figure 5.10. The signal generated by the pencil lead break was processed and analysed in time-domain (with sampling rate of 2.5 MHz), frequency domain using Fast Fourier Transform (FFT) and frequency-time domain using Wavelet Transform (WT). The results are shown in Figure 5.13.
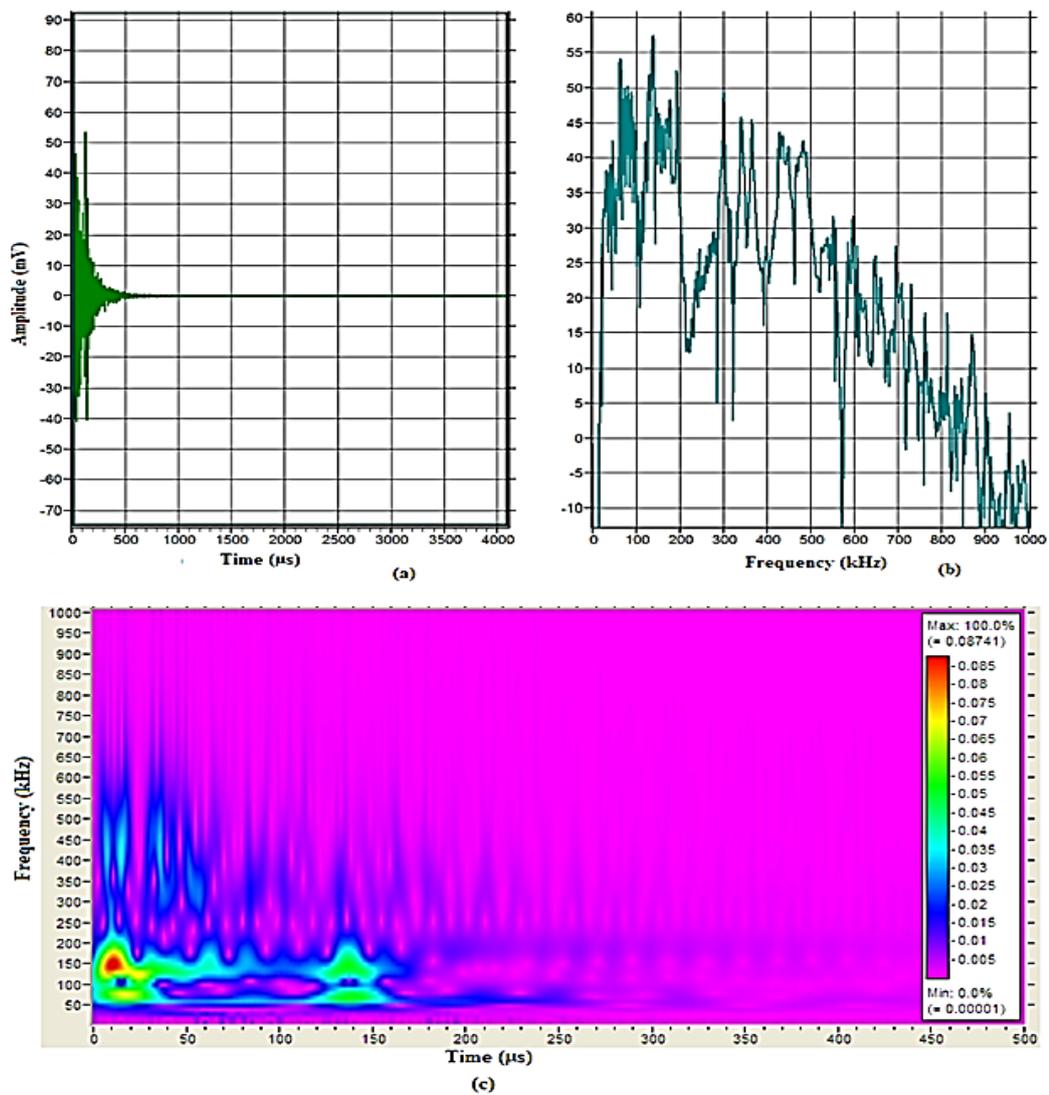
Figure 5.13: Lead pencil break signal results in (a) time-domain, (b) frequency-domain and (c) frequency-time domain.

The time history displayed in Figure 5.13(a) indicates that sensor adequately responded to the pencil lead break which created an AE burst with maximum amplitude of 54 mV and signal duration of less than 300 µs. The frequency-domain (Figure 5.13(b)) of the signal obtained by performing Fast Fourier Transform (FFT) of the AE signal shows a good response of the sensor with frequency range of 100 kHz to 900 kHz and resonant (peak) frequency of 150 kHz. The response conforms to the manufacturer's specifications (wideband frequency 100 kHz to 900 kHz) as shown in Figure 5.10. This means that the sensor can detect AE events occurring between 100 kHz and 900 kHz and will be suitable for erosion-corrosion measurements [173]. This is important because the sensitivity of AE sensor to corrosion, erosion and/or erosion-corrosion can be increased by matching the response frequency of the sensor to the frequency range of corrosion, erosion and/or erosion-corrosion events.

It is also important to note that the sensor frequency response (especially the resonant frequency) can change with different calibration procedures, material, distance from source, etc due to attenuation (reduction of signal strength in form of amplitude) and the wave behaviour of the AE in different materials [194]. For example, ASTM E976, steady state, face to face excitation calibration of the sensor in similar materials may give higher resonant frequency. For the sensor calibrated in this study (VS900-M), the resonant frequency can go up to 350 kHz [194] when steady state, face to face excitation calibration is used but the wideband frequency range (100 kHz to 900 kHz) will still be the same as the transient pencil lead break calibration.

5.4 Experimental Procedures

For pure erosive wear tests, a non-saline solution (tap-water) saturated with nitrogen was used so as to make the solution inert (pH ≈ 7), reduce oxygen concentration and minimise the effect of corrosion. A synthesised oilfield process water (brine) with composition and analysis in Tables 5.2 and 5.3 saturated with CO_2 to reduce oxygen to

10 ppb (for at least eight hours) was used to simulated oilfield corrosive environment for tests involving flow-induced corrosion and erosion-corrosion (pH of 5.5 ± 0.2).

Table 5.2: Simulated formation water composition, quantity per litre and ion analysis

S/N	Salt Name	Specified Quantity (g/L)	Ion Analysis (g/L)	
1.	Sodium Chloride (NaCl)	24.090	Na^+	9.484
2.	Potassium Chloride (KCl)	0.706	K^+	0.371
3.	Calcium Chloride di-hydrate ($CaCl_2.2H_2O$)	1.387	Ca^{2+}	0.378
4.	Magnesium Chloride hexa-hydrate ($MgCl_2.6H_2O$)	9.310	Mg^{2+}	1.099
5.	Barium Chloride di-hydrate ($BaCl_2.2H_2O$)	0.016	Ba^{2+}	0.009
6.	Strontium Chloride di-hydrate ($SrCl_2.2H_2O$)	0.033	Sr^{2+}	0.015
7.	Sodium Sulfate ($NaSO_4$)	3.522	SO_4^{2-}	2.382
8.	Sodium Hydrogen Carbonate ($NaHCO_3$)	0.304	HCO_3^-	0.222

The above analysis was based on the 50-litre capacity jet impingement rig with the measured salt quantities and atomic weight of the elements as follows:

S/N	Salt	Quantity (g/50L)	Atomic Mass of Element (g/mol)	
1.	$BaCl_2.2H_2O$	0.800	Ba	137.330
2.	$CaCl_2.H2O$	69.330	Ca	40.080
3.	KCl	35.280	K	39.098
4.	$MgCl_2.6H_2O$	465.490	Mg	24.305
5.	$NaCl_2$	1204.520	Na	22.990
6.	$NaHCO_3$	15.210	HCO_3	61.018
7.	Na_2SO_4	176.110	SO_4	96.070
8.	$SrCl_2.2H_2O$	1.674	Sr	87.62

The specimen is first polished, rinsed with water, dried with compressed air, weighed three times to determine initial weight before experiment and carefully fitted into the test cell/specimen holder. The set-up is coupled to the rig that has been pre-heated to 50°C and the reservoir covered. The necessary wire connections are made before the

pump is started and adjusted to the required frequency corresponding to the desired flow velocity of the fluid. When the pump stabilises, the desired quantity of sand is added to the reservoir and after a few minutes, the acoustic emission due to solid-liquid impingement through the nozzle onto the flat specimen surface is recorded with the LPR or EIS measurement throughout the test duration of 2 hours.

The AE sampling rate, filter and threshold were set at 2.5 MHz, 90 – 850 kHz and 40 dB respectively for all the tests. AE signals were sampled at 2.5 MHz sampling rate in accordance with Nyquist criterion (or sampling theorem) and to avoid signal aliasing [156]. The signals were filtered and amplified with band filter frequency of 90-850 kHz (to eliminate pump and electrical interference) and threshold set at 40 dB (justification of threshold setting is discussed in details in section 5.5) for all tests. For LPR measurement, the potential was shifted at a scan rate of 0.25 mV/s from 50 mV negative to the free corrosion potential to 50 mV positive to free corrosion potential of the sample under impingement conditions. Measured data was used to compute corrosion rate for each test. At the end of each test, the specimens are rinsed with water, cleaned with Clarke's solution and weighed with precision weighing scale to determine the weight loss. The AE, LPR and EIS data are copied to EXCEL for analysis. The measured AE data are of two types: Hits (primary) and transient (waveform) data. From the primary data, AE energy, event counts, threshold crossing counts, rise-time, amplitude, duration and Root Mean Square (RMS) can be computed, while the Fast Fourier Transform (FFT) to determine the frequency spectrum of the AE events is obtained from the waveform. Though only AE energy, event counts, threshold crossing counts and FFT were determined and used in this study.

Each test was repeated three times with great care in attaching and coupling the sensor onto the specimen to ensure repeatability. It should be noted that crude and uncontrolled attachment methods with lack of control of couplant thickness might cause fluctuations in measured signals which may affect repeatability. The tests are

conducted for three different flow velocities (7, 10 and 15 m/s) and sand loading values (50, 200 and 500 mg/L) at 90° impingement angle and constant temperature of 50°C. At the end of each test, the mass loss, average AE energy, event, count and corrosion rates were determine and used for analysis.

5.5 AE Detection Gain Optimisation

Determining the correct threshold setting is vital to ensuring that only signals resulting from the solid-liquid impingement onto the specimen are measured. This is important because operating below the correct threshold can lead to complication of signals by background noise while going very high might lead to loss of important signals.

A series of short noise tests were performed to optimise the instrumentation sensitivity range while limiting false signals emanating from background noise and interferences. This was done in static conditions by increasing the threshold from 25 dB using 5 dB increments until 35 dB which corresponds to the peak noise amplitude. A comparison of the amplitude was made when the pump was running at 7 m/s and it was observed that adding 5 dB to achieve setting of 40 dB is a good threshold setting and corresponds to published [194] threshold setting for measurement in metallic materials. A display of the noise test raw data when the pump is running at 7 m/s flow velocity with 40 dB threshold is shown in Figure 5.14.

The threshold was shifted to 50.9 and AE recorded for all the flow velocities (7, 10 and 15 m/s as shown in Figure 5.15. From the Figure, it is clear that shifting the threshold to 50.9 leads to loss of some data.
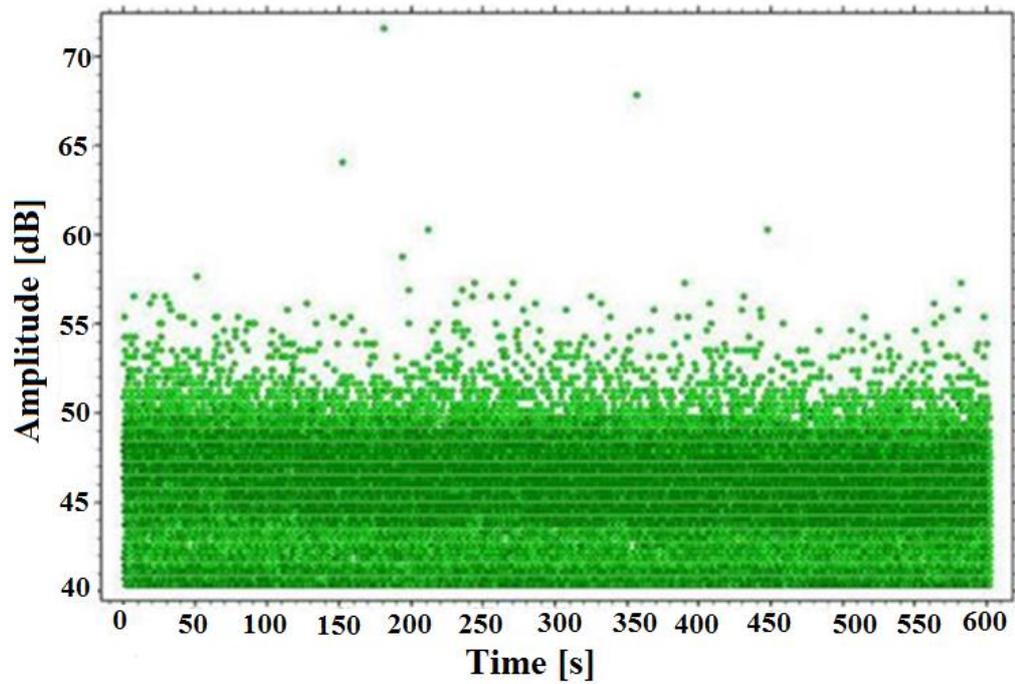
Figure 5.14: Raw data of noise test with pump running at 7 m/s flow velocity and threshold set at 40 dB.
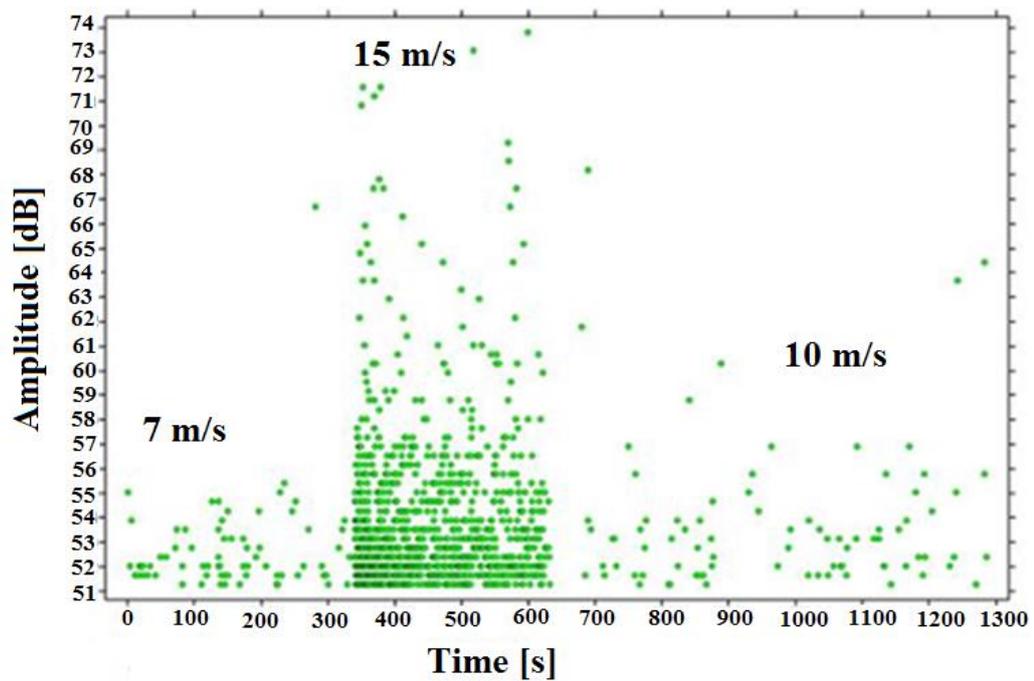
Figure 5.15: Raw data of noise test with pump running at varied flow velocities (7, 10, 15 m/s) and threshold set at 50.9 dB.

To verify the background noise has been eliminated completely at static condition and that only flows and particle impact create AE events, 20 g of glass beads were added to the reservoir and the test repeated in static conditions, 7, 10 and 15 m/s flow velocities, and the results of the measurements are shown in Figure 5.16.

From the Figure, it is evident in the scatter plot of the amplitude against time that no events (hits) occurred at static condition but the hits, amplitude and energy (Figure 5.17) increased appreciably as the flow velocity was increased with the 15 m/s flow velocity having the highest maximum amplitude, hits and peak energy as expected because more energy is added to the system as flow velocity increases.
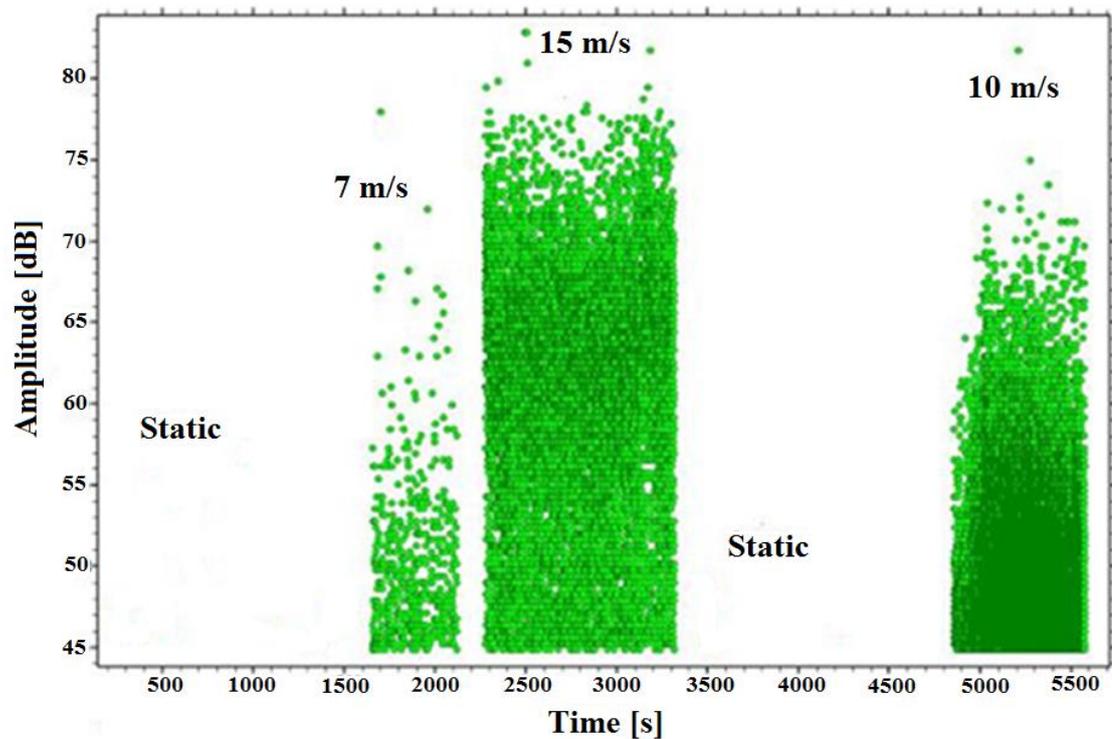
Figure 5.16: Raw Data of AE test with sand loading for static condition and 7, 10 and 15 m/s flow velocities.
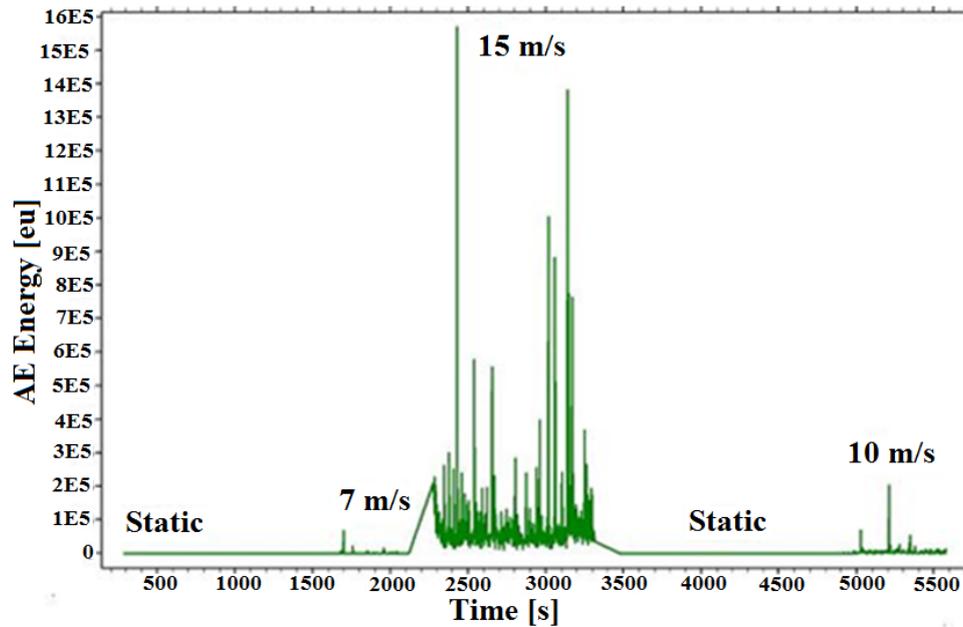
Figure 5.17: Variation of AE energy with time for the data in Figure 5.16.

Confirmatory tests were carried out for the threshold setting by adding 200 mg/L of sand each for the flow velocities (7, 10, and 15 m/s) and increasing the threshold from 40 dB to 50.9 dB and to 69.7 dB for each test. The data was analysed and the average AE energy values were obtained at the various settings. The values are plotted in Figure 5.18 for threshold from 69.7 dB down to 40 dB.
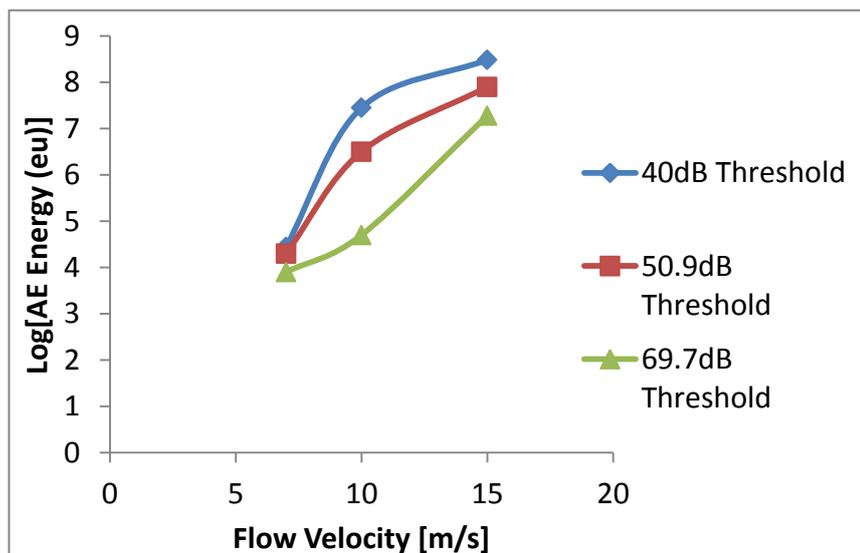
Figure 5.18: Illustration of the optimized threshold setting used in all test at 90° impingement angle, 200 mg/L sand loading and 50°C temperature, tap-water saturated with N_2 (pH ≈ 7.0).

Looking at the detection gain optimisation from the perspective of the sampled AE waveform raw data, the measured AE signal amplitude (A) output of the sensor is in mV and its value in dB is calculated using the relationship [154, 168, 194]:

$$A_{AE}[dB] = 20\log_{10}(\frac{V_{out}}{V_{in}}) \hspace{2cm} (5.1)$$

where A_{AE} is the AE signal amplitude in decibel (dB), V_{out} is the sensor output voltage in (mV) and V_{in} is the input voltage also known as the reference voltage (1µV) and it corresponds to 0 dB.

From equation 5.1, decibel (dB) scale can be developed with its corresponding voltage values as follows:

Table 5.3: Decibel (dB$_{AE}$) scale [194]

dB$_{AE}$ Value (dB)	Output Voltage Value (mV)
0	0.001
20	0.01
40	0.1
60	1
100	100

Using this scale, it can be seen in the measured AE waveform in Figure 5.19 that reducing the threshold below 40 dB leads to recording of unwanted background noise signals which may complicate the desired signals while increasing it beyond 40 dB leads to loss of substantial data.

Moreso, the detection threshold value depends on calculated gain which is used to scale the results peak amplitude, RMS and the energy. The value is initiated by the preamplifier gain when an input device is assigned to the channel [168]. Therefore, it is reasonable to set the threshold at 40 dB since the preamplifier gain is 34 dB. The threshold was set at 40 dB for all tests.
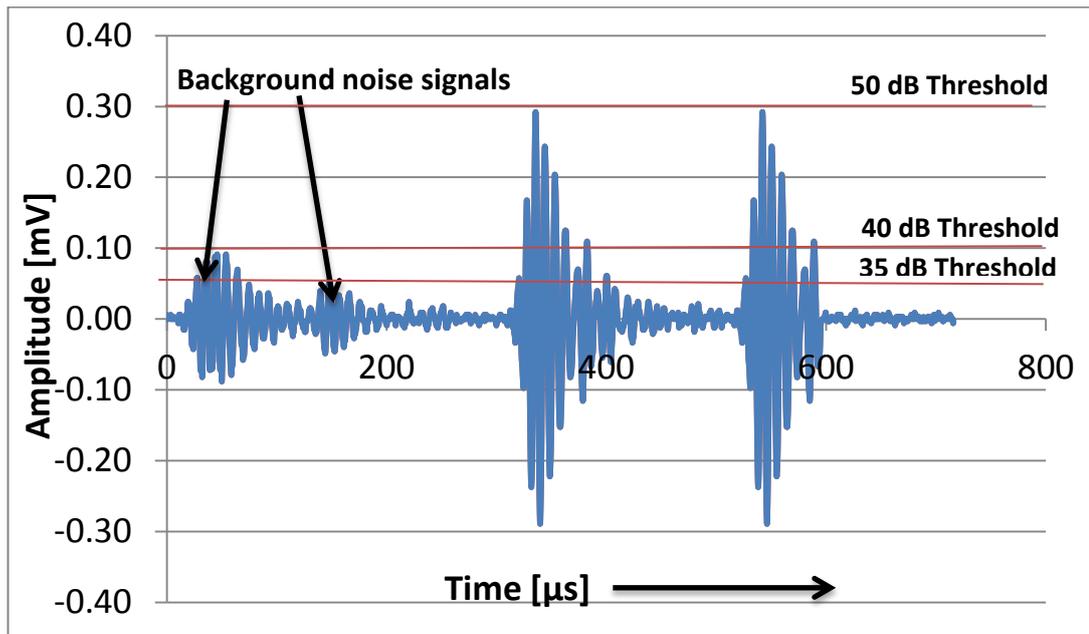
Figure 5.19: Illustration of optimized threshold setting using measured waveform at 7m/s flow velocity, 200 mg/L sand loading, 90° impingement angle and 50°C temperature with tap-water saturated with N_2 (pH ≈ 7.0).

Chapter 6 Results and Discussion: Erosive Wear Investigation

6.1 Introduction

This chapter focuses on the application of acoustic emission (AE) energy analysis to quantify the erosive wear damage of X65 carbon steel. However, an *in-situ* linear polarisation resistance (LPR) method was also coupled to the set-up to ensure that corrosion rate is negligible when investigating erosive wear damage.

The degradation rate of the samples was determined by weight loss after each test. This was correlated with the average AE energy for different flow velocities and sand loading. Surface analysis using visual examination, Scanning Electron Microscopy (SEM) and 3D profilometry were conducted on the tested samples to investigate the surface degradation mechanisms of the erosive wear processes.

6.2 Results

Erosive wear processes involve the interaction of energy between the impinging particles and the substrate. During impact, the kinetic energy of the impinging particles is dissipated into plastic work, rebound kinetic energy (KE) and elastic wave (AE) energy [176]. The plastic work is used to plastically deform the surface and it manifests itself as heat and stored energy; the rebound KE is the energy the particle possesses after impact that enables it to return to rest or equilibrium position; and the elastic wave (AE) energy is radiated as surface waves which propagate on the surface of the substrate and can be detected by an AE sensor. As an energy transformation process, the first step in studying the process using the AE technique is to investigate the transfer of particle KE during deformation to AE energy. This was done by performing single impingement tests using a glass bead with a well-controlled size and shape and correlating its KE energy with AE energy. This is followed by more realistic investigations similar to those obtained in an industrial environment in the form of multiple impingement tests using sand particles.

6.2.1 Single Impingement Tests

The single impingement test was conducted by starting the pump, selecting the required nominal flow velocity and putting the glass beads (with shape and size shown in Figure 6.1) one by one into the reservoir and observing changes in the measured signal to identify AE events created by each glass bead impinging on the test specimen. An example of the measured AE signal generated by a glass bead is shown in Figure 6.2 with the signal burst clearly separated in time from those of flow and background noise. The signal is analysed to calculate the signal energy and RMS value for each nominal flow velocity. The Vallen AMSY-6 system outputs the AE energy in energy unit [eu], $(eu = 10^{-14}V^2 s = 10^{-18}J$ [194]. The glass bead was assumed to be a rigid non-deforming sphere of diameter $d = 0.2\ cm$ and density $\sigma = 1.6\ g/cm^3$. The mass m of one bead was calculated using the expression $m = 4\pi r^3 \sigma / 3$ and its kinetic energy at nominal impact velocity (free stream velocity) v is $KE = mv^2/2$. The result of the correlation between KE at each nominal flow velocity and the corresponding measured AE energy and RMS is shown in Figure 6.3. These relationships which show linear dependence of AE energy and RMS with the glass beads KE are in agreement with the work of Oltra *et al.* [186] and Ferrer *et al.* [187].
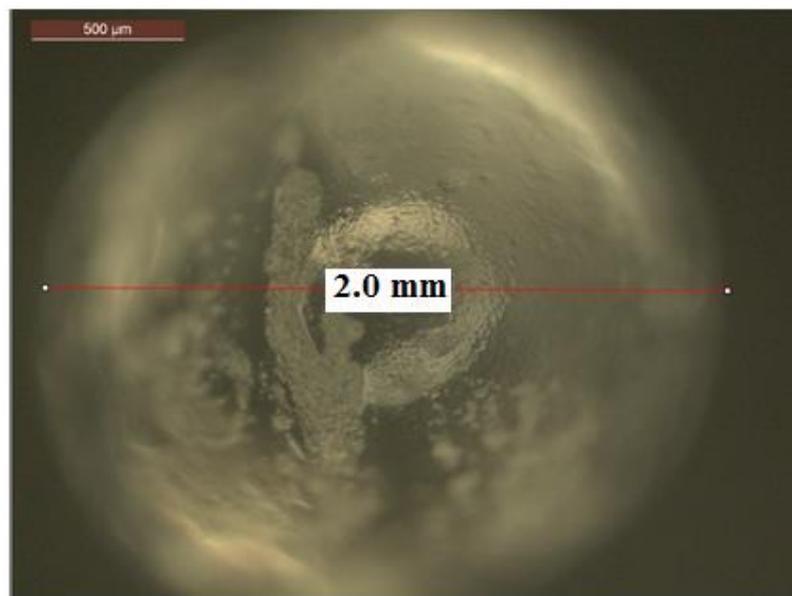
Figure 6.1: Optical microscope image of the spherical glass bead
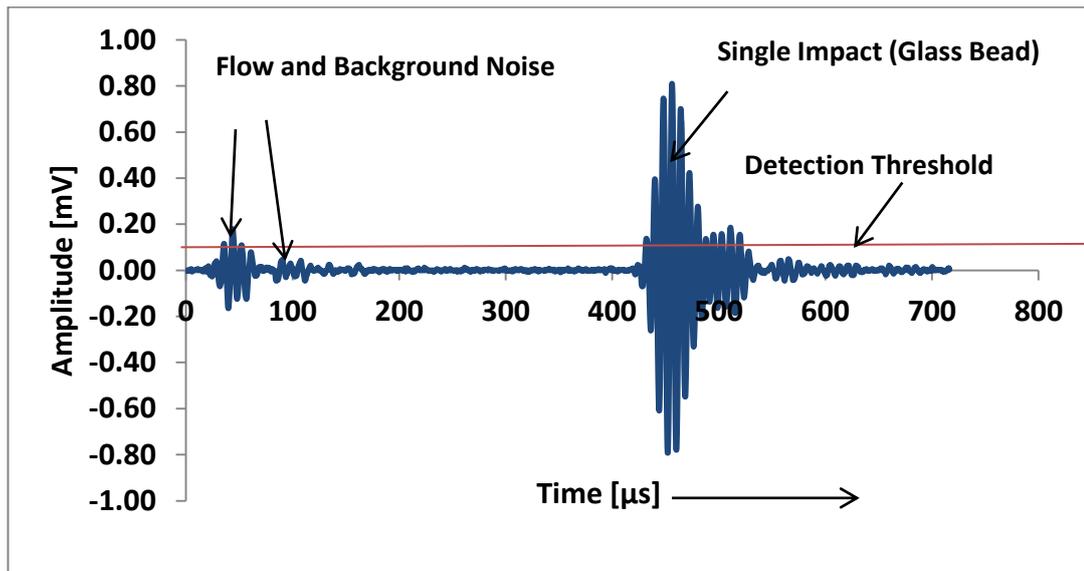
Figure 6.2: Measured AE signal waveform due to glass bead with flow and background noise at 7m/s flow velocity, 90° impingement angle and 50°C temperature with tap-water saturated with N_2 (pH ≈ 7.0).
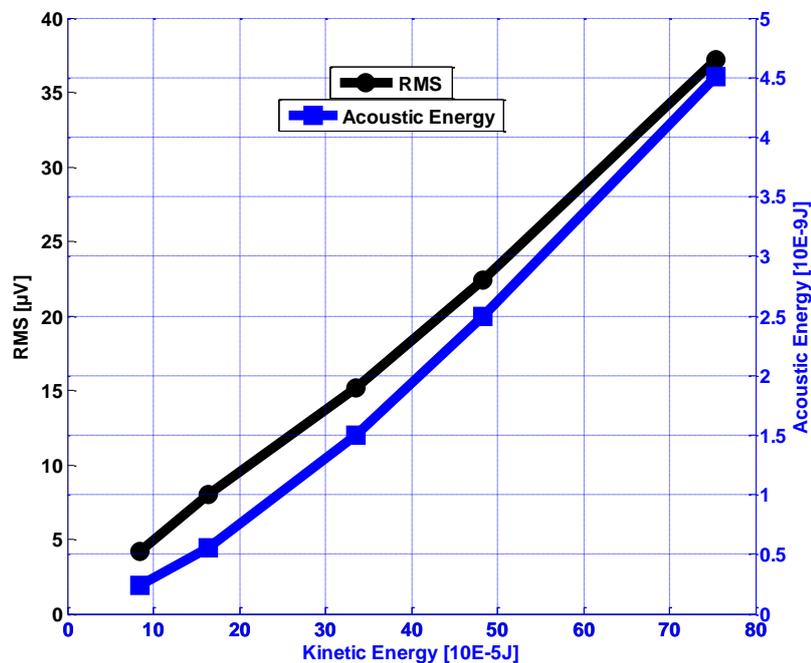
Figure 6.3: Relationship between AE energy and RMS due to single glass bead impact and its kinetic energy at 90° impingement angle and 50°C temperature with tap-water saturated with N_2 (pH ≈ 7.0).

6.2.2 Multiple Impingement Tests

In the multiple impingement tests, the relationship between the average AE energy during the erosive wear of the X65 carbon steel and flow velocity together with sand particle concentration was investigated in an attempt to establish a correlation between the degradation rate and the average AE energy per second. Measured time series waveform of multiple impingements of sand particles during one of the tests are shown in Figure 6.4 (whilst waveforms due to flow i.e. without sand are illustrated in Figure 6.24 in discussion under frequency spectrum analysis). For each test, the average AE energy per second was monitored for 2 hours and plotted to study the effect of flow velocity, sand loading and CO_2 corrosion on the degradation rate of the specimen.
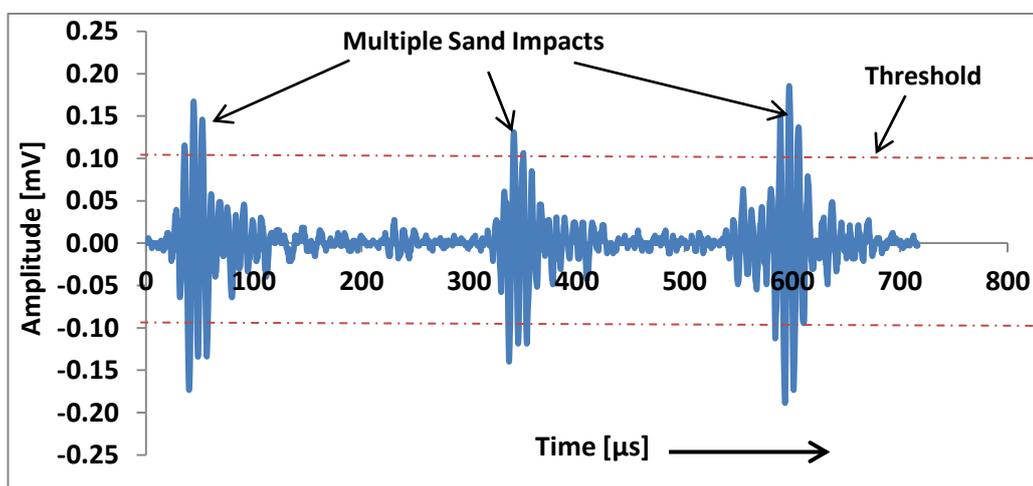
Figure 6.4: Measured AE signal waveform due to multiple sand impacts at 7m/s flow velocity, 90° impingement angle and 50°C temperature with tap-water saturated with N_2 (pH ≈ 7.0).

6.2.2.1 Effect of Flow Velocity

The effect of flow velocity on the average AE energy per second was investigated for different sand loadings (0, 50, 200 and 500 mg/L) and the results are shown in Figures 6.5 to 6.8. From the results, it is evident that there is a general increase in AE energy with increase in flow velocity from 7 to 15 m/s with and without sand loading. This is reasonable because fluid and/or sand particles with higher velocity carry greater

energy and will in turn generate higher AE energy as well as deform the specimen more upon impingement.
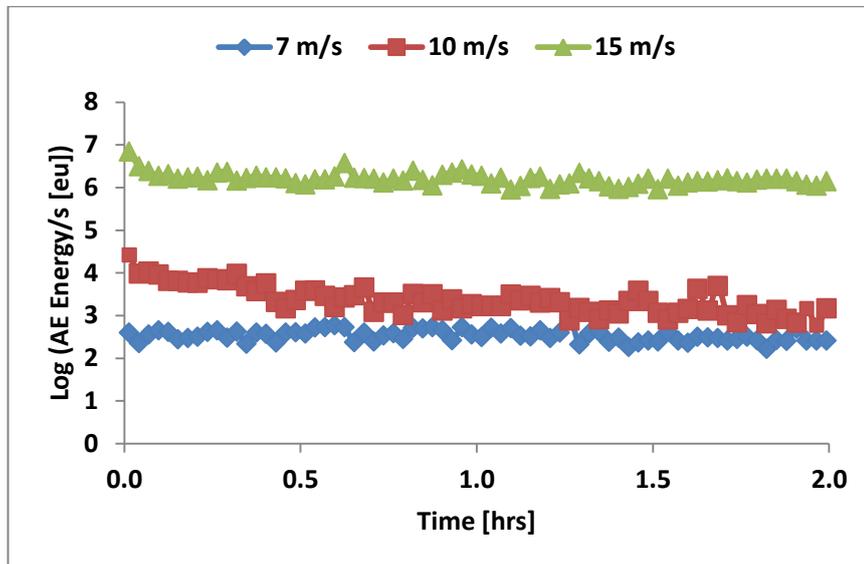
Figure 6.5: Variation of average AE energy with time for different flow velocities and zero sand loading at 90° impingement angle and 50°C temperature in tap-water saturated with N_2 (pH ≈ 7.0).
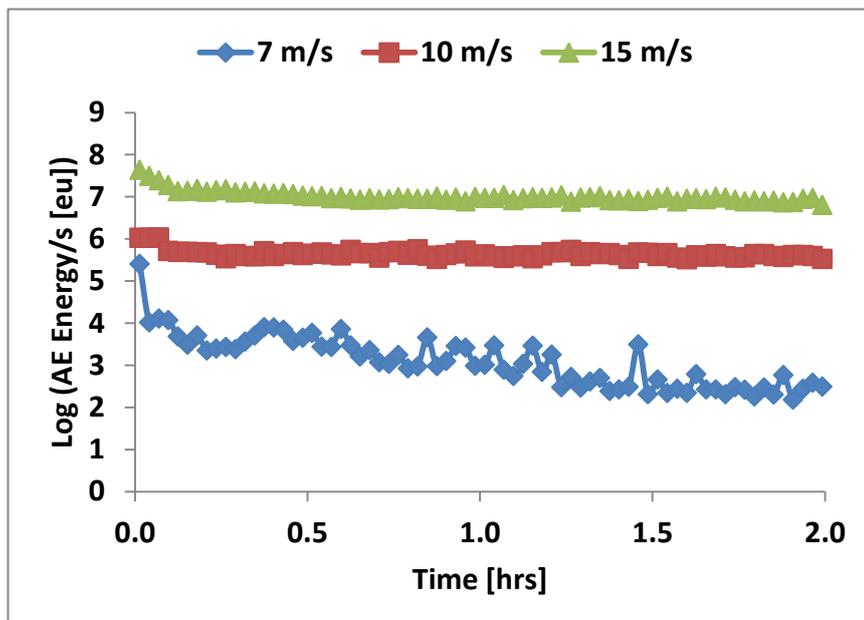
Figure 6.6: Variation of average AE energy with time for different flow velocities and fixed sand loading of 50 mg/L at 90° impingement angle and 50°C temperature in tap-water saturated with N_2 (pH ≈ 7.0).
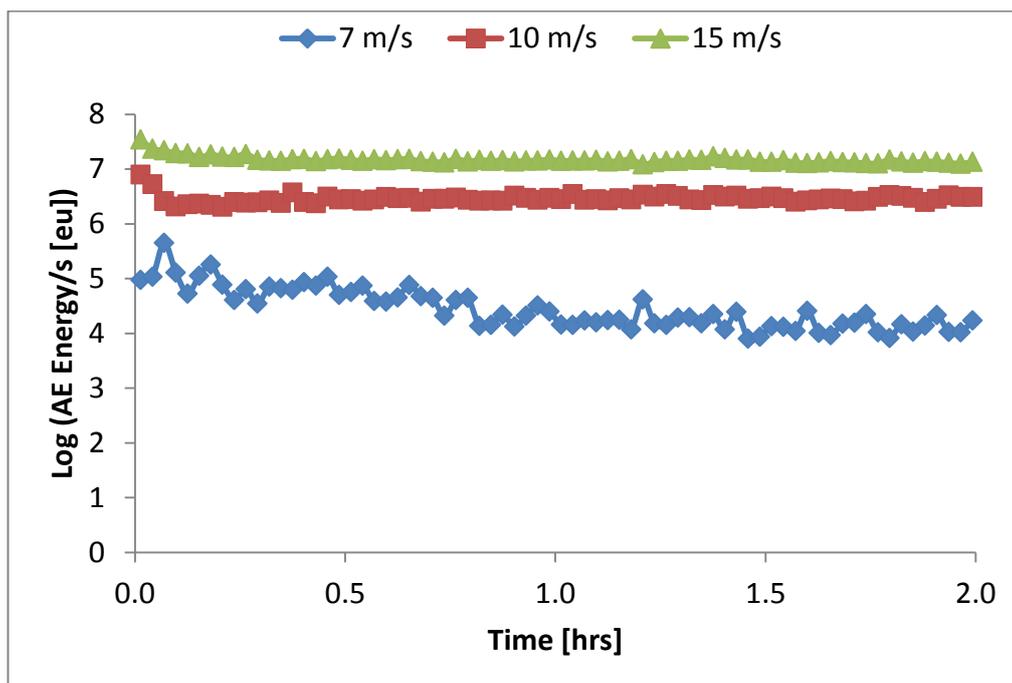
Figure 6.7: Variation of average AE energy with time for different flow velocities and fixed sand loading of 200 mg/L at 90° impingement angle and 50°C temperature in tap-water saturated with N$_2$ (pH ≈ 7.0).
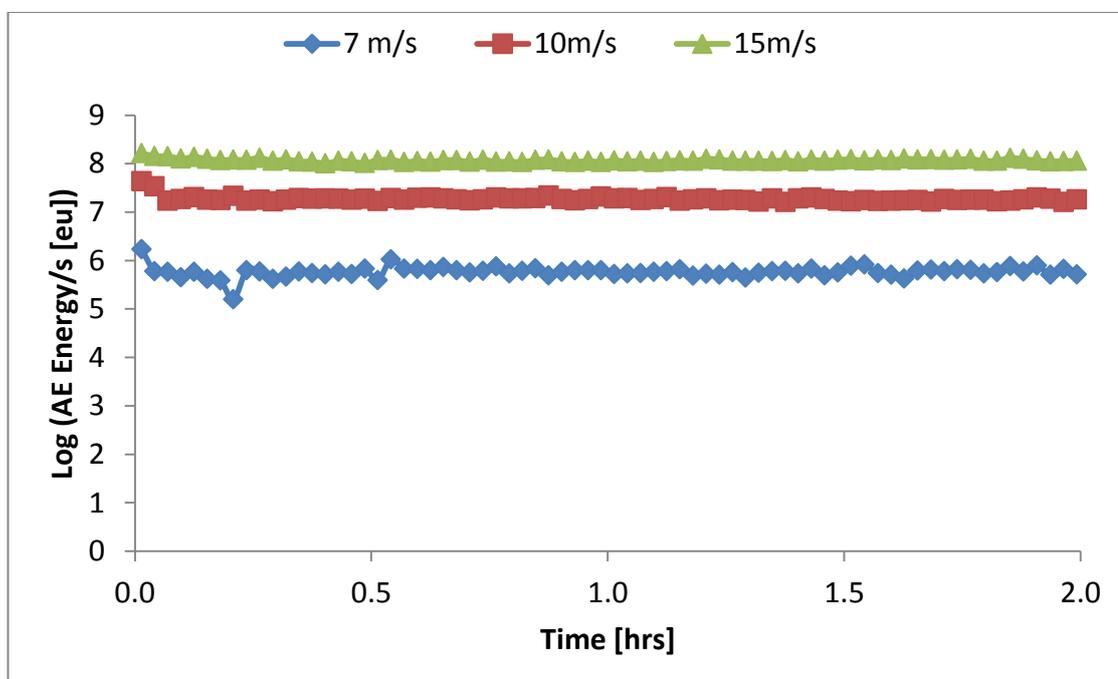
Figure 6.8: Variation of average AE energy with time for different flow velocities and fixed sand loading of 500 mg/L all at 90° impingement angle and 50°C temperature in tap-water saturated with N$_2$ (pH ≈ 7.0).

Figure 6.9 shows the variation of the X65 carbon steel mass loss rate with the different flow velocities. The error bars indicate the maximum and minimum values of the average of three tests (i.e. three repeats). The plot indicates that at 7 m/s and below the mass loss rate is low and almost insignificant because of a low impact energy which seems insufficient to cause damage on the material. This signifies that mass loss is less dependent on sand loading at 7 m/s and below, and an increase in flow velocity leads to an increase in mass loss rate thus confirming the findings in previous studies for X65 carbon steel [42] that material removal is relevant to the combined effects of sand loading and flow velocity.
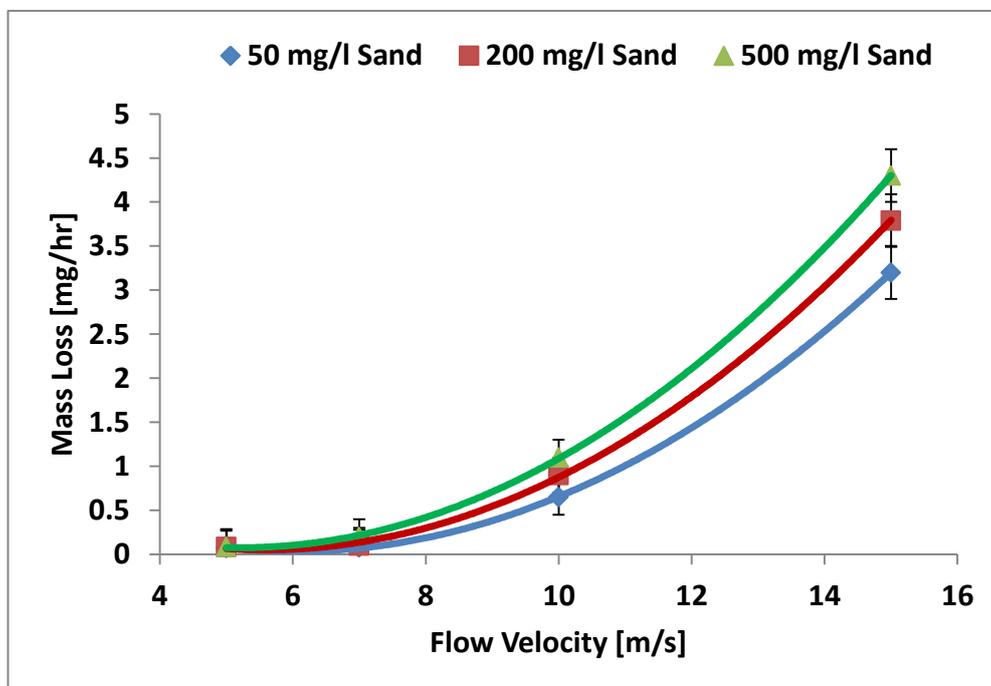
Figure 6.9: Variation of mass loss with flow velocity test with tap-water saturated with N_2 (pH ≈ 7.0) at 90° impingement angle and 50°C temperature.

6.2.2.2 Effect of Sand Loading

Similarly, the effect of sand loading on AE energy for different velocities (7, 10 and 15 m/s) was investigated to confirm that the AE set-up is sensitive to variation in sand loading with results shown in Figures 6.5 to 6.8.

6.2.2.3 Estimating Corrosion Effects

Furthermore, the effect of CO_2 corrosion on measured AE energy as well as the material degradation was studied using representative oilfield process brine saturated with CO_2 at 10 m/s flow velocity, 200 mg/L sand loading and 50^oC temperature. AE and LPR measurements were done simultaneously with and without CO_2 saturated brine to have an insight of the behaviour of the system in the presence of CO_2 and to confirm that corrosion rate is low in tap-water saturated nitrogen. The corrosion rate in CO_2 environment was correlated with AE energy and a similar trend was observed as shown in Figures 6.10. Note that the jump in data in Figure 6.10 represents the response to the addition of sand (shown by the arrow in the expanded view shown in Figure 6.11) which is different from previous data where measurements started when sand particles have already been added and re-circulated in the rig.

The polarisation behaviour of the X65 carbon steel in tap-water with N_2 and brine with CO_2 with and without sand is illustrated in Figure 6.12. The corrosion rate in tap water with N_2 was very low (0.31 mm/year) confirming the efficacy of elimination of corrosion with N_2 but it averaged 4.8 mm/year in the presence of CO_2 saturated brine as shown in Figure 6.15(b). The corrosion rate was calculated by determining the polarisation resistance (gradient in $Ohm.cm^2$) of the potential-current density plot (Figure 6.13 for tap-water saturated with N_2 and Figure 6.14 for brine saturated with CO_2) and applying Stern-Geary equation (Equation 2.32 with Stern-Geary Coefficient of 26 mV) to compute corrosion current density (i_{corr} in Amp/cm^2) which is then substituted in Equation 2.30 to obtain corrosion rate in cm/s. This is converted to corrosion rate in mm/year by multiplying 3.15×10^7 sec/yr x 10 mm/cm. using the tap-water saturated with N_2 data in Figure 6.15 to illustrate calculation of R_p:

$$R_p (Ohms.cm^2) = \frac{Change\ in\ Potential\ (\Delta V)}{Change\ in\ Current\ Density\ (\Delta V)}$$

$$= \frac{V_2 - V_1}{i_2 - i_1} = \frac{-0.41430 - (-0.33566)}{(-4.77000 - 3.55)x\ 10^{-5}} = \boldsymbol{946\ \Omega.cm^2}$$

Substituting this value of R_p into Stern-Geary Equation (Equation 2.32) with Stern-Geary Coefficient (K = 26 mV) yields:

$$i_{corr} = \frac{1}{946}[26\ x\ 10^{-3}] = 0.02748\ x\ 10^{-3} = \mathbf{2.75\ x\ 10^{-5}} \mathbf{\textit{Amp/cm}^2}$$

Subsituting this value of i_{corr} into Faraday Equation for Corrosion Rate, CR (Equation 2.30) repeated here for emphasis, gives:

$$CR = \frac{M}{nF} \cdot \frac{i_{corr}}{\rho}$$

where, $M = 55.85g,\ n = 2, \rho = 7.87\ g/cm,\ F = 96{,}500\ C\ and\ i_{corr} = 2.75\ x\ 10^{-5}\ Amp/cm^2$

$$CR = \frac{55.85g}{2\ x\ 96500\ Amp.s} \cdot \frac{2.75\ x\ 10^{-5}\ Amp/cm^2}{7.87g/cm} = \frac{153.59\ x\ 10^{-5}\ cm/s}{1518910} = \mathbf{1.01\ x\ 10^{-9}\ \textit{cm/s}}$$

$$CR\ (\frac{mm}{yr}) = 1.01\ x\ 10^{-9}\frac{cm}{s}\ x\ 3.15\ x\ 10^7\frac{s}{yr}\ x\ 10\frac{mm}{cm} = \mathbf{0.31 \textit{mm/yr}\ \textit{which is low}}.$$
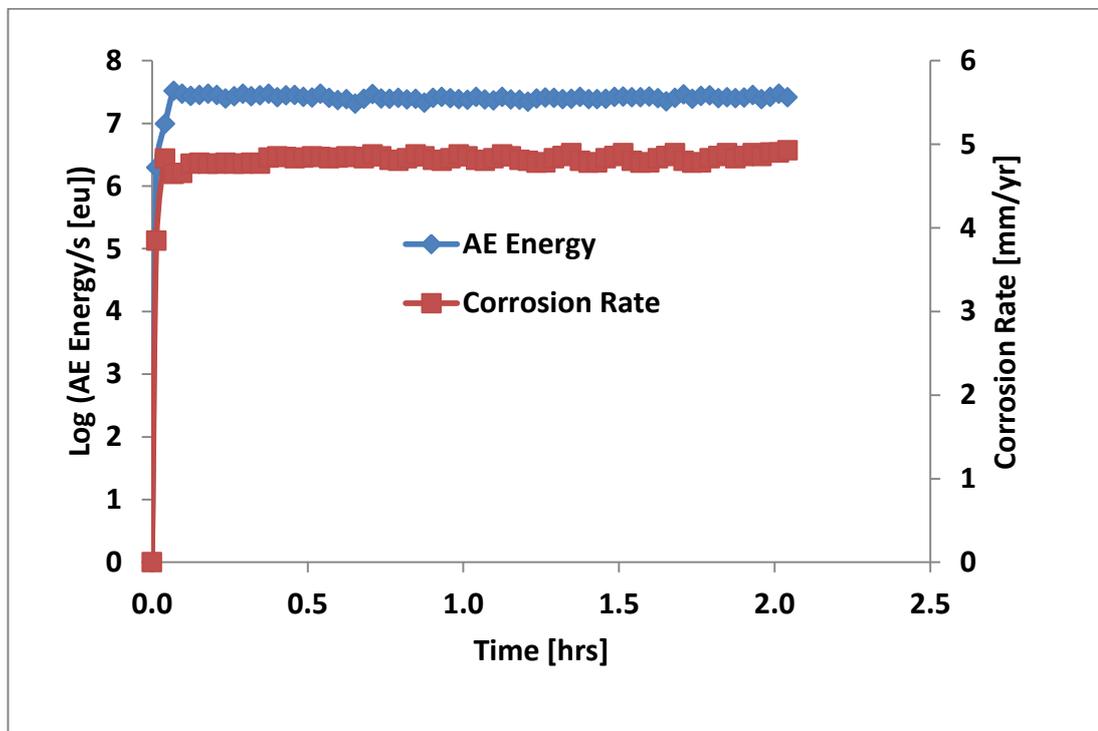
Figure 6.10: Correlation of AE energy with corrosion rate at 90° impingement angle, 50°C, 10 m/s flow velocity and 200 mg/L sand loading in brine saturated with CO₂ (pH=5.5).
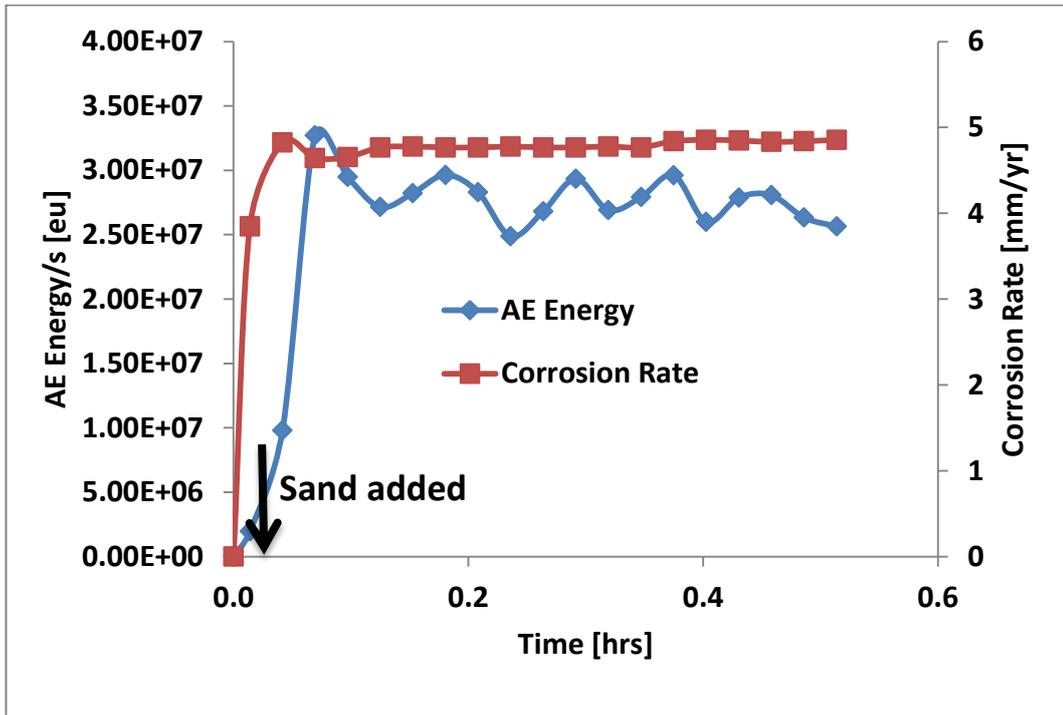
Figure 6.11: Expanded view of the initial period of Figure 6.10.
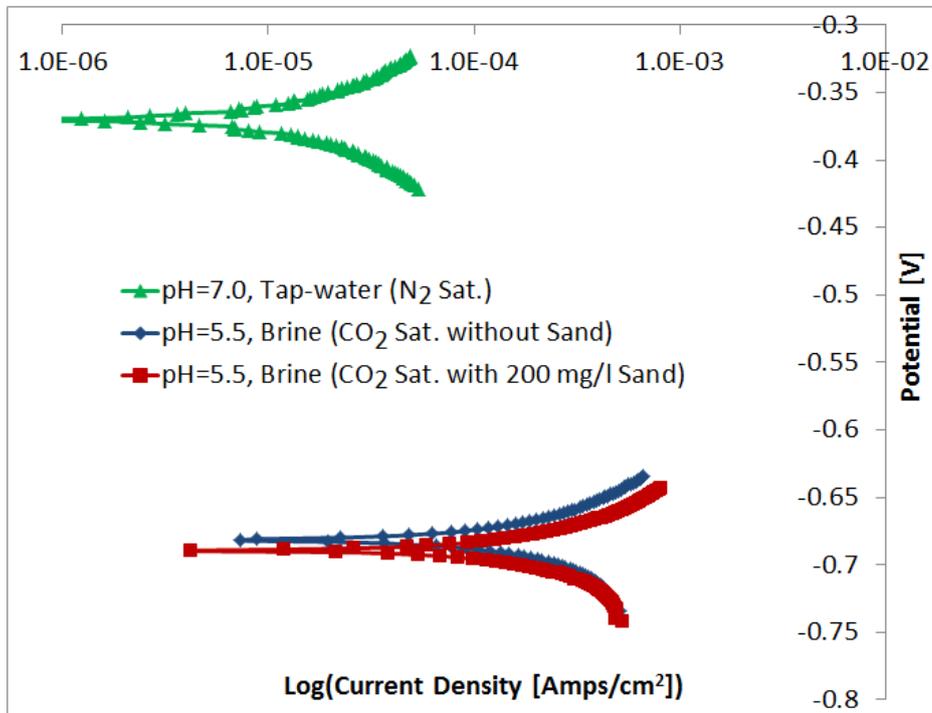
**Figure 6.12: Polarization behaviour of X65 carbon steel under impingement at 90°
impact angle, 50°C and 10 m/s flow velocity with process brine saturated with
CO_2 (pH=5.5) and tap-water saturated with N_2 (pH≈7.0).**
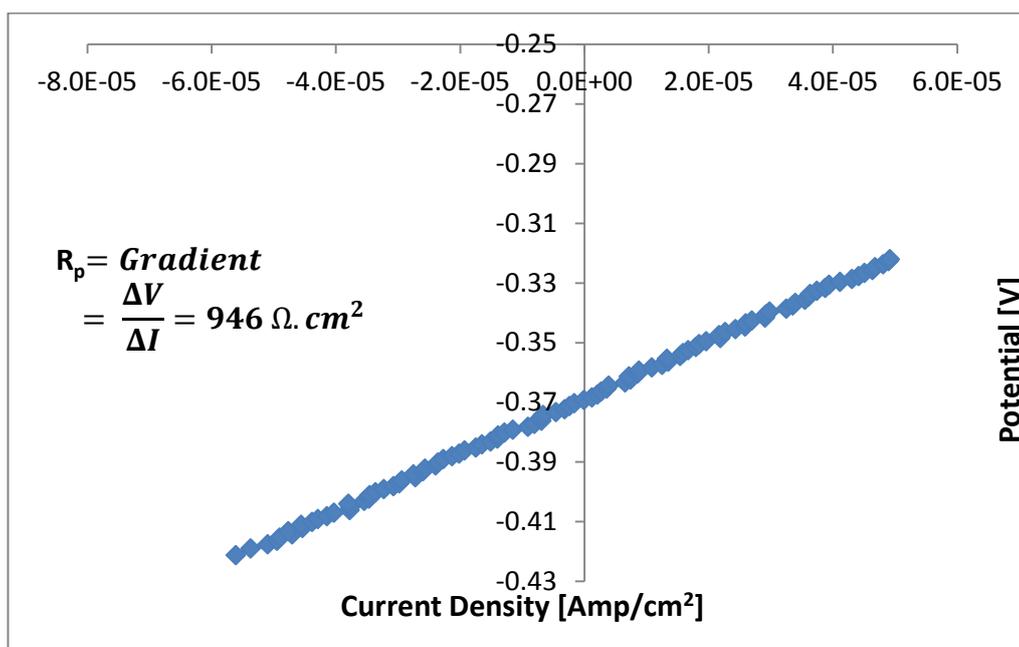
Figure 6.13: LPR data of X65 carbon steel under impingement at 90° impact angle, 50°C and 10 m/s flow velocity with tap-water saturated with N_2 (pH≈7.0).
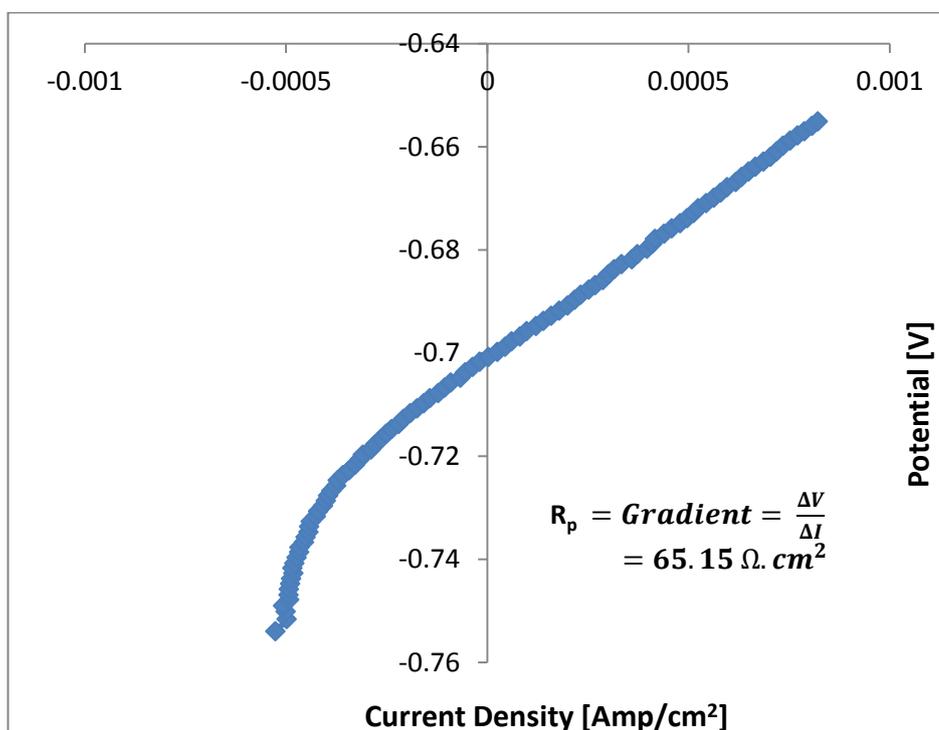
Figure 6.14: LPR data of X65 carbon steel under impingement at 90° impact angle, 50°C and 10 m/s flow velocity with brine saturated with CO_2 (pH=5.5).

The effect of CO_2 corrosion on the overall degradation of X65 was further assessed by determining the total weight loss for 50 mg/L and 200 mg/L sand loading at 10 m/s velocity with and without CO_2 and the results are shown in Figures 6.15 (a) and (b).

(a)

(b)
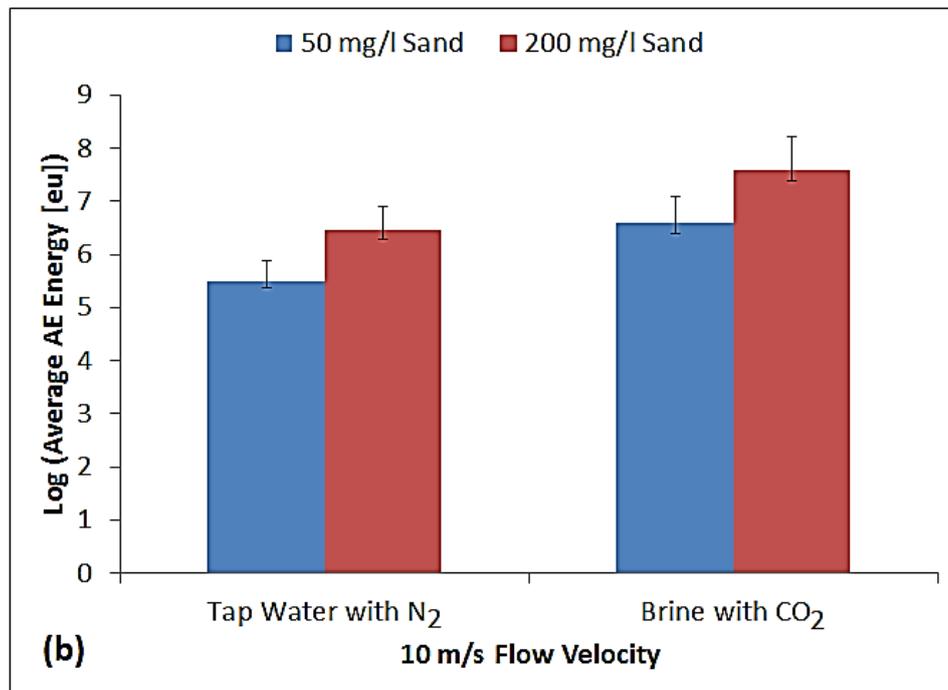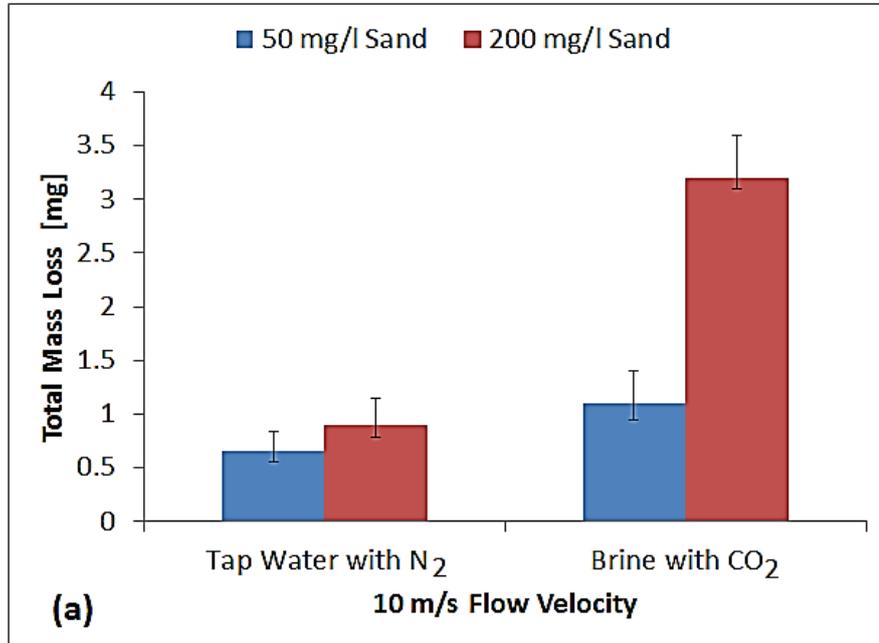
Figure 6.15: Comparison of X65 behaviour in corrosive and inert environment using (a) total weight loss and (b) average AE energy.

6.2.3 Surface Analysis

Visual inspection and Scanning Electron Microscopy (SEM) were used to assess the specimen's surface morphology after each test and the mechanism of degradation process on the specimen.

Figure 6.16 (a) shows the surface wear regions from visual inspection of test specimen and three different zones corresponding to zones predicted by a previous CFD study of Gananvelu [110] which is illustrated in Figure 6.16 (b).

The three zones are zone 1 (stagnation region), zone 2 (transition region) and zone 3 (wall jet zone).

(a)   (b)
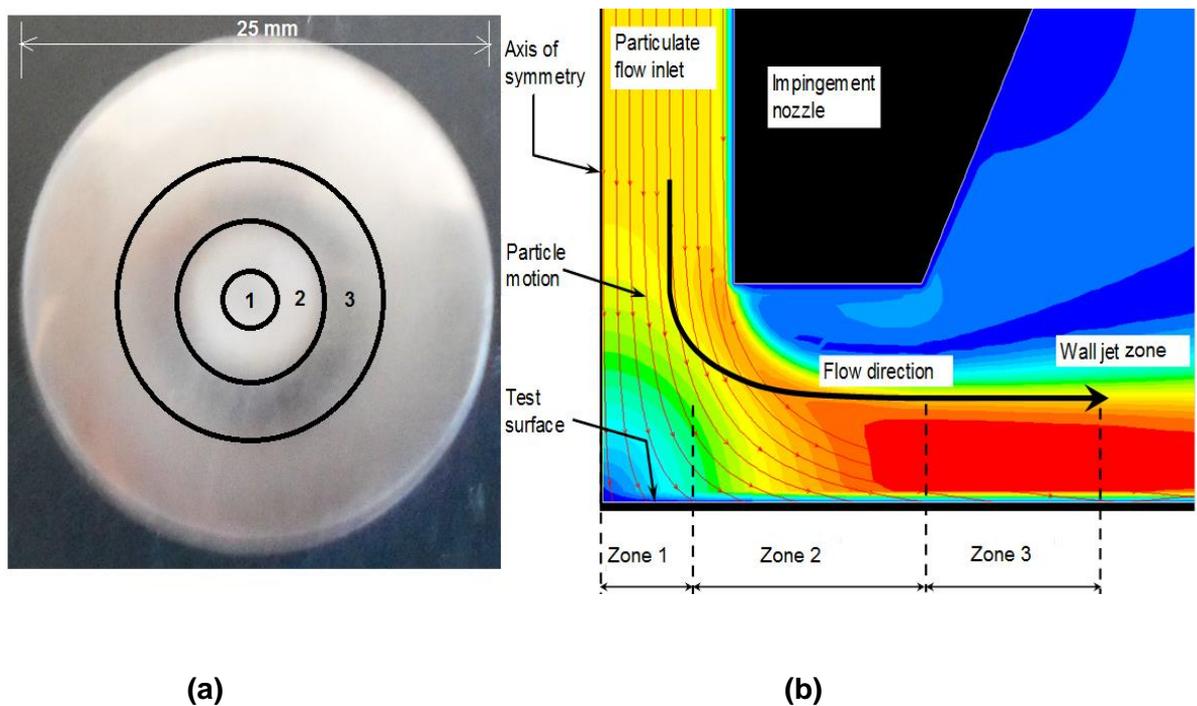
Figure 6.16: (a) Surface wear zones on tested specimen, (b) CFD prediction of the zones

The Scanning Electron Microscopy (SEM) images showing the X65 pipeline material degradation mechanisms at the three different zones are shown in Figures 6.17 to 6.19.
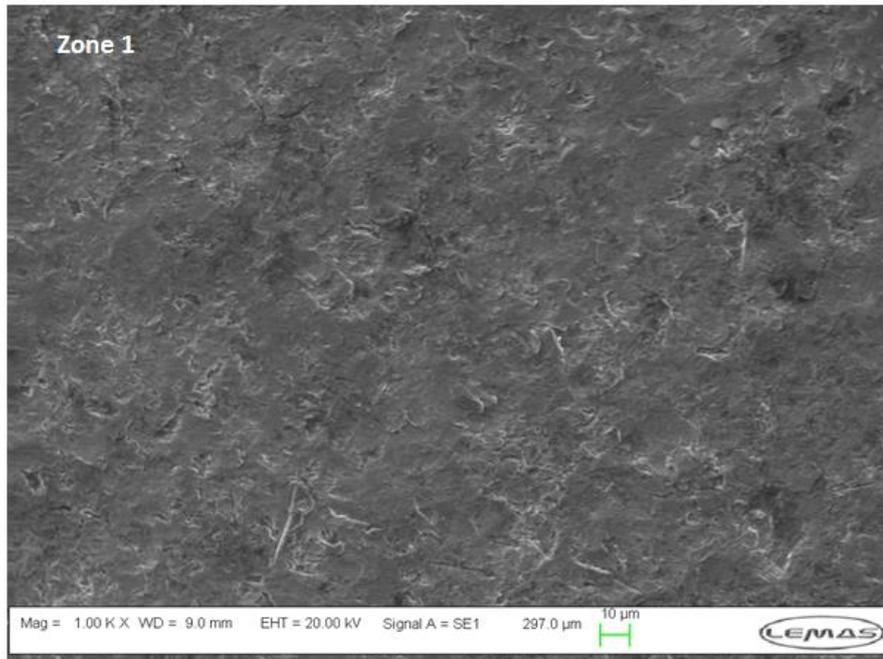
Figure 6.17: SEM image showing the degradation mechanisms of zone 1, the stagnation region for 15 m/s flow velocity, 500 mg/L sand and temperature of $50^{\circ}C$ in tap-water saturated with N_2 (pH≈7.0).
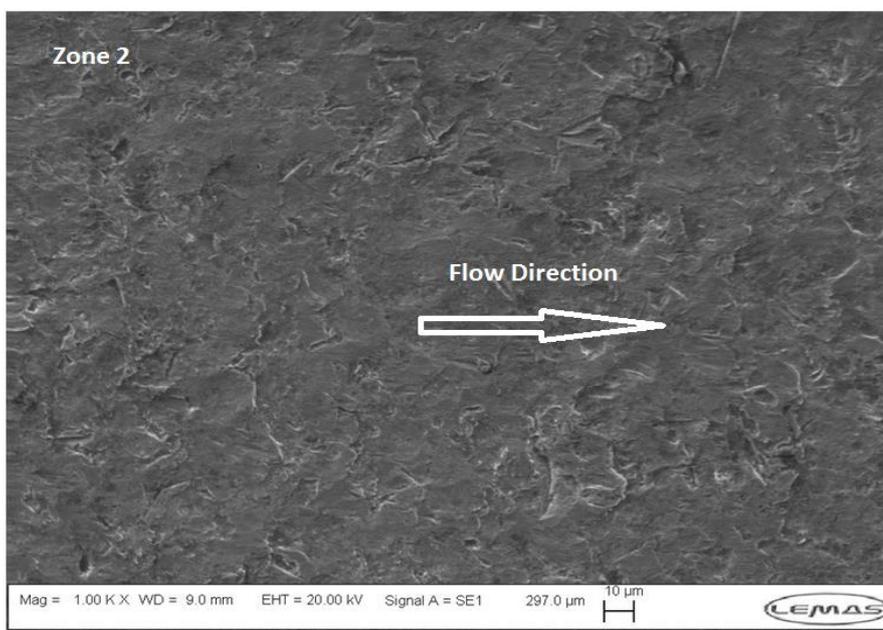
Figure 6.18: SEM image showing the degradation mechanisms in zone 2, the transition region for 15 m/s flow velocity, 500 mg/L sand and temperature of $50^{\circ}C$ in tap-water saturated with N_2 (pH≈7.0).
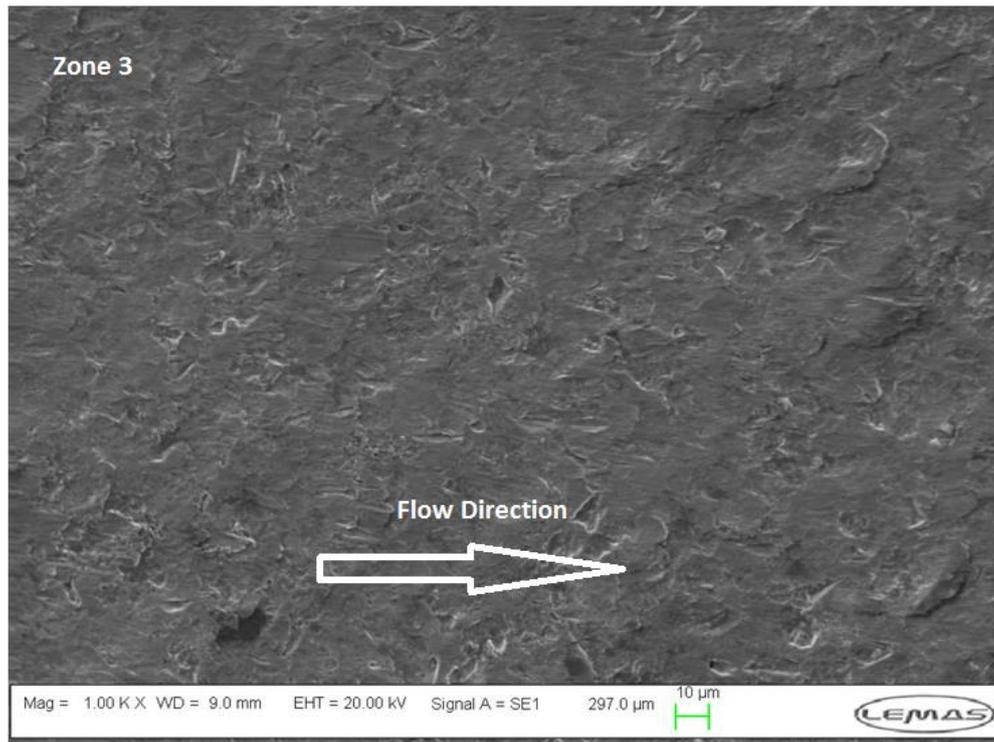
Figure 6.19: SEM image showing the degradation mechanism in zone 3, the wall jet region for 15 m/s flow velocity, 500 mg/L sand and temperature of 50°C in tap-water saturated with N_2 (pH≈7.0).

The size and profile of the 3D profilometry wear scar analysis on the specimen for 15 m/s (50 and 500 mg/L sand concentrations) are shown in Figure 6.20 (a) and (b), and Figure 6.20 (c) shows the wear scar depth along the specimen surface including results for 10 m/s (50 and 500 mg/L sand concentrations) to indicate the effect of increasing both sand loading and flow velocity on the erosive wear of the X65 carbon steel.
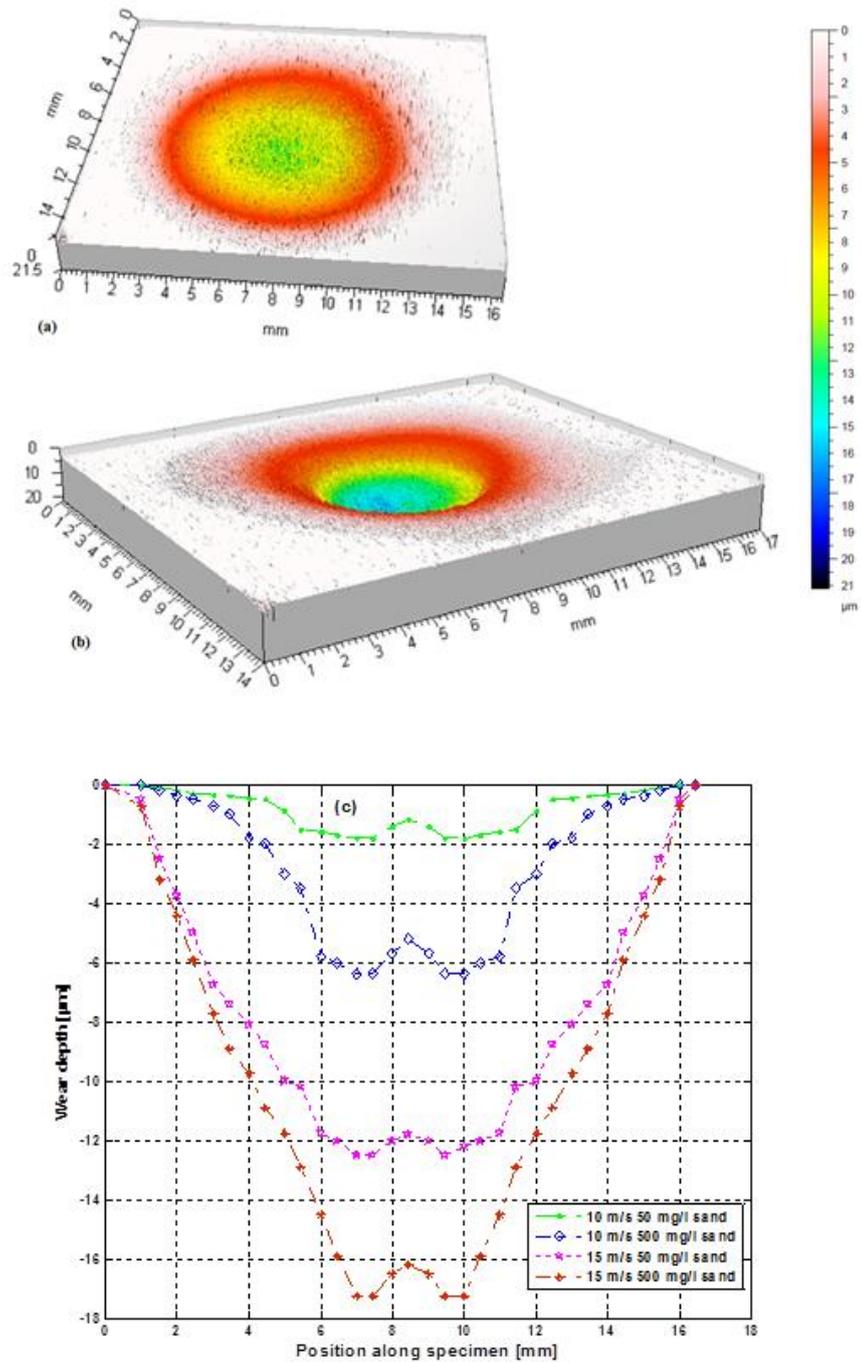
Figure 6.20: 3D profilometry of the erosion scars on the X65 carbon steel for 15 m/s flow velocity (a) 50 mg/L (b) 500 mg/L sand concentrations and (c) the profile of the wear scar depth across the specimen's surface for 2 hours test duration in tap-water saturated with N_2 (pH≈7.0).

6.3 Discussion

6.3.1 Single Impingement Test

As can be seen in Figure 6.2, the single impact signal ring-down count is significantly above the detection threshold and duration of approximately 100 μs; it is distinct from those of flow and background noise. Also, the peak amplitude of the burst is 0.8 mV which is higher than those created by multiple sand impacts of the same flow velocity (Figure 6.4) as expected because the diameter of the glass bead is considerably larger than the mean diameter of each sand particle. The AE energy and RMS for each impact associated with a particular flow velocity were determined and plotted against the kinetic energy (KE) of the impacting glass bead as shown in Figure 6.3.

From Figure 6.3, it is evident that there is a monotonous increase in AE energy and RMS as the KE of the impacting glass bead increases thus confirming the theory that impact on the material generates AE signal. This increase is consistent with the Pollock model [180] and supports his assertion that larger deformation events give a larger relative yield of AE energy. For example, 7 m/s nominal flow velocity with incident KE of 16.42 x 10E-5J yields AE energy of 0.5 x 10E-9J whilst 10 m/s nominal flow velocity with incident KE of 32 x 10E-5J gives AE energy of 1.5 x 10E-9J. This signifies that the measured AE energy for the flow velocities investigated is more than one part per 10,000 of the incident kinetic energy which is in agreement with the work of Ferrer *et al.* [187] and Oltra *et al.* [186] both for stainless steel materials.

In dry conditions, Hunter [174] performed a related investigation for a normal elastic impact using a hard steel sphere on steel target. He discovered that the energy converted into elastic waves is less than 1% of the incident KE. His finding was lower than that of Reed [195] who suggested that the elastic wave energy was about 4.5% of the incident KE. With similar analysis, Hutchings [176] extended the study to plastic deformation of the target and proposed that 1-5% of the incident KE is radiated as elastic waves majorly in form of Rayleigh waves, with 90% used up in plastic work

while the remaining proportion goes into rebound KE. Using Finite Element simulation Wu *et al.* [196] observed that for elastic impact the energy dissipation due to elastic wave propagation is less than 1% of the total KE if there is more than one reflection during the contact which is in line with Hunter's analysis. If there is no reflection within the contact duration, a significant amount of KE is dissipated due to stress wave propagation, whereas for plastic impact, the energy loss due to elastic wave propagation becomes negligible and the KE is mainly dissipated due to plastic deformation.

In this single impact study conducted in a submerged impinging jet rig, the percentage of the incident KE radiated as AE energy in the carbon steel material is far below 1%. This could be because of the inertia, drag effects and hydrodynamic boundary layer deceleration of impacting beads in the flowing stream [104-106, 110, 178]. The inertia arises due to its weight; the drag effect originates from buoyancy forces and its weight which try to resist the forward movement; and the bead must penetrate the boundary layers of the liquid on the specimen surface before impacting it. The penetration of this layer can decelerate the beads and reduce the impact velocity. When all these happen, the KE available on impact may be lower than that available in dry conditions hence giving rise to lower percentage of the measured AE energy in wet conditions.

Having established the relationship between the KE and the AE energy for single impact test, it was pertinent to apply the AE energy to quantify the material loss since the rate of material loss from the eroding surface is a function at which the kinetic energy of the impacting particles is dissipated [99]. This was done by conducting a series of multiple impingement tests at different flow velocities and sand loading and investigating the dependence of AE as well as material loss on them.

6.3.2 Multiple Impingement Tests

6.3.2.1 Effect of Flow Velocity

From Figures 6.5 to 6.8, the AE energy increases with increase in flow velocity. It appears slightly high at the beginning of the test and stabilises after a few minutes of the start of the experiment. Three factors can contribute to the decrease of AE energy with time. The first factor could be the initial period of the transient and unsteady state particle impacts, and it is associated with higher and irregular number of sand particles impact per second on the specimen's surface than the steady state with almost equal and regular number of particles hitting the target per second. The second factor may be the effect of strain hardening of the particle impact on the material. This may be possible because the initial impact may cause the stress field in the material to increase which leads to increase in the average dislocation velocity as well as acoustic emission rate until the onset of strain hardening [177]. Then the majority of the dormant dislocations suddenly begin to move. It is this sudden mass mobilization involving plastic deformation and/or cutting off of pinned dislocations that can cause the sudden rise in emission activity at the beginning. With strain hardening, an increase in dislocation density may follow which results in a reduction in average dislocation motion, thus causing lower emission activity [177]. The third factor can be attributed to the establishment of constant particle impact rate on the specimen surface and the possibility of sand becoming less abrasive after some time since the amount of the energy released by an acoustic emission is related to the magnitude and velocity of the source event.

It is important to note that the variation of AE energy with time as the flow velocity or sand loading is either increased or reduced agrees with the 'Kaiser Effect' [154, 156, 160] which states that when a defined stress has been applied on a material to cause acoustic emission, detectable AE will not be induced in to the material until the defined stress level is exceeded, even if the load is completely removed and reapplied. However, it has been observed by some authors [197, 198] that when there is a major

change in the property or internal structure of the material due to plastic deformation, micro-defects, phase transformation and so on, Kaiser Effect vanishes and AE is generated under a lower load than previously. They stressed that Kaiser Effect may be applicable in the detection of internal defects generated newly in a material.

6.3.2.2 Effect of Sand Loading

As can be seen in the results (Figures 6.5 to 6.8), an increase in sand loading leads to an increase in AE energy and also promotes erosive wear (Figure 6.9) for all the flow velocities studied. This is straight forward because erosion with more sand loading will generate higher AE energy and certainly remove more material from the test specimen. It is observed that at 7 m/s the AE energy of 50 mg/L sand is almost the same with zero sand loading at the end of the 2-hour test signifying that either the impact energy is not enough to cause sand impact or the sand particles have smoothened or settled at the corner of the reservoir. Another important observation is at high velocity (15 m/s), the variation of the sand loading with AE energy becomes smaller when compared with other velocities which could be as a result of reduction in instrumentation sensitivity (saturation of the preamplifier) or due to overlap of sand impingement events. As the velocity increases, the number of particle impacts per second increases from a few thousand to many thousands; this may lead to overlapping of the transmission paths, or to particle interactions at or near the surface, both of which would reduce the amount of energy being recorded at the sensor [182].

6.3.2.3 Estimating Corrosion Effects

It can be seen from the results (Figure 6.15) that the CO_2 saturated brine increases the weight loss from 0.65 mg to 1.1 mg for 50mg/L sand loading and 1.1 mg to 3.2 mg for 200 mg/L sand loading. The effect is also observed in the log values of measured AE energy which increased from 5.5 to 6.2 for 50 mg/L sand loading and from 6.45 to 7.6 for 200 mg/L sand loading thereby confirming the sensitivity of the AE set-up to CO_2 corrosion. The increase in AE energy could be as a result of increased corrosion

activity (hydrogen evolution, cracking and removal of corrosion products) at the specimen surface which will create a noisier environment giving rise to high emission rate that will lead to increase in AE energy.

The increase in the weight loss is due to the combined effects of CO_2 electrochemical corrosion and mechanical erosion. Each enhances the other in a synergistic manner thereby causing more material loss. Different researchers have proposed different mechanisms involved in the enhancement of erosion by corrosion. Dave *et al.* [37] suggested that the corrosion process roughens the metal surface which in turn increases the erosion rate (because the erosion damage is very sensitive to impact angle of the solid particles), thereby exposing more fresh surfaces to more corrosion attack. Li *et al.* [119] observed that corrosion affects erosion rate through detachment of flakes formed by repeated solid particles impingement. Reyes and Neville [120] proposed that the preferential dissolution of a matrix would lead to easy removal of the hard particles in micro-structure which results to acceleration of erosion. Matsumura *et al.* [121] recommended that the impingement of the particles would damage the passive film and enhance the dissolution of the work-hardened layer, which degrades the erosion resistance of material. Recently, Lu *et al.* [48] pointed out that since erosion rate increases with decreasing hardness, the hardness-degradation caused by the anodic dissolution (enhancing mobility in the surface layer) is an important mechanism of corrosion-enhanced erosion loss.

6.3.3 Surface Analysis

From the visual inspection results (Figure 6.16), three zones are clearly shown. These regions are zone 1 (stagnation region), zone 2 (transition region) and zone 3 (wall jet zone). The stagnation region is the zone next to perpendicular intersection axis of the nozzle and the specimen surface. It is characterised by high impact angle (approximately 80°) but low impact velocity due to decelerating effect of the fluid [110]. The transition region is the zone between the stagnation region and wall jet region

where particles impacts at medium to low angles between 15° and 40° with local high turbulence as the fluid jet accelerates along the radial direction by aligning itself to the test specimen's surface. The particle inertia drives the particles to impact the surface whereas the fluid drags particles away from the surface. In wall jet region, the particle motion and impacts are purely governed by fluid flow with high velocity, and turbulence which decays to the surrounding. The particles follow streamline that enables impact at low angles (below 15°) by rubbing and scratching along the surface.

In the SEM images (Figures 6.17 to 6.19), it can be seen that at zone 1 (Figure 6.17), impact is at high angle (nearly 80°) and material degradation is through heavy indentation and forging with the normal indentation marks and extrusion material flakes associated with the processes. The surface dips may be as a result of sputtering, when local micro-crack forms because of the residual stresses after the particle impacts and the material sputters and adheres to flying particle at its impacts and removed by the particle.

At zone 2 (Figure 6.18), impact is between 40 and 15°, plastic deformation and cutting action become the key mechanisms of material degradation. Deformation through chipping created by the cutting action dominates the material removal process because the component of the impact force normal to the specimen becomes high enough to enable a particle to penetrate into the specimen while the component tangential to the surface is still adequate to proceed the cutting. The ductile cutting together with plastic deformation serve as the most effective material removal mode in mechanical erosion which is the main reason for the high erosion rates between 15 and 40° impact angles as proposed by Finnie [99], Bitter [81, 82] and Hutchings [83].

At zone 3 (Figure 6.19), impact is at low angles (below 15°), it is observed that material removal was mainly by rubbing and scratching as evidenced by the ductile rubbing and scratching marks aligned in flow direction. Mechanism by rubbing and scratching is well established in past studies [110].

The profilometry analysis (Figure 6.20) revealed a depressed 'W' shape wear scar on the flat specimen which signifies the ductile nature of the material subjected to the solid-liquid impinging jet of the flow stream. The maximum material loss results from the mechanisms of cutting action and plastic deformation occurring at medium to low impact angles as described above. It can be seen in Figure 6.20 (c) that the depth of the wear scar becomes greater as either the flow velocity and/or sand loading is increased, and the amount of the material removed is in line with the weight loss results. The wear scar is in good agreement with the results reported in past investigations [42] on X65 carbon steel material.

6.3.4 Mass Loss and AE Energy

The erosive wear expressed as mass loss rate together with the measured average and cumulative AE energy for all the sand loading and flow velocities investigated was analysed to establish a relationship between the mass loss and AE energy on one hand and the flow velocity and the AE energy on the other hand. These relationships are shown in Figures 6.21 to 6.23. The mass loss relationship with average AE energy (Figure 6.21) indicates that significant mass loss does not occur until average AE energy exceeds a certain critical value which is equal to $10^6 eu$ for 50 and 200 mg/L sand concentrations and 10^7 eu for 500 mg/L sand loading. The variation in critical AE energy values as the sand loading increases may be due to the variation in sand particle sizes which is 212 to 300.

This critical value corresponds to 7 m/s flow velocity which signifies that the mass loss at this flow velocity. This finding agrees well with previous study on X65 pipeline material [42] as the determination of the critical values of the sand loading and flow velocity indicates that the impact intensity on the material surface which generates acoustic emission is a key factor in material degradation of X65 pipeline material. Also two regions were identified in the plot. The first region (within 7 m/s flow velocity) is the region of pure elastic impacts which generate AE but do not cause erosive wear as

proposed by Hunter [174]. The second region is the region of plastic deformation, ploughing and cutting leading to significant erosion damage with associated AE as proposed by Miller and Pursey [175] and confirmed by Hutchings [176]. This region occurs above 7 m/s flow velocity. Therefore, increasing the velocity beyond 7 m/s leads to increase in kinetic energy of the particle which will cause large erosive wear scar and would accelerate erosion rates.

However, with cumulative AE energy, a linear relationship is proposed (Figure 6.22) which is in agreement with the work of Oltra *et al.* [186] who did similar study on stainless steel materials for high sand loading using cumulative RMS values. This is also in agreement with acoustic emission study by Ferrer *et al.* [187] on stainless steel. They attenuated the influence of fluid flow on the specimen by reducing the specimen area to a small value so as to only capture particle impacts on zones 1 and 2 and proposed a linear relationship between the mechanical erosion and cumulated AE energy after 2 hours for high sand concentration 1-8% wt (10,000-80,000 mg/L) and 1-16 m/s flow velocities. All these previous studies did not provide information on the minimum AE energy parameter (critical value) above which material degradation becomes significant so as to apply it as a guide in monitoring and predicting the erosive wear rate in pipelines and related structures. Hence, this study provides this threshold energy and agrees with all the past studies that the measurement of acoustic emission energy can be used to quantify the mechanical damage due to pure erosion.

The relationship between flow velocity and cumulative AE energy is shown in Figure 6.23 which indicates an exponential behaviour at 50 and 200 mg/L sand concentrations and linear behaviour at high sand concentration of 500 mg/L. Thus, indicating a linear dependence of AE with flow velocity at high sand loading.
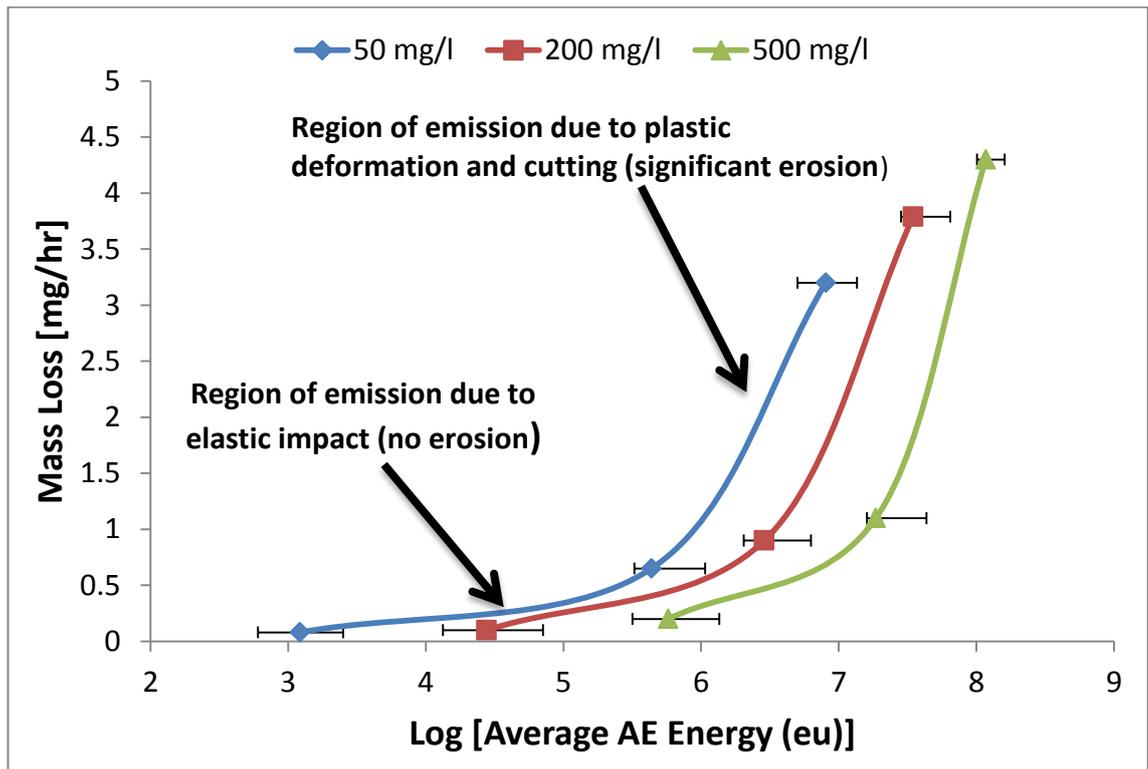
Figure 6.21: Relationship between mass loss and average AE energy for the flow velocities and sand loading investigated with tap-water saturated with N$_2$.
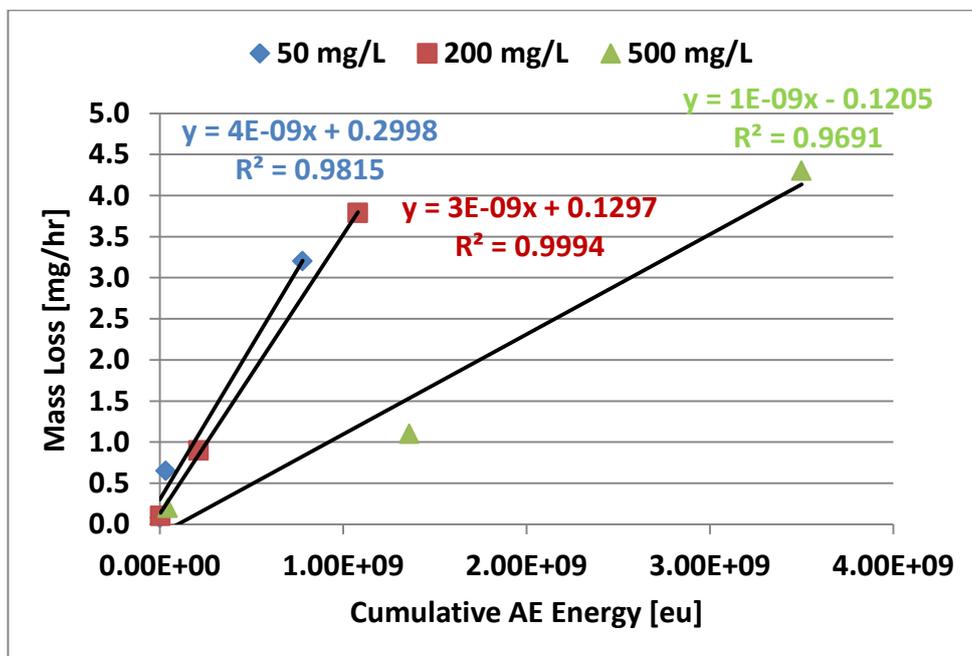
Figure 6.22 Relationship between mass loss and cumulative AE energy for the flow velocities and sand loading investigated with tap-water saturated with N$_2$.
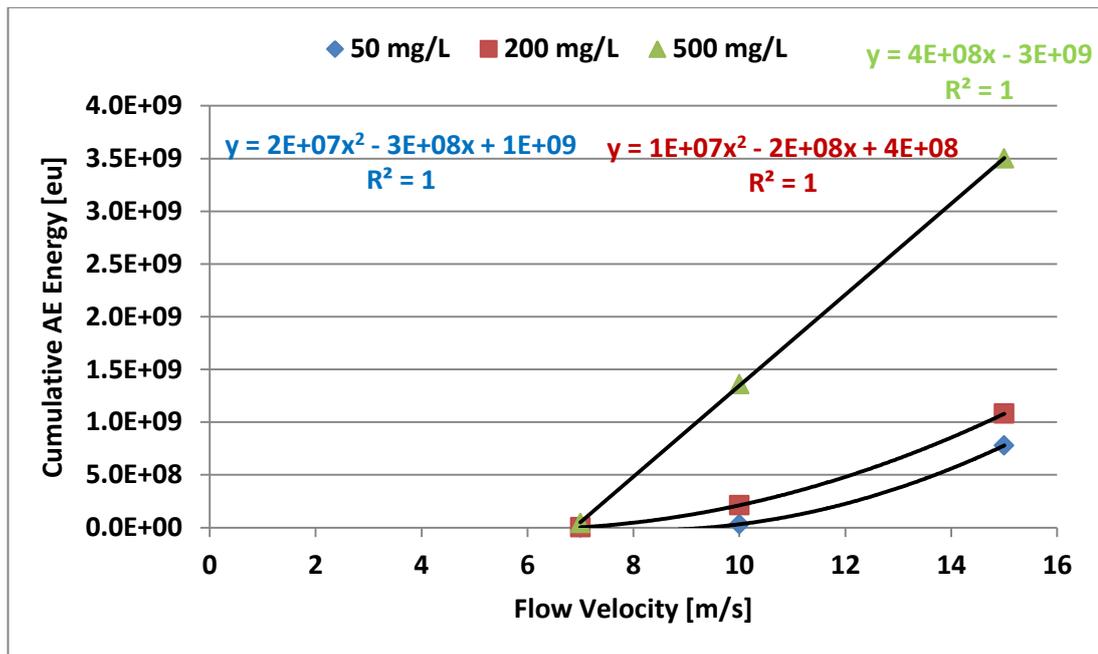
Figure 6.23: Relationship between cumulative AE energy and flow velocity for all the sand loadings investigated with tap-water saturated with N_2.

6.3.5 Frequency Spectrum Analysis

The previous sections applied information from the measured signals' time series to determine the AE energy which was used to characterise the X65 pipeline material erosive wear rate in tap-water saturated with N_2.

The knowledge of the frequency content of the signals can be very important in characterising the measured signals [199, 200]. This importance arises because the manner in which the frequency spectrum displays information will often reveal details of a signal that are too subtle to observe in time domain, in spite of the fact that the frequency spectrum of a signal has no more information in it than the time domain signal.

Hence, this analytical power of spectral analysis makes it an attractive technique for characterising acoustic emission signals because each source mechanism should have a characteristic frequency spectrum based upon its size and velocity of operation.

The frequency spectrum was analysed from waveform signal raw data spectral using ORIGINLAB because the program gave an excellent fast result with low computer memory requirement. This was achieved by uploading the time series input text file generated after each test into ORIGINLAB for analysis.

6.3.5.1 Zero Sand Loading

The waveform of the measured AE signals for the flow velocities (7, 10, and 15 m/s) without sand are shown in Figure 6.24 and the associated frequency spectrum in Figure 6.25.
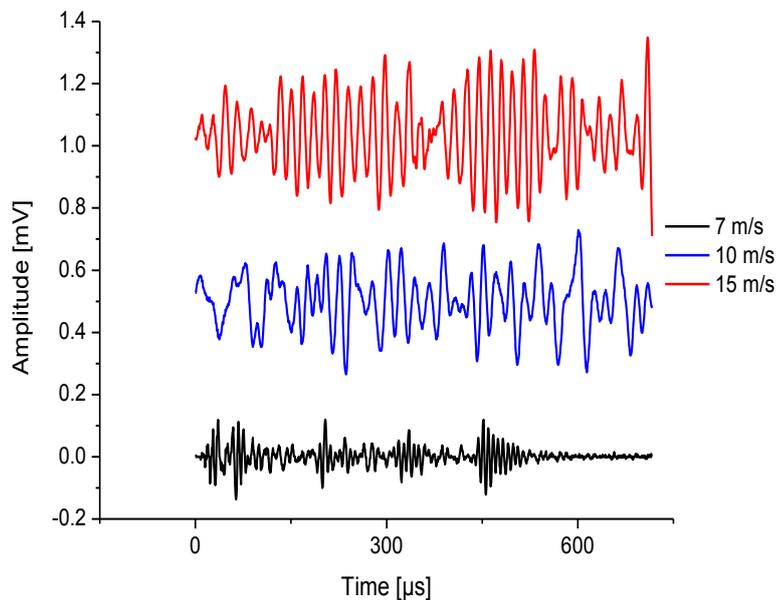
Figure 6.24: Measured time-domain (waveforms) without sand for 7, 10 and 15 m/s at 90° impingement angle and 50°C temperature in tap-water saturated with N$_2$ (pH ≈ 7.0).
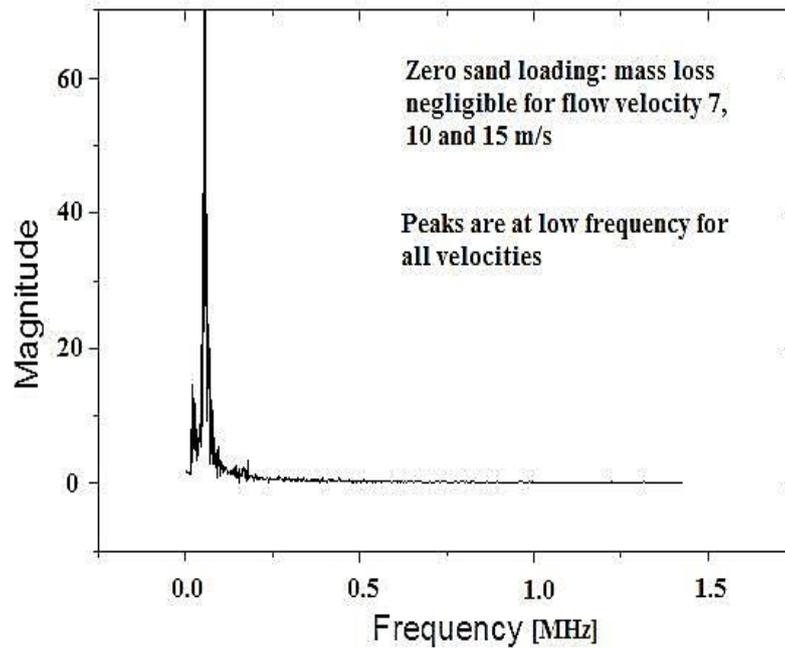
**Figure 6.25: Frequency spectrum of AE waveform without sand at 90°
impingement angle and 50°C temperature in tap-water saturated with N₂ (pH ≈
7.0).**

These waveforms are selected representative of the common nature of the waveform
in each particular condition for the two hours test duration in each case. Visual
examination of the waveforms indicates that they are continuous in nature and have
appearance similar to background noise with average time between emissions of
similar amplitude less than the duration of the emission. As the velocity increases, the
amplitude of the waveform also increases signifying the increase in the momentum of
fluid flow. The magnitude of the amplitude is also seen in frequency spectrum indicates
peaks at low frequency range (<0.1 MHz) for all the flow velocities investigated.

6.3.5.2 With Sand Loading

With addition of sand, the waveform changes to discrete bursts corresponding to
individual sand impact. The amplitude of the waveform increases with increase in flow
velocity as shown in Figures 6.26 to 6.28.
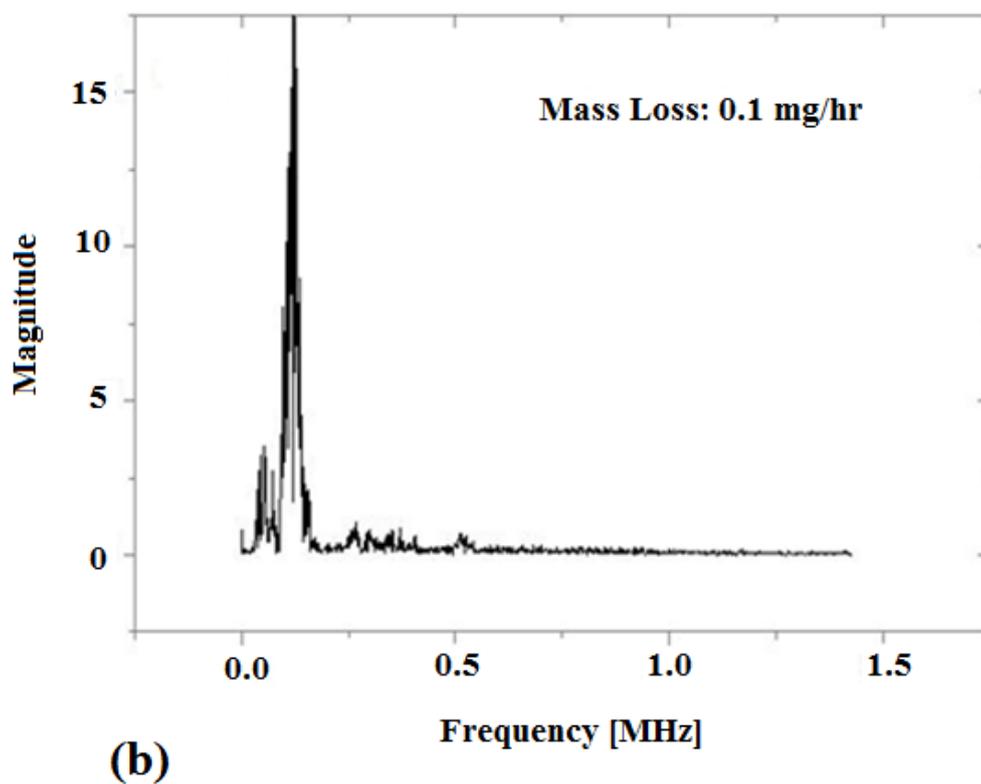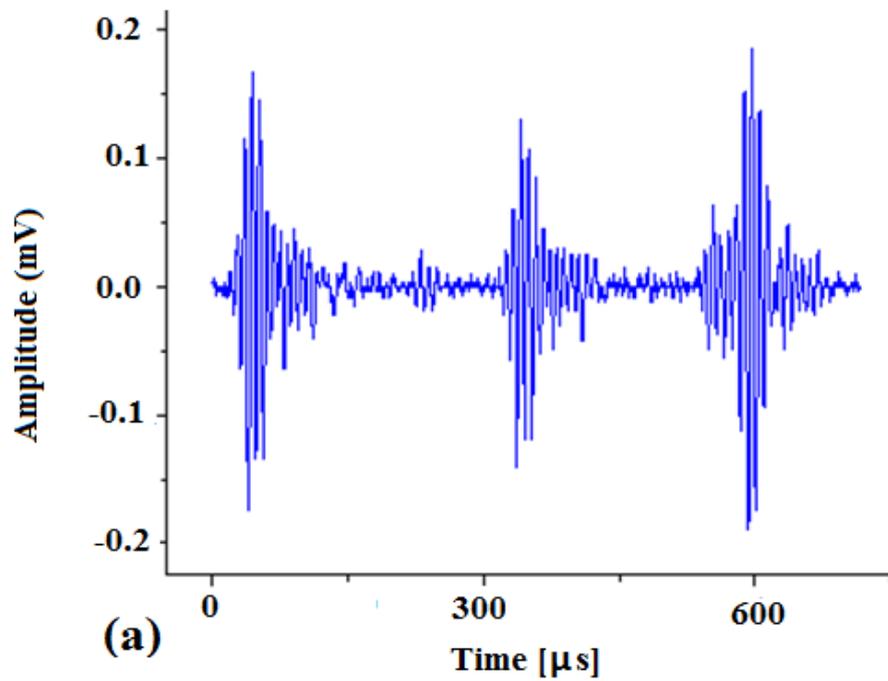
Figure 6.26: (a) Measured AE waveform (time-domain) and (b) frequency-domain for 7 m/s flow velocity, 200 mg/L sand loading at 90° impingement angle and 50°C temperature in tap-water saturated with N$_2$ (pH ≈ 7.0).
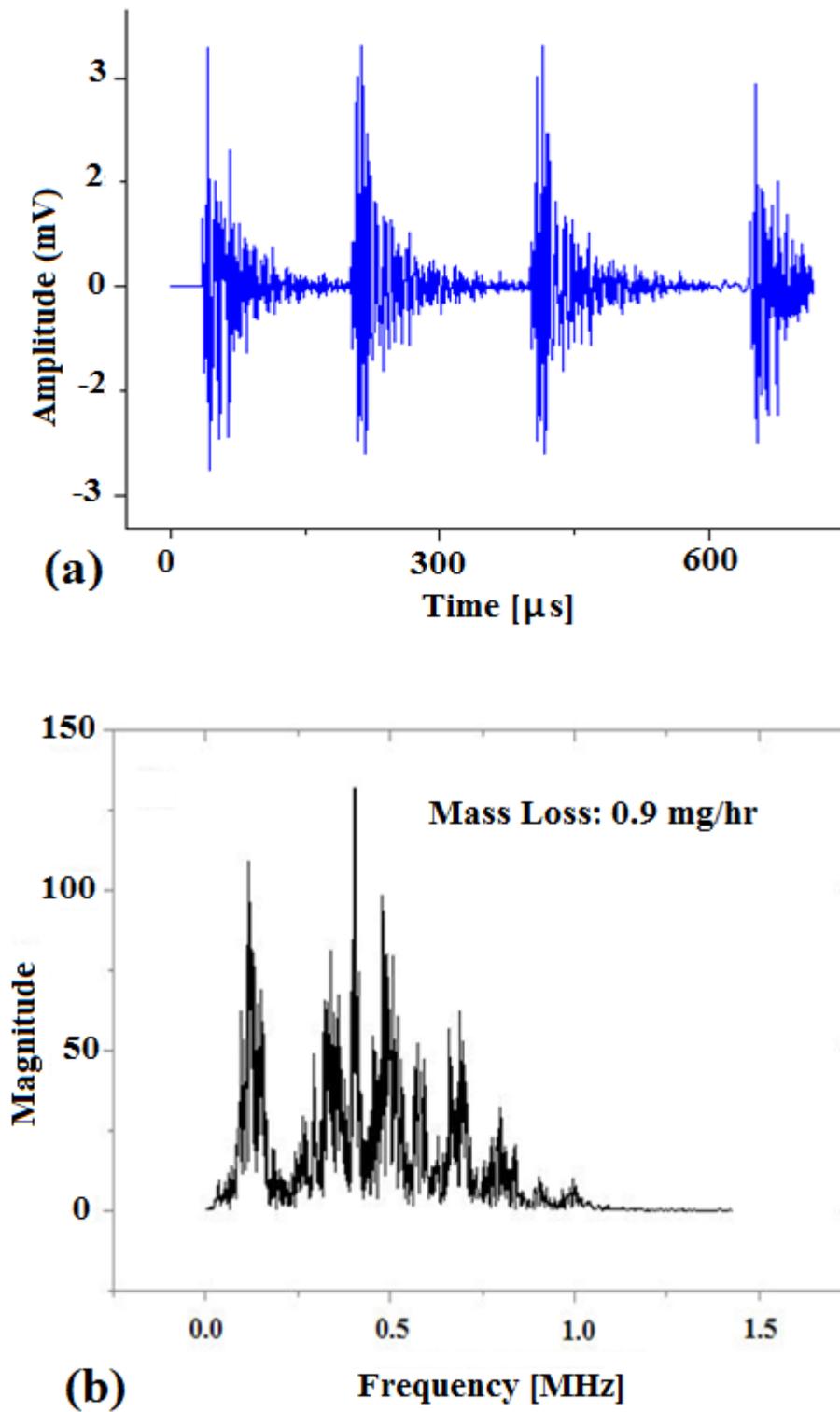
Figure 6.27: (a) Measured AE waveform (time-domain) and (b) frequency-domain for 10 m/s flow velocity, 200 mg/L sand loading at 90° impingement angle and 50°C temperature in tap-water saturated with N$_2$ (pH ≈ 7.0).
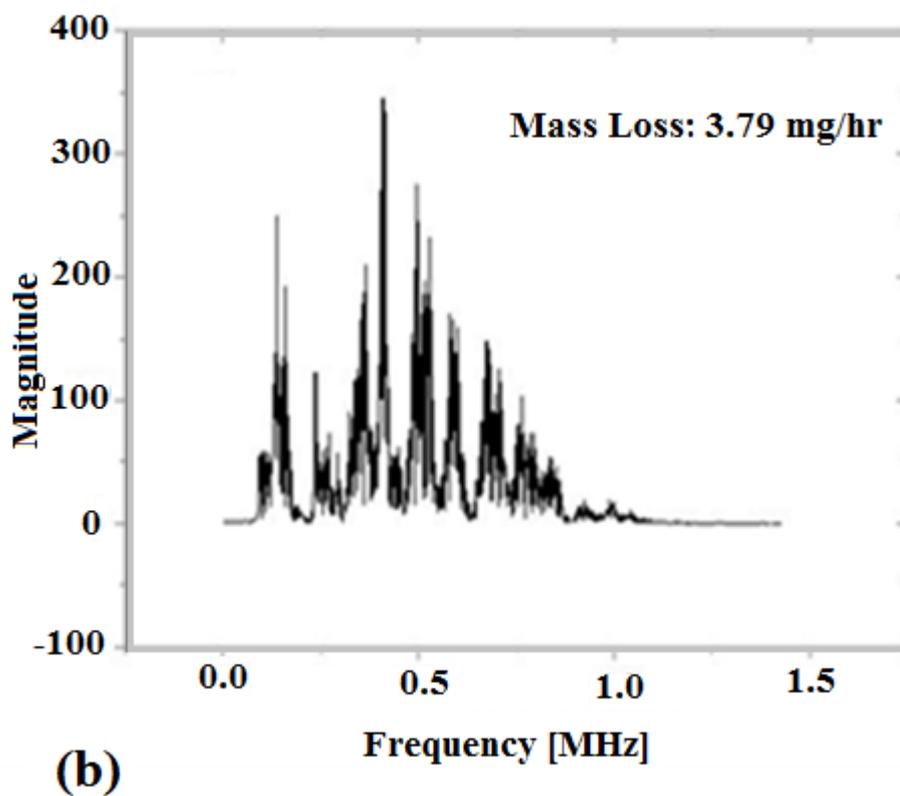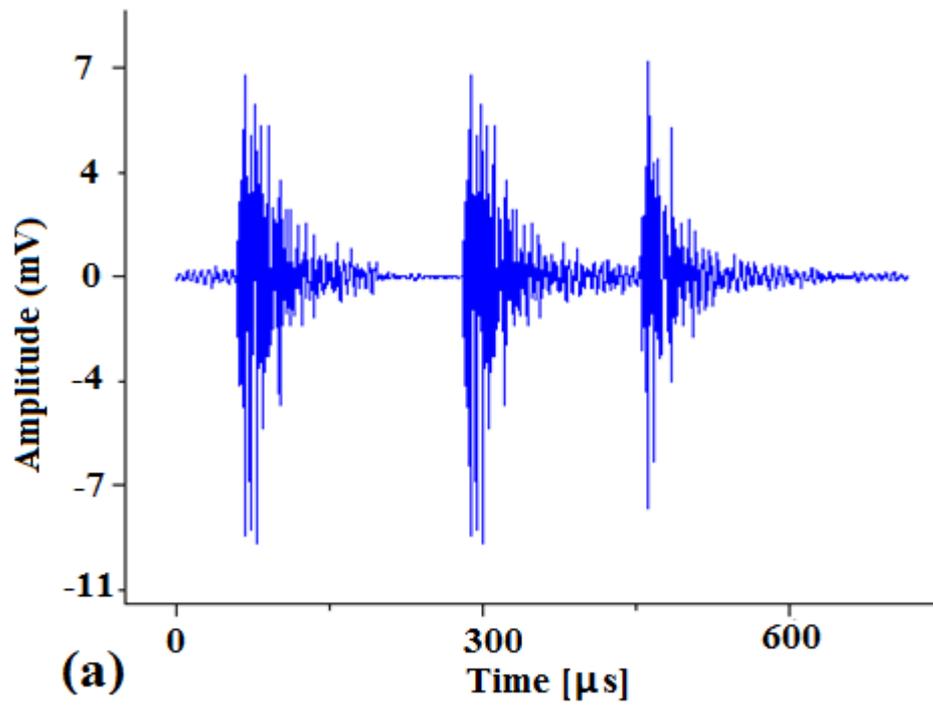
Figure 6.28: (a) Measured AE waveform (time-domain) and (b) frequency-domain for 15 m/s flow velocity, 200 mg/L sand loading at 90° impingement angle and 50°C temperature in tap-water saturated with N_2 (pH ≈ 7.0).

The associated frequency spectra show large peaks in the higher frequency region when the damage becomes significant as indicated in Figures 6.27 (b) and 6.28 (b). These large peaks may be as a result of the plastic deformation of the X65 material associated with the sand impacts. From these results, it is evident that frequency analysis provides a means of differentiating and classifying different emitted signals during erosion of X65 pipeline materials, and thus of discriminating between kinds of source deformation mechanisms from the sand impacts. With further research in future study, it may be possible to read and interpret the spectra and provide a stage-by-stage description of the deformation and overall material degradation processes.

6.4 Summary

The measured AE energy from the signal time domain was used to investigate single and multiple particles impingement in SIJ rig at 90° impact angle and constant temperature of 50^oC. In single impact study (using glass beads), it was observed that there is a monotonous increase in AE energy and RMS as the KE of the impacting glass bead increases thus confirming the theory that impact on the material generates AE signal. For multiple impact study (using sand particles), the measured average AE energy increased with increase in flow velocity and sand concentration which becomes higher in the presence of CO_2 corrosion. Within the experimental parameters investigated, the erosive wear of the material expressed as mass loss increased with increase in measured averaged AE energy and there exist a critical AE energy below which no significant damage is done to the material.

For frequency-domain analysis, frequency peak is observed at low frequency region when the material damage is negligible but when damage becomes significant, large peaks appear in the higher frequency region which may be due to plastic deformation of the materials.

Chapter 7 Results and Discussion: Particle Impact and Impact Energy Quantification

7.1 Introduction

This chapter describes the implementation of AE in a submerged impinging jet (SIJ) rig to quantify the number of sand particle impacts per second using the AE event count rate which is verified with theoretical predictions. Particle impact energy calculated from Computational Fluid Dynamics (CFD) in conjunction with particle tracking code was correlated with measured AE energy per second of the impacts to ascertain the dependence of AE energy on the impact energy. The AE event count rate was also correlated with the material degradation rate expressed as mass loss with a view to establishing a guide that can be used in monitoring and predicting erosion damage of pipeline materials (X65) in service.

7.2 Understanding Particle Impact Detection and Interpretation

In this study, optimisation of the detection threshold was achieved at a 40 dB setting (see Chapter 5, section 5.5), sampling rate of 2.5 MHz, and filter applied between 90-850 kHz so as to capture adequate emissions due to sand impacts while excluding noise from background interference. The event count rate and energy analysis were chosen because each sand particle impact generates a discrete AE signal with a clear beginning and end that is recorded by the counter and the energy analysis can give a continuous measurement of the amplitude of the emission which can be standardised and used for comparative experiments.

The beginning of the AE signal from each sand impact called a 'hit' is defined by its first threshold crossing, the end, by the absence of threshold crossing for a defined period of time known as the Duration Discrimination Time (DDT) [192, 194] which was set at 100 µs for all tests. This is illustrated in Figure 7.1. The energy analysis also provides data that may be readily relatable to the mechanisms and processes of the impacts

and erosion occurring on the material. Just as stated in previous chapters, AE energy is the integral of squared or absolute amplitude (A) over time of signal duration (t) [154, 168, 183, 192, 194, 200]. The energy measurement is realised in AE tests by sensing the signal, converting the signal to a electrical signal, filtering, amplifying and squaring the resulting signal to obtain a curve. The area under the resulting curve within the specific time gives a measure of the AE signal energy expressed in energy unit (eu) $[1eu = 10^{-14}V^2s = 10^{-18}J]$ [192, 194].
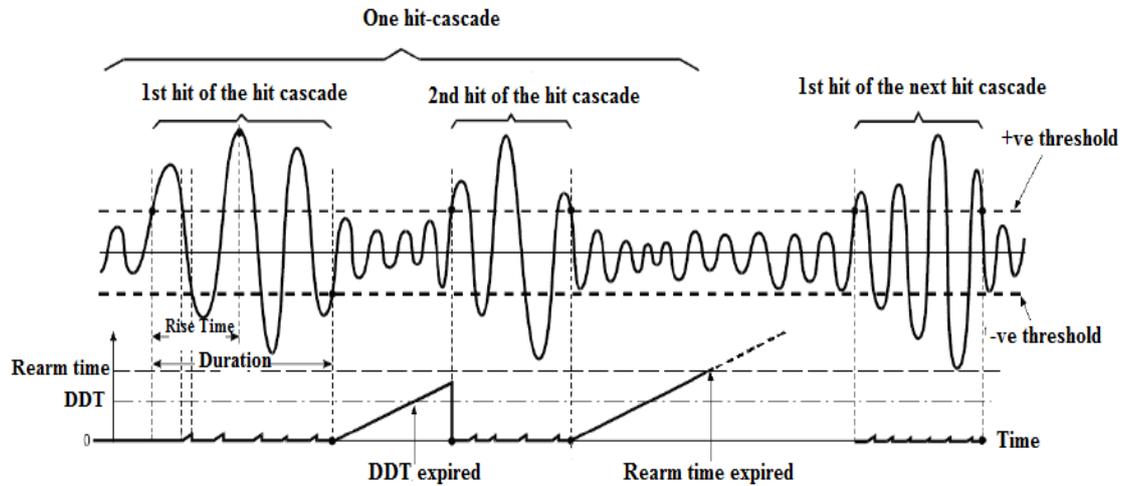
Figure 7.1: Schematic illustration of duration discrimination time (DDT) [192].

If a single sand particle with mass, m, impinges the specimen as shown in the illustration of generation of AE signal from single sand impact (Figure 7.2), the particle has a velocity, v, that forms an incident angle θ with the specimen's surface. The change of the particle's momentum due to impact and the impulse imparted onto the specimen is given by $mv(1 + e)\sin\theta$, where e is the coefficient of restitution (the ratio of the velocities after and before an impact, taken along the line of impact) and is less than unity. The corresponding AE signal (S_p) that can be measured on the back of the specimen can be approximated as follows [201]:

$$S_p = d_0(1 + e)mv\sin\theta \qquad\qquad (7.1)$$

where, d_0 is a factor representing the transfer function for the impulse imparted onto the specimen to form the voltage from the AE sensor. This factor accounts for energy dispersion and damping due to the transmission of acoustic energy from one material to another [201].

In order to determine the contribution of the AE signal from multiple sand particles impinging on the specimen with associated signals measured by the AE sensor in a given period of time, t, then the particles' flux (k) in the solid-liquid mixture impinging the specimen per time which depends mainly on the kinematic viscosity, η, and the average particle velocity, $\bar{v}$, can be expressed as, $k(\eta, \bar{v}) < 1$ [201]. The particles exiting the nozzle and impinging the specimen per second will have a total mass, M (g/sec) and will impinge the specimen with vertical velocity component, $\bar{v} \sin \theta$.

Hence, the total AE signal due to the solid-liquid mixture impingement per second, S_p measured by the sensor will be given by [201]:

$$S_p(t, \bar{v}, M) = d_t k_t M \bar{v} \sin \theta + S_f(v_f) \qquad (7.2)$$

where, $d_t = d_0(1 + e)$; k_t is a fraction of the particles hitting the surface per time which depends on the kinematic viscosity of the fluid, η, and the average velocity of the particles, $\bar{v}$; and $S_f(v_f)$ is signal due to background noise and flow.

The technique and validity of measuring S_p rely on the increase in the integrated AE signals with increasing sand loading when compared with the stable value of the integrated signal without any sand in the flow. The AE signal without sand is given by $S_p(t, \bar{v}, M = 0)$, and is equal to S_f. To determine the amount of sand impinging the specimen per second, equation (4) becomes [201]:

$$M = \frac{S_p - S_f}{(d_t k_t) \bar{v} \sin \theta} \qquad (7.3)$$
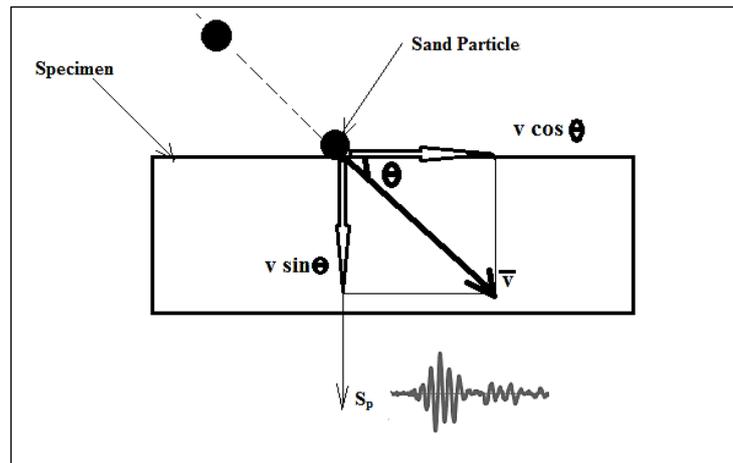
Figure 7.2: Illustration of generation of AE signal from single sand impact [201].

In theory and practice, the AE signals without sand given by $S_p(t, \bar{v}, M = 0 \ldots)$, can be subtracted from the AE signal with sand, $S_p(t, \bar{v}, M > 0)$, to determine the amount of sand, M or the number of sand impacts per second using the measured AE count rate. The subtraction technique relies on the hypothesis that the measured AE signal is stable if sand is not present in the flow. The presence of sand can be deduced from the observation of changes in the residual of the subtraction.

This signal interpretation technique has been successfully applied by the Cawley group [202, 203] at Imperial College London in the application of guided acoustic waves in health monitoring of structures. In their approach, the component under test is interrogated with guided acoustic waves from an exciting transducer (sensor) and the scattering of the waves by a defect in the structure captured by a receiving transducer gives an indication of the integrity of the structure. The part under test plays a passive role, and the only contribution it makes to the test is its ability to absorb or scatter energy in unique ways.

In this study, the AE technique eliminates the passive nature of the structure and makes it an active participating member of the test. This is accomplished by using the transducing action of the sand impingement with associated deformation in an elastic stress field as a secondary source of energy in the test, and the primary energy being

supplied by the solid-liquid mixture impingement onto the specimen. The technique is applied to quantify the number of sand impacts per second using AE event count rate. A baseline signal measurement (zero sand) was established for all the flow velocities studied and measurements with sand were taken for each sand loading and flow velocity.

The baseline AE event count rate for each velocity was then subtracted from AE event count rate of each sand loading measurement to obtain the particle impacts at the specific velocity and sand loading. The measured signal showing the sensor's response to multiple sand impacts is shown in Figure 7.3. The validity of this technique was verified by comparing the results with theoretical prediction from volumetric flow rate calculations with the assumption that all sand particles passing the nozzle strike the target.
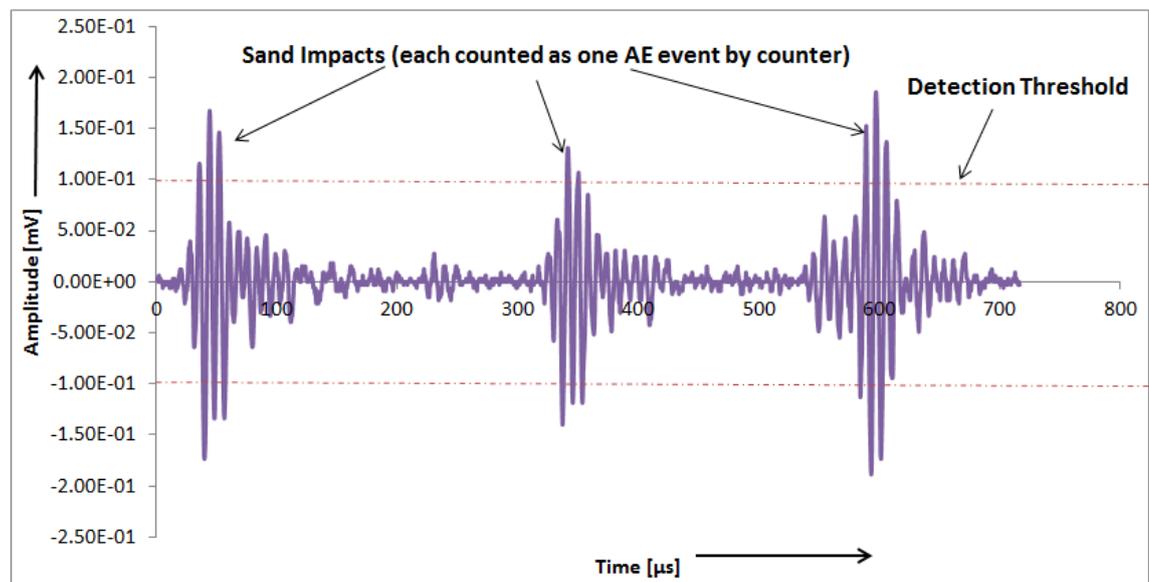
Figure 7.3: Measured AE signal waveform due to multiple sand impacts at 7m/s flow velocity, 90° impingement angle and 50°C temperature with tap-water saturated with N_2 (pH ≈ 7.0).

7.3 Results for Particle Impact

The liquid-solid impingement onto the surface of the specimen is the main source of the AE signals detected and analysed in all the tests. Since the operation of the centrifugal pump is the only driving force to the flow of the liquid-solid mixture and its eventual impact on the specimen, the pump output throughout each of the two-hour test duration will also affect the detected AE signals. This necessitated the use of the subtraction technique to eliminate the pump and flow effects, and other background interferences on the measured signal when determining the particle impacts.

Also, due to the scattering nature of the AE event counts per second, an EXCEL code that averages every 50 data points were applied to establish good, simplified and interpretable information from the measured AE data.

7.3.1 AE Event Count Rate

The event count rate analysis was conducted to provide a benchmark for the determination of the particle flux (sand impacts) using the subtraction technique described in the previous section. Figures 7.4 to 7.6 show the variation of log values of the measured AE event counts per second with time in each of the two hour tests for the range of flow velocities and sand concentrations investigated. The log values were used for ease of comparison of the results because the baseline (zero sand) count rate results were in most cases three orders of magnitude lower than the count rate with a sand loading of 500 mg/L.

The average values at the point of steady state (towards the end of each test) are plotted in the summary graph of all the results shown in Figure 7.7 with upper and lower error bars corresponding to the highest and lowest measured values within the steady state point towards the end of each test.
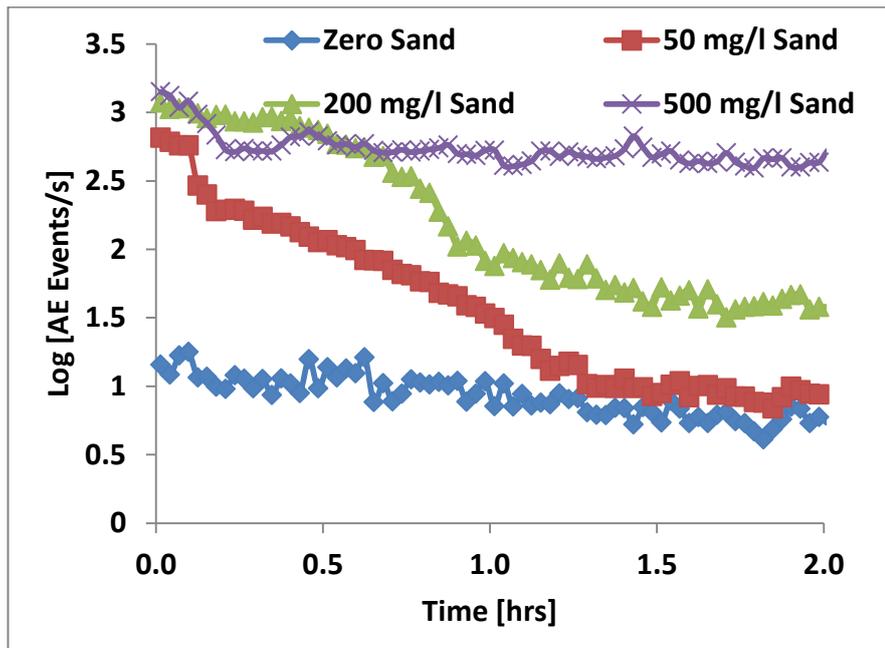
Figure 7.4: AE event count rate for baseline and different sand concentrations for 7 m/s at 90° impingement angle and 50°C temperature in tap-water saturated with N$_2$ (pH ≈ 7.0).
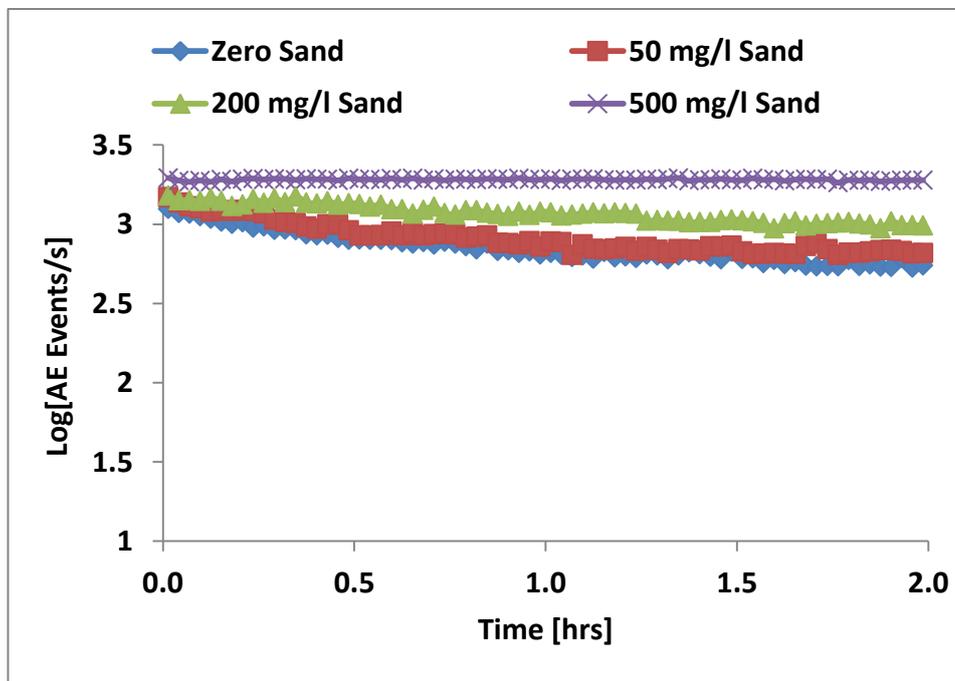
Figure 7.5: AE event count rate for baseline and different sand concentrations for 10 m/s at 90° impingement angle and 50°C temperature in tap-water saturated with N$_2$ (pH ≈ 7.0).
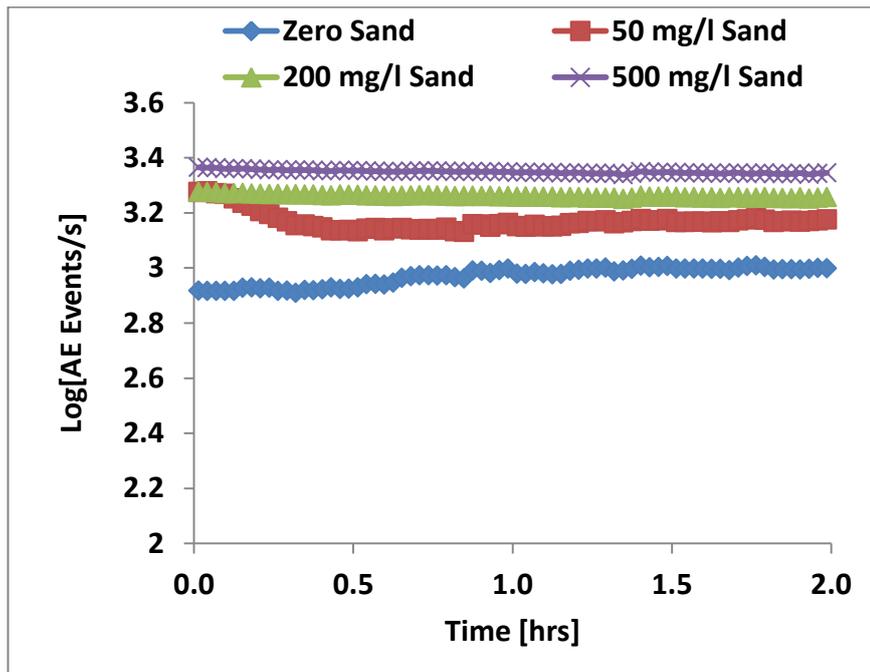
Figure 7.6: AE event count rate for baseline and different sand concentrations for 15 m/s at 90° impingement angle and 50°C temperature in tap-water saturated with N$_2$ (pH ≈ 7.0).
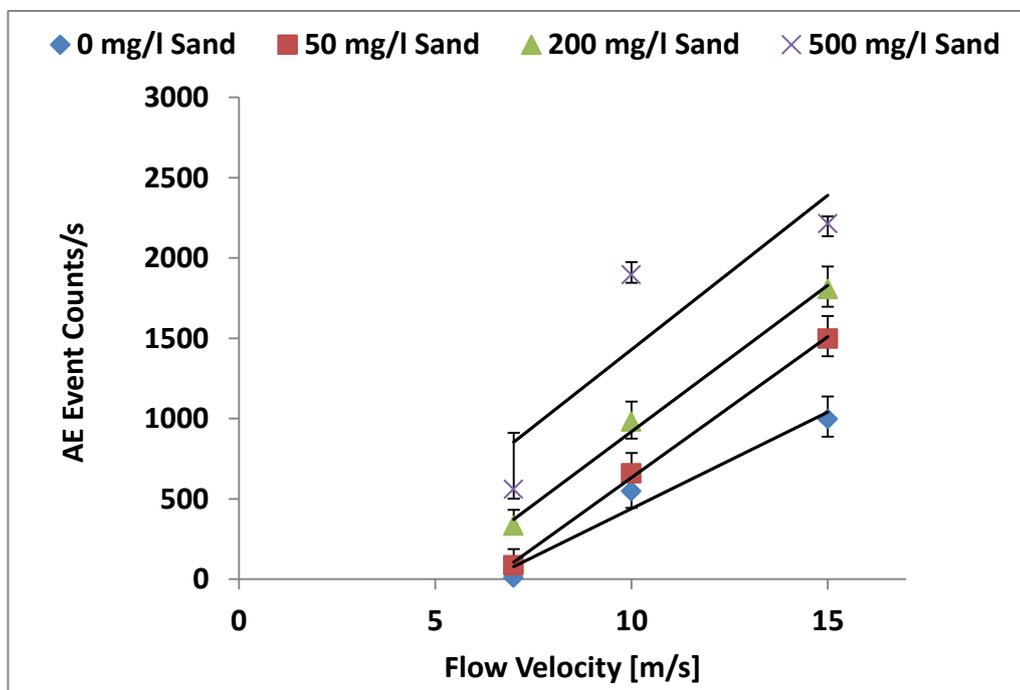
Figure 7.7: Summary of the results for AE event count rate for baseline and different sand concentrations and flow velocities at 90° impingement angle and 50°C temperature in tap-water saturated with N$_2$ (pH ≈ 7.0).

7.3.2 Particle Impacts Determination

Using the results of the measured AE event count rate, the number of sand impacts per second was calculated by subtracting the zero sand event count rate from the event count rate with sand for all the sand loading and flow velocities studied. The results of the particle flux in each test obtained from the subtraction are shown in Figures 7.8 to 7.10 with a summary of the average values at the point of steady state illustrated in Figure 7.11 with upper and lower error bars corresponding to the highest and lowest measured values within the steady state point at the end of each test.

The representation of the nature of the particle impact data scattering (for the entire duration of each test) is presented in box plots shown in Figures 7.13 to 7.15 for purpose of comparison with theoretical predictions. The meaning of the box plot parameters is illustrated in Figure 7.12.
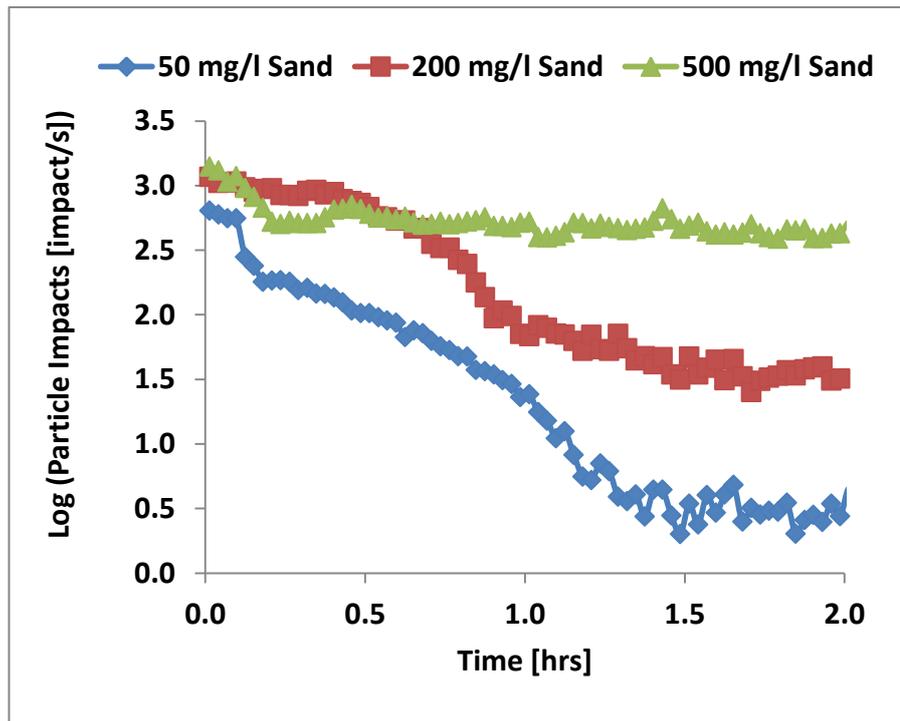
Figure 7.8: Variation of particle impacts with time for different sand concentrations for 7 m/s all at 90° impingement angle and 50°C temperature in tap-water saturated with N$_2$ (pH ≈ 7.0).
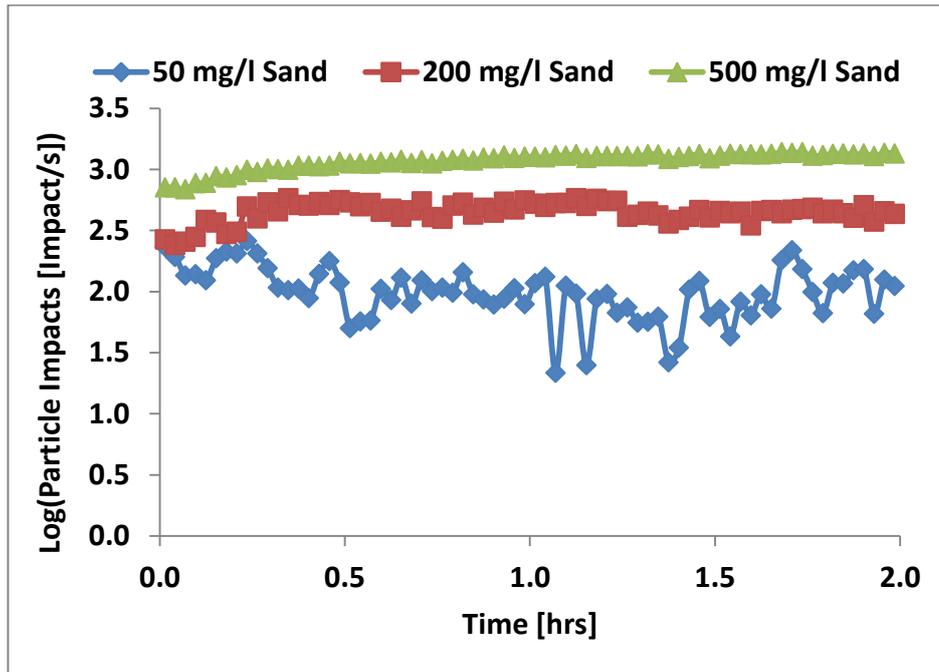
Figure 7.9: Variation of particle impacts with time for different sand concentrations for 10 m/s all at 90° impingement angle and 50°C temperature in tap-water saturated with N_2 (pH ≈ 7.0).
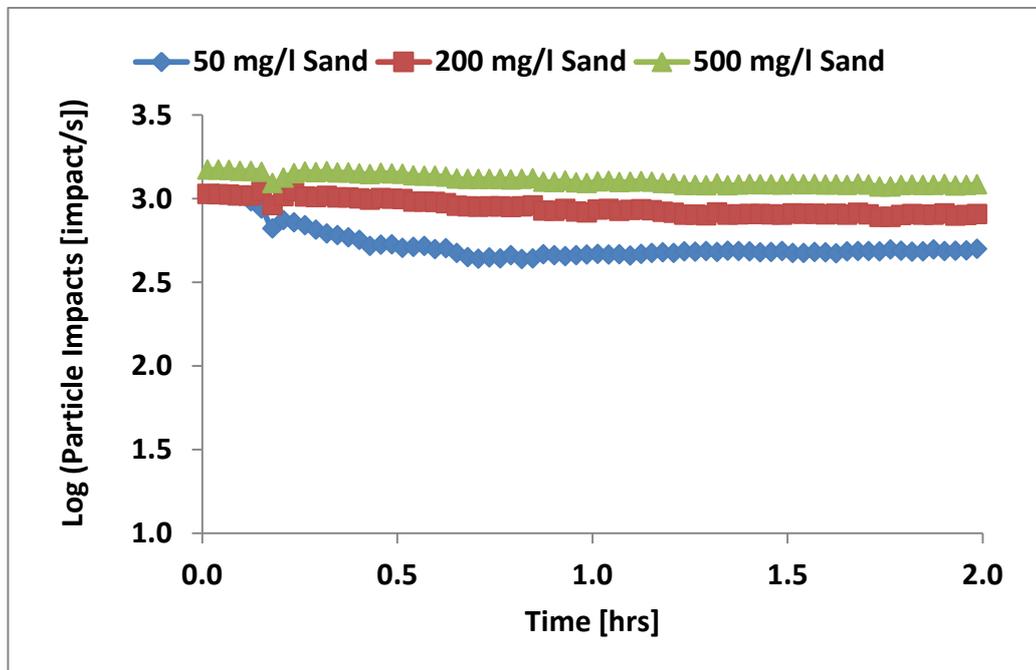
Figure 7.10: Variation of particle impacts with time for different sand concentrations for 15 m/s all at 90° impingement angle and 50°C temperature in tap-water saturated with N_2 (pH ≈ 7.0).
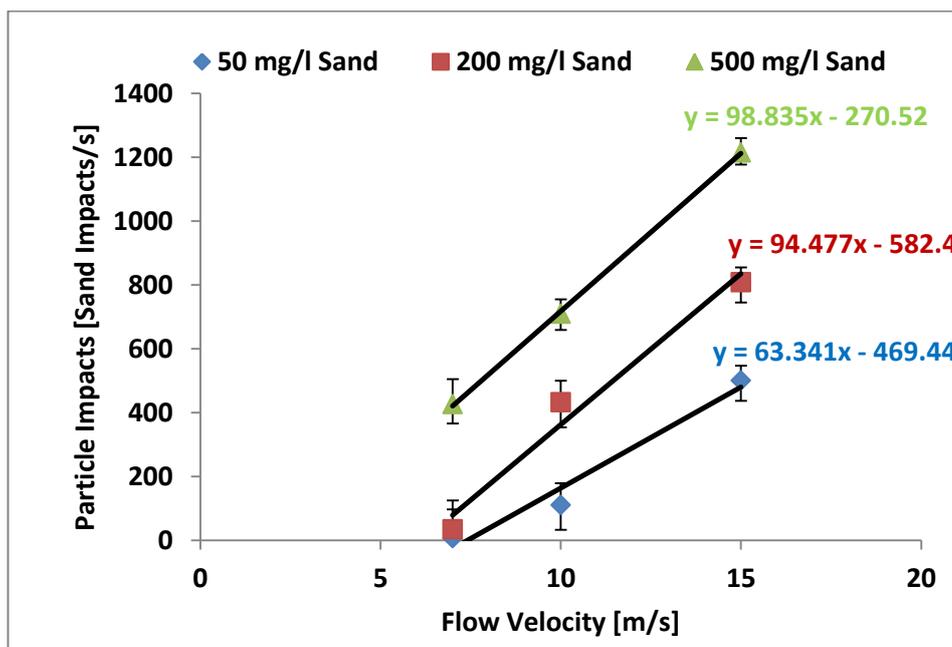
Figure 7.11: Variation of particle impacts with time for different sand concentrations and flow velocities at 90° impingement angle and 50°C temperature with tap-water saturated with N_2 (pH ≈ 7.0).

7.3.3 Particle Impacts Comparison with Theoretical Prediction

The theoretical prediction was estimated from a volumetric flow rate calculation with the assumption that all sand particles exiting the nozzle hit the target and that the sand particles are spherical rigid bodies with mean diameter of 250 µm and density of 2.56 g/cm^3. This assumption is consistent with the study by Clark [104] who suggested that at lower viscosity (i.e. viscosity of water, 0.66 cc at 40°C) and large particles sizes (212-250 µm), the impact efficiency approaches unity meaning that almost all the particles lying in the path of the erosion specimen impacted with it. He maintained that at high viscosities, relatively few particles will collide with the specimen, that a liquid of high viscosity will exert greater drag force on a particle than a liquid of low viscosity and that greater effect is observed on smaller particles of 75 µm diameter. In this study, the viscosity of the tap water is considered low at 50°C with sand particle size distribution (212 to 300 µm), it is expected that fluid viscosity effect will be negligible, thus allowing all the sand particles to hit the sample because the jet is directed towards the sample.

Other parameters used in the theoretical calculation using sand mean diameter, 250 µm and density, 2.56 g/cm^3 are:

Nozzle area $[A(m^2) = \pi r_{nozzle}^2]$, volumetric flow rate $[v(m^3/s) = A. v_{flow}]$, mass of sand per second $[M(mg/s) = \dot{v}. \text{sand loading}(mg/m^3)]$, number of particles per second (particle flux = mass of sand per second, M/mass of one particle, m) where, $[m =$ volume of sand x density of sand $= \frac{4}{3}\pi r_{sand}^3$ x ρ_{sand}].

The results of the comparison between the measured particle impacts and theoretical prediction are shown in Figures 7.13, 7.14 and 7.15 for 7, 10 and 15 m/s respectively. The box plot is used to show the nature of the particle impact data scattering (for the entire duration of each test) in a data set of average of three repeats for the purpose of comparison with theoretical predictions. Illustration of the box plot parameters is shown in Figure 7.12a where the first quartile (Q1) is the middle number between the minimum number and the median (second quartile, Q2), the third quartile (Q3) is the middle value between the median and the maximum value and the inter-quartile range (Q3-Q1) is the mid-spread. Comparing the box plot with a normal distribution data set in Figure 7.12b may be a useful tool for understanding the box plot where σ is the standard deviation.
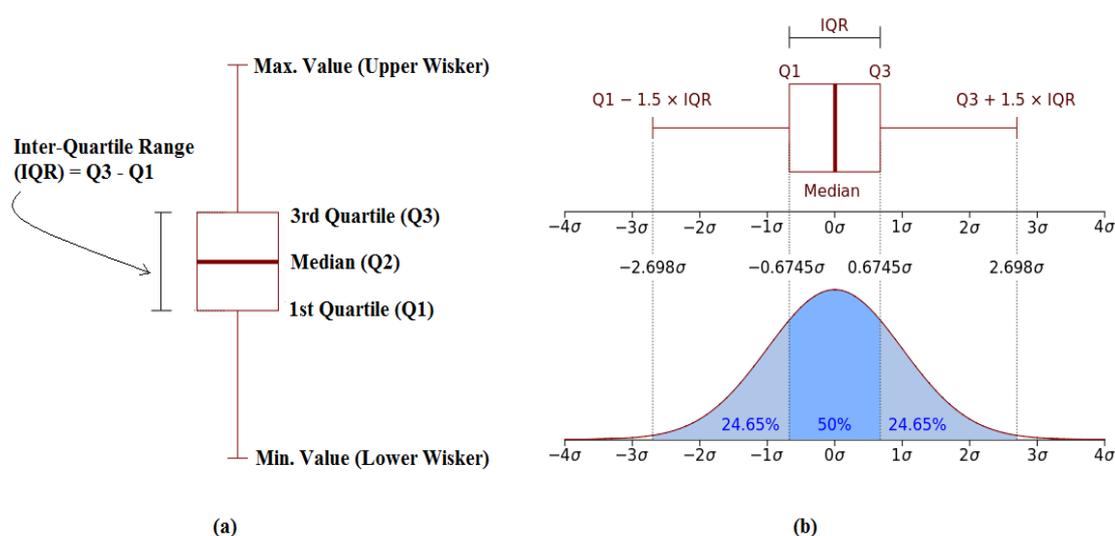
Figure 7.12: Illustration of box plot parameters.
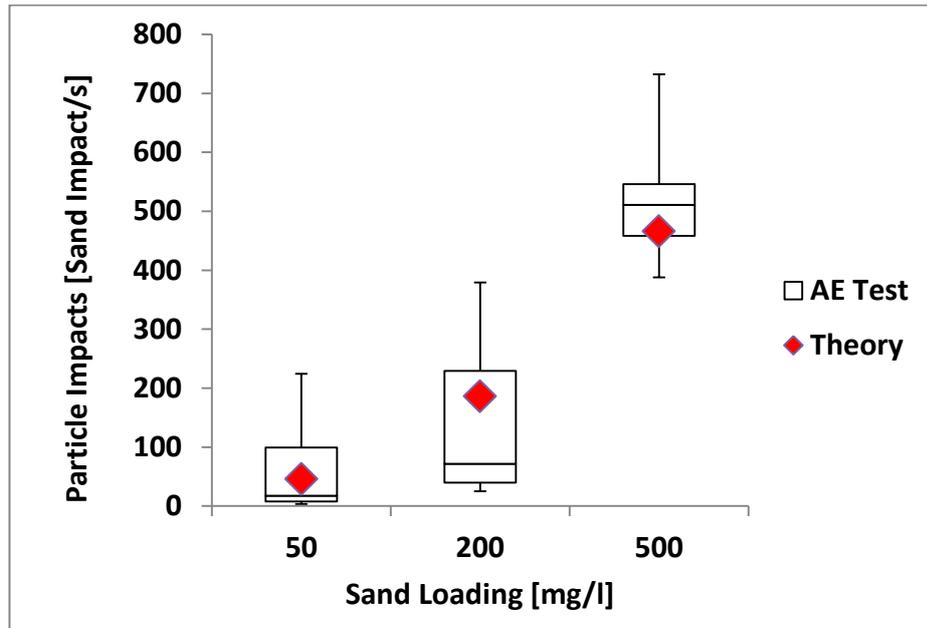
Figure 7.13: Comparison of measured particle impacts with theory for 7 m/s flow velocity.
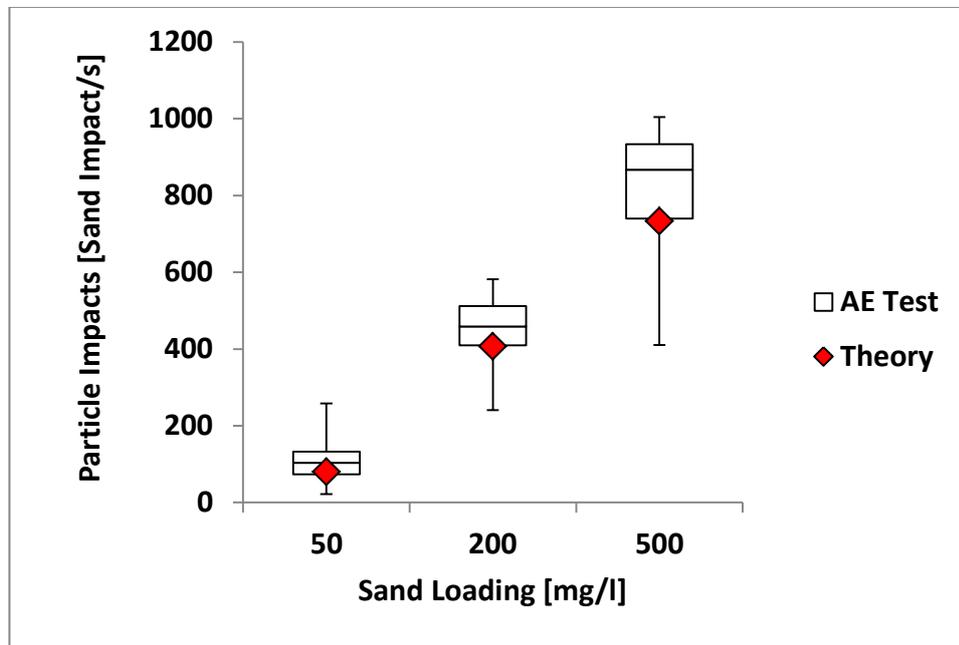
Figure 7.14: Comparison of measured particle impacts with theory for 10 m/s flow velocity.
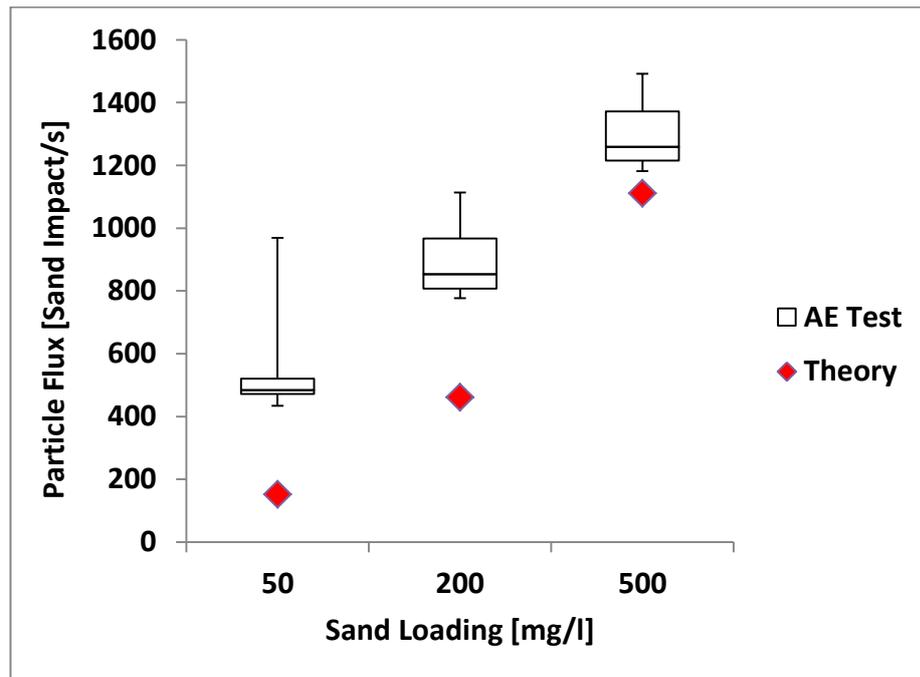
Figure 7.15: Comparison of measured particle impacts with theory for 15 m/s flow velocity.

7.4 Discussion for Particle Impact

7.4.1 AE Event Count Rate

It can be seen from the results (Figures 7.4 to 7.6) that the AE event count rate is dependent on sand concentration and flow velocity as it increases with increase in both parameters. The dependence is stronger from lower to higher values of these parameters which confirm the sensitivity of the AE set-up to detect changes in sand impact energy and sand concentrations.

For all the flow velocities, it is seen that even when no sand is present there are some AE events per second. These events are zero level noise which are associated with noise created by fluid flow. The summary of the AE event results in Figure 7.7 showed a good correlation between the AE events per second and the flow velocity with and without sand. A linear relationship is proposed between the AE events and flow velocity. Though, the linear correlation is not accurately proven by the data as non-

linear correlation could be fitted to Figure 7.7 but at this stage the linear relationship is considered the simplest of the data.

The scattering nature of the events is expected and may arise from different sources during the test. One source is the shape of the impact scars, which are certainly not uniform as shown in the SEM image in Figures 6.19 to 6.21. This arises because each impact occurs on an already microscopically rough surface which was either originally polished or pre-impacted surface. Succinctly put, the events increase with increase in flow velocity and sand loading. At low flow velocity (7 m/s), the sand concentration influence on the AE is significantly noticed after the 50 mg/L sand loading is exceeded and the AE increases rapidly with increase in sand concentration. This effect is much more significant at 10 and 15 m/s flow velocities, signifying the influence of impact energy of the sand particles on AE release.

7.4.2 Particle Impact Determination

Applying the subtraction technique on the measured AE events gave a linear relationship between the sand impacts per second and flow velocity for all the sand loading investigated using average values at the steady state region as shown in Figure 7.11. The experimental data (in Figures 7.8 to 7.10) revealed that sand particle impacts appear to be high at the start of the test and decrease to a steady state. This behaviour is significant at low flow velocity (7 m/s) where it was observed that for 50 mg/L sand loading; the impacts per second can be as high as 640 at the start of the experiment and can decrease after one hour to a value between 35 to 40, and as low as 7 at the end of the experiment.

This variation in the measured particle impacts with time may be the reason why some of the previous studies [104, 204, 205] on particle impact determination did not last for more than 60 seconds. Though Burstein and Sasaki [130] have argued that the scattered nature of the AE data should be expected since more intense AE is expected to arise from a more intense impact. The AE is lower at more oblique impact angles,

because the AE energy transferred to the surface and recorded by the sensor depends on the component of the elastic wave resolved perpendicular to the surface. It follows that the recorded AE due to particle impact may vary since the particles impact on the surface at different impact angles. In addition, the explanation for this phenomenon may be because of the settling down of the sand at the corners of the reservoir due to the low energy which does not enhance proper mixing and recirculation of the sand in the reservoir. To give a clearer picture of the impacts, the data scattering behaviour (for each test duration) is represented in box plots (Figure 7.13 to 7.15) for the purpose of comparison with the theoretical predictions.

Using the average values at the region of steady state, the sand impacts per second at 7 m/s flow with 50, 200, 500 mg/L sand were estimated as 7.0, 35.0, and 426.0 respectively, 10 m/s flow with 50, 200, 500 mg/L sand loading, were 110.0, 432.0, and 709.0 respectively, and at 15 m/s flow with 50, 200, 500 mg/L sand loading, the impacts per second were 501.0, 808.0, and 1215.0 respectively.

In the literature, Oltra *et al.* [186] reported an estimate of 3×10^3 impacts per second at 9 m/s flow velocity for high abrasion glass beads in order of g/L (1000 mg/L) concentrations. Lynn *et al.* [205] proposed 2.9×10^4 impacts per mm^2 per minute for a 250 μm diameter SiC particle with loading of 1.2 wt% (12,000 mg/L) at 18.7 m/s flow velocity. Rajahram *et al.* [206] suggested between 1.7×10^5 and 1×10^6 impacts per second for sand concentration between 1 wt.% (10,000 mg/L) and 5 wt.% (50,000 mg/L) respectively at 9 m/s flow velocity.

These results are all expected due to the high particle loading involved. Since low sand loading and flow velocity similar to this work was not located in the literature for comparison, the accuracy of the results was verified by comparing the results with theoretical prediction from volumetric flow rate calculation of the sand exiting the nozzle per second. The box plots (Figure 7.13 to 7.15) were used in the comparison as discussed in the next paragraphs.

7.4.3 Measured Particle Impact Comparison with Theoretical Prediction

The comparison of the measured sand particle impacts per second with the theoretical prediction (Figure 7.13 to 7.15) revealed a good agreement for 7 and 10 m/s flow velocities in all the sand concentrations investigated whilst at 15 m/s flow, the AE technique gave higher values than the theoretical predictions.

The box plots indicate that the theoretical predictions at 7 and 10 m/s flow velocities fall within the inter quartile range (25% above the mean and 25% below the mean values) of the measured data, whilst at high flow velocity (15 m/s), the AE technique predicts higher values of impacts per second than theoretical prediction. This signifies that the impact energy of the impacting particles is actually responsible for the generation of AE signals. It is possible that at high flow velocity, signals due to rebounded sand particles which are expected to be high at high flow velocity were equally detected which led to higher values of measured sand impacts at 15 m/s.

Another possible reason for the large deviation at high flow velocities could be particle-particle interactions [104] at the surface of the sample which can lead to pseudo impacts that may also be detected and recorded. Also, the much shorter interval between the particle impacts which may cause excessive overlap of the impact acoustic signals can be responsible for the large error obtained at high flow velocity and sand loading.

7.5 Impact Energy Investigation

In this aspect of the study, the average impact energy per particle for each flow velocity was calculated and used to determine the overall impact energy per second of the impacting sand particles (predicted from theory) for each sand concentration. This overall impact energy per second for each flow velocity and sand concentration was then correlated with the measured acoustic emission (AE) energy per second associated the measured number of sand impacts per second for each flow velocity

and sand concentration. Computational Fluid Dynamics (CFD) was used in conjunction with particle tracking to model the submerged impinging jet system and predict the impact velocity and impact angle distribution on the surface of the sample. Data was used to predict the impact energy which was then correlated with the measured AE energy and material loss from gravimetric analysis.

FLUENT was chosen as the CFD Program to characterise the submerged impinging jet (SIJ) system. This software uses the finite volume method with the second order upwind interpolation scheme selected for this particular approach. The k-ε model [110, 207, 208] was applied to resolve turbulence with standard wall functions used to represent near wall effects. A converged solution to the models was obtained after 20 minutes on a 3 GHz dual core desktop PC for all models.

7.5.1 Submerged Impinging Jet (SIJ) Model

The SIJ CFD modelling has been extensively performed by Gnanavelu [110] at the University of Leeds. The same approach is applied in this investigation in collaboration with Barker *et al.* [79, 207]. A detailed discussion of the geometry, mesh generation, selection of fluid properties, boundary conditions and turbulence model, as well as verification of computational mesh, domain size and particle tracking can be located in the investigation by Gnanavelu [110].

A review of the study is presented in the next paragraphs for clarity and proper understanding.

7.5.1.1 Geometry and Mesh Generation

The SIJ and specimen configuration simulated in this study are assumed to be axisymmetric about the centreline of the nozzle. A 2D model was used to model the impingement at 90°. Hence, the resulting flow domain on any particular plane along this centreline and perpendicular to the test surface is expected to be representative of the entire flow domain. Similar approach was adopted by Gnanavelu [110] in which the 2D,

incompressible, steady state model was used. Adopting this technique helped to minimise computing resources without compromising solution accuracy.

Figure 7.16 indicates how the physical domain has been represented using a computational domain. Fluid exiting the nozzle undergoes sudden changes in direction once it comes into contact with the sample surface. It is advisable that the majority of computational cells should be used to resolve this region in particular, especially as the wall shear stress of the sample is the main parameter of interest in this study.
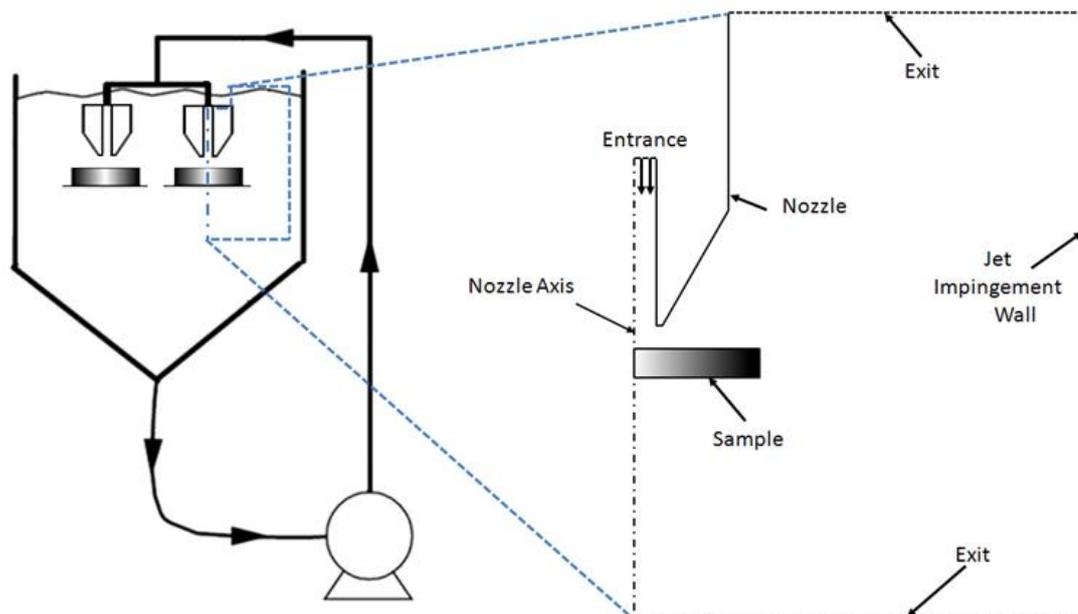
Figure 7.16: Schematic illustration of the physical domain (left) and computational domain (right) of the submerged impinging jet.

The computational mesh generated is shown in Figure 7.17 and consists of approximately 130,000 triangular elements mapping the whole domain, with the mesh becoming finer around the specimen surface. The computational mesh was refined to ensure that the boundary layer was adequately resolved and grid independence obtained.
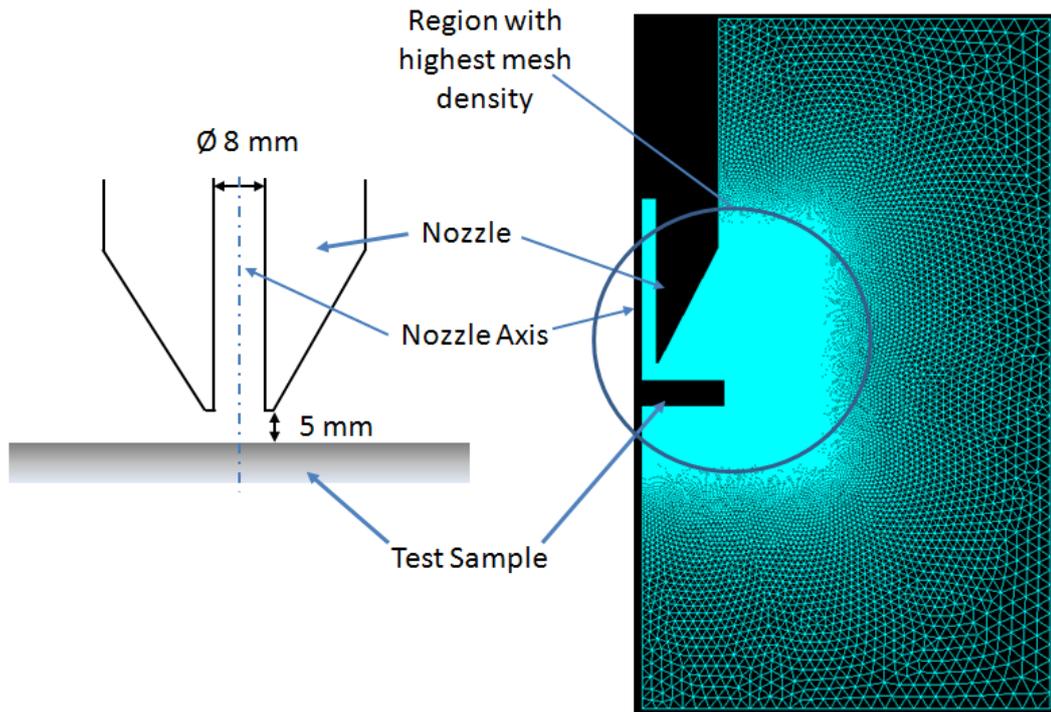
Figure 7.17: Illustration of actual geometry (left) and flow domain simplified to 2D using Gambit (right) (domain size is 120 mm x 220 mm and mesh consists of approximately 130,000 elements).

7.5.1.2 Boundary Conditions and Fluid Properties

The implemented boundary conditions are shown in Figure 7.18 for a viscous, turbulent, incompressible and isothermal fluid. All solid walls in the system are defined, and by definition the velocities are zero for the walls bounding the fluid domain. For the inflow condition, the mean fluid jet velocity at which the fluid enters the domain is specified. The length of the inlet was adjusted to at least 10 times the internal diameter of the jet to ensure the flow became fully developed within the nozzle [110]. The outflow boundaries are defined in Figure 7.18. Only one outlet condition is specified with atmospheric pressure being the property imposed in this case. The symmetry condition was used along the nozzle axis to reduce computational time. The final condition to assign to the system was to associate the interior of the computational domain as being representative of the fluid solution within the reservoir.

The values of the density of the salt water solution and dynamic viscosity at 50 $^{\circ}$C were 1019 kg/m^3 and 6 x 10^{-4} Pa.s for all simulations.
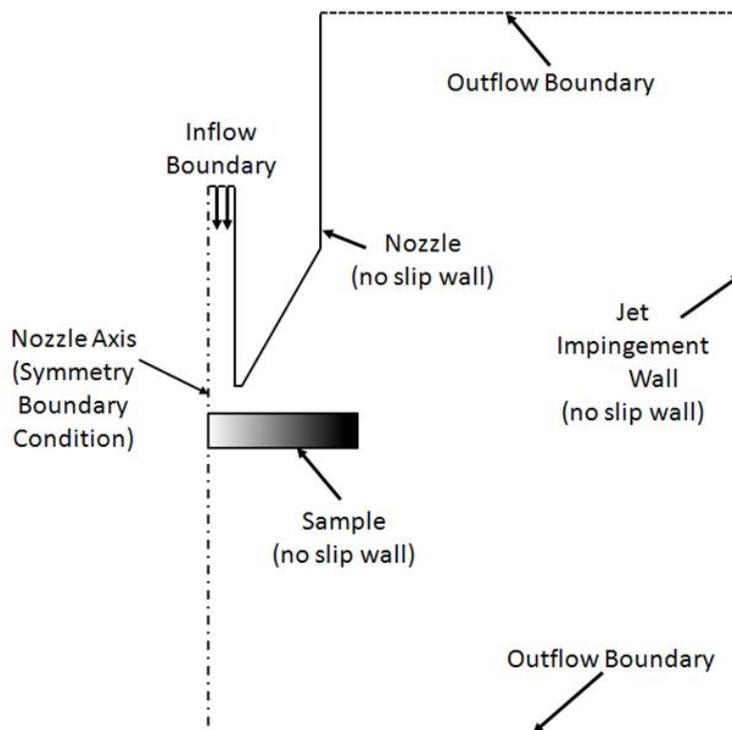
Figure 7.18: The geometry of the SIJ with boundary conditions and computational domain developed using Gambit.

7.5.1.3 Turbulence Effects and Convergence Criteria

The k-ε model [208] was chosen to numerically simulate the effects of turbulence within the submerged impinging jet. All numerical simulations were solved using the second order upwind interpolation scheme. The SIMPLE algorithm [208] was also employed to guarantee a cross linkage between the pressure and velocity, which predominantly accounts for the mass conservation within the flow domain. All numerical simulations were converged when the residuals of all flow parameters fell below 1 x 10^{-5}.

7.5.2 Prediction of Particle Motion and Impact Condition

7.5.2.1 Particle Phase Modelling

Solid particle tracking equations are either solved discretely over the already solved flow field or coupled together with the flow equations and solved together. This depends upon the extent to which the physical presence of particles affects the local

flow regime. Two basic approaches are commonly used to predict particulate motion in fluid flows: Eulerian and Lagrangian [110].

Eulerian models are generally referred to as continuum models because the particles are treated as an additional continuous phase within the main fluid phase. Along with the governing flow equations, an extra set of equations are solved for the particulate phase and coupling between the two phases takes place through inter-phase transfer terms. This approach is ideally suited to model slurries with moderate to high concentrations where particle motion can possibly influence fluid flow. Since particulate phase equations are solved along with the main phase numerical iterations, computational resources used can be very high, which is the main drawback of this approach. For a particular simulation, particle properties are fixed and hence for particle parameter studies the simulations have to be re-run.

In the Lagrangian formulation, the particles are assumed to be discrete. In this approach continuum fluid equations are solved for the fluid phase after which Newtonian equations of motion are solved over the already obtained solution to determine the trajectories of individual particles (or groups of particles). Particles of different size and densities can be studied for a given flow field without any re-runs. This approach is ideally suited for studying lightly loaded particulate flows where the presence of particles and its subsequent motion has no effect on the fluid phase. Using the Lagrangian method can reduce computational costs but determining particle impact data can consume a lot of user time.

It is thus essential to determine the appropriate model to describe particle motion, which can be aided by calculation of particle loading and Stokes number. The particle mass loading is expressed as the ratio of particulate mass per unit volume of flow to fluid mass per unit volume of flow and is expressed as [110]:

$$\beta = \frac{r_p \rho_p}{r_f \rho_f} \qquad (7.4)$$

where r is the volume fraction, ρ is density and the subscripts p and f refer to particle and fluid phases respectively. Significant two way particle fluid coupling is generally expected for particle mass loadings greater than 0.2 [110]. The particle mass loading for this investigation is 0.01 and hence it can be assumed that the effect of particles on flow regime is negligible and thus the Lagrangian approach was chosen to determine particle motion tracks.

7.5.2.2 Particle Tracking Equations

Based on Newton's law of motion, Clift *et al.* [209] proposed the governing of particle motion given as:

$$m_p \frac{dV_P}{dt} = F_d + F_p + F_b + F_a \tag{7.5}$$

where m_p is the mass of a particle, V_P is local particle velocity and t denotes time. The terms on the right hand side are described below.

Drag force (F_d): The force acting on the surface of the body due to the viscous effects of the fluid medium and this force accounts to the cohesion between a particle and fluid streamlines. The drag force is given by [209]:

$$F_d = C_d \frac{\pi d_p^2}{8} \rho_f \left(V_f - V_p\right)\left|V_f - V_p\right| \tag{7.6}$$

V_f and V_P are local fluid and particle velocities respectively, where C_d is the drag force coefficient for a spherical particle defined by:

$$C_d = \frac{24}{Re_p}\left(1 + 0.15Re_p^{0.687}\right) \tag{7.7}$$

where Re_p is the relative particle Reynolds number expressed as:

$$Re_p = \frac{\rho_f}{\eta}\left|V_f - V_P\right|d_P \tag{7.8}$$

where η and ρ_f are the dynamic viscosity and density of fluid respectively, d_p and ρ_p are particle diameter and density respectively.

Pressure gradient force (F_p): The effect of the local pressure gradient gives rise to a force in the direction of the pressure gradient and is given as [209]:

$$F_p = \frac{1}{4}\pi d_p^3 \nabla . P \qquad (7.9)$$

where $\nabla . P$ is the divergence of pressure and is defined similar to $\nabla . u$. It is assumed that the pressure gradient is constant over the volume of the particle.

Buoyancy force (F_b): This is the upward force on the particle due to fluid pressure opposing the weight of the particle and is expressed as [209]:

$$F_b = \frac{1}{6}\pi d_p^3 \left(\rho_p - \rho_f\right)g \qquad (7.10)$$

where, g stands for acceleration due to gravity.

Virtual force (F_a): This is also known as added mass. An accelerating or decelerating particle in a fluid medium displaces some volume of the surrounding fluid in order to move. The analogy here is that the added mass is the force the surrounding fluid will gain at the expense of the work done on it by a particle and it can be a major factor if the fluid medium is denser than the particle. This force is expressed as [209]:

$$F_a = -\frac{1}{12}\pi d_p^3 \rho_p \frac{dV_P}{dt} \qquad (7.11)$$

It is important to note that local particle (V_p) and fluid (V_f) velocities are required to solve the force balance Equation (7.5). Particles are released into the fluid flow with zero velocities and the local fluid velocity at the release point is given by CFD simulations. These data put into Equations (7.5 to 7.11), would provide particle velocity until the next fluid velocity data point, where new values for particle velocities will be calculated based on local data. Equations (7.5 to 7.11) can be resolved into horizontal and vertical components and thus tracing the direction of motion.

7.5.2.3 Wall Interactions

In a flow field, the nature and type of particle impacts occurring within the domain can be modelled using Stokes number, (St) which is the ratio of particle response time (τ_p) to a time characteristic of the fluid motion (τ_f). This is expressed as [210]:

$$St = \frac{\tau_p}{\tau_f} = \frac{\rho_p d_p^2 V_f}{18\eta L_f} \qquad (7.12)$$

where d_p and ρ_p are particle diameter and density respectively, η is the dynamic viscosity of the fluid, V_f is the characteristic fluid velocity and L_f is the length scales. It is worthy to note that for $St > 2.0$, particulate flows are highly inertia and in the presence of an obstruction would be dominated by particle-wall interactions. For $St < 2.5$, minimal particle wall interactions can be expected and generally particles are tightly coupled to the fluid due to viscous drag [110].

The St based on nozzle-sample separation of 5 mm and mean particle size (250 µm) was calculated to be approximately 6.3, 9.0 and 13.5 for 7, 10 15 m/s flow velocities respectively, indicating the dominance of particle inertia over viscous drag and hence high numbers of impacts are to be expected and hence wall interactions should be treated accordingly.

Particles are assumed to transfer the majority of their kinetic energy on to the impact surface prior to rebound. The post collision velocity depends on the particle properties, target material and the fluid phase and is provided by restitution coefficient [110] for that particular condition. Grant and Tabakoff [211] reported that restitution relations improved prediction capability especially when a particular particle undergoes several impacts, which can be significant at low angles of impact. In the SIJ flow field, particles can impact at a wide range of angles [110]. Restitution factors vary locally depending upon local impingement angles, and for the case of SIJ, the effect of secondary impacts can vary locally [107, 208] and needs to be captured accurately.

In FLUENT, particles are presumed to be a point in the flow field. Although physical values for density and diameter are specified for calculations, the actual physical presence of a particle is not considered. This leads to impacts at the wall which should not occur in reality. Implying particle motion is determined all the way to the horizontal surface (Y= 0) whereas in reality rebound occurs at particle radius as illustrated in Figure 7.19. However, this Figure is at variance with the Legrangian simulation [210] which states that there exist a particle rebound distance or layer which can be determined by finding the location where the normal velocity component of the reflected particle goes to zero.
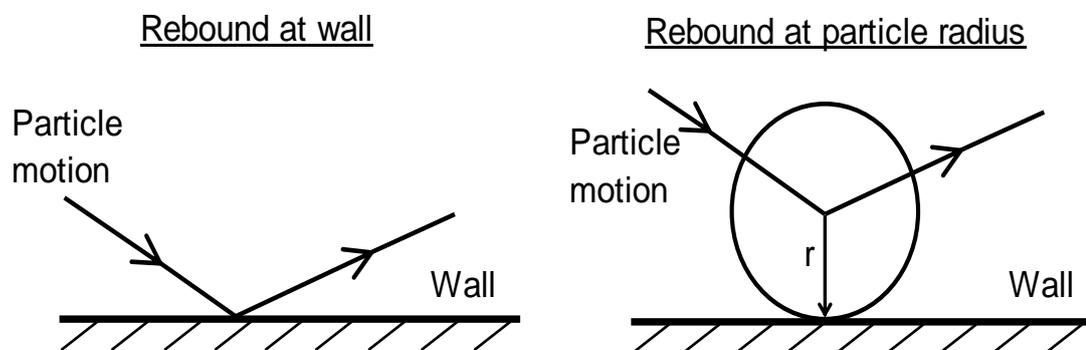
Figure 7.19: Illustration of particle rebound at wall and rebound at particle radius, with 'r' representing particle radius which was set to125 μm [110].

Non-physical impacts at the wall can result in erroneous wear predictions. Rebounding at particle radius increased predicted local impact velocities by nearly 8% in comparison to a particle treated as a point [106]. Thus impact data was manually determined at y = 0.125 mm in all the analysis. Due to this only the initial impact can be considered due to non-physical impacts (thus nullifying the use of a restitution factor) and secondary impacts are not considered, although it was pointed out that secondary impacts can have a significant effect [106, 212, 213].

The particle impact counting analysis using AE which is discussed in section 7.4.3 shows that the secondary impacts are important and can have significant effect because signals due to rebounded sand particles which are expected to be high at high

flow velocity were equally detected which led to higher values of measured sand impact at 15 m/s than theoretical prediction.

7.5.2.4 Turbulent Interactions on Particle Motion

The flow field is assumed to be steady, although in reality local velocities for a turbulent flow vary with time and these variations can be small [110]. At certain conditions these small variations (along with the mean flow) can also influence particle motion and the effect of which can be entirely random. To capture this, empirical models are suggested which considers the effect of turbulence on particle dispersion. Chen *et al.* [107] studied the erosion behaviour using a CFD based method in plugged tee-joints and observed that predictions were 15% greater than experimental results when turbulence dispersion was neglected. Zhang *et al.* [214] proposed that including turbulence dispersion affected small sized particles (<100 μm), but had negligible influence on larger sized particles and attributed this to high particle inertia. Considering the average size of particles used in our case (250μm), turbulence dispersion was not considered.

7.5.2.5 Initial Conditions of Particles

In FLUENT the particle is released with zero velocity into the impinging jet and the subsequent motion is traced. The distance between the release point and the sample surface should be adequate enough for particles to gain momentum and reach a dynamic state similar to its practical counterpart during test. Improper release positions can lead to impact conditions different from actual conditions and resulting in poor solution accuracy. Hence, a systematic study was performed by releasing particles with zero velocity within the nozzle stream at various distances from the surface and particle velocities gradients close to the surface were monitored. Injecting particles into fluid at 5 mm from the surface with zero velocity resulted in impacts occurring at nearly 2 m/s. Releasing particles further away from the surface resulted in impacts at relatively lower velocities. It was observed that particle velocity gradient when released at 20 mm

above the surface was similar to the case when released at a position 40 mm from the surface. Therefore, all particles were released into the jet stream at a position 40 mm above the surface. It must be noted that particle rebound in this study is assumed to occur at 0.125 mm above the surface. Although, particle motion is traced to the surface to study the sensitivity of predicted particle motion to release position.

7.5.2.6 Summary of All Assumptions

The following sections provide a summary of all the assumptions made during particle tracking and impact data calculations and is listed below:

- Particle shape was assumed to be spherical in order to develop a simple but robust method.

- Particle size was set to 250 μm which was considered to be a good representation of the average size of the sand distribution (212-300 μm) used for testing.

- Particle-particle interactions were considered negligible, which has been shown to be reasonable assumption while simulating erosion wear at low particle flux [215].

- Particles were released into the flow at zero velocities and 40 mm from the surface.

- Rebound was assumed to occur at particle radius, contrary to the procedure suggested in FLUENT which nullifies the use of restitution factors. Thus, secondary impacts of a particle were ignored.

- The effect of local flow fluctuations due to turbulence on particle motion were assumed to be negligible since particles were greater than 100 μm [214].

- Particle density was set to 2650 kg/m^3 and was similar to the sand particles used during experimental testing.

7.5.2.7 Impact Data Calculation Procedure

The CFD simulations were conducted on the geometry with boundary conditions imposed as specified in Figure 7.18 with conditions and assumptions made above. Lagrangian particle trajectory equations were then solved on the obtained flow solution using the assumptions to determine impact data (local impact velocity, angle and rate) as a function of radial position on the surface of the specimen.

Particle impact angles are defined as the angle subtended by the tangent of particle path prior to impact to the horizontal and local particle impact velocity is defined as the relative magnitude of particle velocities at this point. These data were recorded for every impact along the surface.

7.5.3 Results for Impact Energy Investigation

The results of the particle impact angle and velocity variation along the radial distance of the test specimen are illustrated in Figure 7.20.
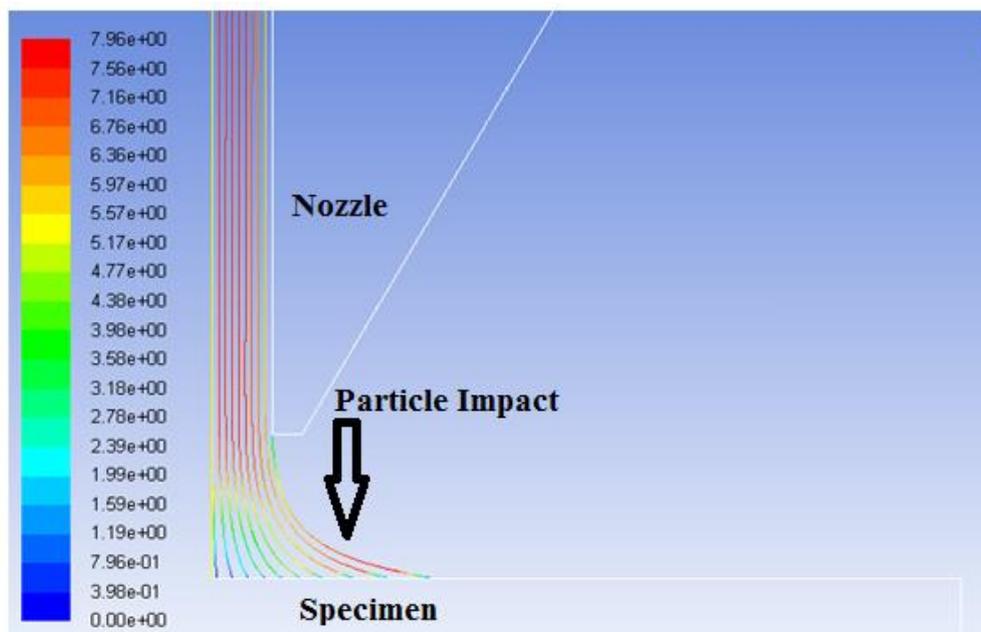
Figure 7.20: Illustration of sand particle motion within the impingement jet and subsequent impact on the specimen surface as predicted by CFD.

Simulations for 7, 10 and 15 m/s were run and their results indicate a decrease in impact angle and increase in impact velocity along the radial distance as illustrated in Figures 7.21 and 7.22 respectively. The impact angle varied between 85 and 10° from the stagnation point to a radial distance of 8 mm on the wall jet region for all the impact velocities studied. The impact velocity varied between 2.3 and 4.5 m/s; 3.2 and 6.9 m/s and 4.5 and 11.9 m/s for 7, 10 and 15 m/s flow velocities respectively.
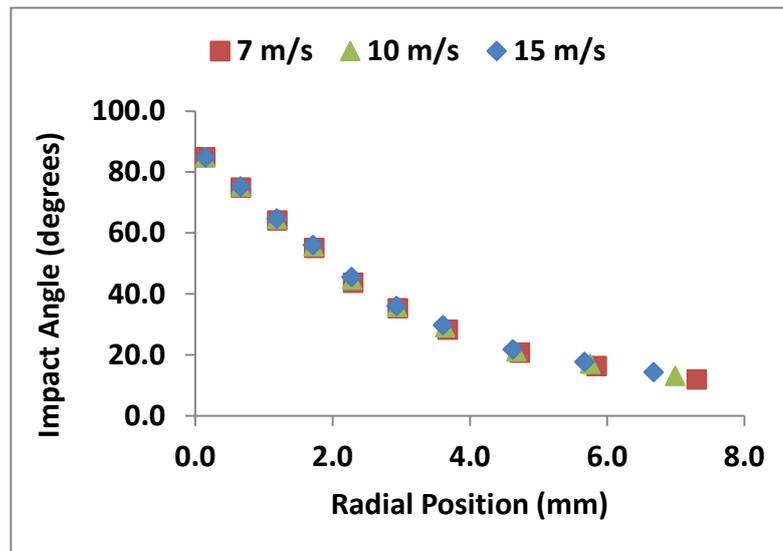
Figure 7.21: Predicted variation of particle impact angle with radial distance.
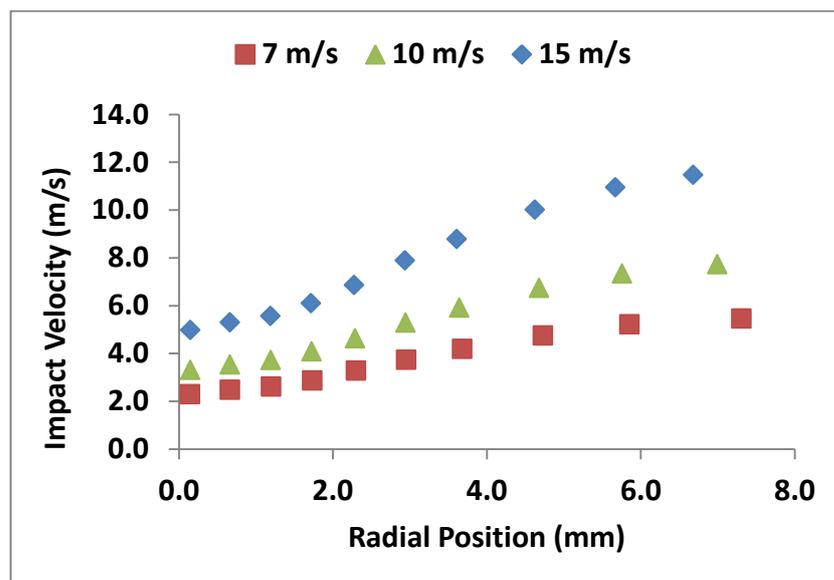
Figure 7.22: Predicted variation of particle impact velocity with radial distance.

The predicted impact velocity was used to calculate the corresponding impact energy of the particle along the radial distance as shown in Figure 7.23 for the flow velocities studies.
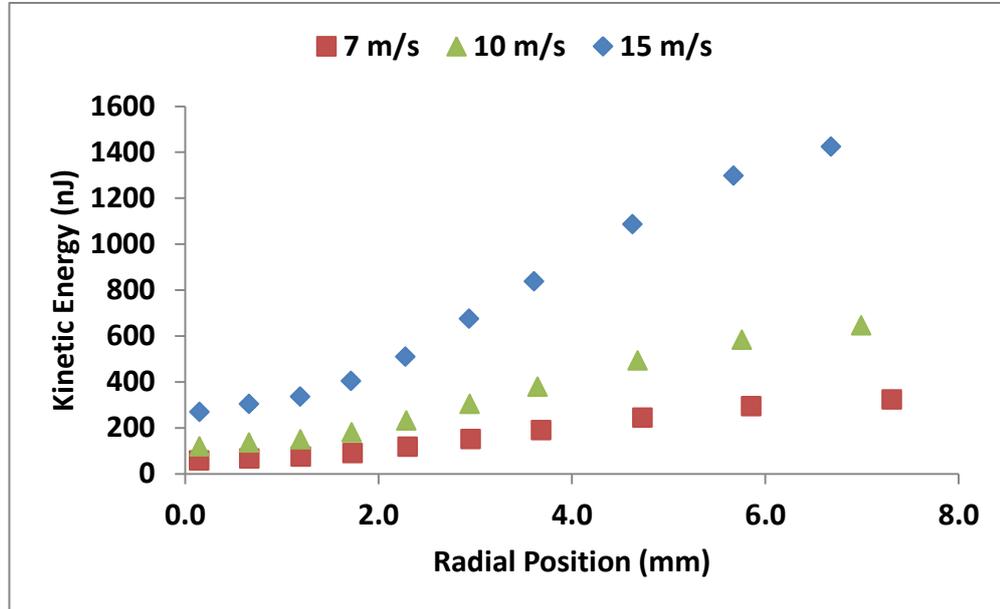
Figure 7.23: Predicted variation of particle impact energy with radial distance.

From Figure 7.23, it can be deduced that the impact energy of each particle is in the order of nano joules which increases along the radial distance up-to 8 mm with 7 m/s having lowest impact energy and 15 m/s having highest impact energy as expected. The average impact energy per particle for each flow velocity was calculated and used to determine the overall impact energy per second of the impacting sand particles (predicted from theory) for each sand concentration. This overall impact energy per second for each flow velocity and sand concentration was then correlated with the measured acoustic emission energy per second associated the measured number of sand impacts per second for each flow velocity and sand concentration.

The measured acoustic emission energy is correlated with the impact energy to ascertain the relationship between the acoustic emission energy and the impact energy. The results of the correlation for all the sand concentrations investigated are shown in Figure 7.24.
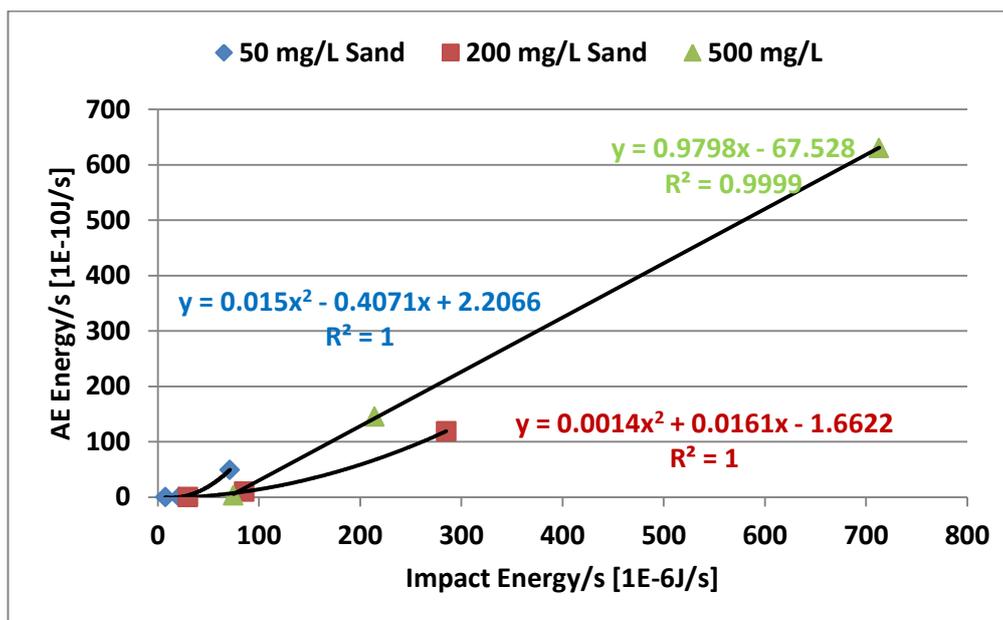
Figure 7.24: Relationship between measured AE energy and impact energy predicted from theory for 50, 200, 500 mg/L sand loading multiple impacts.

7.5.4 Discussion for Impact Energy Investigation

The calculated average impact energy per particle (250 μm mean diameter spherical sand) for 7, 10, and 15 m/s flow velocities are 160, 320 and 713 nJ respectively which are in agreement with the previous work of Sasaki and Burstein [216] who determined the threshold impact energy required to depassivate stainless steel surface to be of the order of 30 nJ per spherical particle of diameter (150-180 μm) with flow velocity of 1.71-3.5 m/s.

To determine the total impact energy of the particles per second, the average impact energy per particle was multiplied by total number of sand impacts per second from theoretical prediction for each flow velocity and sand loading. At 7 m/s flow velocity for example, a total of 7, 29 and 74 μJ/s for 50, 200 and 500 mg/L sand concentrations respectively were obtained. The values of the impact energies (in order of 10^{-6} J/s) are consistent with the previous work of Lynn *et al.* [205] who proposed a mean impact energy of 2.02 x 10^{-6} J for particles with mean diameter of 250 μm impacting on P100 steel sample at 18.7 m/s flow velocity. These impact energies were correlated with the corresponding measured acoustic emission energies of the impacts per second which

were in order of 10^{-10} J/s as shown in Figure 7.24 for the flow velocities and sand concentrations studied. From the Figure, it is evident that the AE energy is proportional to the kinetic energy (KE) within the entire range of the flow velocities and sand concentration investigated which is consistent with the single impact study correlation of AE energy with KE using glass beads discussed in Chapter 6. A linear relationship is observed for high sand loading of 500 mg/L whilst polynomial relationship of order two is observed for lower sand concentrations of 50 and 200 mg/L. As the particle energy is lowered either by lowering the impact velocity or sand loading, there is a corresponding reduction in AE energy which signifies that the particle impacts generated the AE signals that were measured. Furthermore, the AE event count rate and impact energy were correlated with the erosion rate expressed as mass loss per hour as described in the next section.

7.6 Erosion Rate Estimation

The erosion rate expressed as mass loss per hour was also determined after each test and correlated with the AE event count rate for all the flow velocities and sand concentrations investigated on one hand (Figure 7.25) and impact energy on the other hand (Figure 7.26). In Figure 7.25, the mass loss increases with increase in AE event count rate in an exponential trend within the range of the flow velocities and sand concentrations studied whilst in Figure 7.26 the mass loss increases linearly with the impact energy.

At 7 m/s flow, the mass loss is very low and insignificant with the event counts per second being a few hundred for all the sand loadings studied. A significant mass loss is observed when the event counts per second approaches 10^3 and above, an indication that the AE set-up is very sensitive in detecting changes in the test condition that causes degradation of the X65 carbon steel material. A closer look at Figure 7.25 reveals that significant mass loss does not occur until the average AE count rate exceeds a certain critical value which can be referred to here as 'critical event count

rate' which is approximately 10^3 events per second for all the flow velocities and sand concentrations investigated. This critical event count rate can be also serve as a useful guide in monitoring and predicting erosion damage of X65 pipeline material in oil and gas production using the AE technique.
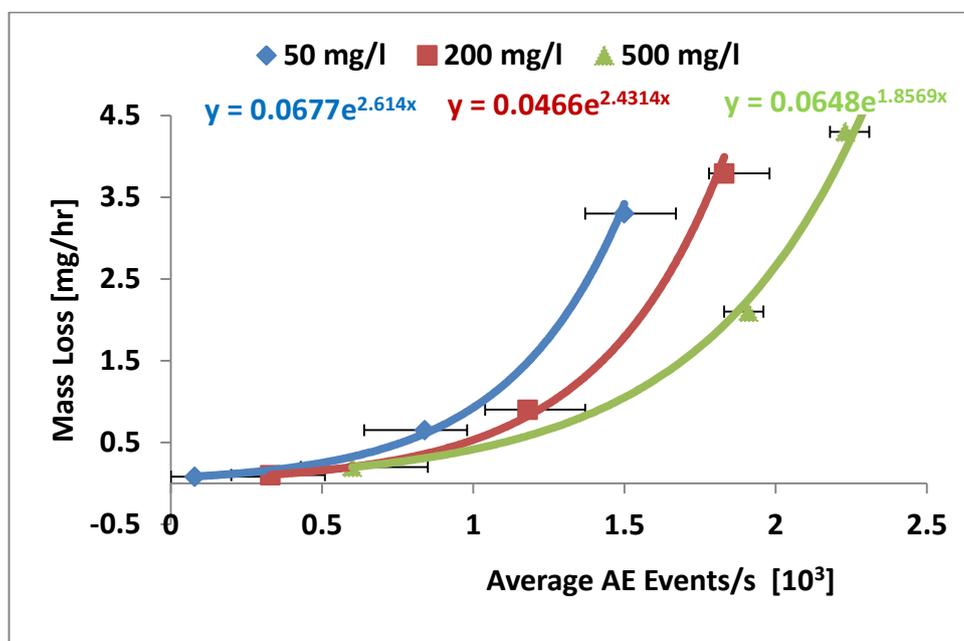
Figure 7.25: Relationship between mass loss and AE event count per second. Tests performed at 90° impingement angle and 50°C temperature in tap-water saturated with N_2 (pH ≈ 7.0).

In Figure 7.26, it is observed that particular impact energy can give rise to different mass losses. This is because particular impact energy can have different erosion efficiency (ratio of wear to particle loading) depending on the sand concentration meaning that specific impact energy can cause different degrees of damage on the materials depending on the sand concentration. This is due to the fact that the erosion efficiency decreases with increase in particle loading according to a power law of the particle loading in the slurry with an exponent of approximately 0.33, and above a loading of approximately 13%, the erosion efficiency becomes constant as a result of particle-particle interaction [115]. Another possible explanation for this phenomenon is that an increase in sand loading can lead to higher amount of rebounding particles at the surface, hence protecting the surface from incident particles. This also leads to

greater particle-particle interaction which can reduce the number of particles impacting the surface.
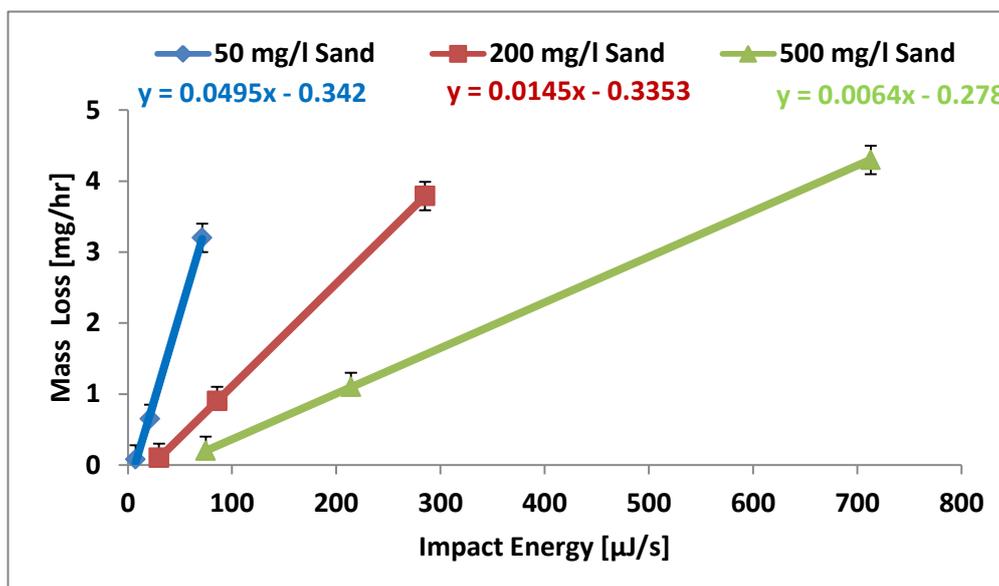
Figure 7.26: Relationship between mass loss and impact energy per second. Tests performed at 90° impingement angle and 50°C temperature with tap-water saturated with N_2 (pH ≈ 7.0).

7.7 Summary

Measured particle impact per second agreed well with impact predicted from theory for 7 and 10 m/s flow velocities whilst there is a deviation for 15 m/s flow velocities. These deviations were attributed to error due to rebounded particles that were equally detected with sand impacts on one hand and the overlapping of AE events that were difficult to separate in time for accurate counting on the other hand.

The impact energy per second (in the order of 10^{-6} J/s) correlated well with the measured AE energy per second (in the order of 10^{-10} J/s). The correlation reveals a linear relationship between for 500 mg/L sand and non-linear 50 and 200 mg/L sand for flow velocities investigated which indicates the dependence of the AE on the kinetic energy of the impacting particles. Mass loss increased with an increase in AE events and impact energy.

Chapter 8 Results and Discussion: Combined *In-Situ* AE and LPR Investigation of CO_2 Flow-Induced Corrosion and Erosion-Corrosion

8.1 Introduction

This chapter presents the aspect of the PhD study involving combined in-situ acoustic emission (AE) and linear polarisation resistance (LPR) measurement in a submerged impinging jet (SIJ) rig to investigate flow-induced corrosion and erosion-corrosion degradation of X65 pipeline materials in CO_2 saturated oilfield process brine at $50^{o}C$. The erosion aspect has been covered in chapters 6 and 7. In this investigation, the specimen's corrosion behaviour was assessed for 7, 10 and 15 m/s flow velocities without sand for flow-induced corrosion and with sand for erosion-corrosion. The AE signal count rate as well as the AE energy during each test was measured and analysed simultaneously with corrosion rate from LPR measurement. Average count rate was correlated with corrosion rate while cumulative counts were correlated with polarisation resistance to explain the mechanisms of the material degradation in each case. The overall material damage during each erosion-corrosion test was determined using a gravimetric technique; and the results were used to establish a relationship between degradation rate and AE energy within the experimental conditions studied.

8.2 Results and Discussion

8.2.1 Flow-Induced Corrosion

Figures 8.1 to 8.6 present the results of the corrosion rates correlated with AE count rates and cumulative counts correlated with polarization resistance; both correlations are given as a function of time during the two hour test duration used to investigate flow-induced corrosion for 7, 10, and 15 m/s flow velocities. Figure 8.7 gives the correlation of the results using AE energy. The corrosion rate as well as count rate increases with increase in flow velocity with three distinct regions observed in all the results.

The first is the initial period (less than half an hour) of high count rate with high corrosion rate. This period is a high corrosion transient period characterised by active iron dissolution and high turbulence on the fresh material surface which gives corresponding high acoustic emission rate.

The second period is from half an hour up to one hour, the acoustic activity and corrosion rate decrease vividly which may be due to partial formation of a layer of corrosion product with established flow pattern which tends to reduce corrosion and emission rates.

The third period is after one hour of testing when a corrosion product may be fully formed, though not totally protective; the material was still corroding at a rate that averaged 2.8, 3.9 and 4.9 mm/y and an AE count rate that averaged 675, 912 and 12713 counts per second at the stabilised period (after one hour) for 7, 10 and 15 m/s flow velocities respectively. Although it has been reported that iron carbonate film is more protective at a higher temperature [217], the cumulative counts correlated with the polarisation resistance clearly show that acoustic activity and corrosion did not stop completely during the stabilised period.

These observations are in agreement with those made in previous studies [170, 172] that iron dissolution and hydrodynamic local conditions seem to be sources of acoustic emission because they create increased micro displacements on the specimen's surface which are detected by the acoustic emission sensor.

The local hydrodynamics generate turbulence, cavitation and gas bubbles which enhance mass transport of corrosive species and products to and from the material surface. This ultimately leads to higher material loss and acoustic emissions as the flow velocity increases.
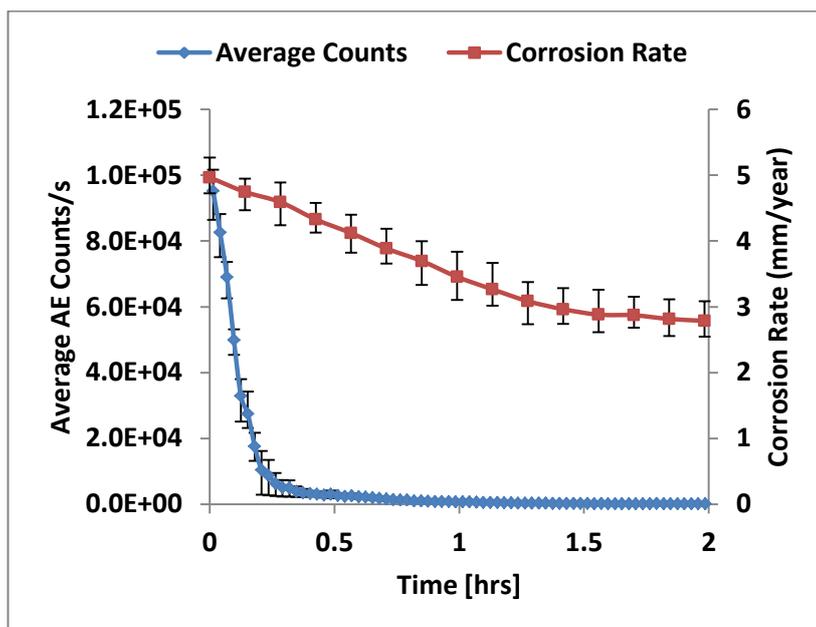
Figure 8.1: Flow-induced corrosion rate variation with AE count rate for 7 m/s flow in CO_2 saturated brine (pH 5.5) at 50°C. Corrosion rates were obtained from LPR measurement using Stern-Geary Coefficient of 26 mV.
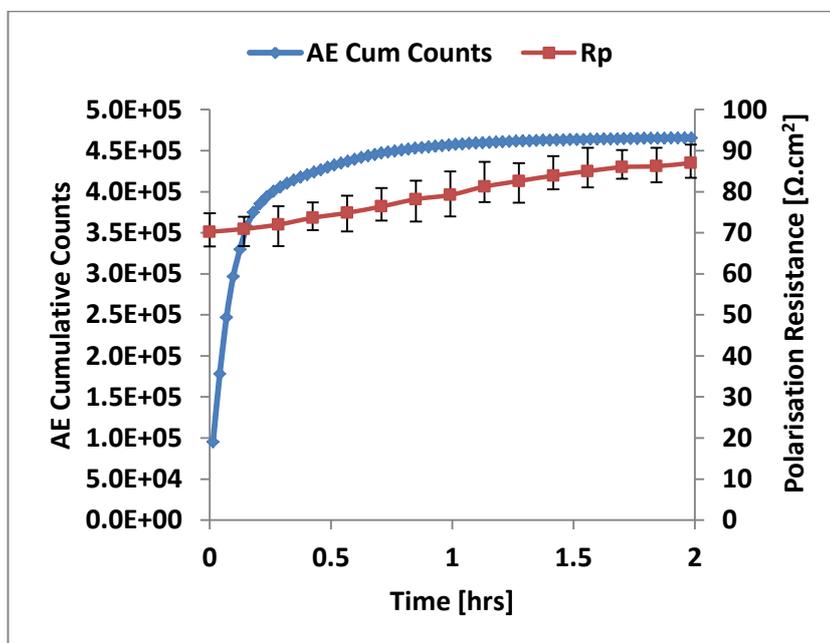
Figure 8.2: Polarisation resistance variation with AE cumulative counts for 7 m/s flow in CO_2 saturated brine (pH 5.5) at 50°C.
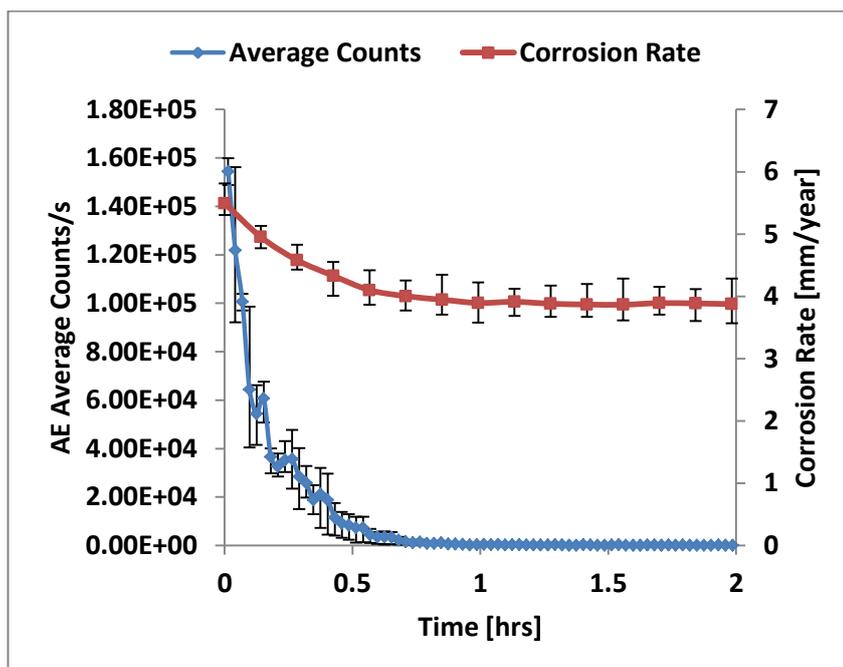
Figure 8.3: Flow-induced corrosion rate with AE count rate for 10 m/s flow in CO$_2$ saturated brine (pH 5.5) at 50°C. Corrosion rates were obtained from LPR measurement using Stern-Geary Coefficient of 26 mV.
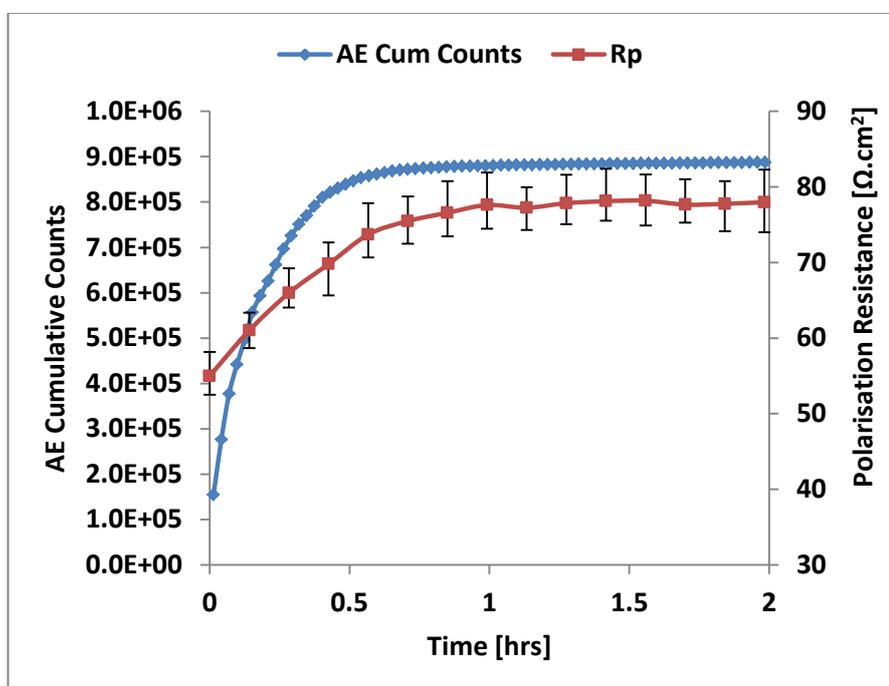
Figure 8.4: Polarisation resistance variation with AE cumulative counts for 10 m/s flow in CO$_2$ saturated brine (pH 5.5) at 50°C.
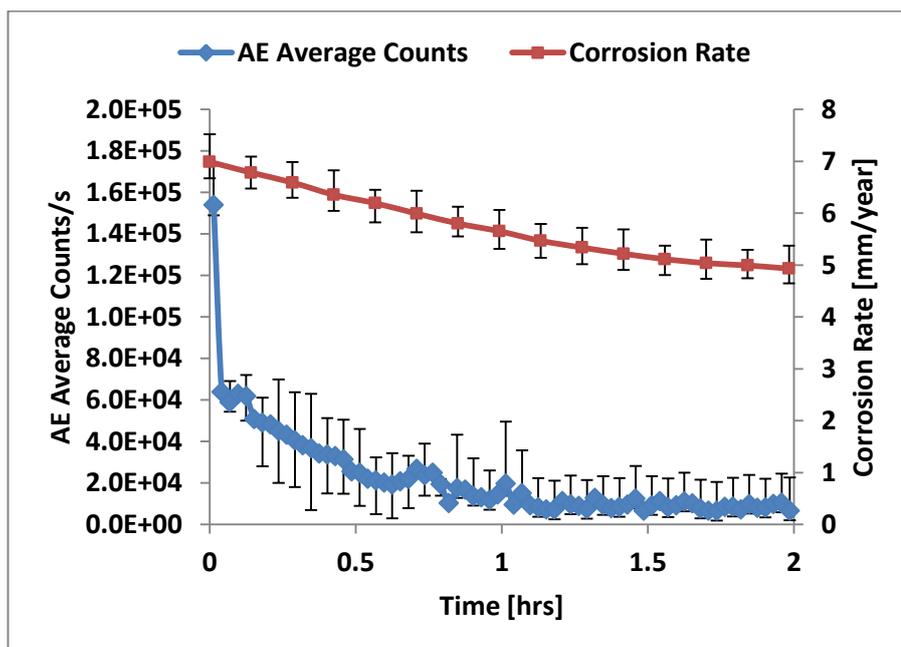
Figure 8.5: Flow-induced corrosion rate variation with AE count rate for 15 m/s flow in CO$_2$ saturated brine (pH 5.5) at 50°C. Corrosion rates were obtained from LPR measurement using Stern-Geary Coefficient of 26 mV.
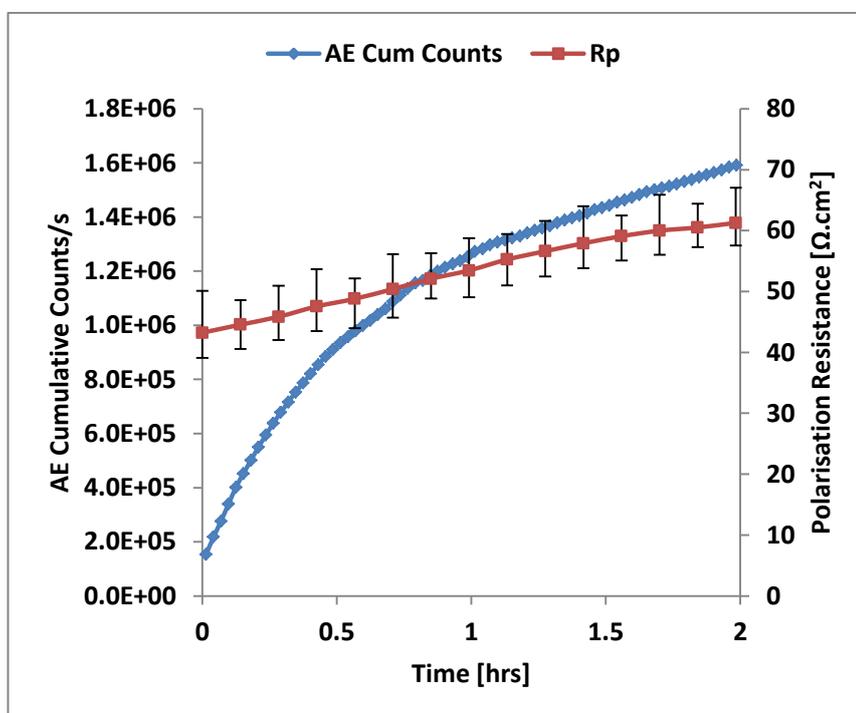
Figure 8.6: Polarisation resistance variation with AE cumulative counts for 15 m/s flow in CO$_2$ saturated brine (pH 5.5) at 50°C.
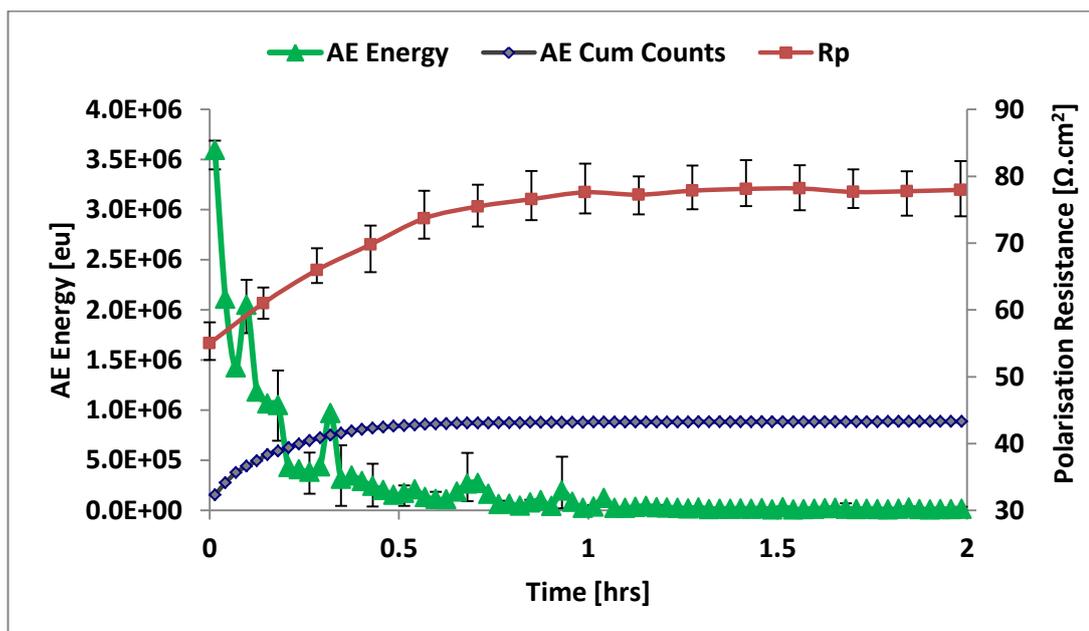
Figure 8.7: Results of AE Energy and cumulative counts with polarisation resistance for 10 m/s flow in CO_2 saturated brine (pH 5.5) at 50^oC. Corrosion rates were obtained from LPR measurement using Stern-Geary coefficient of 26 mV.

8.2.2 Erosion-Corrosion

Sand concentrations of 50, 200 and 500 mg/L were each added to the reservoir to simulate erosion-corrosion environments commonly encountered in oil and gas production; the material degradation rate was assessed together with acoustic emission count rate and energy during each test.

Figures 8.8 to 8.13 show the result of the corrosion rate correlated with AE count rate as well as cumulative count correlated with the polarisation resistance for the flow velocities and sand loadings studied. As expected, the corrosion rate as well as the AE count rate increases with an increase in flow velocity and sand concentrations. These corrosion rates are significantly higher than those obtained in flow-induced corrosion (without sand) assessments. For 7 m/s (Figures 8.8 and 8.9), the addition of 50, 200 and 500 mg/L sand to the system increased the corrosion rate from 2.90 mm/y to 4.31, 4.40, and 4.87 with corresponding AE count rate from 675 counts per second to 8317, 13696 and 25621 counts per second respectively.
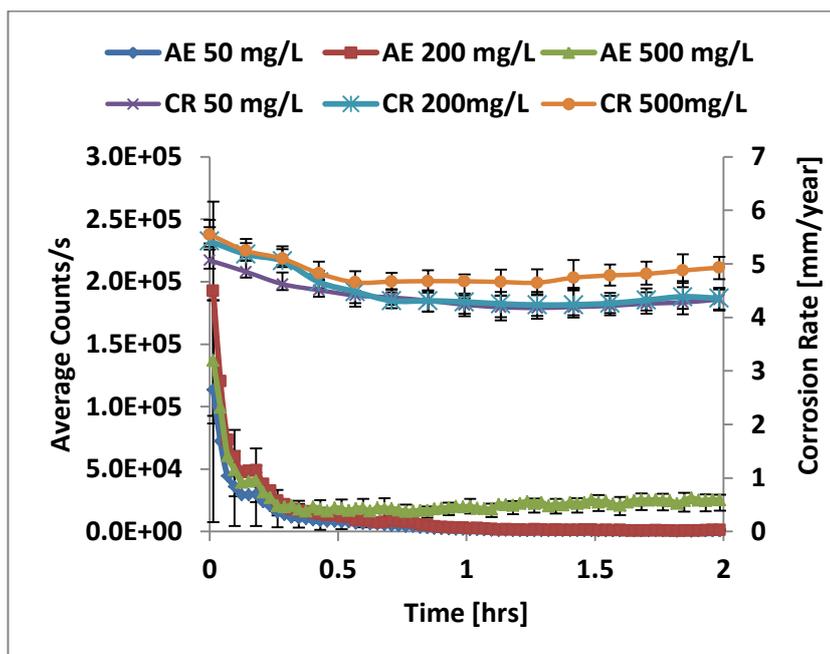
Figure 8.8: Results for erosion-corrosion test showing corrosion rate with AE count rate for 7 m/s in CO$_2$ saturated brine (pH 5.5) at 50°C. Corrosion rates were obtained from LPR measurement using Stern-Geary coefficient of 26 mV.
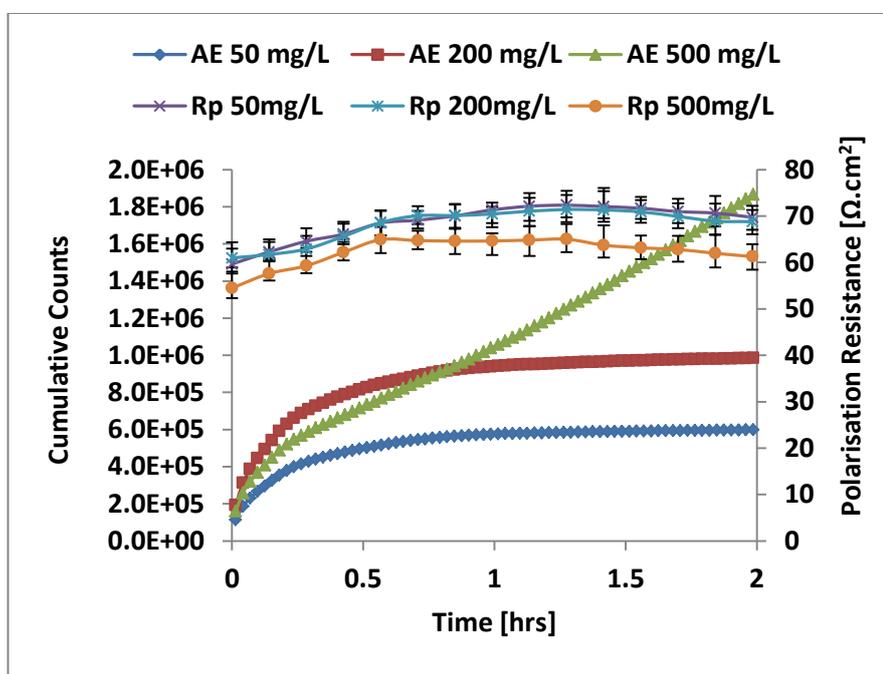
Figure 8.9: Results for erosion-corrosion test showing polarisation resistance variation with AE cumulative counts for 7 m/s in CO$_2$ saturated brine (pH 5.5) at 50°C.

With the same sand concentrations for 10 m/s (Figures 8.10 and 8.11), the corrosion rate increased from 3.85 mm/y to 4.45, 4.87, and 5.14 mm/y with corresponding AE count rate from 912 counts per second to 1.18E+05, 1.48E+05, and 2.24E+05 counts per second respectively.

Higher values were obtained for 15 m/s as illustrated in Figures 8.12 and 8.13. The effect of sand loading on the corrosion potential is illustrated in Figure 7.14 using 15 m/s flow velocity. When the sand loading is increased from 50 to 500 mg/L, the potential decreased from -670 mV to -700 mV which corresponds to more degradation of the material as the corrosion rate increase is considerable.
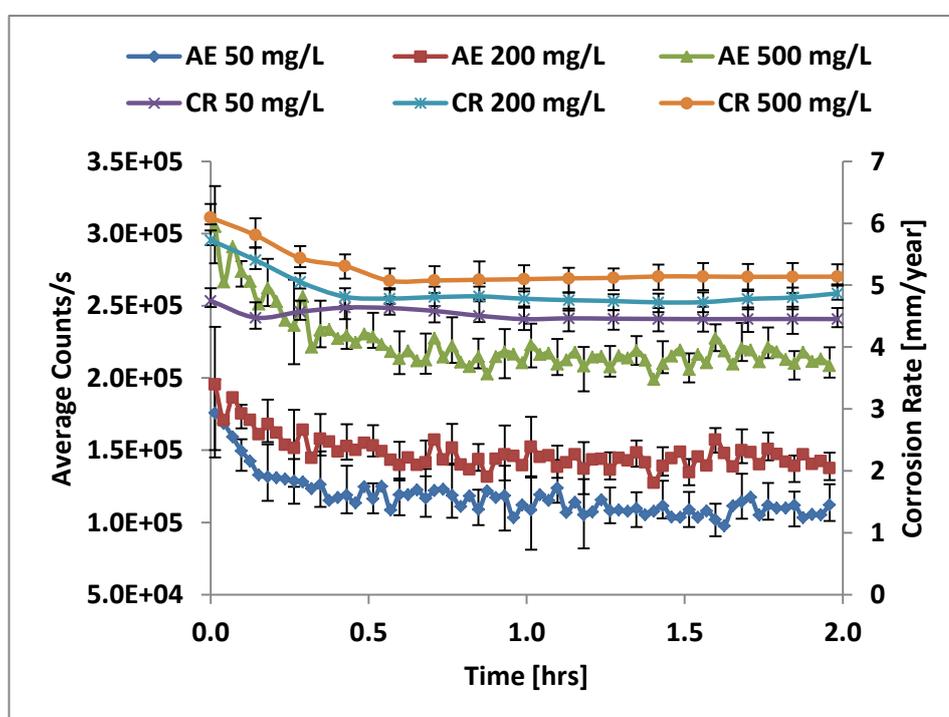
Figure 8.10: Results for erosion-corrosion test showing corrosion rate with AE count rate for 10 m/s in CO$_2$ saturated brine (pH 5.5) at 50°C. Corrosion rates were obtained from LPR measurement using Stern-Geary coefficient of 26 mV.
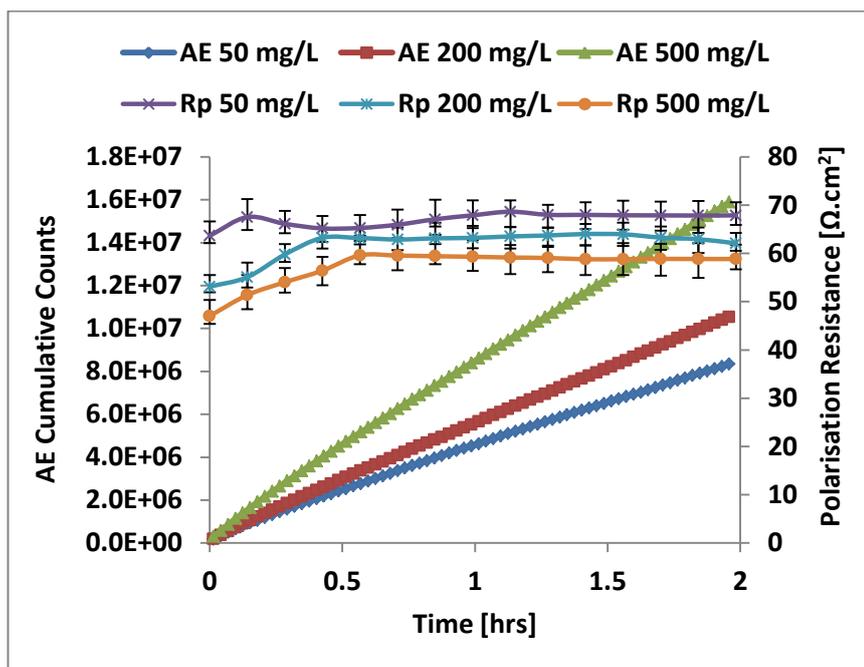
Figure 8.11: Results for erosion-corrosion test showing polarisation resistance variation with AE cumulative counts for 10 m/s in CO$_2$ saturated brine (pH 5.5) at 50°C.
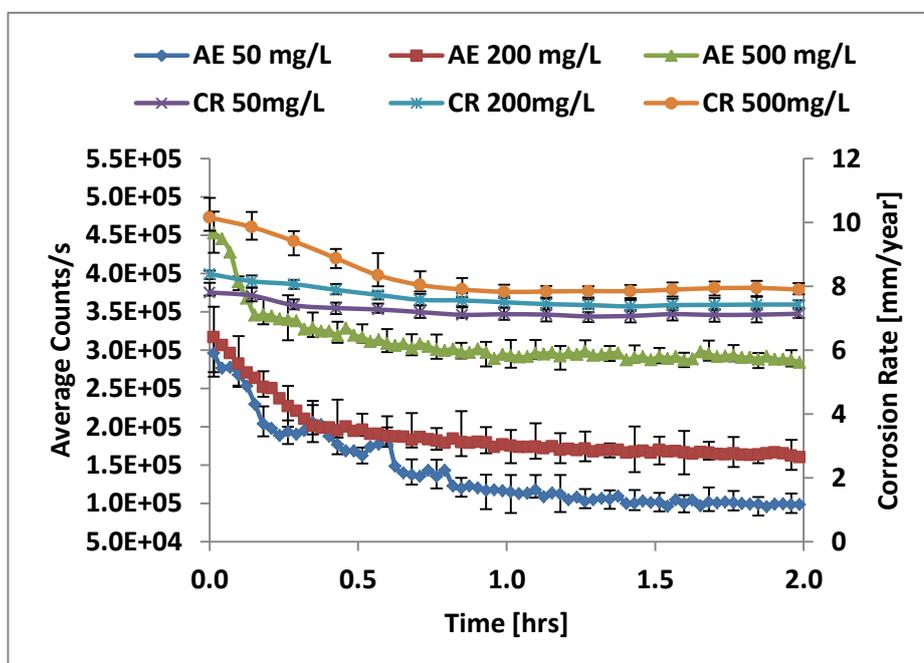
Figure 8.12: Results for erosion-corrosion test showing corrosion rate with AE count rate for 15 m/s in CO$_2$ saturated brine (pH 5.5) at 50°C. Corrosion rates were obtained from LPR measurement using Stern-Geary coefficient of 26 mV.
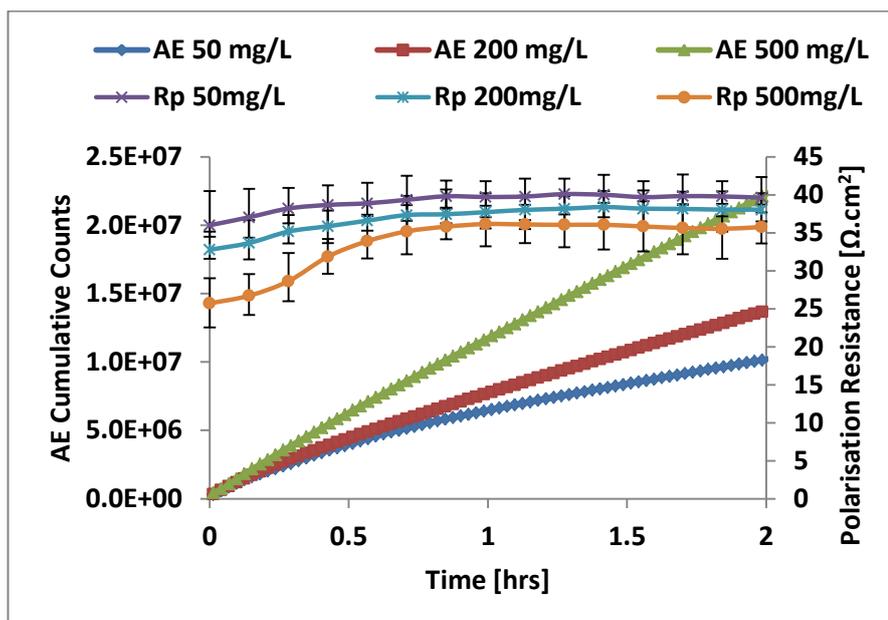
Figure 8.13: Results for erosion-corrosion test showing polarisation resistance variation with AE cumulative counts for 15 m/s in CO$_2$ saturated brine (pH 5.5) at 50°C.
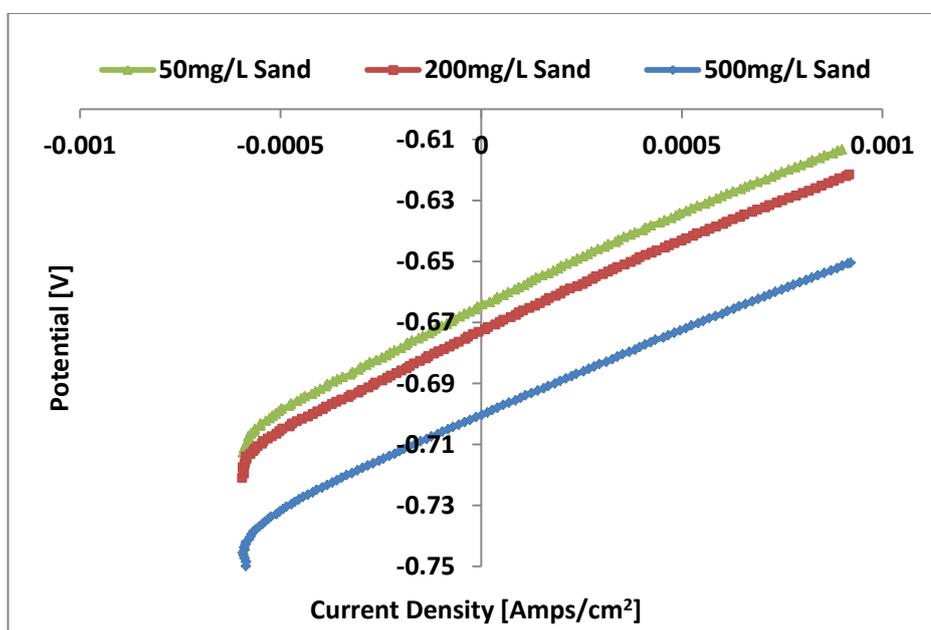
Figure 8.14: LPR data for 15 m/s erosion-corrosion test showing the effect of sand on corrosion potential in CO$_2$ saturated brine (pH 5.5) at 50°C.

The summary of all the results for flow-induced corrosion and erosion-corrosion are displayed in Figure 8.15 for corrosion rate and average count rate, and in Figure 8.16

for cumulative counts and polarisation resistance. From the summary, it is evident that without sand (flow-induced), corrosion rate and polarisation resistance as well as the acoustic activities (average count rate and cumulative counts) are linearly related to the flow velocity. With addition of sand the relationship changes to an exponential function for corrosion rate and polynomial function for the acoustic activity. The change clearly shows the relevance of kinetic energy (mass of solid and velocity) with velocity as the controlling factor, thus leading to a small increase in corrosion rate for low velocity (7 m/s) when sand loading is increased from 50 to 200 mg/L. This indicates that the regime is within the category of 'mild' erosion-corrosion which agrees well with previous studies [42]. A small increase is also observed in the measured acoustic activity for 7 m/s which is an indication that the measured AE is actually from the material degradation mechanisms. Higher flow velocities (10 and 15 m/s) gave significant changes in measured AE for all the sand concentrations studied, thus signifying the effect of flow velocity and sand loading in the material loss which was adequately detected by the AE set-up.
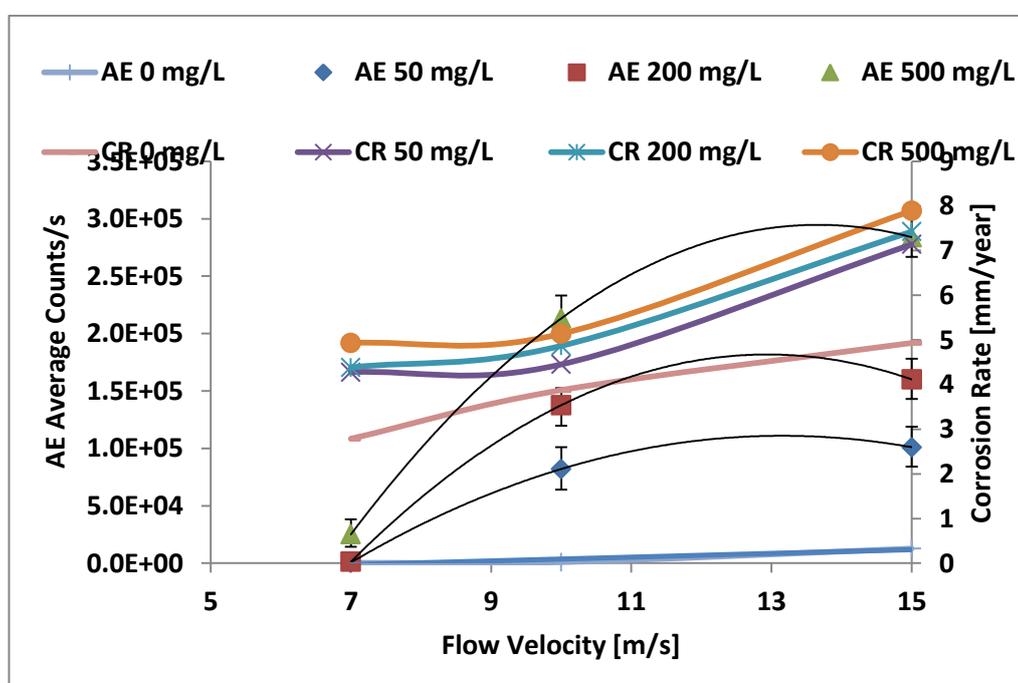
Figure 8.15: Summary of results for corrosion rate and AE count rate. Tests with brine saturated with CO_2 at 1 bar.
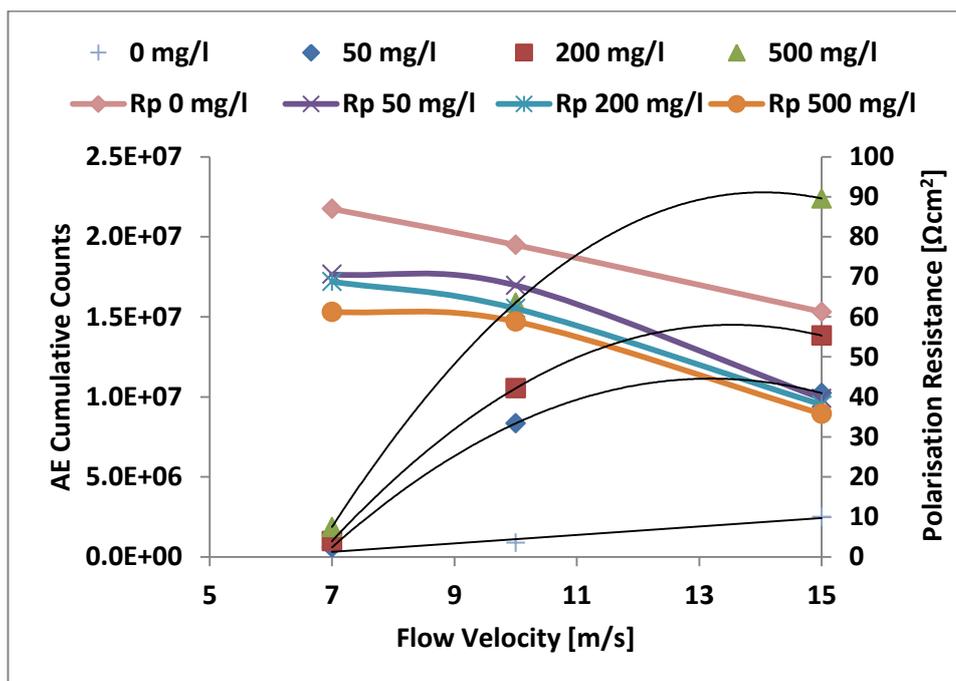
Figure 8.16: Summary of results for polarisation resistance and AE cumulative Counts. Tests with brine saturated with CO_2 at 1bar.

8.2.3 Weight Loss and AE Energy

Figures 8.17 to 8.20 present the total weight loss results together with measured average acoustic energy per second which is a representative of the energetic flux of impacting particles. From these results, it is deduced that the weight loss and acoustic energy increased with increase in flow velocity and sand loading. The increase in weight loss as the flow velocity and sand loading are increased is expected and confirms the findings in previous studies that material removal in CO_2 erosion-corrosion environment is due to combined effect of sand loading and flow velocity [42]. The corresponding increase in AE energy could be a result of increased erosion and corrosion (iron dissolution, mass transport, cracking and removal of corrosion products) at the specimen surface which will create more micro displacements and/or noisier environment giving rise to high emission rate that leads to an increase in acoustic energy. Being a measure of the energetic flux of impact particles, the acoustic energy can give an insight of the mechanical damage contribution as it increases monotonously with increase in the overall damage.
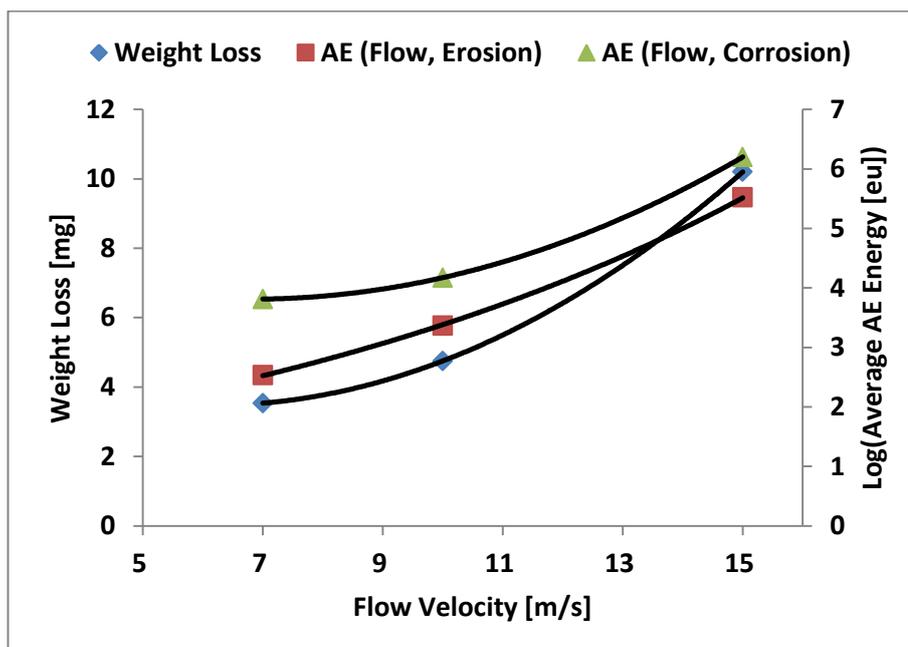
Figure 8.17: Results of the total weight loss with measured average AE energy in energy units ([eu], 1eu=1E-18J) in the presence and absence of corrosion for 0 mg/L sand concentration.
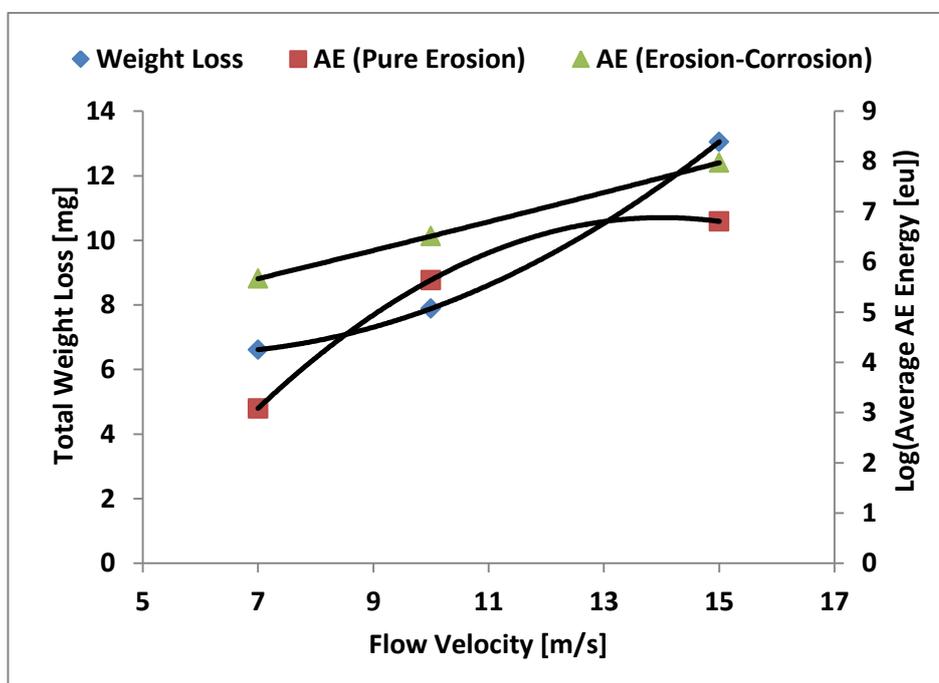
Figure 8.18: Results of the total weight loss with measured average AE energy in energy units ([eu], 1eu=1E-18J) in the presence and absence of corrosion for 50 mg/L sand concentration.
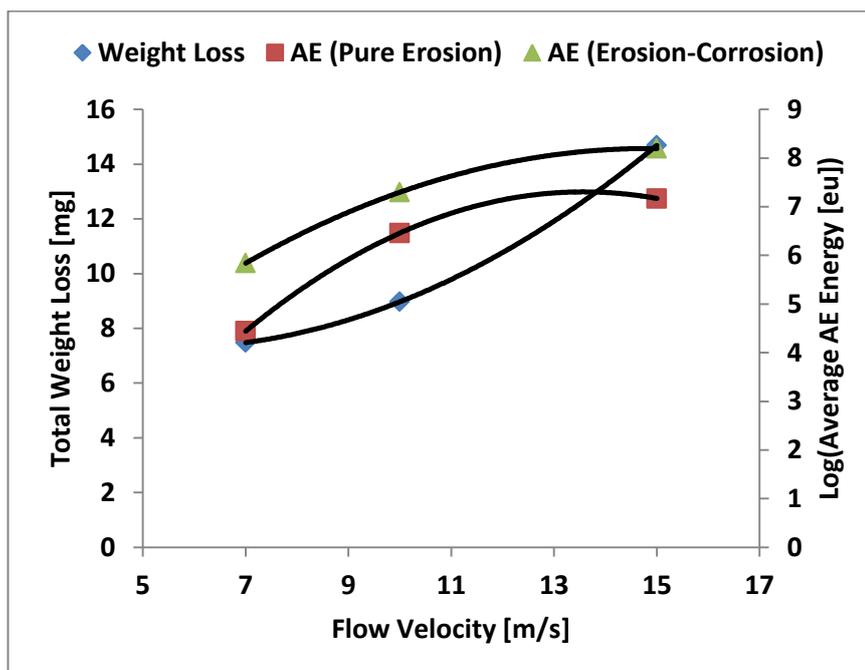
Figure 8.19: Results of the total weight loss with measured average AE energy in energy units ([eu], 1eu=1E-18J) in the presence and absence of corrosion for 200 mg/L sand concentration.
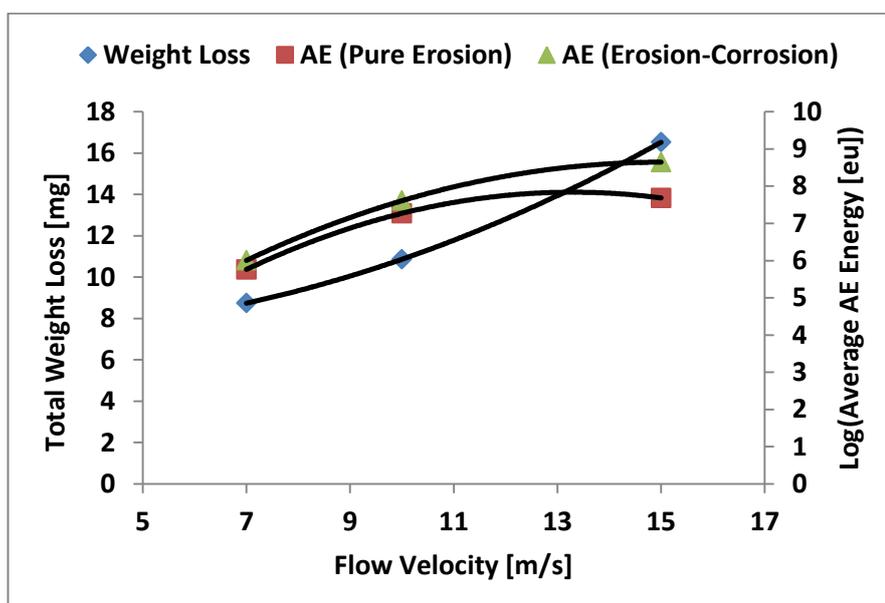
Figure 8.20: Results of the total weight loss with measured average AE energy in energy units ([eu], 1eu=1E-18J) in the presence and absence of corrosion for 500 mg/L sand concentration.

8.2.4 Main Findings

The total material degradation expressed as total weight loss was plotted against the measured average AE energy for all the flow velocities and sand concentrations as shown in Figure 8.21. There is a significant weight loss of about 4 mg after 2 hours with associated acoustic emission energy value of 10^4 eu which is far below the critical value of 10^6 eu without corrosion established in Chapter 6. This indicates that the presence of corrosion can exacerbate material loss considerably and it becomes very clear that the major contribution to the material degradation in erosion-corrosion may be the erosion enhancement of corrosion which has been defined in many studies [42] as 'synergistic' effects. Thus, electrochemical techniques can be used to monitor the electrochemical damage with application of suitable inhibitor to reduce the corrosion rate while the acoustic emission can be used to monitor the mechanical damage in CO_2 erosion-corrosion integrity monitoring of X65 oil and gas pipeline materials. However, a good understanding of the corrosion mechanisms can be essential in combining the two techniques. The corrosion mechanisms are discussed in Chapter 9.
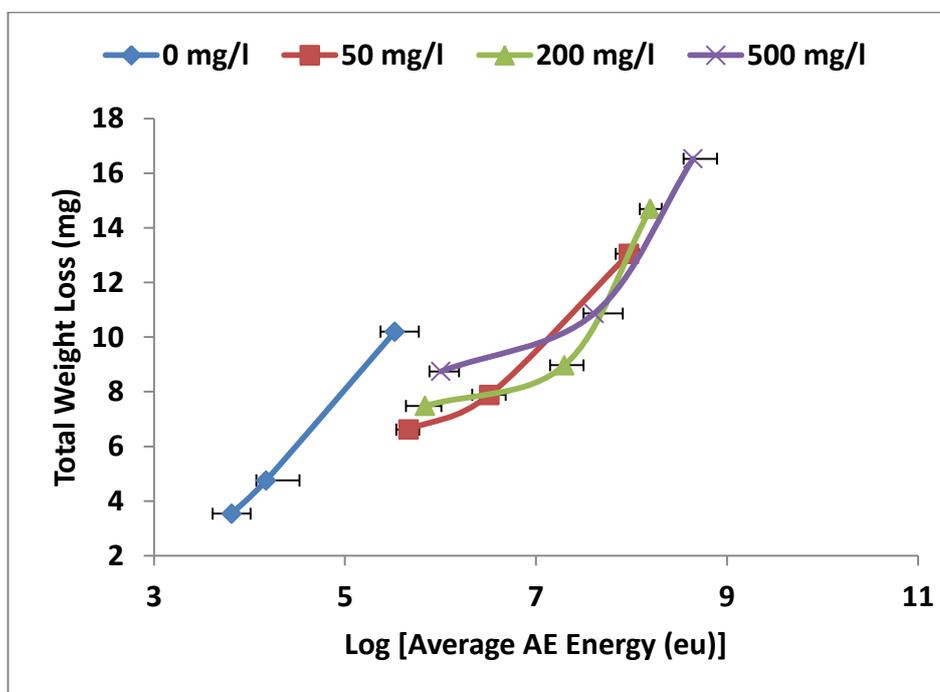
Figure 8.21: Relationship between total weight loss and measured average AE energy for CO_2 flow-induced corrosion and erosion-corrosion (1eu=1E-18J).

8.3 Summary

Results revealed that corrosion rate correlates well with AE count rate with and without sand in CO_2 saturated oilfield brine for 7, 10 and 15 m/s flow velocities.

The material degradation rate and the AE energy become considerably higher in a CO_2 corrosion environment (when compared with AE energy from pure erosion) with significant damage done at a value below the pure erosion critical AE energy value which is an indication that the key contribution to material degradation in erosion-corrosion is corrosion.

Results equally revealed that AE energy is representative of the energetic flux of impacting particles which suggests that AE technique can be used to effectively quantify and monitor the mechanical damage contribution of the erosion-corrosion material degradation while electrochemical method can monitor corrosion damage so as to operate safely and avoid unplanned production outages in oil and gas production.

Chapter 9 Results and Discussion: Mechanistic and Quantitative Evaluation of Erosion-Corrosion and Its Components with Combined EIS and AE

9.1 Introduction

This chapter gives the results and discussion of the part of the PhD investigation that applied electrochemical impedance spectroscopy (EIS) to investigate the surface reactivity of the corroding metal and acoustic emission (AE) to capture the sand impact contribution which is expressed as acoustic emission energy during the erosion-corrosion process. The objective is to further have a proper understanding of the mechanistic and quantitative evaluation of CO_2 erosion-corrosion damage and its components for X65 pipeline materials. This is because an accurate description of the surface not only helps to identify the prevailing form of corrosion but also its prescription of necessary corrosion inhibition processes.

Specifically, the benefits of EIS over linear polarisation resistance (LPR) are that:

- It produces values of solution and charge-transfer resistances and electrical double layer (EDL) capacitance; and these quantities can give more accurate information on the corrosion behaviour and rates.
- It can also give an insight into the corrosion rate-controlling mechanisms at the surface within an electrolyte which LPR neglects or misses.

EIS measurements were performed with a sinusoidal potential excitation of ±10 mV amplitude in a frequency range of 20 kHz to 0.1 Hz. Equivalent electrical circuits and curve-fitting were investigated using ZView analysis software. AE signals were measured simultaneously with EIS and sampled at 2.5 MHz sampling rate, filtered and amplified with band filter frequency of 90-850 kHz and threshold set at 40 dB for all tests.

9.2 Results

First of all, it was necessary to characterise the dissolution behaviour of the X65 carbon steel in the CO_2 saturated brine without sand so as to determine the baseline corrosion rate and dissolution mechanisms prior to tests with sand. This was to examine the effect of sand particles on the corrosion behaviour of the materials from the perspective of the combined technique of EIS and AE and also to know if combining EIS and AE can help capture the mechanisms of electrochemical corrosion and mechanical erosion with good understanding of the reactivity at the sample's surfaces.

To achieve this, EIS measurement was performed every 10 minutes for 2 hours on the sample with DC and open circuit potential (OCP) measurements taken in between each impedance measurement for 7, 10 and 15 m/s flow velocities with variation of 0, 50, 200 and 500 mg/L sand concentrations for each flow velocity. Measurements were done simultaneously with AE recording.

9.2.1 Tests without Sand

The detected AE signals for the tests without sand were basically representative of the AE from flow induced effects and similar to those reported in 6.3.5. The impedance spectra (Nyquist plots) collected during each of the two-hour tests are shown in Figures 9.1 to 9.3. The impedance behaviour showed a slight increase to a steady state when plotted as a function of time which signifies a slight reduction of corrosion rate to a steady state with time. Three different repeats were performed at each flow velocity and a similar trend was observed in all the results. The impedance response as a function of flow velocity showed a decrease of impedance as flow velocity increases (Figure 9.4), an indication of increase in material dissolution process as expected. The impedance behaviour for 7 m/s flow velocity was observed to be different from those of 10 and 15 m/s flow velocities. At 7 m/s, the impedance plot has a capacitive loop at the high frequency (HF) region and an inductive loop at low frequency (LF) region (Figure 9.1) whilst at 10 and 15 m/s one capacitive loop is observed (Figures 9.2 and 9.3). The

HF domain is a depressed semicircle with its centre on the real impedance axis and the LF domain is towards the highest real impedance value as shown in Figure 9.1.
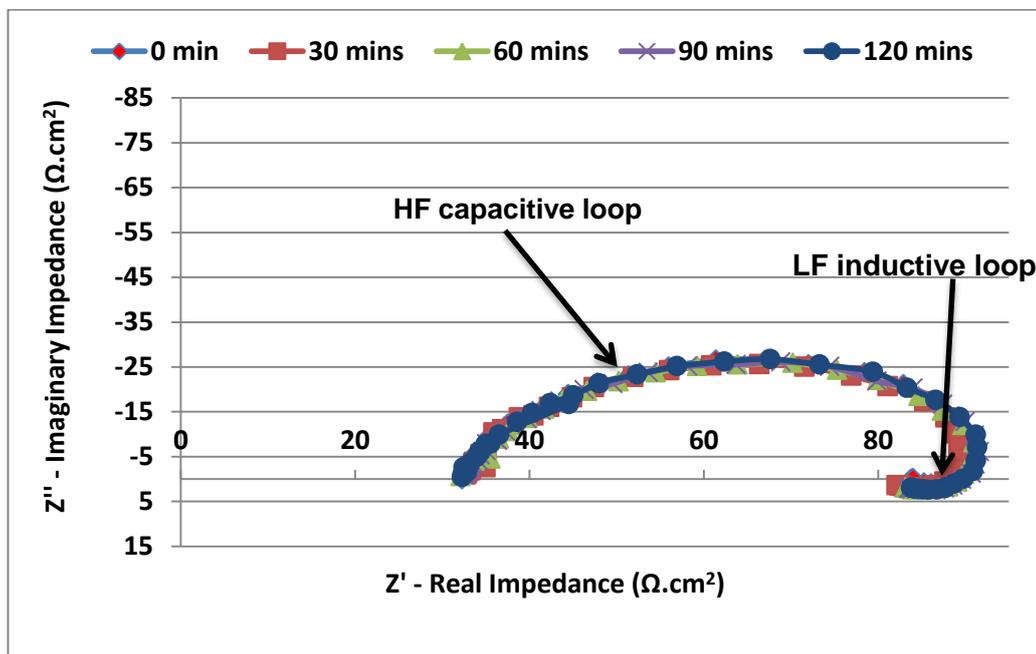
Figure 9.1: Nyquist plot at different exposure times for 7 m/s with process brine without sand, 50°C and CO$_2$ saturated at 1 bar.
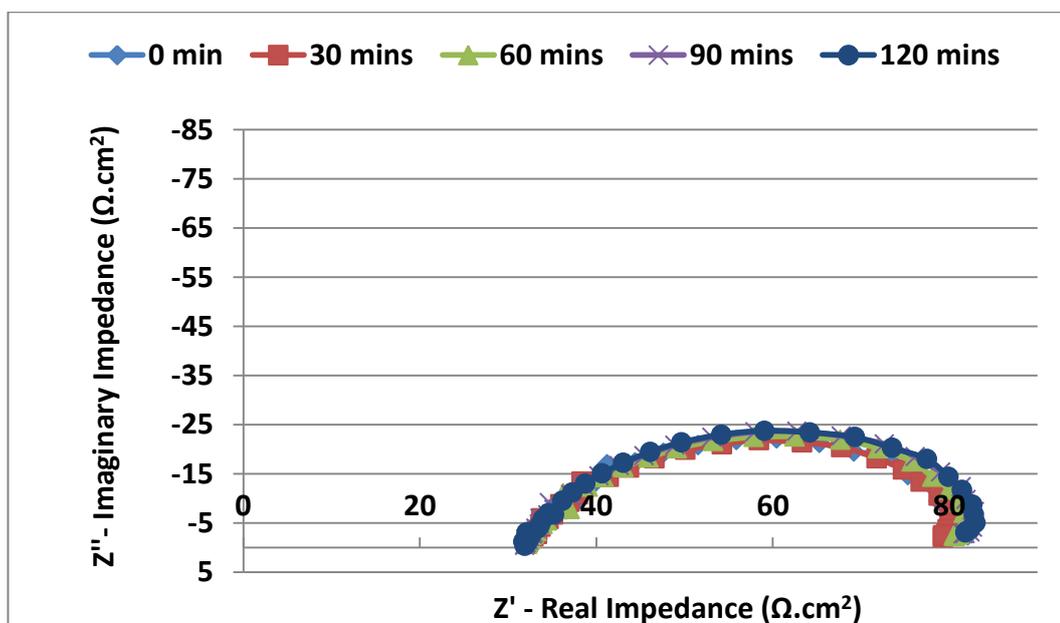
Figure 9.2: Nyquist plot at different exposure times for 10 m/s with process brine without sand, 50°C and CO$_2$ saturated at 1 bar.
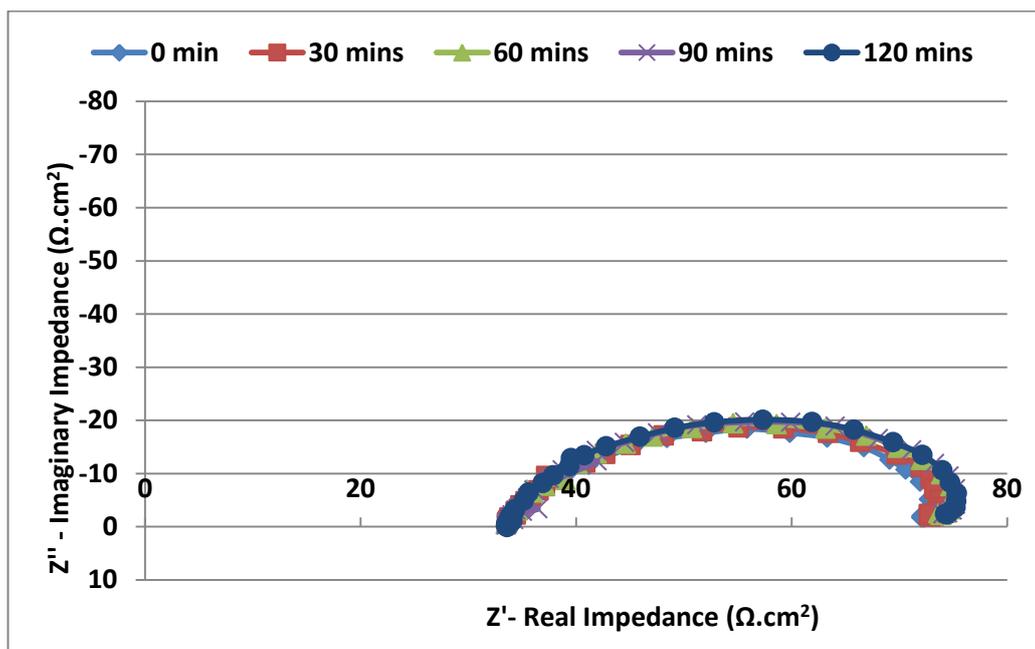
Figure 9.3: Nyquist plot at different exposure times for 15 m/s with process brine without sand, 50°C and CO_2 saturated at 1 bar.

The impedance plot for each of the flow velocities after the two-hour test duration is shown in Figure 9.4. As observed before, the influence of flow velocity is seen on the plot. The magnitude of the impedance decreases and the LF inductive loop disappears as the flow velocity increases. This suggests that flow velocity effects play an important role in the material dissolution process.
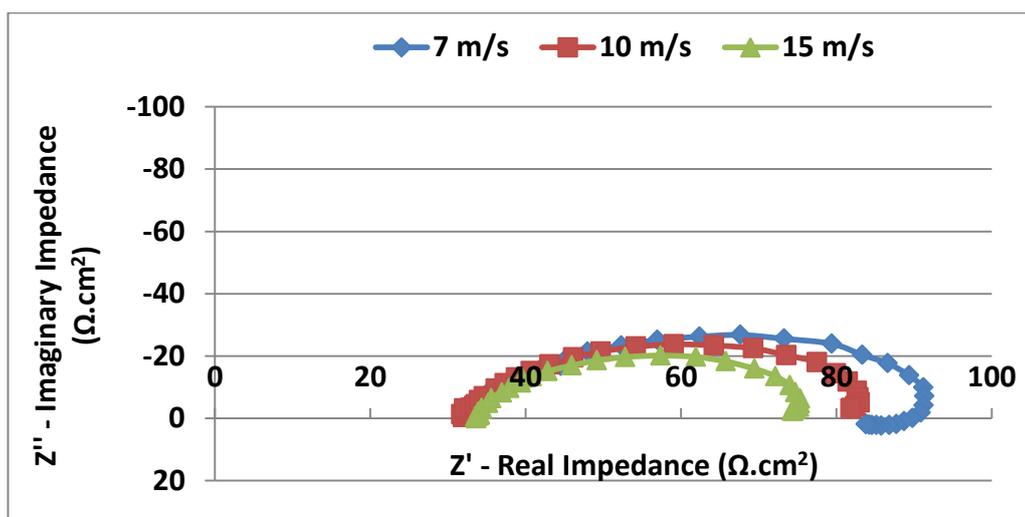
Figure 9.4: Summary of the Nyquist plots of all the flow velocities after 120 minutes with process brine without sand, 50°C and CO_2 saturated at 1 bar.

9.2.2 Test with Sand

A sample of detected AE signal waveform during the test is shown in Figure 9.5 and similar to those detected in previous erosion test in Section 6.3.2. Each signal burst is associated with single sand impact as established in previous investigation in Chapter 7. For each test, AE energy (the integral of squared or absolute amplitude over time of signal duration) of emitted signals per second was determined and used for analysis. Figures 9.6, 9.7 and 9.8 show the Nyquist plots as a function of time for 7, 10 and 15 m/s flow velocities each with 500 mg/L sand loading respectively. The changes observed for 50 and 200 mg/L sand concentrations at each flow velocity were not significant and have been omitted for clarity. Like the baseline tests without sand, the impedance behaviour showed a slight increase to a steady state when plotted as a function of time, and also the data revealed the same behaviour in terms of a capacitive loop and an inductive loop at high frequency (HF) and low frequency (LF) regions respectively for 7 m/s flow velocity, and one capacitive loop for both 10 m/s and 15 m/s flow velocities.
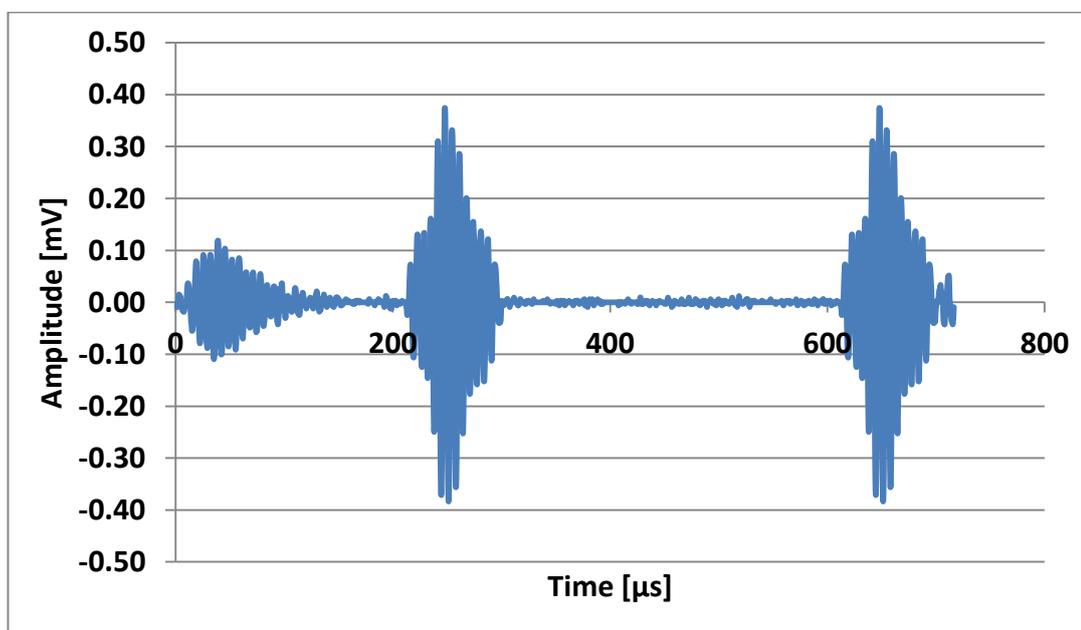
Figure 9.5: Detected AE signal waveform. Test conditions: process brine, 7 m/s flow velocity with 200 mg/L sand loading, 50°C and CO$_2$ saturated at 1 bar.
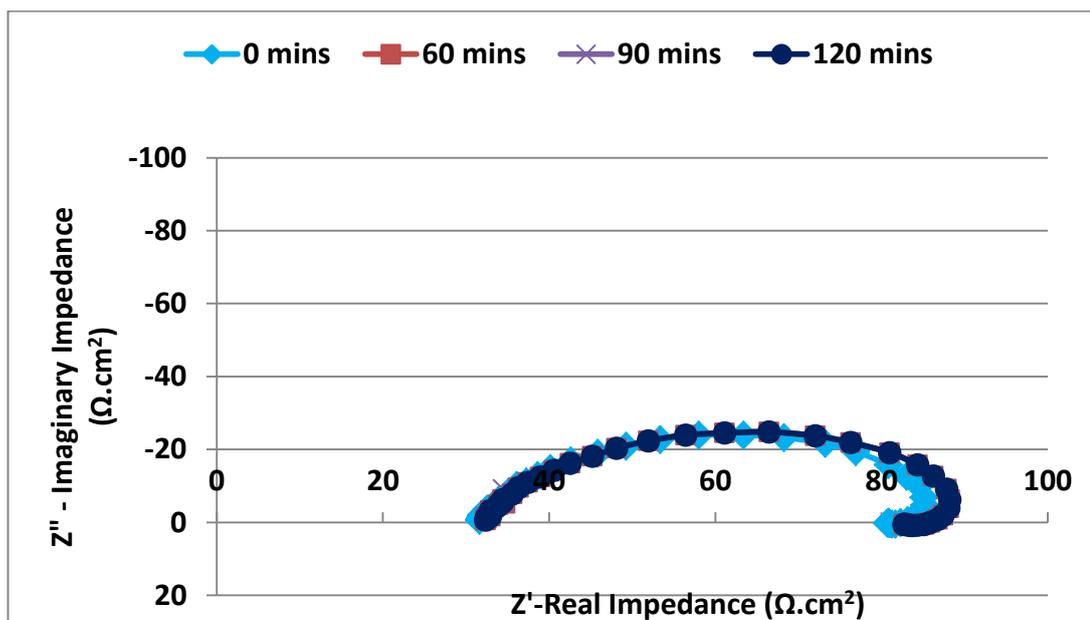
Figure 9.6: Nyquist plot at different exposure times for 7 m/s with process brine, 500 mg/L sand loading, 50°C and CO$_2$ saturated at 1 bar.
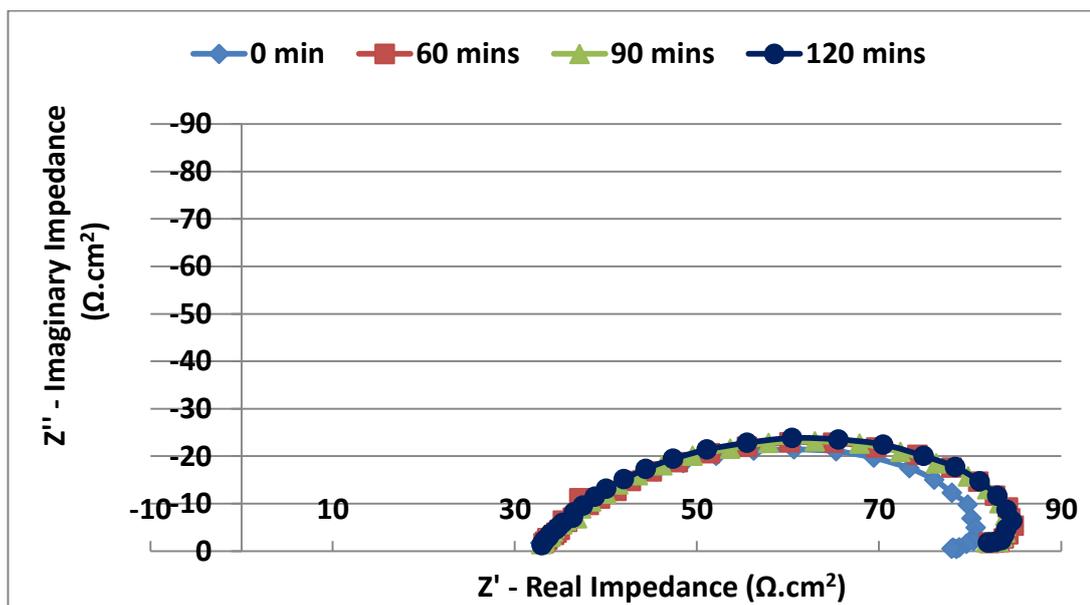
Figure 9.7: Nyquist plot at different exposure times for 10 m/s with process brine, 500 mg/L sand loading, 50°C and CO$_2$ saturated at 1 bar.
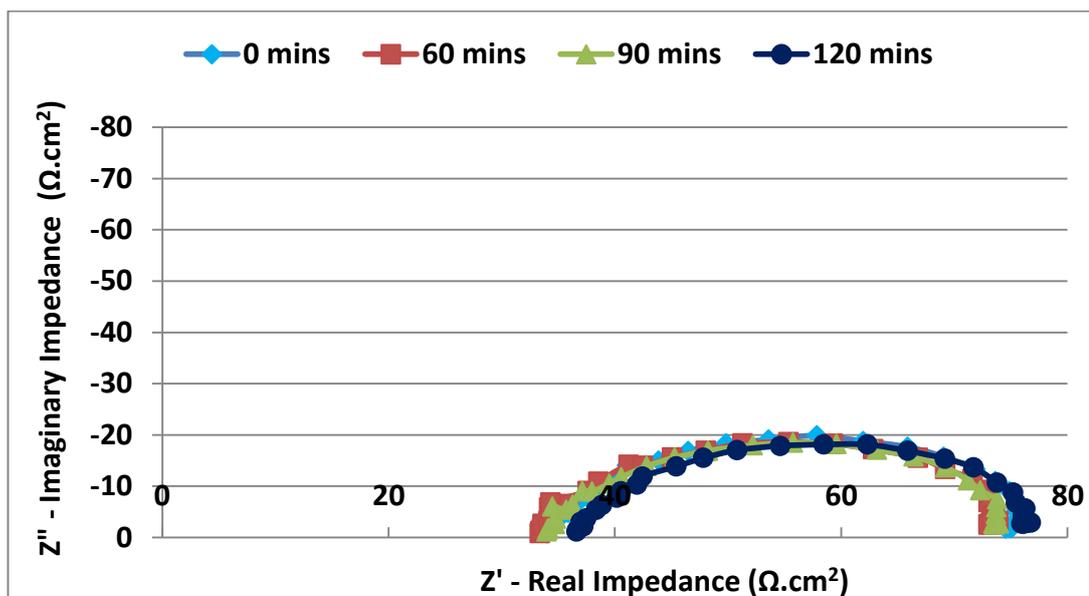
Figure 9.8: Nyquist plot at different exposure times for 15 m/s with process brine, 500 mg/L sand loading, 50°C and CO_2 saturated at 1 bar.

Using the 500 mg/L sand loading data, the Nyquist plot for the flow velocities after the two-hour test duration is illustrated in Figure 9.9. As observed in the results of the tests without sand, the influence of flow velocity is seen on the plot. The magnitude of the impedance decreases and the LF inductive loop disappears as the flow velocity increases indicating the influence of flow velocity on the material dissolution process.

The effect of the sand loading on the impedance plots for 7 and 10 m/s flow velocities was not significant when compared to the effect on 15 m/s flow velocity. Hence, the 15 m/s flow velocity data is used to show the effect of sand loading on the impedance plot. This is shown in Figure 9.10. The data shows a decrease in the impedance semi-circle as the sand loading is increased from 50 mg/L to 500 mg/L which is an indication of increase in corrosion rate.
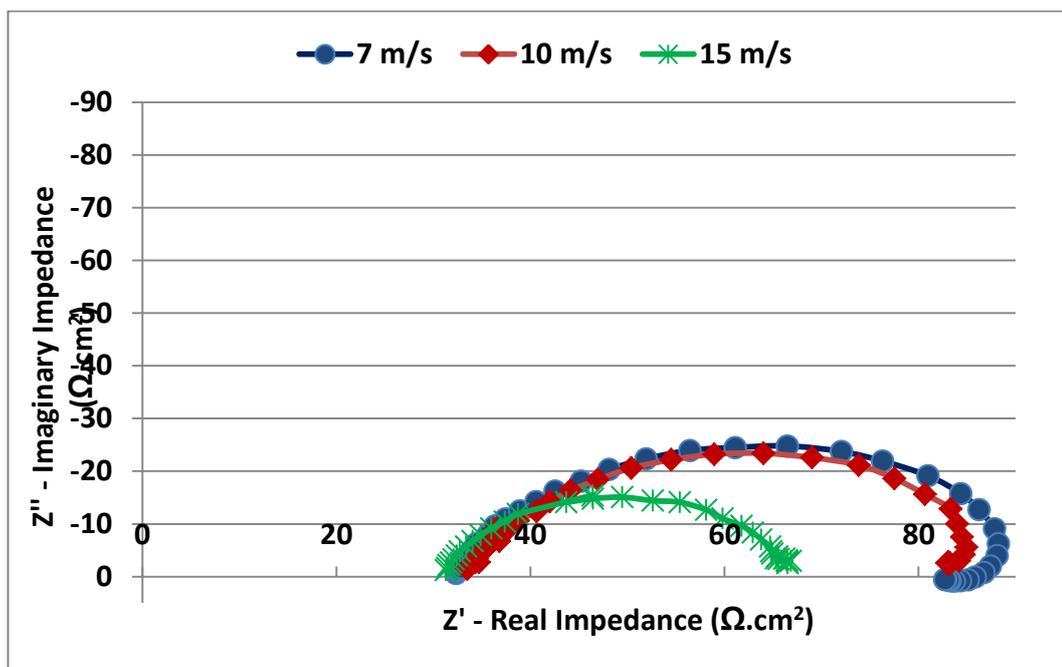
Figure 9.9: Nyquist plots after 2 hours for 7, 10 and 15 m/s flow velocities. Test conditions: process brine, 500 mg/L sand loading, 50°C and CO$_2$ saturated at 1 bar.
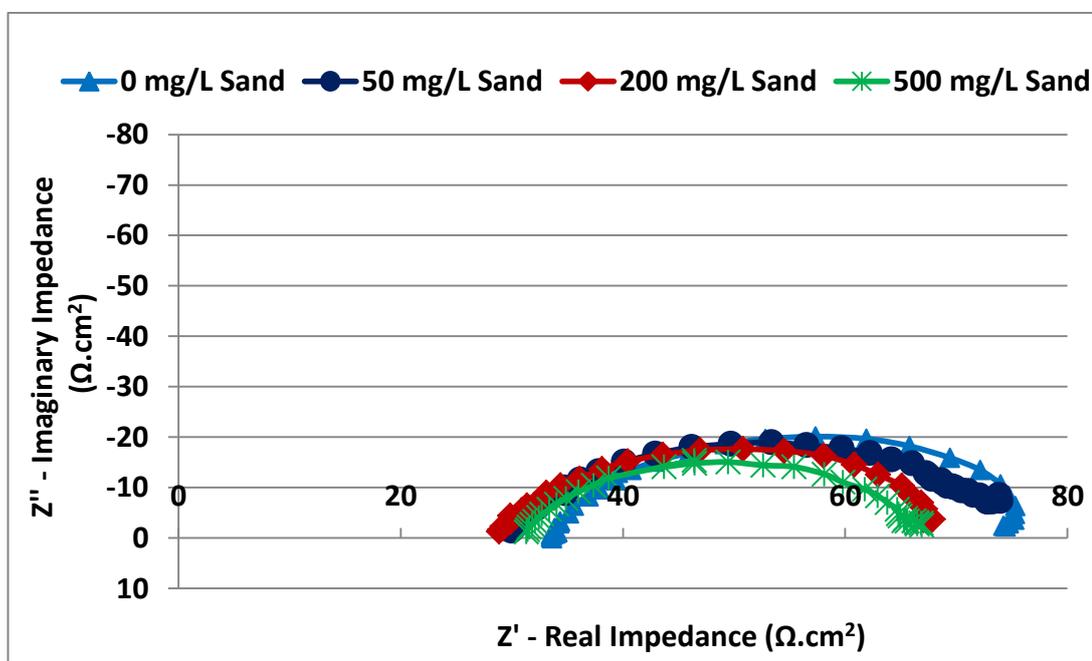
Figure 9.10: Nyquist plot after 2 hours for 15 m/s flow velocity with different sand concentrations. Test conditions: Process brine, 50°C and CO$_2$ saturated at 1 bar.

9.3 Equivalent Circuit Modelling of EIS Plots

The equivalent circuit model in Figure 9.11 was used to capture the mechanisms leading to the evolution of the interface during the tests. The model was proposed by many researchers [207, 218] and has been widely applied to simulate steel-CO_2 interface involving an adsorbed intermediate product and active-charge transfer mechanisms.
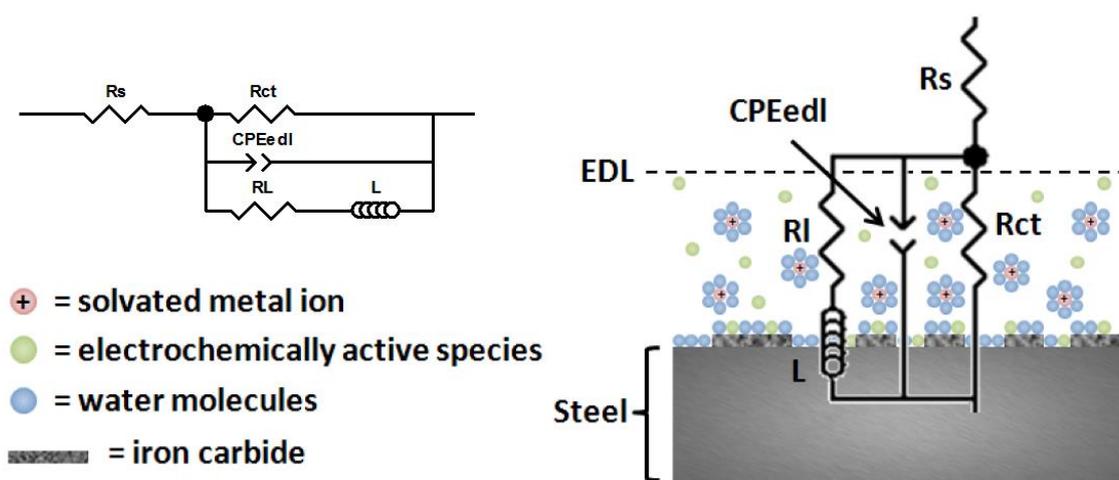
Figure 9.11: Equivalent circuit used for modelling the EIS data: R_s is the solution resistance, CPE_{edl} is a constant phase element describing the capacitance of the electric double layer, R_l is the inductive resistance, L is the inductance and R_{ct} is the charge-transfer resistance [207].

An explanation of the level of agreement between the proposed model in Figures 9.11 and one example of the experimental data is shown in Figures 9.12 and 9.13. The fitting gave an average erorr of 2.98% for Figure 9.12 and 3.32% for Figure 9.13 using Zview^{TM} corrosion software.

Data was extracted after the fitting and used in analysis.
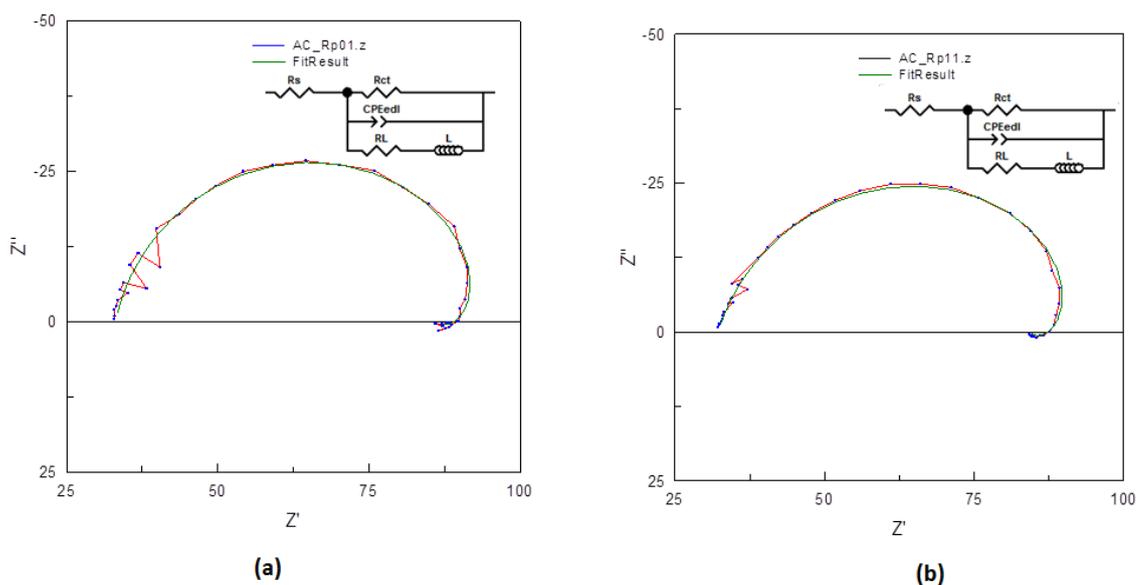
Figure 9.12: Illustration of the fit of the model (green line) with the experimental data (red line) for 7 m/s at (a) the beginning of the test and (b) end of the test.
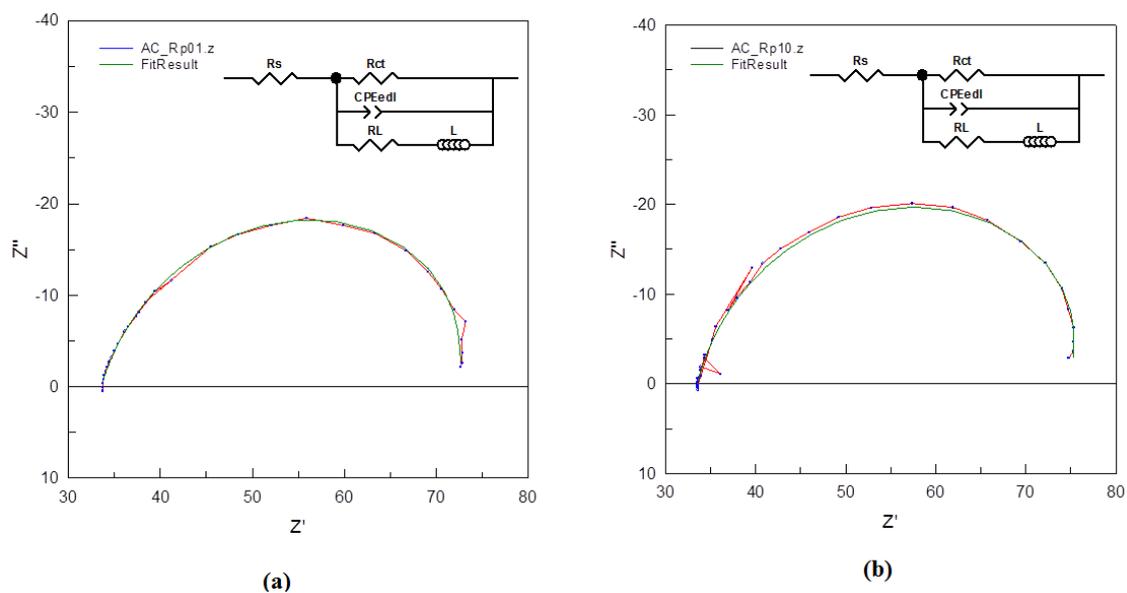
Figure 9.13: Illustration of the fit of the model (green line) with the experimental data (red line) for 10 and 15 m/s at (a) the beginning of the test and (b) end of the test.

The values of the electrical parameters after fitting the experimental data (without sand loading) with the model are shown in Table 9.1 for 7 m/s, Table 9.2 for 10 and Table 9.3 for 15 m/s and presented here for comparison with previous studies by Barker *et al.*

[207] and Farelas *et al.* [218]. An increase in EDL capacitance with time is observed which is in agreement with the values proposed by Barker *et al.* [207] and Farelas *et al.* [218]. This increase with time is as a result of the physical properties of iron carbide [207].

Table 9.1: Values for equivalent circuit parameters for 7 m/s flow without sand

Time (mins)	R_s ($\Omega.cm^2$)	CPE_{edl} (μFcm^2s^{n-1})	n	R_{ct} ($\Omega.cm^2$)
0	33.17(±0.2)	446.71 (±28)	0.87(±0.02)	64.63(±2.1)
30	31.30(±0.3)	507.32(±43)	0.77(±0.04)	65.62(±1.8)
60	31.95(±0.1)	627.12 (±18)	0.79(±0.03)	66.65(±1.6)
90	31.71(±0.2)	748.23(±65)	0.82(±0.02)	67.42(±3.2)
120	32.17(±0.4)	777.41(±43)	0.81(±0.01)	67.54(±1.9)

Table 9.2: Values for equivalent circuit parameters for 10 m/s flow without sand

Time (mins)	R_s ($\Omega.cm^2$)	CPE_{edl} (μFcm^2s^{n-1})	n	R_{ct} ($\Omega.cm^2$)
0	32.25(±0.7)	258.26(±32)	0.92(±0.04)	58.99 (±1.7)
30	32.98(±0.5)	286.05(±64)	0.91(±0.05)	59.30 (±1.4)
60	33.08(±0.2)	434.34(±56)	0.92(±0.02)	60.81(±2.5)
90	32.71(±0.3)	499.11(±73)	0.93(±0.02)	62.06(±2.8)
120	32.72(±0.4)	587.46(±41)	0.93(±0.04)	64.18(±1.8)

Table 9.3: Values for equivalent circuit parameters for 15 m/s flow without sand

Time (mins)	R_s ($\Omega.cm^2$)	CPE_{edl} (μFcm^2s^{n-1})	n	R_{ct} ($\Omega.cm^2$)
0	34.80(±0.8)	242.39(±34)	0.95(±0.02)	50.85(±1.3)
30	34.57(±0.2)	401.54(±57)	0.93(±0.02)	50.58(±1.5)
60	34.51(±0.5)	505.92(±78)	0.93(±0.04)	51.23(±2.3)
90	34.44(±0.2)	568.35(±86)	0.94(±0.05)	51.50(±1.7)
120	34.49(±0.3)	618.18(±71)	0.95(±0.04)	51.69(±1.6)

According to Barker *et al.* [207] and Farelas *et al.* [218], the magnitude of the EDL capacitance is affected by the area of F_3C which is an electric conductor that governs the evolution of hydrogen. A further comparison was made by establishing a relationship between the charge-transfer resistance and EDL capacitance and it is

observed that the charge-transfer resistance slightly increases to a steady state (i.e. a corrosion rate decreases to a steady state) as the EDL capacitance increases.

This trend is quite different from the trend in the work of Barker *et al.* [207] and Farelas *et al.* [218] as shown in Figure 9.14. This can be attributed to the higher contents of Vanadium and Chromium which tend to reduce the corrosion rate in the carbon steel used in this study.
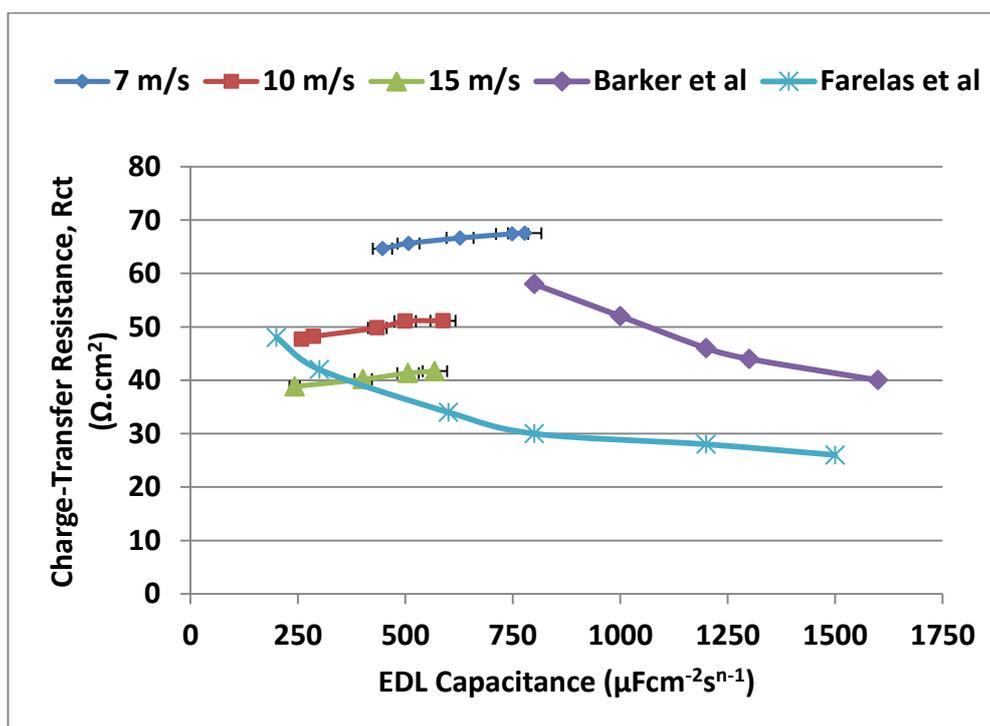
Figure 9.14: Comparison of the relationship between charge-transfer and EDL capacitance in this study and those from Barker *et al.* [207] and Farelas *et al.* [218].

Despite the variation in the behaviour of the charge-transfer resistance in this study and those of Barker *et al.* [207] and Farelas *et al.* [218], all the results indicate a limiting, minimum charge-transfer resistance is being reached as the EDL capacitance increases. Farelas *et al.* [218] proposed that it is as a result of a limiting rate of dissolution on the anodic regions.

9.4 Discussion

The EIS results presented in section 9.2 made it possible for us to have an idea and insight of the corrosion mechanisms and the relative surface reactivity occurring at the interface of the specimen. The observed mechanisms are discussed in the next paragraphs.

9.4.1 7 m/s Flow Velocity

At 7 m/s flow velocity, without and with sand, the mechanism exhibited through the EIS measurements represents that of an active-adsorption state similar to those proposed by Barker *et al.* [207] and Farelas *et al.* [218]. Experiments performed in similar conditions but with ASTM A106 grade B carbon steel by Barker *et al.* [207] and an investigation conducted in 3% NaCl saturated with CO_2 under 0.5 m/s flow velocity with C1018 steel by Farelas *et al.* [218] produced impedance plots similar to those obtained in this study and are illustrated in Figures 9.15 and 9.16 for comparison. Except the impedance change with respect to time which increased slightly to a steady state, all other behaviours in this work and those of Barker *et al.* [207] and Farelas *et al.* [218] indicate the same material dissolution characteristics regardless of the differing conditions. Two time constants were observed during the exposure of the material to the solution; a capacitive loop at the high to medium frequency region and an inductive loop at the low frequency region.

With and without sand loading, the capacitive loop amplitude slightly increases to a steady state with respect to time indicating that the charge-transfer process becomes decreasingly favourable which is different from the results of Barker *et al.* [207] and Farelas *et al.* [218] that increased with time. The decrease to a steady-state with time in the dissolution process can be attributed to the presence of higher quantities of elements such as Vanadium, Chromium, Silicon, Nickel, Copper, Titanium and Aluminium contents in the carbon steel material used in this study which makes the material to be more corrosion resistant than the carbon steel materials used in previous

studies by Barker *et al.* [207] and Farelas *et al.* [218]. The Vanadium and Chromium contents are 0.057% and 0.11% in the X65 carbon steel used in this study whilst they are 0.00% and 0.06% in A106 for Barker *et al.* [207], 0.001% and 0.063% in C1018 for Farelas *et al.* [218]). Investigations by Kermani *et al.* [219] have shown that addition of Vanadium has the greatest effect on reducing corrosion rate, closely followed by Chromium and then Copper. Also, it is possible that that the difference in composition of the brine has contributed partly to the difference in observed corrosion behaviour.

(a)

(b)
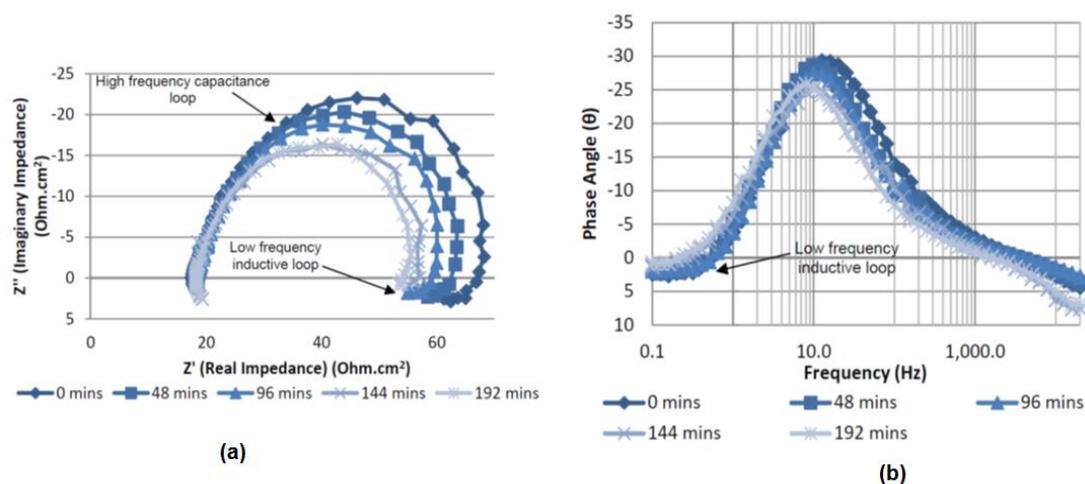
Figure 9.15: (a) Nyquist and (b) phase plots by Barker *et al.* [207] for ASTM A106 grade B carbon steel in oilfield process brine under 7 m/s flow velocity, 45°C and CO$_2$ saturated at 1 bar.

(a)

(b)
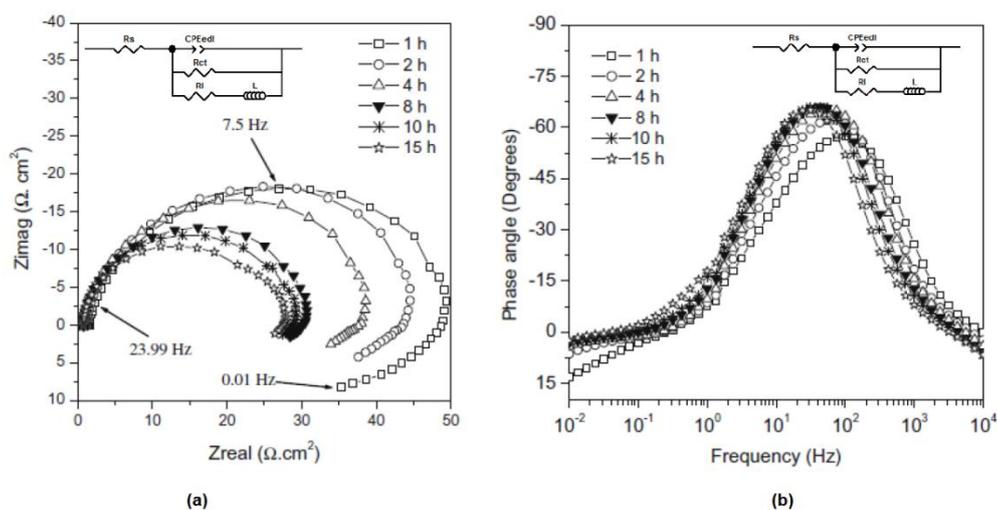
Figure 9.16: (a) Nyquist and (b) phase plots by Farelas *et al.* [218] for C1018 steel in 3% NaCl saturated with CO$_2$ under 0.5 m/s flow velocity and 45°C.

The impedance plots suggest that the material is still corroding but stable as the corrosion kinetics at the electrode surface slowly stablised to a constant rate. It has been reported that the dissolution process is governed by the revealing of iron carbide (Fe_3C) on the surface of the material [218, 220]. To confirm this assertion, an SEM image of the sample after the test without sand was taken and displayed in Figure 9.17. This SEM image shows the appearance of the iron carbide layer on the sample's surface after the test. A closer look at the image reveals darker spots which are believed to be signs of pit propagation that may be related to Fe_3C as proposed by Crolet *et al.* [220].
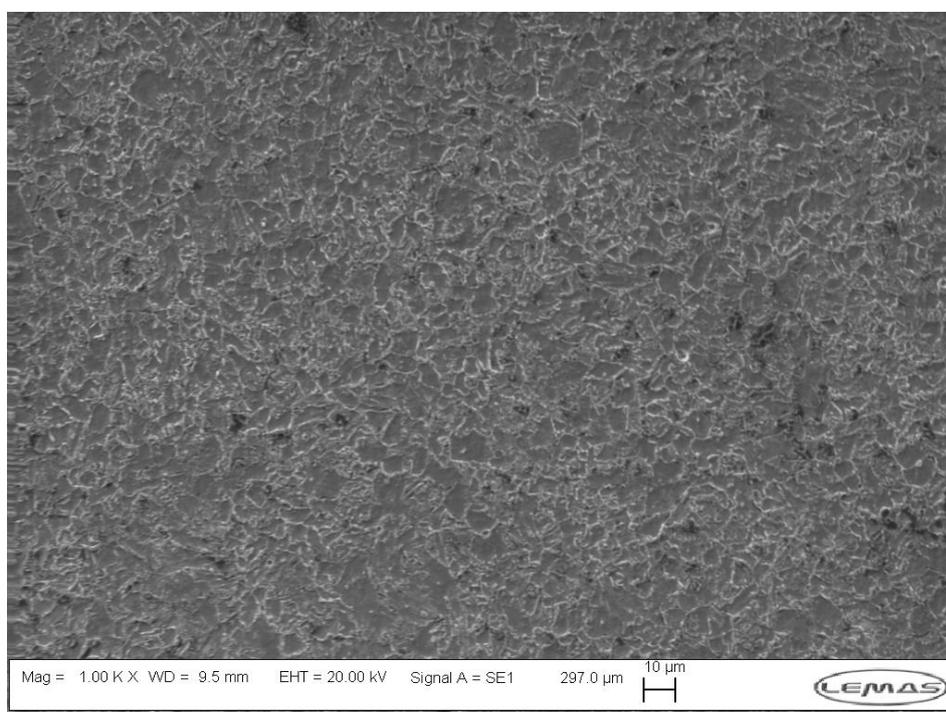
Figure 9.17: SEM image of X65 carbon steel sample after test for 7 m/s flow velocity without sand revealing Fe₃C on the sample's surface

It has been established in CO_2 corrosion studies of carbon steel that Fe_3C acts as an electronic conductor where the reduction of hydrogen ions takes place following the intermediate reactions at the interface [207, 218, 220]. Investigations by Lopez *et al.* [221] and Crolet *et al.* [220] have shown that the dissolution of ferrite can leave behind a cementite network which forms preferential cathodic sites with a lower overpotential

that favours hydrogen evolution. They maintained that this process creates microgalvanic cells between the Fe_3C and the ferrite phases, leading to selective dissolution of the ferrite phase (α-Fe) and thereby affecting the corrosion kinetics through galvanic coupling.

Iron carbide enhances the cathodic reaction, with the electrons being supplied from the anodic pit [207]. The production of metal ions attracts anions, particularly Cl^-, into the pit and the soluble chlorides formed hydrolyse and reacts with water to produce hydrochloric acid thereby increasing the local pH which can enhance materials dissolution. An illustration of this process is shown in Figure 9.18.

The production of Fe^{2+} causes Cl^- ions to migrate towards the pit. The hydrolysis of cations to produce hydrochloric acid would then lower pH:
$$FeCl + H_2O \rightarrow FeOH + HCl$$
This is the internal acidification process under the Fe_3C layer

Surrounding Fe_3C acts as a site for hydrogen evolution
$$2H^+ + 2e^- \rightarrow H_2$$

Anodic pitting site (ferrite)
$$Fe \rightarrow Fe^{2+} + 2e^-$$

Pits form as a result of micro-galvanic cells created between Fe_3C (cathodic) and ferrite phase (anodic) because of their potential difference

Figure 9.18: An illustration of anodic pit with a large cathodic Fe₃C surface which enhances the material dissolution [207].

Kermani and Morshed [9] have reported that Fe_3C can influence the corrosion kinetics and may increase corrosion rate by a factor of 3 to 10 in certain conditions. They further proposed that Fe_3C can play a significant role as well as creating galvanic coupling with local acidification, Fe^{2+} enrichment and film anchoring. The influence of the cathodic sites of Fe_3C was suggested by Farelas et al. [218] to have great effect at carbon content of more than 0.1 wt.%. The carbon content in this study is 0.12 wt.% which is in line with their statement.

9.4.2 Investigation of the Inductive Loop in the 7 m/s EIS Plots

The EIS plots for 7 m/s flow velocity presented in Figure 9.1 indicate the presence of an inductive loop at LF region which did not disappear after the two hours test. Similar observations have been made by Barker *et al.* [207], Farelas *et al.* [218], and Li *et al.* [222]. Barker *et al.* [207] and Farelas *et al.* [218] observed that the inductive loop disappears on its own accord with time after three hours whilst Li *et al.* [222] noted that applying impedance measurements at increasing levels of anodic potential from E_{corr} to 1600 mV resulted in the change of the inductive loop into a capacitive loop. Although EIS measurements were performed at only E_{corr} in this study which is similar to Barker *et al.* [207] work, the theories they used in explaining their data can be applied here to explain the inductive loop observed in this study.

The mechanisms of the carbon steel corrosion in the active dissolution region may entail a series of reactions and the theories used in the past to explain the active adsorption and charge-transfer mechanisms operating on the active corroding surface sites may be based on the 'catalysed mechanism' of Heusler [223] for highly active material with a high density of multidimentional crystal imperfections, or the 'consecutive (non-catalysed) mechanism' of Bockris *et al.* [224] for high-purity iron with low surface activity. Keddam *et al.* [225], Schweickert *et al.* [226] and Li *et al.* [222] have used either of these nechanisms to explain the inductive loops in their EIS results.

Keddam *et al.* [225] investigated the dissolution of iron in acid medium and their impedance data revealed three inductive loops at low frequencies in addition to a high-frequency capacitive loop. They maintained that the inductive loops were due to adsorption of different corrosion intermediates from three dissolution paths that are surface structure dependent. Their work was in agreement with the work of Schweickert *et al.* [226] who proposed that a polycrystalline metal surface such as iron is inhomogeneous and is marked with discontinuities in the form of grain boundaries, atomic step lines, kinks and others. Such a surface is subdivided in different

microregions with different electrochemical behaviour depending on the crystal orientation, micro-roughness, and dislocation density. Following the mechanism proposed by Bockris *et al.* [224], Li *et al.* [222] suggested that Reactions 9.1 to 9.3 can be used to explain the EIS results from their tests with carbon steel in 0.5 M H_2SO_4:

$$Fe + H_2O \leftrightharpoons (FeOH)_{ads} + H^+ + e^- \qquad\qquad (9.1)$$

$$(FeOH)_{ads} \rightarrow FeOH^+_{sol} + e^- \qquad\qquad (9.2)$$

$$FeOH^+_{sol} + H^+ \leftrightharpoons Fe^{2+}_{sol} + H_2O \qquad\qquad (9.3)$$
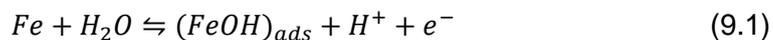
For the particular condition in their tests, Li *et al.* [222] proposed that at potential close to E_{corr}, most of the $FeOH_{ads}$ formed is taken up by Reaction 9.2 which is believed to create the inductive behaviour and that the influence of its coverage do not affect Reaction 9.1. They maintained that increasing the applied anodic potential of the AC measurements resulted in enhancement of metal dissolution and the build-up of $FeOH_{ads}$ on the surface which shifts the equilibrium of Reaction 9.1. The adverse influence of the adsorption on the surface resulted in the change of the inductive loop to a low frequency capacitive loop.

In view of the above, the inductive loop observed in this study can be attributed to adsorption of FeOH on the sample's surface which did not disappear for two hours test duration. Extending similar test to four hours, Barker *et al.* [207] proposed that instead of the increasing anodic potential of the impedance measurements applied by Li *et al.* [222], it is the gradual formation of Fe_3C that enhances the dissolution process through the creation of more favourable cathodic sites for hydrogen evolution. They maintained that the increase in the rate of metal dissolution results in the accumulation of $FeOH_{ads}$ on the surface. As the adsorption of the intermediate product becomes more significant, the inductive loop begins to disappear, which is in line with the work of Farelas *et al.* [218] and Zhang and Chang [227].

9.4.3 10 and 15 m/s Flow Velocities

At 10 and 15 m/s flow velocities with and without sand loading, one capacitive loop is observed. The capacitive loop characterises the active corrosion state upon exposing the sample to the solid-liquid impingement of CO_2 saturated brine and the charge transfer process generated at the interface of the steel and solution [228].

For the velocity effect, it was observed that the amplitude of the capacitive semicircle decreases with increase in flow velocity (Figure 9.9) meaning that the metal dissolution (corrosion rate) increases with increase in flow velocity. Similar observation has been made by Orazem and Filho [229] who used SIJ to investigate the influence of fluid velocity on corrosion of X52 carbon steel in CO_2 saturated brine for 24 hours. Their impedance response showed no particular trend when plotted as a function of time as shown in Figure 9.19a whilst the response as a function of jet velocity (expressed as hydrodynamic constant) fell into three zones as illustrated in Figure 9.19b.

According to them, at low jet velocities, the impedance decreased with increasing hydrodynamic constant, and mass transfer was controlled by diffusion through a film coupled with convective diffusion. At intermediate jet velocities, the value of their impedance was independent of velocity, suggesting that mass transfer was controlled by diffusion through a film. At higher velocities, surface films were removed by hydrodynamic shear forces, and the impedance response was again influenced by convective diffusion.

In comparison therefore, since there was no protective film formed in this study, increased mass transfer at the sample's surface as the flow velocity increases may be responsible for the increased metal dissolution rate as the flow velocity increases.
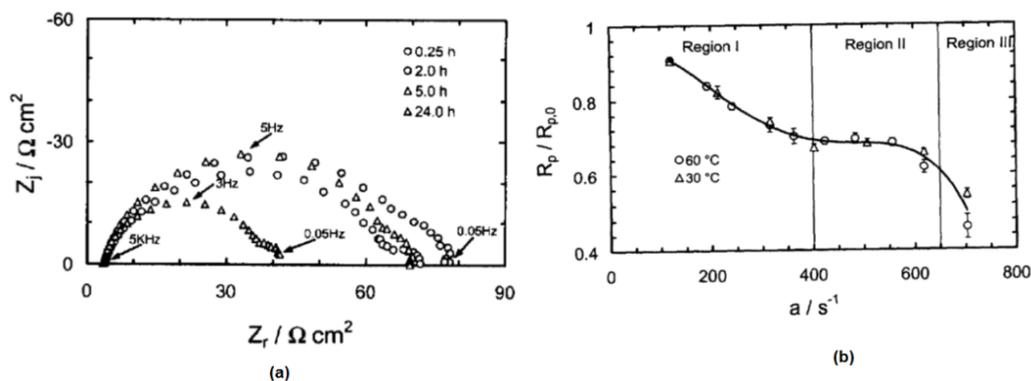
Figure 9.19: (a) Nyquist plot and (b) AC impedance parameter as a function of hydrodynamic constant by Orazem and Filho [229].

For the sand loading influence, it was noticed that the amplitude of the capacitive semicircle decreases slightly with increase in sand loading (Figure 9.10), an indication that EIS measurements were not very sensitive to the effect of the sand loading on the metal dissolution rate, even at a high flow velocity of 15 m/s where it is believed that the selective dissolution of a ferrite phase would lead to easy removal of the hard particles in micro-structure which can result to acceleration of the material damage through erosion process. The changes in the capacitive semicircle identified from the associated changes in the charge-transfer resistance (R_{ct}) as the flow velocity increases without and with sand loading are summarised in Figure 9.20 with their corresponding cumulative AE energy after each of the two hours test duration.

The material dissolution effect was quite visible on changes in charge-transfer resistance (R_{ct}) as flow velocity increases, whilst the sand loading effect on the R_{ct} was very small when compared with the effect on AE energy (as shown in Figure 9.20), an indication that AE measurement detected the changes in the sand loading that are not sensed by the EIS measurements. Though there was a significant total material loss as sand loading is increased as determined by gravimetric technique and plotted in Figure 9.21, EIS did not sense this significant difference which was as a result of the interaction between corrosion and erosion. A great deal of information regarding the interaction of corrosion and erosion is missed by using EIS alone. Therefore combining

the EIS measurements with AE monitoring can help give an insight to understanding the interaction and the extent of mechanical damage contribution during erosion-corrosion degradation of carbon steel materials in CO_2 environment.
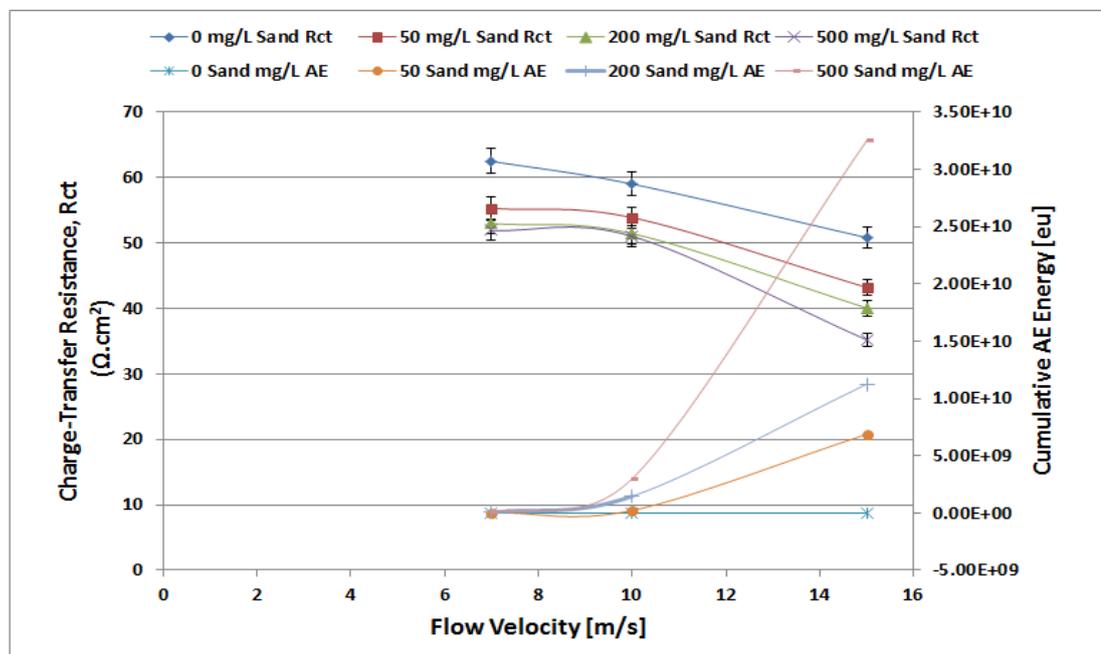
Figure 9.20: The relationship between the charge-transfer resistance and flow velocity (LHS) with Cumulative AE and flow velocity (RHS) for all sand concentrations.
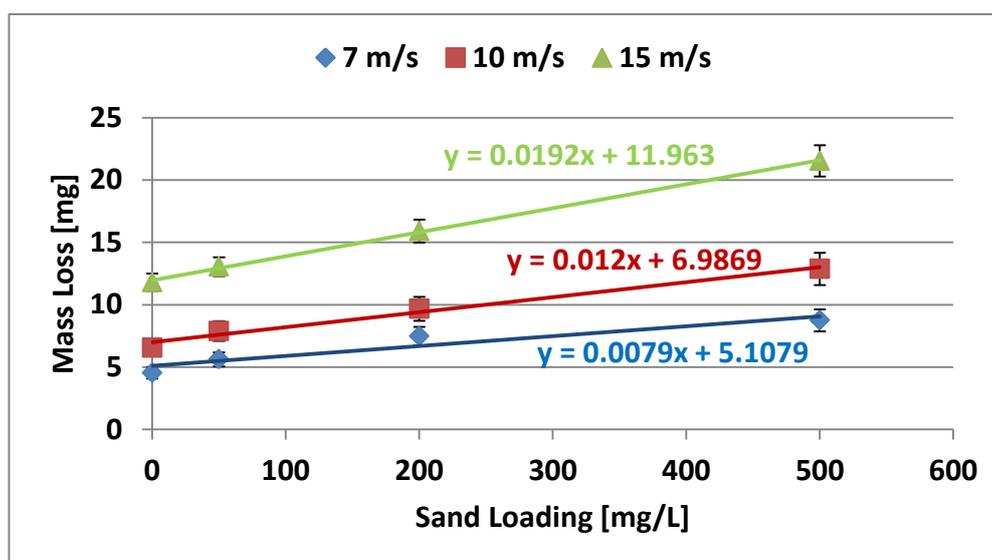
Figure 9.21: Total mass loss vs. sand loading from gravimetric technique.

9.4.4 Determination of Corrosion Rate

The DC technique which was applied in this study in Chapter 8 mainly used linear polarisation resistance (LPR) for determining corrosion rate. It was the investigations of Epelboin *et al.* [230] on iron in H_2SO_4 with propargylic alcohol that stimulated interest in the use of electrochemical impedance spectroscopy (EIS) technique for determination of corrosion rate. Though, they observed that EIS may have some uncertainties regarding interpreting corrosion rates when the plots become complicated and manifest additional capacitive or inductive loops as encountered in this study.

Two approaches were identified in determining corrosion rate from EIS data [230, 231, 232]. One is the use of charge-transfer resistance (R_{ct}) value of the equivalent circuit model [230] whilst the other is the use of the resistance value (termed 'R_p') [232] determined when the inductive loop is extrapolated to the x-axis by simulating the behaviour down to zero frequency as shown in Figure 9.22.

The charge-transfer resistance, R_{ct}, can be obtained directly from the equivalent circuit model, whilst the polarisation resistance R_p can be estimated by applying the equation proposed by Lorenz and Mansfeld [232] and Aksut *et al.* [233] who assumed that in the limit of zero frequency, the impedance approaches the DC resistance, and involves modelling the behaviour down to zero frequency and deducting the solution resistance from the value obtained:

$$R_p = \lim_{\omega \to 0} |Z| - R_s \qquad (9.4)$$
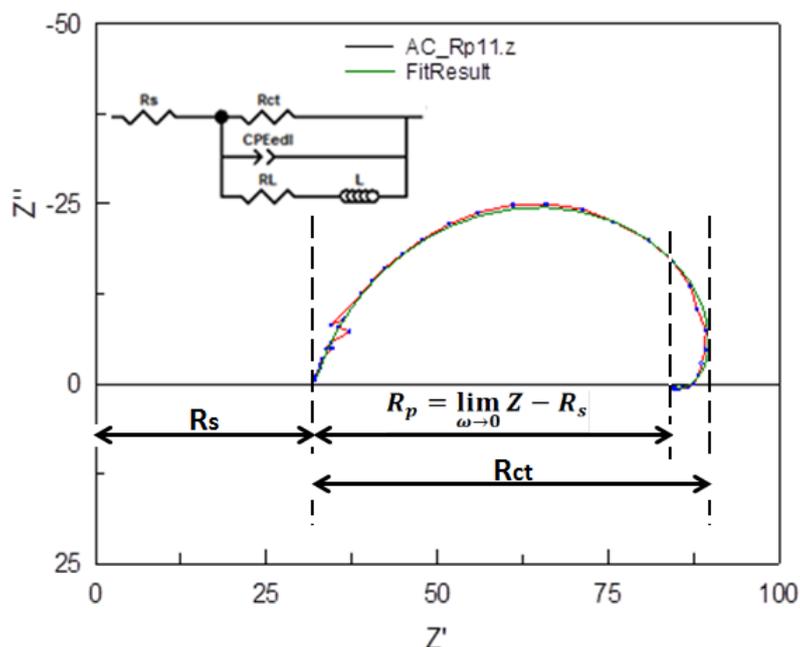
Figure 9.22: Estimation of R_p and R_{ct} from EIS data with inductive loop.

Epelboin *et al.* [230] have applied the first approach whilst Lorenz and Mansfeld [232] have applied the second approach in the respective studies. From Figure 9.22, it is evident that R_{ct} equals R_p only when one capacitive semicircle occurs in the EIS plot which signifies that such mechanism is only estimated by the process of charge-transfer controlled reactions. However, in most corrosion systems just like the one considered in this study, the EIS diagrams can contain additional inductive and capacitive loops.

Due to the existence of the additional loop for 7 m/s flow velocity data, both R_{ct} and R_p values were estimated from the EIS plots as a function of time and shown in Table 9.4 for the purpose of comparison with R_p values from DC (linear polarisation resistance, LPR) technique. The R_p values from EIS using the zero frequency approach are closely in agreement with the R_p values from LPR, thus confirming the accuracy and efficacy of the AC in determining corrosion rate. For 10 and 15 m/s flow velocities with one capacitive loop, R_{ct} is equal to the EIS R_p. The values are shown in Tables 9.5 and 9.6.

Table 9.4: Comparison of R_p from EIS with R_p from LPR for 7 m/s flow without sand

Time (mins)	$R_p = \lim_{\omega \to 0} Z - R_s$ ($\Omega.cm^2$)	R_p from LPR (less R_s) ($\Omega.cm^2$)	R_{ct} ($\Omega.cm^2$)
0	50.08(±1.8)	51.13(±2.7)	64.63(±2.1)
30	53.24(±2.3)	52.78(±1.6)	65.62(±1.8)
60	55.37(±2.4)	54.12(±2.2)	66.65(±1.6)
90	55.33(±1.2)	54.03(±1.3)	67.42(±3.2)
120	55.33(±1.4)	54.03(±1.2)	67.54(±1.9)

Table 9.5: Comparison of R_p from EIS with R_p from LPR for 10 m/s flow without sand

Time (mins)	R_p from LPR (less R_s) ($\Omega.cm^2$)	R_p from EIS = R_{ct} ($\Omega.cm^2$)
0	47.96(±1.4)	58.99 (±1.7)
30	48.51(±1.7)	59.30 (±1.4)
60	49.23(±1.3)	60.81(±2.5)
90	50.72(±1.2)	62.06(±2.8)
120	50.64(±1.3)	64.18(±1.8)

Table 9.6: Comparison of R_p from EIS with R_p from LPR for 15 m/s flow without sand

Time (mins)	R_p from LPR (less R_s) ($\Omega.cm^2$)	R_p from EIS = R_{ct} ($\Omega.cm^2$)
0	40.28(±2.4)	50.85(±1.3)
30	40.84(±1.8)	50.58(±1.5)
60	41.02(±1.5)	51.23(±2.3)
90	42.45(±1.3)	51.50(±1.7)
120	43.38(±1.4)	51.69(±1.6)

To determine the corrosion rate at the end of each test, the corrosion current density was calculated using the relationship:

$$i_{corr} = \frac{B}{R_p} \qquad (9.5)$$

where i_{corr} is the corrosion current density (Amp/cm^2), B is the Stern-Geary coefficient (mV) and R_p is the polarisation resistance ($\Omega.cm^2$). Using the R_p at the end of the 7 m/s

flow velocity test as an example and Stern-Geary coefficient of 26 mV, the corrosion current density was estimated to be approximately 0.5 x 10^{-3} Amp/cm^2. Applying Faraday's law (Equations 2.30 and 2.31) gives corrosion rate of 5.80 mm/yr which is higher than the corrosion rate of 2.8 mm/yr obtained at the end of the 7 m/s flow velocity without sand using R$_p$ of DC measurement with uncompensated solution resistance presented in Chapter 8. This implies that using the R$_p$ of DC technique with uncompensated solution resistance under-estimates the corrosion rate whilst AC technique gives accurate measurement.

9.5 Evaluation of Erosion-Corrosion Degradation and Its Components

Erosion-corrosion degradation process can be considered to compose of four different components as follows:

$$TML = (E + dE_C) + (C + dC_E) \qquad (9.6)$$

Electrochemical measurement gives information on corrosion contribution $(C + dC_E)$ whilst gravimetric analysis determines overall degradation in form of total mass loss (TML), the balance is mechanical erosion contribution $(E + dE_C)$ where E is pure erosion in the absence of corrosion (estimated in previous study with tap-water saturated with N$_2$), dE_C is corrosion enhancing erosion, C pure corrosion in the absence erosion (normally determined in static condition) and dC_E is erosion enhancing corrosion. The R$_p$ obtained from EIS measurement (Equation 9.4) was then used to calculate corrosion rate in mm/year by applying Stern-Geary equation (Equation 9.5) and Faraday's Law (Equations 2.30 and 2.31) and converted to mass loss in mg to get the electrochemical damage component $(C + dC_E)$ using the expression [234, 235]:

$$Corrosion\ Rate, CR\ \left(\frac{mm}{yr}\right) = \frac{Mass\ Loss\ (g)x\ K}{Density\left(\frac{g}{cm^3}\right)x\ Area\ (cm^2)x\ Time\ (hr)} \qquad (9.7)$$

where K is a factor with value 8.76 x 10^4.

The corrosion component mass loss ($C + dC_E$) was then subtracted from TML obtained from gravimetric technique to get the mechanical damage component ($E + dE_C$).

Figures 9.23 to 9.27 show the mass loss results together with measured cumulative acoustic emission energy after each of the 2 hours test which is a representative of the energetic flux of impacting particles. The test results for flow-induced corrosion (0 mg/L sand loading) tests were included for clarity and to show the effect of sand in the material damage.
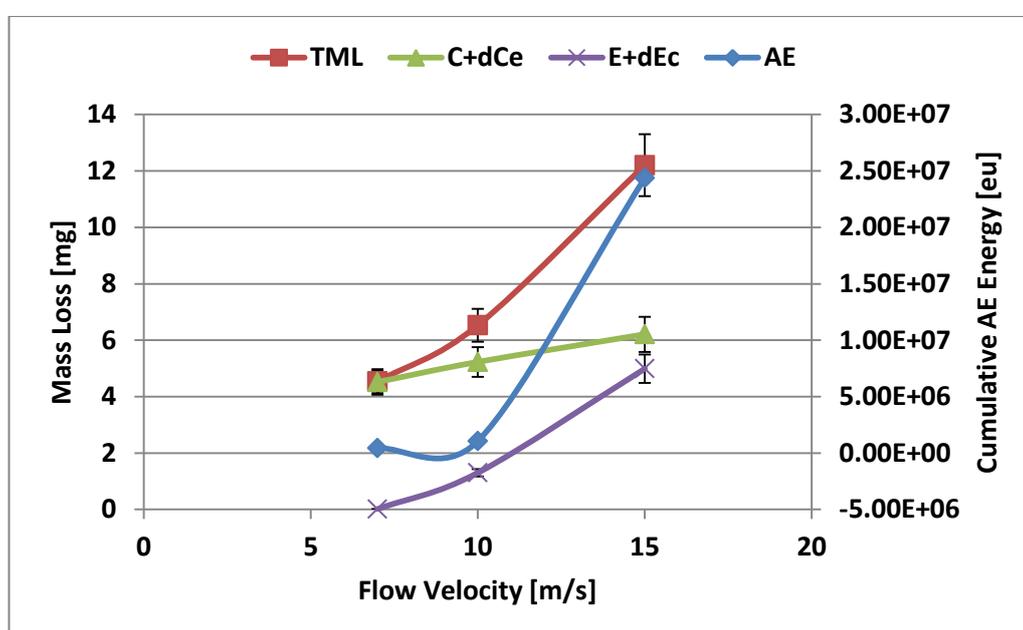
Figure 9.23: Total erosion-corrosion damage with its components and measured cumulative AE Energy for 2 hours expressed in energy unit [eu, 1eu =1E-18J] for all the flow velocities investigated without sand.
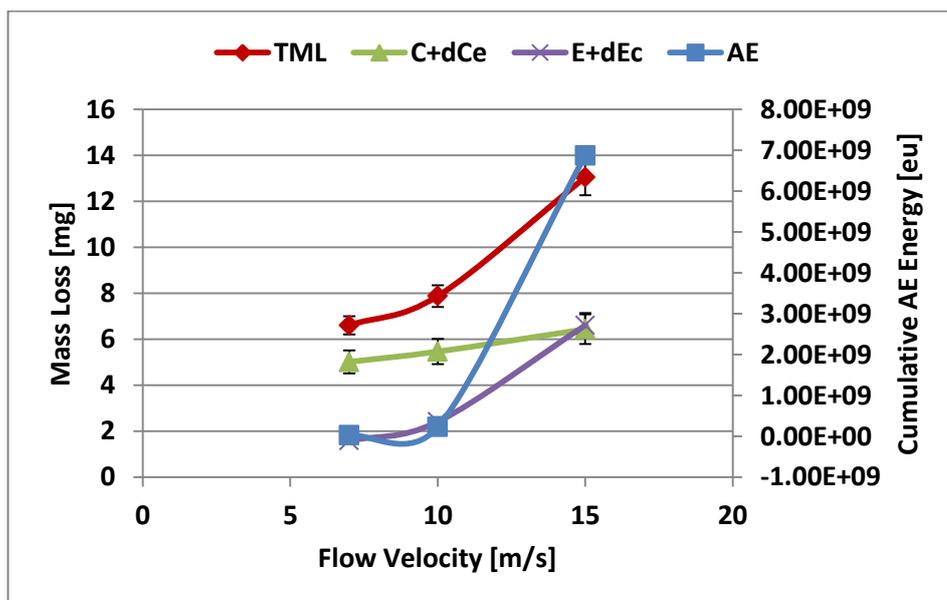
Figure 9.24: Total erosion-corrosion damage with its components and measured cumulative AE Energy for 2 hours expressed in energy unit [eu, 1eu =1E-18J] for all the flow velocities investigated with 50 mg/L sand loading.
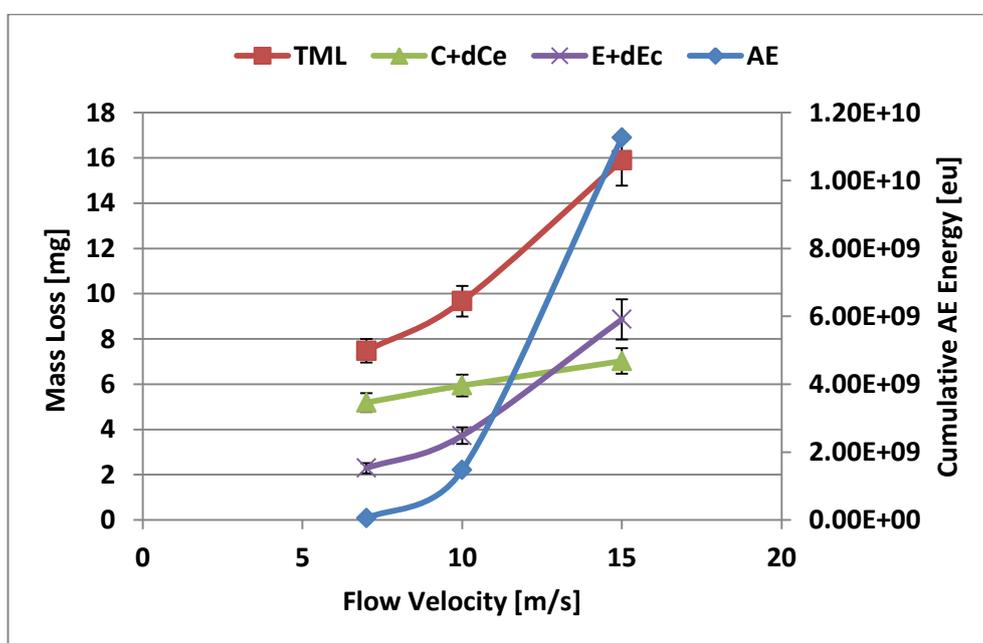
Figure 9.25: Total erosion-corrosion damage with its components and measured cumulative AE Energy for 2 hours expressed in energy unit [eu, 1eu =1E-18J] for all the flow velocities investigated with 200 mg/L sand loading.
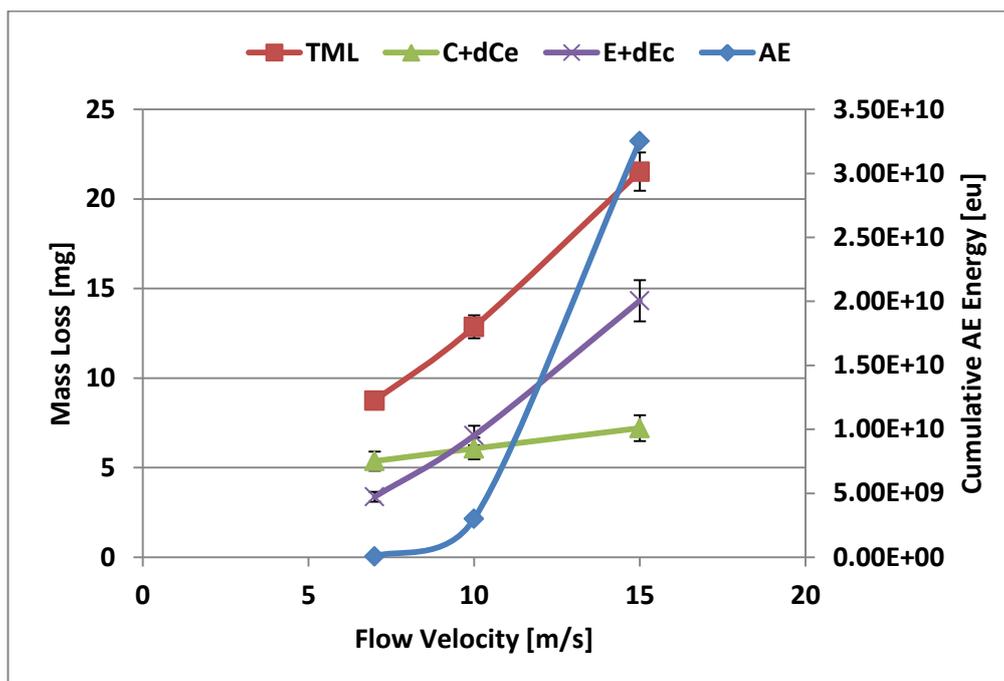
Figure 9.26: Total erosion-corrosion damage with its components and measured cumulative AE Energy for 2 hours expressed in energy unit [eu, 1eu =1E-18J] for all the flow velocities investigated with 500 mg/L sand loading.

From these plots in Figures 9.23 to 9.27, it is observed that without sand loading, increasing the flow velocity from 7 m/s to 15 m/s led to an increase in total mass loss (TML) from 4.5 mg to 12.2 mg as well as the cumulative AE energy from 4.3 x 10^{5} eu to 2.4 x 10^{7} eu. These values increase monotonously with respective increase in the sand concentrations.

At low flow velocity (7m/s) without sand loading, corrosion damage contribution is dominant whilst erosion damage contribution is insignificant. As the flow velocity and sand loading are increased, the effect of sand erosion is noticed significantly in the total mass loss (TML), the erosion component $(E + dE_C)$ and the cumulative AE energy whilst the corrosion component $(C + dC_E)$ did not change significantly. This means that the AE technique was quite sensitive to changes in the materials degradation as a result of the sand loading which the EIS measurement neglected. This observed increase in TML with its components agrees well with the previous study of Hu and Neville [41, 42] where critical values of sand loading and flow velocity were established

to show the change of the degradation mechanism from flow-induced corrosion regime to erosion-corrosion regime.

At higher flow velocity and sand loading (15 m/s and 500 mg/L), erosion damage component becomes dominant and contributes over 66% of the total material degradation. These results are in agreement with tests performed by Neville and Wang [43, 236] at 20 m/s and 50°C with 500 mg/L sand loading onto similar carbon steel samples and brine where the corrosion contribution of $(C + dC_E)$ only amounted to 30% because of the severity of the erosion component and the total degradation rate exceeded 20 mm/year. It is important to also note that the *in-situ* corrosion rate $(C + dC_E)$ contribution did not change significantly with addition of sand for all the flow velocities investigated, signifying that the damage when sand was added came from the mechanical damage contribution $(E + dE_C)$.

Furthermore, it may be expected that since no protective film was formed (because supersaturation of ions to form $FeCO_3$ film can hardly be reached on the surface as the Fe^{2+} ions produced by the corrosion process are constantly flushed away by the flow) [42], the sand addition failed to significantly influence the *in-situ* corrosion rate as was also observed in similar previous studies [40, 236]. Thus, the total mass loss would therefore be expected to comprise entirely of pure electrochemical corrosion (C) and pure erosion (E).

The effect of the mechanical damage which was not sensed by the *in-situ* corrosion measurement using EIS was significantly noticed by the AE method that gave rise to much increase in cumulative AE energy as the sand loading and flow velocity were increased. These detected changes may be as a result of increased erosion damage as a result of sand impacts which will create more micro displacements on ths specimen's surface, thus giving rise to high acoustic emission rate. Being a measure of the energetic flux of impact particles, the AE energy can give an insight of the mechanical damage contribution as it is very low when the mechanical damage is

negligible and increases monotonously with increase in mechanical damage. This will be very useful in monitoring the material damage at the erosion dominant regimes of the erosion-corrosion degradation processes.

9.6 Summary

A technique combining EIS and AE has been used to assess erosion-corrosion degradation of X65 pipeline materials in saturated CO_2 environment and at $50^{\circ}C$. Results indicate that EIS captured the electrochemical corrosion damage component with a mechanism of active charge-transfer and adsorption at low flow velocity and pure charge-transfer mechanism at medium to high flow velocities.

The mechanical erosion damage component which was not sensed by EIS was adequately captured by the AE technique via sand impact effects. Hence, combining of these two techniques can help in *in-situ* monitoring of both the electrochemical and mechanical damage contributions in the erosion-corrosion degradation of petroleum pipelines in service for effective integrity monitoring and maintenance planning of the pipelines.

Chapter 10 Overview and General Discussion

10.1 Introduction

The combination of acoustic emission (AE) and electrochemical monitoring in this study has helped in understanding the mechanical and electrochemical damage due to the interaction between erosion and corrosion processes on X65 carbon steel sample's surface. Figure 10.1 shows the steps followed in the course of the study to understand the interaction between erosion and corrosion.

This chapter follows these steps to sum up all the discussion presented in previous chapters with a view to linking all the chapters' discussion together.
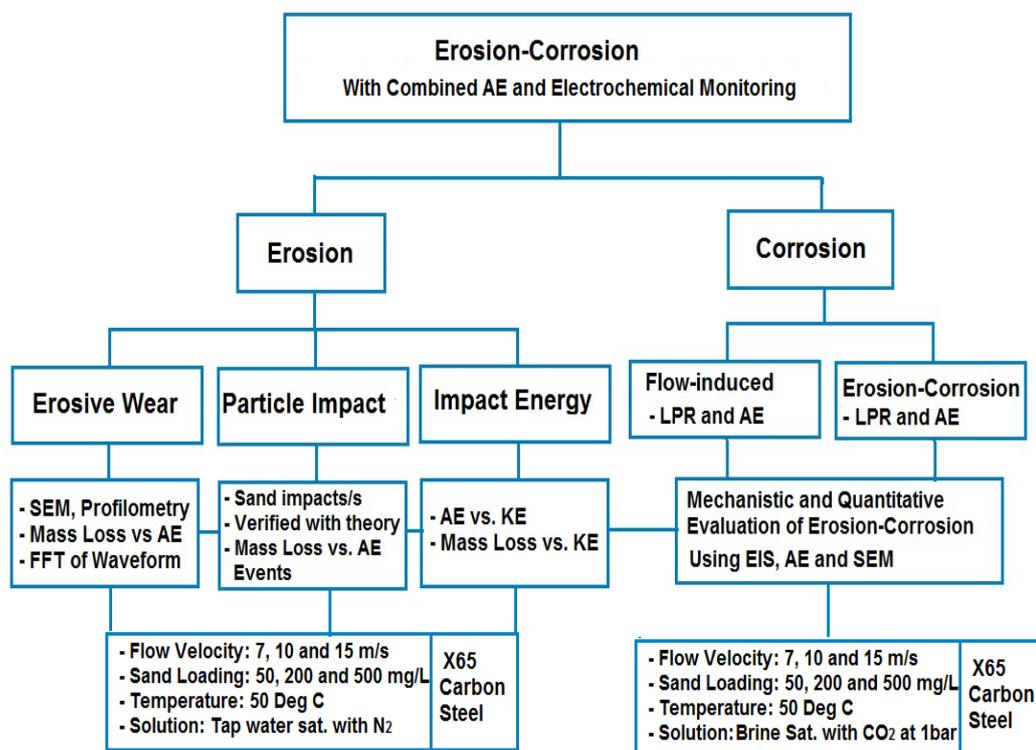
Figure 10.1: An overview of study and the approaches applied to gain proper understanding of the interaction between erosion and corrosion

10.2 Erosion

In the erosion aspect, the importance of applying AE in the quantification of mechanical damage readily comes to mind. This is based on established theory [101, 174, 175,

176] that an impact on a solid material gives rise to the release of AE. This theory was confirmed in this study by performing single impingement experiment using glass beads. The AE parameter in the form of AE energy and RMS value was plotted against the KE of the impacting glass beads, and a relationship was established which is in agreement with previous investigations by Oltra *et al.* [186] and Ferrer *et al.* [187]. It was observed that the percentage of KE emitted as AE during the impingement is lower in this study than those obtained by them [177, 178] which may be as a result as different configuration of the impinging jet.

The impinging jet in this study is a submerged jet whilst they [186, 187] used non-submerged jet. The submerged jet may create an increase in inertia, drag effects and hydrodynamic boundary layer deceleration of impacting beads in the flowing stream which may reduce the energy of the impinging beads when compared to the non-submerged jet. The inertia arises due to its weight, the drag effect originates from buoyancy forces and its weight which try to resist the forward movement, and the bead must penetrate the boundary layers of the liquid on the specimen surface before impacting it [104]. The penetration of this layer can decelerate the bead and reduce the impact velocity. When all these happen, the KE available on impact may be lower than that available in dry condition hence giving rise to lower percentage of the measured AE energy in wet condition and much more lower in submerged condition. Higher percentages of AE released for a given value of KE which were reported in air-borne impact by Hunter [174] and Hutchings [176] confirm this assertion.

10.2.1   Erosive Wear

Hutchings [83, 101, 176] suggested that the erosive wear of a target material will occur if the impact is plastic i.e. causes plastic deformation or cutting of the target materials. In the past, some investigations have been performed to verify this and characterise the damage related to an individual impact. Specifically, Shimuzu *et al.* [237] performed individual impact erosion tests using spherical glass particles on a copper target which

were conducted in a vacuum to eliminate the fluid-dynamic drag force that retards the particle motion before impact upon the target. They estimated the erosion rate by averaging the mass loss due to several impacts and compared their results with theoretical values based on the model developed by Finnie [99]. Since their results were in agreement with Finnie [99], they believed that the overall damage of the material is by combined plastic deformation and cutting mechanisms. Deformation occurs when each impact is normal i.e. 90° impact angle. Repeated normal impacts of particles gradually make the target material brittle through cold working and the surface is broken into small fragments at a certain subsequent attack. On the other hand, cutting erosion occurs when particles collide upon the target with relatively small angle i.e. when the collision is tangential to some extent. Sharp corners of oncoming particles scratch the surface when they move on it and this becomes serious when the target is made of a ductile material. The effect for ductile material is that erosion rate reaches maximum when the impact angle is from 20° to 30° which will be mainly cutting mechanism and minimum when the impact angle is from 60° to 90° with deformation mechanisms. Based on this proposition, the erosion damage of the target is sum of the damage done by multiple impacts.

Therefore, the mass loss from multiple sand impact erosion tests was determined in this study by gravimetric technique and correlated with average AE energy. The relationship indicates that significant mass loss does not occur until average AE energy exceeds a certain critical value which is equal to $10^{6}eu$ for 50 and 200 mg/L sand concentrations and 10^{7} eu for 500 mg/L sand loading. The variation in critical AE energy values as the sand loading increases may be due to the variation in sand particle sizes. Also, two regions were identified in the plot. The first region is the region of pure elastic impact which generates AE but does not cause erosive wear as proposed by Hunter [174]. This region falls within the low flow velocity (7 m/s) data and is in agreement with the work of Buttle and Scruby [235] who conducted a particle impact study by quantitative AE using bronze and glass spherical particles on steel

target and discovered that at low flow velocities (2.5 to 7.1 m/s), the impacts are purely elastic and no erosion occurred. The second region is the region of plastic deformation, ploughing and cutting leading to significant erosion damage with associated AE as proposed by Miller and Pursey [175] and confirmed by Hutchings [176]. This region occurs above 7 m/s flow velocity.

Thus, increasing the flow velocity beyond 7 m/s leads to increase in kinetic energy of the particle which will cause large erosive wear scar and would accelerate erosion rates. Particles with higher velocity, thus larger kinetic energy will deform or cut deeper into the surface and produce more wear debris which is carried away by the flowing fluid jet. The increase in flow velocity also causes higher number of impacts per second for a given concentration, hence increasing material removal during each impact. It was also observed that an increase in sand loading beyond 7 m/s flow velocity leads to significant material loss. This is because an increase in sand concentration increases the number of particles impacting the surface. This increase would lead to higher density of impact and lips formed on the surface which can lead to higher material loss.

Visual inspection, SEM and profilometry images of the tested sample confirm that the mass loss of the material was as a result of the deformation, ploughing and cutting mechanisms at different impact angles which are consistent with the studies by Gananvelu *et al.* [110], Li *et al* [119], Matsumura et al. [121], and Zu *et al.* [238, 239].

Furthermore, frequency spectra of some of the detected AE waveforms from the erosive wear investigation were equally evaluated using fast Fourier Transform (FFT) of ORIGINLAB software. It was observed that frequency peaks occur at low frequency region (< 0.2 MHz) when erosion damage is negligible i.e. when impact is more or less elastic. On the other hand, when impact becomes plastic as a result of deformation, ploughing or cutting leading to significant erosion, then the frequency peaks appear at high frequency (> 0.2 MHz) in addition to the low frequency peaks. Whilst the high frequency peaks can be attributed to the damage mechanisms occurring at the

samples surface, the low frequency peaks may be associated with the sample's resonances [240]. A comparison of the frequency spectra results was made with the results obtained by Lee *et al.* [241] in their AE condition monitoring of check valves showing disk wear failure modes in a nuclear power plants as illustrated in Figure 10.2 and a similar appearance was observed on both spectra. Both results have the low frequency peaks at 150 kHz believed to be the sample's resonances [240] and high frequency peaks associated with damage mechanism which is 425 kHz in this study and 225 kHz in Lee *et al.* [241] study. This information can give an insight of the damage mechanisms and may provide information for stage-by-stage description of the damage and overall material degradation.

(a) This study: mass loss(0.9 mg/hr)

(a) Lee et al. disk wear (1.0 mm)

(b) This study: mass loss(3.79 mg/hr)

(b) Lee et al. disk wear (2.00 mm)
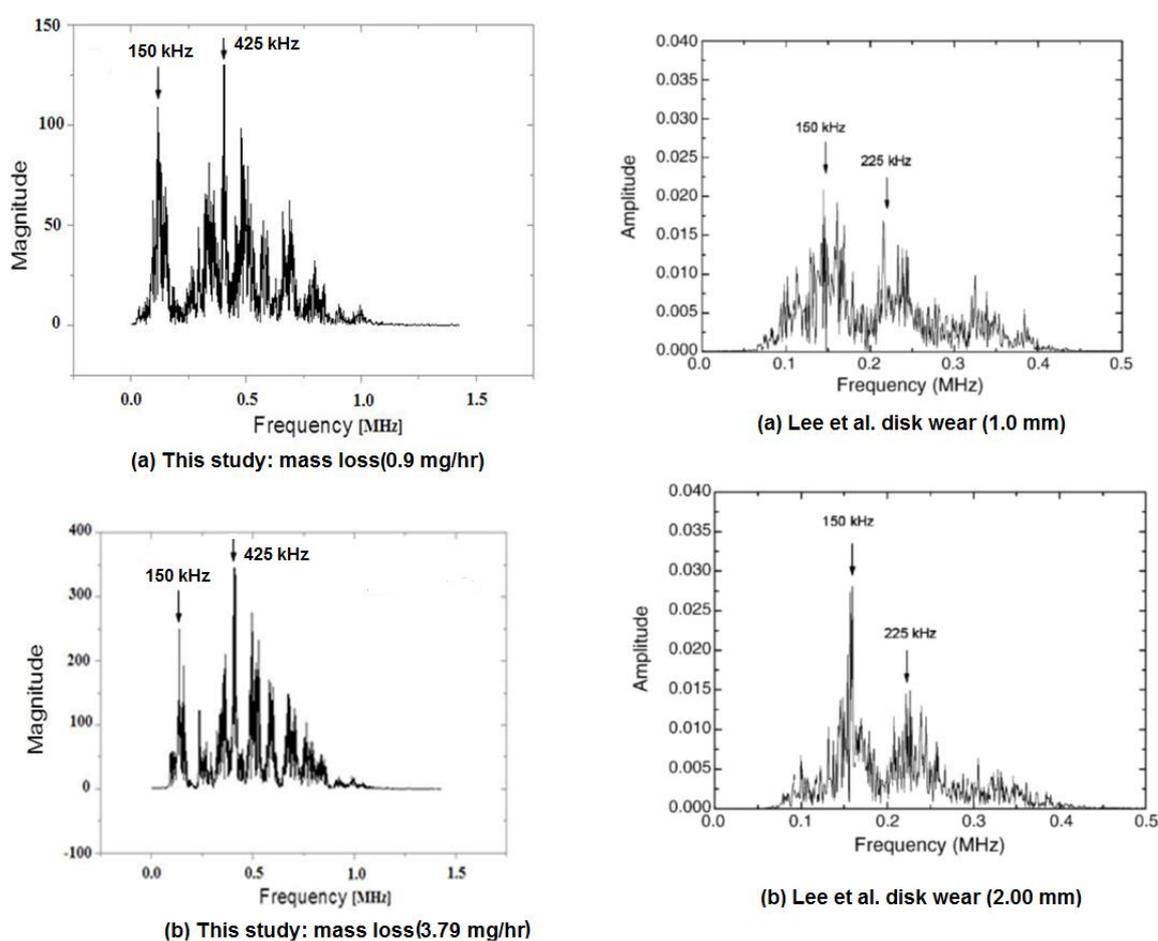
Figure 10.2: Comparison of the frequency spectra of waveform in this study (LHS) with frequency spectra from Lee *et al.* [241] (RHS) disk wear study.

10.2.2   Particle Impact Determination

A subtraction technique that deducts baseline (without sand) AE events from events associated with sand in a particular time, was used to obtain the actual AE events related to sand impacts per second.

A comparison of the measured particle impacts with the theoretical prediction revealed a good agreement for 7 and 10 m/s flow velocities in all the sand concentrations investigated whilst at 15 m/s flow, the AE technique gave higher values than the theoretical predictions. The box plots indicate that the theoretical predictions at 7 and 10 m/s flow velocities fall within the inter quartile range (25% above the mean and 25% below the mean values) of the measured data, whilst at high flow velocity (15 m/s), the AE technique predicts higher values of impacts per second than theoretical prediction. This signifies that the impact energy of the impacting particles is actually responsible for the generation of AE signals. It is possible that at high flow velocity, signals due to rebounded sand particles which are expected to be high at high flow velocity were equally detected which led to higher values of measured sand impacts at 15 m/s.

Another possible reason for the large deviation at high flow velocity could be particle-particle interactions [104] at the surface of the sample which can lead to pseudo impacts that may also be detected and recorded. Also, the much shorter interval between the particle impacts may cause excessive overlap of the impact acoustic signals and may be responsible for the large error obtained at high flow velocity and sand loading.

10.2.3   Impact Energy Quantification

The average impact energy per particle for each flow velocity was calculated using CFD with particle tracking and used to determine the overall impact energy per second of the impacting sand particles (predicted from theory) for each sand concentration. This overall impact energy per second for each flow velocity and sand concentration was then correlated with the measured acoustic emission (AE) energy per second

associated the measured number of sand impacts per second for each flow velocity and sand concentration. The impact energy was then correlated with the measured AE energy and material loss from gravimetric analysis.

The impact energy (in the order of 10^{-6}J/s) correlated well with the measured AE energy per second (in the order of 10^{-10}J/s) with a linear relationship for 500 mg/L sand and a polynomial relationship of order of two for 50 and 200 mg/L sand in all the flow velocities investigated. This signifies the dependence of the AE on the kinetic energy of the impacting particles.

The mass loss increased linearly with impact energy and it was observed that a particular impact energy can give rise to different mass losses. This is because a particular impact energy can have different erosion efficiency (ratio of wear to particle loading) depending on the sand concentration meaning that specific impact energy can cause different degrees of damage on the materials depending on the sand concentration. This may be due to the fact that the erosion efficiency decreases with increase in particle loading [115] as a result of higher amount of rebounding particles at the surface, thus protecting the surface from incident particles. The increase in sand loading also leads to greater particle-particle interaction which can reduce the number of particles impacting the surface.

10.3 Corrosion

On the aspect of corrosion, a linear polarisation resistance (LPR) measurement was first performed using a computer-controlled potentiostat which was used to apply potential change of ± 50 mV from the open circuit potential (E_{corr}) with a scan rate of 0.25 mV/s and the corresponding current measured by the potentiostat. A plot of linear graph of potential vs. current density shows that anodic current density is positive while the cathodic current density is negative. The slope of the graph near E_{corr} gave the polarisation resistance (R_p) which was used to calculate the corrosion current density

(i_{corr}) using Stern-Geary coefficient of 26 mV (assuming Tafel slope $\beta a = \beta c = 120$ mV per decade). This was then used to calculate corrosion rate in mm/year using Faraday equations. The associated AE signals were equally recorded where numbers of counts per second and average AE energy were determined for each test condition.

10.3.1   Flow-Induced Corrosion

Tests without sand gave the results for flow-induced corrosion rates which were correlated with AE count rates and cumulative counts correlated with polarisation resistance (R_p). A correlation of the results using AE energy was equally presented. The corrosion rate as well as count rate and AE energy increased with increase in flow velocity whilst the R_p decreases with increase in flow velocity as expected due to enhanced flow turbulence, wall shear stress and mass transfer of the corrosive species which ultimately leads to higher materials losses [97].

A comparison was made with the investigation of Ferrer *et al.* [172] on XC18 carbon steel in sulphuric acid solution in a flow loop at flow velocities of 0.2 to 2 m/s and some similarities were observed despite the differing conditions. Both results showed that corrosion rate increased with increase in AE activity as flow velocity increases. Ferrer *et al.* [172] proposed two explanations for this phenomenon. One is that the metal surface is subjected to a passive-active transition which can generate acoustic emission. Two is that as the flow velocity is increased, hydrodynamic local conditions in the test cell generate turbulent areas which will either generate gas bubbles or cavitation that would impact the metal surface. These impacts are sources of acoustic emission signals.

Another important observation which is believed to be related to the mechanism of the corroding surface is a decrease to steady state of the corrosion rate and AE activity with time. The initial time at the start of the test can be regarded as a high corrosion transient period characterised by active iron dissolution and high turbulence on the fresh material surface which gives corresponding high acoustic emission rate. The

steady state period could be an indication that there is a partial formation of a layer of corrosion product with established flow pattern which tends to reduce corrosion and acoustic emission rates. A similar observation was made by Wang *et al.* [43] on similar tests and material. They proposed that corrosion products might form on the surface with time and these may lessen the corrosion rate of the system. The corrosion products which are coarse in structure under this temperature and pressure also can be removed by the flowing fluid, therefore not providing protection towards corrosion.

However, Schmit and Bakalli [75] observed that when a protective scale is formed on the surface, then a critical flow intensity is required for the scale removal which can lead to increase in material loss. They believed that near-wall micro-turbulence elements cause local thinning of the scale which locally becomes porous and is finally carried away completely by the flow. Once a scale free, unprotected local surface area has formed, the local flow intensity prevents the re-formation of the protective scale, and local penetrations start producing the characteristic pattern of flow-induced localised corrosion (FILC) [75].

Hence, it can be established in this study that iron dissolution and hydrodynamic local conditions seem to be sources of acoustic emission because they create increased micro displacements on the specimen's surface which are detected by the acoustic emission sensor.

10.3.2 Erosion-Corrosion

Tests with sand loading gave the erosion-corrosion results. Similar behaviour (as in flow-induced corrosion) was observed on the variation of corrosion rate with acoustic emission activity but with higher values due to the sand impact effects. The summary of the results indicate the relevance of kinetic energy (mass of solid and velocity) with velocity as the controlling factor, thus leading to a small increase in corrosion rate for low velocity (7 m/s) when sand loading is increased from 50 to 200 mg/L. There was also a slight increase in the measured acoustic activity at 7 m/s flow which is an

indication that the measured AE actually emanated from the material degradation mechanisms. At higher flow velocities (10 and 15 m/s), significant changes were observed in the measured AE for all the sand concentrations studied, signifying the influence of flow velocity and sand loading on the overall material loss which was adequately detected by the AE set-up. The effect of sand was quite significant on the AE activity than on the R_p or corrosion rate from LPR.

The total mass loss obtained from gravimetric technique showed a significant material damage due erosion-corrosion which was different from those obtained in pure erosion investigation. This is expected because of the combined effect of sand loading and flow velocity that leads to interaction between corrosion and erosion, each affecting the other in a synergistic manner [97]. The relationship between mass loss and AE energy showed a different behaviour when compared with the relationship in pure erosion. There is significant material damage coming from corrosion at the region of elastic sand impact where there is no erosion. Hence, a good understanding of the corrosion mechanisms can be essential in combining the two techniques. Understanding the corrosion mechanisms at the sample's surface cannot be achieved using LPR, thus the need to apply a more powerful electrochemical technique known as electrochemical impedance spectroscopy (EIS).

10.3.3 Mechanistic and Quantitative Evaluation of Erosion-Corrosion

EIS was applied in understanding the corrosion mechanisms at the interface of the sample because it gives an insight into the corrosion rate-controlling mechanisms which LPR neglects. It produces values of solution and charge-transfer resistances and electrical double layer (EDL) capacitance; and these quantities can give more accurate information on the corrosion behaviour and rates. EIS and AE measurements were performed simultaneously. Two different mechanisms at the interface of the samples were identified at low flow (7 m/s) and medium to high flow (10 to 15 m/s) velocities with and without sand loading.

At 7 m/s flow velocity, without and with sand loading, the mechanism is that of an active-adsorption state similar to those proposed by Barker *et al.* [207] and Farelas *et al.* [218]. The active dissolution process evidenced in a capacitive loop at high frequency region is governed by the revealing of iron carbide (Fe_3C) on the surface of the material whilst the adsorption mechanism, evidenced in an inductive at low frequency region is due to adsorbed $Fe[OH]_{ads}$ species on the sample surface. The revealing of Fe_3C was proved by an SEM image and it is believed that Fe_3C acts as an electronic conductor where the reduction of hydrogen ions takes place following the intermediate reactions at the interface [207, 218, 220]. Previous investigations by Crolet *et al.* [220] and Lopez *et al.* [221] proposed that the dissolution of ferrite can leave behind a cementite network which forms preferential cathodic sites with a lower overpotential that favours hydrogen evolution. They argued that this process creates microgalvanic cells between the Fe_3C and the ferrite phases, leading to selective dissolution of the ferrite phase (α-Fe) and thereby affecting the corrosion kinetics through galvanic coupling. The mechanisms proposed by Li *et al.* [222], Heusler [223] and Bockris *et al.* [224] were used to explain the adsorption mechanism. Li *et al.* [222] suggested that the increase in the rate of metal dissolution results in the accumulation of $FeOH_{ads}$ on the surface. As the adsorption of the intermediate product becomes more significant, the inductive loop begins to disappear.

The mechanism for the 10 and 15 m/s flow with and without sand revealed one capacitive loop which characterises the active corrosion state upon exposing the sample to the solid-liquid impingement of CO_2 saturated brine. The Nyquist plots for all the flow velocities indicate an increase in dissolution process (corrosion rate) as the flow velocity is increased as expected because of the interaction between erosion and corrosion, and evident in the decrease in the amplitude of the impedance loop as velocity increases. This is because corrosion affects erosion rate through detachment of flakes formed by repeated solid particles impingement [119] and the preferential dissolution of the ferrite phase (α-Fe) would lead to easy removal of the hard particles

in the steel microstructure which results to acceleration of material loss [120]. Though, the sand effect on impedance data was not significant as there was a slight decrease in impedance semicircle as the sand loading is increased from 50 mg/L to 500 mg/L at 15 m/s flow. This is in agreement with Guo *et al.* [117] who observed that for active materials, even though the disturbance of sand accelerates the mass transport at the interface, it still cannot affect the corrosion rate. They further maintained that the corrosion products formed in active dissolution system could be loose, non-protective and even soluble so that the removal of the corrosion products by the impingement of solid particles cannot largely affect the dissolution rate. Thus, active metals or alloys are less sensitive to erosion-enhanced corrosion than passive metals or alloys [117].

Equivalent circuit modelling of the impedance plots was used to fit the experimental data to obtain the solution and charge-transfer resistance (R_{ct}) and electrical double layer (EDL) capacitance. Due to the existence of the inductive loop the 7 m/s flow velocity data, polarisation resistance (R_p) was estimated by applying the equation proposed by Lorenz and Mansfeld [232]. For 10 and 15 m/s flow velocities with one capacitive loop, R_{ct} is equal to the EIS R_p. These were then used to calculate the corrosion rate at the end of each test. A comparison of corrosion rate from AC with the one from DC revealed that DC technique with uncompensated solution resistance under-estimates the corrosion rate whilst AC technique gave accurate measurement. The corrosion rate (mm/year) was then converted to mass loss to give the electrochemical corrosion component ($C+dC_e$) using Equation 9.7.

The relationship between the charge-transfer resistance (R_{ct}) and cumulative AE energy with the flow velocity for all the sand concentrations investigated revealed that the material dissolution effect was quite visible on changes in charge-transfer resistance (R_{ct}) as flow velocity increases, whilst the sand loading effect on the R_{ct} was very small when compared with the effect on AE energy, an indication that AE measurement detected the changes in the sand loading that are not sensed by the EIS

measurements. Though there was a significant total material loss as sand loading is increased as determined by gravimetric technique, EIS did not sense this significant difference which was as a result of the interaction between corrosion and erosion. A great deal of information regarding the interaction of corrosion and erosion is missed by using EIS alone.

Based on this, the components of the erosion-corrosion damage consisting of the electrochemical corrosion and mechanical erosion contributions were determined and related to cumulative AE energy. The total mass loss (TML), electrochemical corrosion component ($C+dC_e$), mechanical erosion component ($E+dE_c$) and cumulative AE energy were plotted against the flow velocities without and with sand loading. It was observed that the TML increased via increase in $E+dE_c$ with the associated AE energy whilst $C+dC_e$ remained more or less stable as the sand loading increases. The corrosion component remained stable because no protective film was formed since supersaturation of ions to form $FeCO_3$ film can hardly be reached on the surface as the Fe^{2+} ions produced by the corrosion process are constantly flushed away by the flow [42]. The increase in AE energy is as a result of increase in the energy flux of the impacting sand particles as the sand concentration and velocity increase.

The increase in TML via the mechanical erosion component ($E+dE_c$) is due to corrosion enhancement of the erosion process. Some mechanisms have been proposed to explain this phenomenon. Li *et al.* [119] believed that the detachment of metallic flakes was the main material degradation mechanism during erosion-corrosion. They observed that the flakes tend to be removed by cracking in fragments after multiple particle impacts, unlike pure erosion, where the flakes were removed by ductile fracture. They stressed that corrosion enhances the erosion by localised attack at sites where corrosion product is removed during particle impact. That this localised corrosion process creates cracks at the root of the flakes and propagates with particle impacts, thus making the flakes vulnerable to detachment. Neville *et al.* [242] conducted

erosion-corrosion test on cast iron and discovered that there were corrosive attacks at the graphite/matrix interface which can cause loosening of intermediate grains of metals and subsequent removal by particle impact. Aiming *et al.* [243] suggested that the degradation of the mechanical properties of the metal due to corrosion reduces its wear resistance, making it more vulnerable to erosion attack. Though, no details were given on the mechanical property that was affected by corrosion. Matsumura *et al.* [121] believed that as the particle impacts the corrosion product layer and destroys it, dissolution of the surface leads to the elimination of the work hardened layer and increases the surface roughness which can accelerate erosion. This is because the particle can penetrate deeper into the surface.

It was then deduced that at low flow velocity (7 m/s), the material damage is corrosion dominant and can be regarded as 'corrosion regime'; therefore electrochemical monitoring alone can give an insight into the material loss. At medium to high flow velocity (10 to 15 m/s), the material degradation is erosion-corrosion dominant and can be regarded as 'erosion-corrosion regime'; therefore a combination of AE and Electrochemical monitoring can give a good information on the material loss. Moreover, at high sand loading (500 mg/L) and high flow (15 m/s), mechanical erosion damage appears to be dominant as it contributes over 66% of the material damage. Therefore reading the AE and EIS measurements simultaneously at these conditions in service can help in estimating the total material damage due to erosion-corrosion accurately so as to operate safely and avoid unplanned production outages.

Chapter 11 Conclusions and Recommended Future Work

11.1 Conclusions

In this study, the erosion, CO_2 flow-induced corrosion and erosion-corrosion behaviour of X65 pipeline materials have been investigated, and the mechanisms related to these processes have been identified, analysed and quantified under different conditions using combined acoustic emission and electrochemical monitoring with a view to establishing a portable real-time and on-line monitoring system for effective and efficient integrity management of oil and gas pipeline materials in service.

Based on the discoveries of this study, the following conclusions can be made which are grouped under each Chapter's findings.

11.1.1 Chapter 6 Findings

The following conclusions can be made from the associated experiments and investigations:

- In single impact study (using glass beads), there is a monotonous increase in AE energy and RMS as the KE of the impacting glass bead increases thus confirming the theory that impact on the material generates AE signal.

- In multiple impact study (using sand particles), the measured average AE energy increased with increase in flow velocity and sand concentration.

- At low flow velocity (7 m/s) and low sand loading (50 mg/L) the AE energy is almost the same with zero sand loading at the end of the 2-hour test signifying that either the impact energy is not enough to cause sand impact or the sand particles have smoothened or settled at the corner of the reservoir.

- The variation of AE energy with time as the flow velocity or sand loading is either increased or reduced agrees with 'Kaiser Effect'.

- The erosive wear of the material expressed as mass loss increased with increase in measured averaged AE energy and there exists a 'critical AE energy value' which is equal to $10^6 eu$ for 50 and 200 mg/L sand concentrations and 10^7 *eu* for 500 mg/L sand loading. The variation in critical energy values as the sand loading increases may be due to the variation in sand particle sizes.

- The frequency-domain of measured AE waveform during test revealed that frequency peak is observed at low frequency region when the material damage is negligible but when damage becomes significant, large peaks appear in the higher frequency region which may be due to plastic deformation or cutting of the materials.

- The visual inspection of tested samples revealed three zones: zone 1 (stagnation region), zone 2 (transition region) and zone 3 (wall jet zone) which are in agreement with previous similar erosion studies [110].

- SEM images of the zones helped in understanding the degradation mechanisms of the sand impacts at each zone. At high angle (nearly 80°) and material degradation is through heavy indentation and forging with the normal indentation marks and extrusion material flakes associated with the processes. At medium to low angles (i.e. between 40 and 15°), plastic deformation and cutting action become the key mechanisms of material degradation. The ductile cutting together with plastic deformation serve as the most effective material removal mode in mechanical erosion which is the main reason for the high erosion rates between 15 and 40° impact angles as proposed by Finnie [99], and Hutchings [83]. At low angles (below 15°), that material removal was mainly by rubbing and scratching as evidenced by the ductile rubbing and scratching marks aligned in flow direction.

- The profilometry analysis of the tested samples was in agreement with the visual inspection and SEM images thus revealing a depressed 'W' shape wear scar on the flat specimen which signifies the ductile nature of the material subjected to the solid-liquid impinging jet of the flow stream.

11.1.2 Chapter 7 Findings

Chapter 7 first gave a background of understanding particle impact detection and interpretation using subtraction technique and used AE event count rate to quantify the number of sand particle impacts per second which is verified with theoretical predictions. Furthermore, particle impact energy calculated from computational fluid dynamics (CFD) in conjunction with particle tracking code was correlated with measured AE energy per second of the impacts to ascertain the dependence of AE energy on the impact energy. The findings can be summarised as follows:

- Measured particle impacts per second for each flow velocity and sand loading agreed well with impacts predicted from theory for 7 and 10 m/s flow velocities while there is a deviation for 15 m/s flow velocities. These deviations were attributed to error due to rebounded particles that were equally detected with sand impacts on one hand and the overlapping of AE events that were difficult to separate in time for accurate counting on the other hand.

- The impact energy per second (in the order of μJ/s) correlated well with the measured acoustic energy per second (in the order of tens of nJ/s). The correlation reveals an exponential relationship between the two energies for 50 and 200 mg/L sand loading; and linear relationship between them for 500 mg/L sand loading within the range of the flow velocities investigated.

- Significant mass loss does not occur until the average AE count rate exceeds a certain critical value which is approximately 10^3 events per second for all the flow velocities and sand concentrations investigated. This critical event count

rate can be a useful guide in monitoring and predicting erosion damage of X65 pipeline material in oil and gas production using the AE technique.

11.1.3 Chapter 8 Findings

The major findings in chapter 8 include:

- Without sand (flow-induced), corrosion rate and polarization resistance as well as the acoustic activities (average count rate and cumulative counts) are linearly related to the flow velocity.

- With addition of sand (erosion-corrosion) the relationship changes to an exponential function for corrosion rate and polynomial function for the acoustic activity. The change clearly shows the relevance of kinetic energy (mass of solid and velocity) with velocity as the controlling factor, thus leading to a small increase in corrosion rate for low velocity (7 m/s) when sand loading is increased from 50 to 200 mg/L. This indicates that the regime is within the category of 'mild' erosion-corrosion which agrees well with previous studies [42].

- Higher flow velocities (10 and 15 m/s) gave significant changes in measured AE for all the sand concentrations studied, thus signifying the effect of flow velocity and sand loading in the material loss which was adequately detected by the AE set-up.

- The effect of sand on the open circuit potential (OCP) during the test was also observed, using 15 m/s flow velocity as an example, the OCP changes from 0.658 V (for 50 mg/L sand loading) to 0.697 V (for 500 mg/L sand loading).

- The total weight loss and AE energy increased with increase in flow velocity and sand loading. The increase in weight loss as the flow velocity and sand loading are increased is expected and confirms the findings in previous studies

that material removal in CO_2 erosion-corrosion environment is due to combined effect of sand loading and flow velocity [42].

- The overall degradation rate (total weight loss) and the acoustic emission energy become considerably higher in a CO_2 corrosion environment with damage done at a value below the pure erosion threshold AE energy which an indication that the key contribution to material degradation in erosion-corrosion is corrosion.

11.1.4   Chapter 9 Findings

The summary of chapter 9 findings is as follows:

- Surface reactivity results from EIS revealed that low flow velocity (7 m/s) has a capacitive semi-circle observed at high-medium frequency (HF-MF) ranges and an inductive loop at low frequency (LF) region which represent active charge-transfer and adsorption mechanisms.

- One capacitive loop was identified for 10 and 15 m/s flow velocities. This loop characterises the active corrosion state upon exposing the sample to the solid-liquid impingement of CO_2 saturated brine.

- The active adsorption and charge-transfer mechanisms operating on the active corroding surface sites were explained using the mechanism proposed by Li *et al.* [222].

- The material dissolution effects was quite visible on changes in charge-transfer, whilst the sand impact effect on the charge-transfer was negligible when compared to its effect on AE energy, an indication that AE measurement detected the changes in the sand impact mechanisms that are not adequately sensed by the EIS measurement.

- When the erosion-corrosion damage components were assessed using mass loss from gravimetric evaluation, it was observed that at low flow velocity (7 m/s), corrosion damage contribution is dominant whilst erosion damage contribution is insignificant whereas at high flow velocity (15 m/s), the reverse is the case.

- The *in-situ* corrosion rate ($C + dC_E$) contribution) did not change significantly with the addition and increase in sand loading for all the flow velocities investigated, signifying that the damage when sand was added originated from the mechanical damage contribution ($E + dE_C$).

- The effect of the mechanical damage which was not sensed by the *in-situ* corrosion measurement using EIS was adequately captured by the AE method which gave rise to much increase in AE energy as the sand loading and flow velocity were increased. These detected changes may be as a result of increased erosion damage as a result of sand impacts which will create more micro displacements on the specimen's surface, thus giving rise to high acoustic emission rate.

Hence, the combination of these two techniques can help in *in-situ* monitoring of both the electrochemical and mechanical damage contributions of erosion-corrosion degradation processes in oil and gas pipeline materials in service for effective and efficient integrity monitoring and maintenance planning of the pipelines in service.

11.2 Recommended Future Work

This PhD study using combined AE and electrochemical monitoring opens up the way to further and deeper investigations of degradation mechanisms that take place during erosion-corrosion damage of X65 carbon steel and other pipeline materials (N80,

stainless and duplex steel materials). Specific recommended suggestions for future work include:

- Effect of corrosion inhibitors on AE activity since carbon steel materials in oil and gas production is always used with application of corrosion inhibitor.

- Extend the study to flow loop system so as to also incorporate the AE source location study using wave arrival time instead of only source severity quantification which was the focus of this investigation.

- Influence of different sand particle sizes and concentrations on the AE signal waveform and frequency spectra.

- Investigate AE signal responses to higher flow velocities (15 to 20 m/s) and higher sand loading (above 500 to 10,000 mg/L) with a view to solving the problems of signal overlap and saturation of preamplifiers.

- Investigate the changes of AE signals in frequency-domain for flow-induced corrosion and erosion-corrosion.

- Investigate the influence of different impact angles on the measured AE signals and electrochemistry.

References

[1] Shadley, J.R., Shirazi, S.A., Dayalan, E. and Rybicki, E.F., Prediction of erosion-corrosion penetration rate in carbon dioxide environment with sand, *Corrosion/98*, Paper No. 59, NACE 1998.

[2] de Waard, C. and Milliams, D.E., Carbonic acid corrosion of steel, *Corrosion*, Vol.31, No.5, pp.177-181, NACE, 1975.

[3] Dayalan, E., Vani, G, Shadley, J.R., Shirazi, S.A. and Rybicki, E.F., Modelling CO_2 corrosion of carbon steels in pipe flow, *Corrosion/95*, paper No. 118, NACE 1995.

[4] Dayalan, E., de Moraes, F.D., Shadley, J.R., Shirazi, S.A. and Rybicki, E.F CO_2 corrosion prediction in pipe flow under $FeCO_3$ scale-forming conditions, *Corrosion/98*, Paper No. 51 NACE, 1998.

[5] Iyoho, W.A., In-house training manual, Shell Houston, TX, (Unpublished).

[6] Singh, B., Jukes, P., Wittkower and Poblete, B., Offshore integrity management 20 years on – Overview of lessons learnt post Piper Alpha, OTC 20051, pp 1-30, 2009.

[7] National Oceanic and Atmospheric Administration (NOAA), Oil Spill Response Sheet, Assessment and Restoration, US Department of Commerce, May 2010.

[8] Kermani, M.B. and Harrop, D., The impact of corrosion on the oil and gas industry, *SPE Production Facilities*, Vol.11, No.3, pp.186-190, 1996.

[9] Kermani, M.B. and Morshed, A, Carbon dioxide corrosion in oil and gas production—A compendium, *Corrosion Science*, Vol. 59, No.8, pp.659-683, NACE 2003.

[10] de Waard, C., Lotz, U. and Milliams, D.E., Predictive model for CO_2 corrosion engineering in wet natural gas pipelines, *Corrosion/91*, 47, NACE 1991.

[11] de Waard, C., Lotz, U., Prediction of CO_2 corrosion of carbon steel, *Corrosion/93*, Paper No. 69, NACE 1993.

[12] de Waard, C., Lotz, U., Dugstad, A., Influence of liquid flow velocity on CO_2 Corrosion: A semi-empirical model, *Corrosion/95*, Paper No. 128, NACE 1995.

[13] Gunaltun, Y.M., Combining research and field data for corrosion rate prediction, *Corrosion/96*, Paper No. 27, NACE 1996.

[14] Halvorsen, A.M.K. , Søntvedt, T, CO_2 corrosion model for carbon steel including a wall shear stress model for multiphase flow and limits for production Rate to avoid mesa attack", *Corrosion/99*, Paper No. 42, NACE 1999.

[15] John, R.C., Jordan, K.G., Young, A.L., Kapusta, S.D., Thompson, W.T. SweetCor: An information system for the analysis of corrosion of steels by water and carbon dioxide, *Corrosion/98*, Paper No. 20, NACE, 1998.

[16] Gartland, P.O., Salomonsen, J.E., A Pipeline integrity management strategy based on multiphase fluid flow and corrosion modelling, *Corrosion/99,* Paper No. 622, NACE 1999.

[17] Khajotia, B., Sormaz, D., Nesic, S., Case-based reasoning model of CO_2 corrosion based on field data, *Corrosion/07*, Paper No. 553, NACE, 2007.

[18] Dugstad, A., Lunde, L. and Videm, K. (1994), Parametric study of CO_2 corrosion of carbon steel, *Corrosion/94*, Paper No. 14, NACE 1994.

[19] Crolet, J.L., Bonis, M.R., Prediction of the Risks Of CO_2 Corrosion in Oil and Gas Wells, SPE, Vol. 6, No. 4, p. 449, 1991.

[20] Srinivasan, S, Tebbal, S., Critical factors in predicting CO_2/H2S corrosion in multiphase Systems, *Corrosion/9*8, Paper No. 38, NACE 1998.

[21] Paisley, D., Barret, N., Wilson., O., Pipeline failure: The roles played by corrosion, flow and metallurgy, *Corrosion/99* Paper No. 18, NACE 1999.

[22] Smith, L; and de Waard, K., Corrosion prediction and material selection for oil and gas producing environment, *Corrosion/05*, Paper No. 648, NACE 2005.

[23] Pots, M.F.B., Mechanistic Models for the Prediction of CO_2 Corrosion Rates under Multi-Phase Flow Conditions, *Corrosion/95*, Paper No. 137, NACE, 1995.

[24] Nesic, S, Nordsveen, M, Nyborg, R, A. Stangeland, A mechanistic model for CO_2 Corrosion with protective iron carbonate films, *Corrosion/2001*, Paper No. 40, NACE 2001.

[25] Zhang, R., Gopal, M., Jepson, W.P., Development of a mechanistic model for predicting corrosion rate in multiphase oil/water/gas flows, *corrosion/97*, Paper No. 601, NACE 1997.

[26] Anderko, A., Simulation of $FeCO_3$/FeS scale formation using thermodynamic and electrochemical models, *Corrosion/*2000, Paper No. 102, NACE 2000.

[27] High, M.S., Wagner, J., Natarajan, S., Mechanistic modelling of mass transfer in the laminar sublayer in downhole systems, *Corrosion/2000*, Paper No. 62, NACE 2000.

[28] Nesic, S., Lee, K.L.J., Rusic, V., A mechanistic model of iron carbonate film growth and the effect on CO_2 Corrosion in mild steel, *Corrosion/02* Paper No. 237, NACE 2002.

[29] Nesic, S., Wang, S, Xiao, J., Jiyong, Y. Integrated CO_2 Corrosion-Multiphase flow model, *Corrosion/04*, Paper No. 626, NACE, 2004.

[30] Nesic, S., Li, H., Huang, J., Sormaz, D., An open source mechanistic model for CO_2/H_2S corrosion of carbon steel, *Corrosion/09*, Paper 09572, NACE 2009.

[31] API RP 14E, Recommended practice for the design and installation of offshore production platform piping system, 3rd edition, 1981.

[32] API RP 14E, API recommended practice for design and installation of offshore production platform piping systems, 5th edition, 1991.

[33] Jordan, K., Erosion in multi-phase production, Corrosion/98, Paper No. 58, NACE 1998.

[34] Meng, H.C., Ludema, K.C., Wear models and predictive equations: their form and content, Wear 181-183, pp. 443-457, 1995.

[35] Shadley, J.R., Shirazi, S.A., Dayalan, E., Ismail, M., and Rybicki, E.F, Erosion-corrosion of a carbon steel elbow in a carbon dioxide environment, Corrosion Engineering, Vol. 52, No. 9, NACE 1996.

[36] Rincon, H.E., Shadley, J.R., Roberts, K.P.and Rybicki, E.F, Erosion-corrosion of corrosion resistant alloys used in the oil and gas industry, *Corrosion/2008*, Paper. No.08571, NACE 2008.

[37] Dave, K., Roberts, K.P, Shadley, J.R., Ramachandran, S., Rybicki, E.F., and Jovancicevic, V., Effect of a corrosion inhibitor in oil and gas wells when sand is produced, *Corrosion/2008,* Paper. No. 08570, NACE 2008.

[38] Tummala, K.C, Roberts, K.P, Shadley, J.R., Rybicki, E.F., and Shirazi, S.A., Effect of sand production and flow velocity on corrosion inhibition under scale forming conditions, *Corrosion/2009,* Paper. No. 09474, NACE 2009.

[39] Keating, A., Nesic, S., Numerical prediction of erosion-corrosion in bends, Corrosion Science, Vol. 57, No. 7 NACE 2001.

[40] Addis, J., Brown, B., Nesic, S., Erosion-corrosion in disturbed liquid/particle flow, Corrosion/08, Paper No. 08572, NACE 2008.

[41] Hu, X., Neville, A., Wells, J., and Souza, D.V., Prediction of erosion-corrosion in oil and gas – A systematic approach, *Corrosion/2008*, Paper 08540, NACE 2008.

[42] Hu, X., and Neville, A, CO_2 Erosion-corrosion of pipeline steel (API X65) in oil and gas conditions, A systematic approach, *Wear* 267:2027-2032, 2009.

[43] Wang, C., Erosion-corrosion mitigation using chemicals, PhD Thesis, School of Mechanical Engineering, University of Leeds, LEEDS, UK, 2007.

[44] Jiang, J., Stack, M.M., Modelling sliding wear, from dry to wet environments, Wear 261, pp. 954-965, 2006.

[45] Stack, M.M., Abdelrahman, S.M., Jana, B.D., A new methodology for modelling erosion-corrosion regimes on real surfaces: Gliding down the galvanic series for a range of metal-corrosion systems, Wear 268, pp. 533-542, 2010.

[46] Lu, B.T., Luo, J.L., Mohammadi, F., Wang, K., Wan, M.X., Correlation between repassivation kinetics and corrosion rate over surface in flowing slurry, Electrochimica Acta 53, pp. 70-7031, 2008.

[47] Wang, M., Huang, C. Nandakumar, K., Minev, P., Luo, J., Chiovelli, S., Computational fluid dynamics modelling and experimental study of erosion in slurry jet flows, International journal of CFD, Vol. 23, pp. 155-172, 2009.

[48] Lu, B.T., Lu, J.F., Luo, J.L, Erosion-corrosion of carbon steel in simulated tailing slurries, Corrosion Science Vol. 53, pp. 1000-1008, 2011.

[49] Woollam, R.C. and Hernandez, S.E., Assessment and comparison of CO_2 prediction models. SPE 100673, 2006.

[50] Shreir, L.L., Jarman, R.A., Burstein, G.T., Editors, Corrosion: Metal/Environment Reactions, Vol. 1, 3rd Edition, BH-Jordan Hill Oxford, 2000.

[51] Ahmad, Z., Principles of corrosion engineering and control, UK, Butterworth-Heinemann/IChemE Series, 2006.

[52] Tait, S.W., An introduction on electrochemical corrosion testing for practicing engineers and scientists, Pair O Docs Publications, 1994.

[53] Richardson, T.J.A.(Editor), Shreir's Corrosion, Elsevier B.V. 2010.

[54] An overview of cathodic protection; a practical manual of Cathodic Protection Company Limited, Lincolnshire, United Kingdom September 2013.

[55] NACE, CP3-Cathodic Protection Technologist Training and Certification Manual, 2008.

[56] MacDonald, D.D., Transient Techniques in Electrochemistry, Plenum Press, New York, 1977.

[57] Conway, B.E. Electrochemical supercapacitors: Scientific fundamentals and technological applications, Kluwer Academic/Plenum Publishing, New York, 1999.

[58] Hu, X., The corrosion and erosion-corrosion behaviour of high alloy stainless steels, PhD thesis, Department of Mechanical and Chemical Engineering, Heriot-Watt University, Edinburgh, UK 2003.

[59] Turgoose, Palmer, S.J.W., and Dicken, G.E., Preferential Weld Corrosion of 1% Ni Welds: Effect of Solution Conductivity and Corrosion Inhibitors, Corrosion/2005, paper no. 275, NACE International, Houston, TX, 2005.

[60] Hollingsworth, E.H., and Hunsicker, H.Y., Corrosion of Aluminum and Aluminum Alloys, *Corrosion,* Vol 13, pages 583–609, *ASM Handbook,* ASM International, 1987.

[61] Lee, C.M., Bond S., and Woollin, P., Preferential weld corrosion: Effect of weldment microstructure and composition, Corrosion/2005, paper no. 277, NACE International, Houston TX, 2005.

[62] Nesic, S, Postlethwaite, J., and Olsen, S., An electrochemical model for prediction of CO_2 corrosion, Corrosion/95 Paper No. 131 1995.

[63] Nesic, S., Key issues related to modelling of internal corrosion of oil and gas pipelines - A review, Corrosion Science, 49, 12, pp. 4308-4338, 2007.

[64] Nesic, S, Drazic, D., Thevenot, N., and Crolet, J.L., Electrochemical properties of iron dissolution in the presence of CO_2 - Basics revisited, CORROSION 96, paper no. 3, NACE, 1996.

[65] Bockris, J.O.M., Drazic, D., and Despic, A.R., The electrode kinetics of the deposition and dissolution of iron, electrochimica Acta, 4, 2-4, pp. 325-361, 1961.

[66] Sun, W., Nesic, S., Basics Revisited: Kinetics of iron carbonate scale precipitation in CO_2 corrosion, Corrosion/06, Paper No. 06365, 2006.

[67] Nesic, S, Postlethwaite, J., and Olsen, S., An electrochemical model for prediction of corrosion of mild steel in aqueous carbon dioxide solution Corrosion 52, NACE 1996.

[68] Olsen, S., CO_2 Corrosion Prediction by use of the NORSOK M-506 model - guidelines and limitations, Corrosion/03, Paper No. 03623, 2003.

[69] Nesic, S., Vrhovac, N., Neural network model for CO_2 corrosion of carbon steel, Journal of Corrosion Science and Engineering, Vol. 1 Paper 6, 1997.

[70] Mohammed Nor, A., Suhor, M.F., Mohamed, M.F., Singer, M., Nesic, S., Corrosion in high CO_2 environment: Flow effect, Corrosion/2011, Paper No. 11242, 2011.

[71] Lotz, U., Heitz, E., Flow-dependent corrosion. I. Current understanding of the mechanisms involved. Werkstoffe und Korrosion 34, pp. 454-461, 1983.

[72] Zhang, G.A., Cheng, Y.F., Electrochemical characterization and computational fluid dynamics simulation of flow-accelerated corrosion of X65 steel in a CO2-saturated oilfield formation, Corrosion Science, 52, pp. 2716-2724, 2010.

[73] Efird, K.D., Flow accelerated corrosion testing basics, Corrosion/06, Paper No. 06689, NACE 2006.

[74] Efird, K.D, Wright, E.J., Boros, J.A., Hailey, T.G., Correlation of steel corrosion in pipe flow with jet impingement and rotating cylinder tests, Corrosion Engineering, pp. 992-1003, 1993.

[75] Schmitt, G., Bakalli, M., Advanced models for erosion corrosion and its mitigations, Materials and Corrosion 59, pp. 198-192, 2008.

[76] Jepson, W. P., Bhongale, S., Gopal, M., Predictive model for sweet corrosion in horizontal multiphase slug flow, Corrosion/96, Paper No. 19, NACE 1996.

[77] Hara, T., Asahi, H., Suehiro, Y., Kaneta, H., Effect of flow velocity on carbon dioxide corrosion behaviour in oil and gas environments, Corrosion 56, pp. 860-866, 2000.

[78] Efird, Jet impingement testing for flow accelerated corrosion, Corrosion/00, Paper No. 00052, NACE 2000.

[79] Barker, R., Hu, X., Neville, A., Flow-induced corrosion and erosion-corrosion assessmeny of carbon steel pipework in oil and gas production, Corrosion/2011, Paper No. 11245, NACE 2011.

[80] Martin, J.W., BP-Amoco Erosional guidelines revision 2.1, 1999.

[81] Bitter, J.G.A., A study of erosion phenomena, Part I, Wear, 6, pp 5-21, 1963.

[82] Bitter, J.G.A., A study of erosion phenomena, Part II, Wear, 6, pp 169-190, 1963.

[83] Hutchings, I.M., Wear by particulates, Chemical Engineering Science Journal, Vol. 41, No. 4, pp. 869-878, 1987.

[84] Hutchings, I.M., Tribology: Friction and Wear of Engineering Materials, Edward Arnold, London,UK 1992.

[85] Tilly, G. P., Erosion caused by impact of solid particles, Material Science and Technology, V. 13, pp287-319, 1979.

[86] Levy, A.V., Yau, P., Erosion of steels in liquid slurries, Wear 98, pp. 163-182, 1984.

[87] Hamza, R.B, Erosion-corrosion modelling of materials used in petroleum production, PhD thesis, School of Industrial and Manufacturing Science, Cranfield University, UK, 1994.

[88] McLaury, B.S., Shirazi, S.A., An alternative method to API RP 14E for predicting solids erosion in multiphase flow," ASME Journal of Energy Resource Technology, Vol. 122, pp. 115-122, 2000.

[89] Salama, M.M. and Venkatesh, E.S., Evaluation of API RP 14E erosion at velocity limitations for offshore gas wells, paper OTC4485, 1983.

[90] Salama, M.M., An alternative to API 14E erosional velocity limits for sand laden fluids, OTC8898, 1998.

[91] Mclaury, B.S., and Shirazi, S.A., Generalization of API RP 14 for erosive service in multiphase production, SPE 56812, 1999.

[92] Bourgoyne, A.T., Experimental study of erosion in diverter systems due to sand production, SPE/IADC 18716, 1993.

[93] Watson, S.W., Friederdorf, F.J. Madsen, B.W., Cramer, S.D., Methods of measuring wear corrosion synergism, Wear 181-183, pp. 476-484, 1995.

[94] Gnanavelu, A., Kapur, N., Neville, A., Flores, J.F., An integrated methodology for predicting material wear rates due to erosion, Wear 267, pp. 1935-1944, 2009.

[95] Huser, A. and Kvernvold, O., Predictions of sand erosion in process and pipe components, in the proceedings of 1st North American Conference on Multiphase Technology, Banff, Canada, 1998

[96] Zhang, Y., Mclaury, B.S., Shirazi, S.A., Rybicki, E.F., A two-dimensional mechanistic model for sand prediction including particle impact characteristics, *Corrosion/2010*, Paper 378, NACE 2010.

[97] Hu, X. and Neville, A, Erosion-corrosion of pipeline steel X65 and 22%Cr duplex stainless steel in CO_2 saturated environment, SPE 114078, 2008.

[98] Malka, R., Nesic, S. and Gulino, D.A., Erosion-corrosion and synergistic effects in disturbed liquid-particle flow, *Corrosion/2006*, Paper No. 594, NACE 2006.

[99] Finnie, I., Erosion of surfaces by solid particles, Wear 3, pp. 87-103, 1960.

[100] Neilson, J.H. and Gilchrist, A., Erosion by a stream of solid particles, Wear 11, pp. 111-122, 1968.

[101] Hutchings, I.M., A model for the erosion of metals by spherical particles at normal incidence, Wear, 70, pp. 269-281, 1981.

[102] Sundararajan, G. and Shewmon, P.G., A new model for the erosion of metals at normal incidence, Wear, 84 (1983) 237-258.

[103] Zhang, Y., Reuterfors, E.P., Mclaury, B.S., Shirazi, S.A., Rybicki, E., Comparison of computed and measured particle velocities and erosion in water and airflows, Wear, 263, pp 330-338,.2007.

[104] Clark, H.M., On the impact rate and impact energy of particles in a slurry pot erosion tester, Wear, 147, 1: pp. 165-183, 1991.

[105] Clark, H.M., The influence of the flow field in slurry erosion", Wear, 152, 2: pp. 223-240, 1992.

[106] Clark, H.M., and Hartwich, R.B., A re-examination of the particle size effect in slurry erosion, Wear, 248, 1-2: pp. 147-161, 2001.

[107] Chen, X., McLaury, B.S., and Shirazi, S.A., Application and Experimental Validation of a Computational Fluid Dynamics (CFD)-based Erosion Prediction Model in Elbows and Plugged Tees, Computers and Fluids, 33, 10,: pp. 1251-1272, 2004.

[108] Chen, X., McLaury, B.S., and Shirazi, S.A., Numerical and Experimental Investigation of the Relative Erosion Severity Between Plugged Tees and Elbows in Dilute Gas/Solid Two-Phase Flow, Wear, 261, 7-8: pp. 715-729, 2006.

[109] Mazumder, Q.H., Shirazi, S.A., McLaury, B.S., Shadley, J.R., and Rybicki, E.F., Development and Validation of a Mechanistic Model to Predict Solid Particle Erosion in Multiphase Flow, Wear, 259, 1-6: pp. 203-207, 2005.

[110] Gnanavelu, A., A geometry independent integrated method to predict erosion wear rates in a slurry environment, PhD Thesis, School of Mechanical Engineering, University of Leeds, 2010.

[111] Smart III, J.S., A review of erosion-corrosion in oil and gas production, *Corrosion/90* Paper 10, NACE 1990.

[112] Wood, R.J.K. and Hutton, S.P., The synergistic effect of erosion and corrosion: trends in published results, *Wear* **140** pp. 387–394, 1990.

[113] Zheng, Y., Zhiming, Y., Xiangyun, W., and Ke, W., The synergistic effect between erosion, corrosion in acidic slurry medium, *Wear* **186–187**, pp. 555–561, 1995.

[114] Hubner, W. and Leitel, E., Peculiarities of erosion–corrosion processes, Tribology International, Vol. **29** (3), p. 199, 1996.

[115] James, J.S., Investigations of aqueous erosion-corrosion using rotating cylinder electrodes, PhD thesis, Institute of Science and Technology, University of Manchester, 1997.

[116] Zvandasara, T., Influence of hydrodynamics on carbon steel erosion-corrosion and inhibitor efficiency in simulated oilfield brines, PhD thesis, Department of Mechanical Engineering, University of Glasgow, 2010.

[117] Guo, H.X., Lu, B.T., Luo, J.L., Interaction of mechanical and electrochemical factors in erosion-corrosion of carbon steel, Electrochemical Acta 51, pp. 315-323, 2005.

[118] Lu, B.T., Luo, J.L., Lu, J.F., Chemo-mechanical effect in erosion-corrosion process of carbon steel, Corrosion/2004, Paper No. 04659, 2004.

[119] Li, Y., Burstein, G.T., Hutchings, M.I., The influence of corrosion on erosion of aluminium by aqueous silica slurries, Wear, 186-187, pp 515-522, 1995.

[120] Reyes, M., and Neville, A., Mechanism of erosion-corrosion on cobalt-based alloy and stainless steel UNS S17400 in aggressive slurries, Material Engineering and Performance, 10, pp. 723-730, 2001.

[121] Matsumura, M., Oka, Y., Hiura, H., Yano, M., The role of passivating film in preventing slurry erosion-corrosion of austenite stainless steel, ISIJ International 31 (2) pp. 168-176, 1991.

[122] Barker, K.C., Ball, A., Synergistic abrasive-corrosive wear of chromium containing steels.; British Corrosion Journal; 24, pp. 222-228, 1989.

[123] Bester, J.A., Ball, A., The performance of aluminium alloys and particulate reinforced aluminium metal matrix composites in erosive-corrosive slurry environments, Wear, 162-164, pp. 57-63, 1993.

[124] Levy, A.V., Hickey, G., Liquid-solid particle slurry erosion of steels, Wear, 117, pp. 129-146,1987.

[125] Heitz, E, Chemo-mechanical effects of flow on corrosion, corrosion 47, pp. 135-145, 1991.

[126] Wang, M.C., Ren, S.Z., Wang, X.B., Li, S.Z., A study of sand slurry erosion

of w-Alloy white cast irons, Wear 160, pp. 259-264, 1993.

[127] Blatt, W, Kohley, T., Lotz, U., Heitz, E., The influence of hydrodynamics on

erosion-corrosion in two-Phase liquid-particle flow, Corrosion 45, pp. 793-804, 1989.

[128] Umemura, F., Matukura, S., Kawamoto, T., Electrochemical study of erosion-corrosion in carbon and stainless Steels.; Corrosion Engineering 36, pp. 569-578, 1987.

[129] Madsen, B.W., Measurement of erosion–corrosion synergism with a slurry wear test apparatus, Wear 23, pp. 127-142, 1988.

[130] Burstein, G., Sasaki, K., Effect of impact angle on the slurry erosion-corrosion of 304L stainless steel, Wear 240, pp. 80-94, 2000.

[131] Poulson, B., Complexities in predicting erosion-corrosion, Wear 233-235, pp. 497-504, 1999.

[132] Tsai, W., Humphrey, J.A.C., Cornet, I., Levy, A.V., Experimental measurement of accelerated erosion in a slurry pot tester, Wear 68, pp. 289-303, 1981.

[133] Pitt, C.H., Chang, Y.M., Jet slurry corrosive wear of high-chromium cast iron and high carbon steel grinding ball alloys, Corrosion 42, pp. 312-317, 1986.

[134] Postlethwaite, J., Nesic, S., Erosion in disturbed liquid/particle pipe flow: Effects of geometry and particle surface roughness, Corrosion 49, pp. 850-857, 1993.

[135] Zu, J.B., Hutchings, I.M., Burstein, G.T., Design of a Slurry Erosion Test Rig, Wear 140, pp. 331-344,1990.

[136] Roberge, P., Corrosion testing made easy, erosion-corrosion, B.C. Syrett, Series Editor. NACE International 2004.

[137] Evans, U. R., The Corrosion and Oxidation of Metal: Scientific Principles and Practical Applications, Edward Arnold Ltd. 1977.

[138] Keating, A., A model for investigation of two-phase erosion-corrosion in complex geometries, MSc thesis, Mechanical Engineering, University of Queensland, Australia, 1999.

[139] Zeisel, H., Durst, F., Computations of erosion-corrosion processes in separated two-phase flows, Corrosion/90, Paper No. 29, NACE 1990.

[140] Postlethwaite, J., Nesic, S., Adamopoulos, G., Bergstrom, D.J., Predictive models for erosion-corrosion under disturbed flow conditions, Corrosion Science, Vol. 35, pp. 627-633, 1993.

[141] Willis, M.J., Croft, N.T., Cross, M., Computational fluid dynamic modeling of an erosion-corrosion test method, Corrosion/09, Paper No. 09473, NACE 2009.

[142] Stack, M.M., Abdelrahman, S.M., and Jana, B.D., A CFD model of erosion-corrosion of Fe at elevated temperatures, Advances in Science and Technology, Vol. 72, pp. 75-86, 2010.

[143] Wood, R.J.K., Tribo-corrosion in Shreir's Corrosion, Elsevier, 2010.

[144] Silver, D.C., The rotating cylinder electrode for examining velocity-sensitive corrosion- a review, Corrosion Science and Engineering Vol. 60, No. 11, NACE 2004.

[145] Salama, M.M., Sand production management, Journal of Energy Resources Technology, OTC 2000.

[146] Winning, I.G., Taylor A., and Ronceray, M., Corrosion mitigation, the Corrosion engineers options, SPE 130299, 2010.

[147] Lyons, W.C. and Plisga, G.J., (editors), Standard handbook of petroleum and natural gas engineering, second edition, Elsevier, London, 2005.

[148] Ramachandran, S., Jovancicevic, V., Ward, M.B., and Bartrip, K.A., Inhibition

of the Effects of Particle Impingement, CORROSION 2002, paper no. 498, NACE, 2002.

[149] Ramachandran, S., Bartrip, K.A, Menendez, C. and Coscio, S. Preventing Erosion and Erosion Corrosion Using Specialty Chemicals, International Symposium on Oilfield Chemistry, (Houston, TX: SPE International Symposium of Oilfield Chemistry, 2003).

[150] Jasinski, R., Corrosion of Low-Alloy Steel in Crude Oil/Brine/CO2 Mixtures, Surfaces, Inhibitors and Passivation, 86-87: pp. 139-148. 1986.

[151] Akbar, A., Hu, X, Neville, A., and Wang, C., The Influence of Flow Rate And Inhibitor On The Protective Layer Under Erosion-Corrosion Conditions Using Rotating Cylinder Electrode", CORROSION 2011, paper no. 274, NACE, 2011.

[152] Akbar, A, Hu, X, Wang, C , Neville, A., The Influence of Flow Rate, Sand and Inhibitor On Iron Carbonate Scales Under Erosion-Corrosion Conditions Using A Submerged Impingement Jet", CORROSION 2012, paper no. 1396, NACE, 2012.

[153] Barker, R, Hu, X., Neville, A., and Cushnaghan, S., Inhibition of Flow-Induced Corrosion and Erosion-Corrosion for Carbon Steel Pipe Work from an Offshore Oil and Gas Facility. Corrosion: Vol. 69, No. 2, pp. 193-203, 2013.

[154] Elforjani, M.A., Condition monitoring of slow speed rotating machinery using acoustic emission technology, PhD Thesis, Cranfiled University, UK, 2010.

[155] Rettig, W.T., Felsen, J.M., Acoustic emission method for monitoring of corrosion reactions, Technical Note in Corrosion-NACE 32, pp. 121-126, 1976.

[156] Carlye, J.M., Acoustic emission signal analysis, PhD thesis, Department of Physics, Brunel University, UK, 1982.

[157] Portevin, A., and LeChatelier, F., Sur un Phenomene Observe lors de l'Essai de Traction d'Alliages en Cours de Transformation, Comptes Rendus Hebdomadaires de Seances de l'Academie des Sciences, 176, 507-510, 1923.

[158] Joffe, A., The physics of crystals, McGraw-Hill, New York , 1928.

[159] Mason, W.P., McSkimin, H.J., and Shockley, W., Ultrasonic Observation of Twinning in Tin, Physical Review, 73, 10, 1213-1214, 1948.

[160] Kaiser, J., Untersuchungen uber das auftreten Gerauschen, beim Zugversuch, Ph.D. Thesis, Technische Hochschule, Munich, 1950.

[161] Dunegan, H.L. Using acoustic emission technology to predict structural failure, Metals Engineering Quarterly 15, pp. 8-16, 1975.

[162] Mba, D., Morhain, A., Bearing defect diagnosis and acoustic emission, Proceedings of Institute Mechanical Engineering, Part J: J. Eng. Tribol 217 (4) , pp. 257–272, 2003.

[163] Mba, D, Rao Raj B.K.N., Development of acoustic emission technology for condition monitoring and diagnosis of rotating machines: bearings, pumps, gearboxes, engines, and rotating structures, Shock Vib Dig 38, pp. 3–16, 2006.

[164] Mba, D., Elforjani, M., Natural mechanical degradation measurements in slow speed bearings, Engineering Failure Analysis, 16, pp. 521-532, 2009.

[165] Okada, H., Yukawa, K.I., and Tuma, H., Application of acoustic emission technique to the study stress corrosion cracking in distinguishing between active path corrosion and hydrogen embrittlement, Technical Note in Corrosion-NACE 30, pp. 253-255, 1974.

[166] Rose, J. L., Ultrasonic Waves in Solid Media, Cambridge University Press, 2004.

[167] Mechefske, C.K., Sun, G., and Sheasby J., Using acoustic emission to monitor sliding wear, Insight 44, 2002.

[168] Vallen, H., AE testing: fundamentals, equipment and application, Vallen Systeme GmbH publication, Munich Germany, 2005.

[169] Mathworks Inc. Signal Processing Toolbox User's Guide Version 6.0, 2001.

[170] Seah, W.H.K., Lim, K.B., Chew, C.H., and Teoh, S.H., The correlation of acoustic emission with rate of corrosion, Corrosion Science, 34, pp. 1707-1713, 1993.

[171] Prateepasen, A., Jirarungsatian, C., Implementation of acoustic source recognition for corrosion severity prediction, Corrosion 67, No. 5, pp 1-9, May 2011.

[172] Ferrer, F., Faure, T., Goudiakas, J., Andres, E., Acoustic emission study active-passive transitions during carbon steel erosion-corrosion in concentrated sulfuric acid, Corrosion Science 44, pp. 1529-1540, 2002.

[173] Ferrer, F., Idrissi, H., Mazille, H., Fleischmann, P., Labeeuw, P., A study of abrasion-corrosion of AISI 304L austenitic stainless steel in saline solution using acoustic emission technique, NDT & E International 33, pp. 363-371, 2000.

[174] Hunter, S.C., Energy absorbed by elastic waves during impact, J. Mech. Phys. Solids, 5, pp. 162-171, 1957.

[175] Miller, G.F. and Pursey, H., On the partition of energy between elastic waves in a semi-infinite solid, Proceedings of Royal Society, A223, pp. 521-541, 1955.

[176] Hutchings, I.M., Energy absorbed by elastic waves during plastic impact, J. Phys. D: Applied Physics 12, 1819-1824, 1979.

[177] Dornfeld, D.A., Kannatey-Asibu, E., Acoustic emission during orthogonal metal cutting, International. Journal of Science, Vol. 22. pp. 285-296, 1980.

[178] Elshelby, J.D., The interaction of kinks and elastic waves, Proceedings of the Royal Society, London, A266, pp. 222-246, 1962.

[179] Trochidis, A, Polyzos, B., Dislocation annihilation and acoustic emission during plastic deformation of crystals, Journal of the Mechanics and Physics of Solids, Vol. 42, pp. 1933-1944, 1994.

[180] Pollock, A.A., Acoustic emission-2. Acoustic emission amplitude, Non-destructive Testing Vol. 6, No. 5, pp. 264-269, 1973.

[181] Kinsler, L.E., and Frey, A.R., Fundamentals of Acoustics, Wiley, New York 1965.

[182] Harris, D.O., Bell, R.L., The measurement and significance of energy in acoustic-emission testing, Experimental Mechanics, Vol. 17, No. 9, pp. 347-353, 1977.

[183] Stone, D.E.W, Dingwall, P.F., Acoustic Emission parameters and their interpretation, Non-destructive Testing International 10 (2), 51,1977.

[184] McLaskey, G.C., Glaser, S.D., Acoustic emission sensor calibration for absolute source measurements, Journal of Non-destructive Evaluation, Springer, 2012.

[185] Hill, R., El-Dardiry, S.M.A. A theory for optimization in the use of acoustic emission transducers, Journal of Acoustical Society of America, Vol. 62, No.2, 1980.

[186] Oltra, R., Chapey, B., Renaud, L., Abrasion-corrosion studies of passive stainless steels in acidic media: combination of acoustic emission and electrochemical techniques, Wear 186-187, pp. 533-541, 1995.

[187] Ferrer, F., Idrissi, H., Mazille, H., Fleischmann, P., Labeeuw, P., On the potential of acoustic emission for the characterization and understanding of mechanical damaging during abrasion-corrosion processes, Wear 231, 108-115, 1999.

[188] Bonness, J.R., and McBride, S.L., Adhesive and abrasive wear studies using acoustic emission techniques, Wear, 149, pp. 41-53, 1991.

[189] Lingard, S., Yu, C.W., and Yau, C.F., Sliding wear studies using acoustic emission, Wear, 162, pp. 597-5960, 1993.

[190] Hase, A., Mishrina, H., Wada, M., Acoustic emission in elementary processes of friction and wear: in-situ observation of friction surfaces and acoustic emission signals. Journal of Advanced Mechanical Design, Systems and Manufacturing, Vol. 3, No. 4, pp. 333-344, 2009.

[191] Droubi, M.G., Reuben, R.L., White, G., Acoustic emission monitoring of abrasive particle impacts on carbon steel, Proceedings of IMechE, Vol. 226 Part E: Journal of Process Mechanical Engineering 2012.

[192] Vallen, H, AE-suite software manual, Acquisition, VisualAE, VisualTR, Vallen Systeme GmbH publication, Munich Germany, Version 2011.0303.

[193] Wood, R.J.K. , Wheeler, D.W., Design and performance of a high velocity air-sand jet impingement erosion facility. Wear, 1998. 220(2): p. 95-112.

[194] Vallen Systeme, AMSY-6 Handbook, Vallen Systeme GmbH, Munich Germany, 2011.

[195] Reed, J., Energy losses due to elastic wave propagation during impact, Journal of Physics D: Applied Physics, 12, pp. 29-37, 1985.

[196] Wu, C.Y., Li, L.Y., Thornton, C., Energy dissipation during normal impact and elastic-plastic spheres, Int'l Journal of Impact Engineering, 32 pp. 593-604, 2005.

[197] NDT Resource Centre, Introduction to acoustic emission testing, online as at 25/10/2012. http://www.ndt-ed.org/EducationResources/CommunityCollege/Other%20Methods/AE/AE_Theory-Sources.htm

[198] Hayakawa, K., Nakamura, T., Yonezawa, H., Tanaka, S., Detection of damage and fracture of forging die by fractal property of acoustic emission, Material Transactions, Vol. 45, No. 11, pp. 3136-3141, 2004.

[199] Ramirez, R.W., The FFT: Fundamentals and Concepts, Tektronix, Beaverton, Oregon 1975.

[200] Wadley, H.N.G., Scruby, C.B., Speake, J.H., Acoustic Emission for physical examination of metals, International Metals Reviews, 41, 1980.

[201] Folkestad, T., Myvagnam, K. S., Acoustic measurements detect sand in North Sea flow lines, Oil and Gas Journal, August 27, 1990.

[202] Croxford, A. J., Wilcox, P.D., Drinkwater, B.W., Konstantinidis., G., Strategies for guided-wave structural health monitoring. Proc. Royal Society A., 463, pp. 2961-2981, 2007.

[203] Cicero, T., Signal processing for guided wave structural health monitoring, PhD Thesis, Department of Mechanical Engineering, Imperial College London, 2009.

[204] Buttle, D.J., AND Scruby, C.B., Characterisation of particle impact by quantitative acoustic emission, Wear, Vol. 137, (pp. 63-90), 1990.

[205] Lynn, S.R., Wong, K.K., and Clark, H.M., On the particle size effect in slurry erosion, Wear, Vol. 149, (pp. 55-71), 1991.

[206] Rajahram, S.S., Erosion-corrosion mechanisms of stainless steel UNS31603, PhD thesis, School of Engineering Sciences, University of Southampton, UK, 2010.

[207] Barker, R.J, Erosion-corrosion of carbon steel pipework on an offshore oil and gas facility, PhD thesis, School of Mechanical Engineering, University of Leeds, UK, 2012.

[208] Tu, J., Yeoh, G.H., and Liu, C., Computational Fluid Dynamics: A Practical Approach. 2008: Butterworth-Heinemann.

[209] Clift, R., Grace, J.R., and Weber, M.E. eds. Bubbles, Drops, and Particles. 1978.

[210] Tu, J.Y., Numerical investigation of particulate flow behaviour in particle-wall impaction, Aerosol Science and Technology, 32 (6): pp. 509-526, 2000.

[211] Grant, G. and W. Tabakoff, An experimental investigation of the erosive characteristics of 2024 aluminium alloy. pp. 73-37, 1973.

[212] Forder, A., Thew, M., and Harrison, D., A numerical investigation of solid particle erosion experienced within oilfield control valves. Wear, 216(2): p. 184-193, 1998.

[213] Keating, A. and S. Nesic, Particle tracking and erosion prediction in three-dimensional bends. ASME Fluids Engineering, 10(1), 2000.

[214] Zhang, Y., McLaury, B.S., and Shirazi, S.A., Improvements of Particle Near-Wall Velocity and Erosion Predictions Using a Commercial CFD Code. Journal of Fluids Engineering, 131(3): p. 031303, 2009.

[215] Brown, G.J., Erosion prediction in slurry pipeline tee-junctions. Applied Mathematical Modelling, 26(2): p. 155-170, 2002.

[216] Sasaki, K., Burstein, G.T., Observation of a threshold impact energy required to cause passive film rupture during slurry erosion of stainless steel, Philosophical Magazine Letters, 80:7, 489-493, 2000.

[217] Dugstad, A., Mechanism of protective film formation during CO_2 corrosion of carbon steel", Corrosion/98, paper no. 31, NACE, 1998.

[218] Farelas, F., Galicia, M., Brown, B., Nesic, S., Castaneda, H., Evolution of dissolution processes at the interface of carbon steel corroding in a CO_2 environment studied by EIS." Corrosion Science 52:509-517, 2010.

[219] Kermani, B., Edmonds, D., Gonzales, J.C., Lopez-Turconi, G., Scoppio, L., and Dicken, G., Development of superior corrosion resistance 3%Cr steels for downhole applications, Corrosion 2003, paper no. 116, NACE, 2003.

[220] Crolet, J.L., Thevenot, N, and Nesic, S., Role of conductive corrosion products in the protectiveness of corrosion Layers, Corrosion Science Vol. 54,Issue 3, pp. 194-203, 1998.

[221] López, D.A., Pérez, T, and Simison, S.N., The influence of microstructure and chemical composition of carbon and low alloy steels in CO_2 corrosion. A state-of-the-art appraisal, Materials and Design, 24, 8 pp. 561-575, 2003.

[222] Li, P., Tan, T.C., and Lee, J.Y. Impedance spectra of the anodic dissolution of mild steel in sulphuric acid, Corrosion Science, Vol 38, No. 11, pp. 1935-1955, 1996.

[223] Heusler, K.E., PhD Dissertation, Gottingen 1957.

[224] Bockris, J.O'M, Drazic, D., and Despic, A.R., The electrode kinetics of the deposition and dissolution of iron, Electrochimica Acta 4, No. 2-4, pp. 326, 1961.

[225] Keddam, M., Mattos, O.R., and Takenouti, H., Reaction Model for Iron Dissolution Studied by Electrode Impedance I., Experimental Results and Reaction Model, Journal of Electrochemical Society, Vol. 128, Issue 2, pp. 257, 1981.

[226] Schweickert, H., Lorenz, W.J., Friedburg, H., Impedance Measurements of the Anodic Iron Dissolution, Journal of Electrochemical Society, Volume 127, Issue 8, pp. 1693-1701, 1980.

[227] Zhang, G.A. and Cheng, Y.F., On the fundamentals of electrochemical corrosion of X65 Steel in CO_2-containing formation water in the presence of acetic acid in petroleum production", Corrosion Science, 51, 1, pp. 87-94, 2009.

[228] Gavanluei, A.B., Mishra, B., Al-Abbas, F., Olson, D.L., and Elramady, A., Electrochemical investigation of the evolution of interfacial electrodic processes for downhole tubular steels in CO_2 saturated environments, Corrosion/2012, paper no. 1685, NACE 2012.

[229] Filho, J.C.C. and Orazem, M.E., Application of a submerged impinging jet to investigate the influence of temperature, dissolved CO_2, and fluid velocity on corrosion of pipeline-grade steel in brine, Corrosion/2001 paper no. 58, NACE 2001.

[230] Epelboin, I., Keddam, and M, Takenouti, H., Use of impedance measurements for the determination of the instant rate of metal corrosion, Journal of Applied Electrochemistry, vol.2. pp. 71-79, 1972.

[231] Silverman, D.C, Corrosion rate estimation from pseudo-inductive electrochemical impedance response", *CORROSION*/89,NACE, 1989.

[232] Lorenz, W.J., Mansfeld, F., Determination of corrosion rates by electrochemical DC and AC methods, Corrosion Science, Vol. 21, No 9, pp. 647-672, 1981.

[233] Aksut, A.A., Lorenz, W.J., and Mansfeld, F., The determination of corrosion rates by electrochemical D.C. and A.C. methods - systems with discontinuous steady state polarization behavior, Corrosion Science, 22 (7): pp. 611-619, 1982.

[234] Metal Samples Corrosion Monitoring Systems Online Publication on Corrosion Coupons and Weight Loss Analysis, available online as at 06-05-2014: http://www.alspi.com/cpnintro.htm

[235] ASTM G102, Standard practice for calculation of corrosion rates and related information from electrochemical measurements, 1999.

[236] Neville, A. and Wang, C., Erosion-Corrosion Mitigation by Corrosion Inhibitors - An Assessment of Mechanisms, Wear, 267, 1-4,: pp. 195-203, 2009.

[237] Shimuzu, A., Yagi, Y., Yoshida, H ., and Yokomine, T., Erosion of gaseous suspension flow duct due to particle collision. Experimental determination of erosion rate by individual collision, Journal of Nuclear Science and Technology, Vol. 30 (pp. 881-889), 1993.

[238] Zu, J.B., Hutchings, I.M and Burstein, G.T., Design of a slurry erosion test rig, Wear Vol. 140, (pp. 331-344), 1990.

[239] Zu, J.B., Burstein, G.T., and Hutchings, I.M., A comparative study of the slurry erosion and free-fall particle erosion of aluminium, Wear, Vol. 149, (pp. 73-84), 1991.

[240] Evans, A.G., Nadler, H., and Ono, K., An acoustic emission study of the fractured zinc selenide, Matetials Science and Engineering, Vol 22 (pp. 7-14) 1976.

[241] Lee, J., Lee, M., Kim, J, Luk, V., Jung, Y., A study of the characteristics of the acoustic emission signals for condition monitoring of check valves in nuclear power plants, Nuclear Engineering and Technology Design, Vol 236, (pp. 1411-1421), 2006.

[242] Neville, A., Hodgkiess and Hu, X., An electrochemical and microstructural assessment of erosion-corrosion of cast iron, Wear, 233-235 (pp. 523-534) 1999.

[243] Aiming, F., Jinming, L., and Ziyun, T., An investigation of the corrosive wear of stainless steel in aqueous slurries, Wear, 233-235, (pp. 596-607), 1999.

[244] Rowlett, N., Tata Steel UK Ltd, Sheffield, Cast No. K5401A, April 2011.

Appendices

Appendix 1: Summary of selected CO$_2$ corrosion empirical models

Input	LIPUCOR	NORSOK	SWEETCOR	CORPOS	CBR-TS	Meaning of Input Terms
			Model Name			
PCO$_2$	x	x	x	x	x	CO$_2$ Partial Pressure
T	x	x	x	x	x	Temperature
pH	x	x		x	x	Solution pH
FR	x	x	x	x	x	Flow rate
FRM	x					Flow regime
SF	x	x	x	x	x	Scaling factor
P$_{tot}$	x	x		x	x	Total pressure
SP	x				x	Steel properties
WW	x	x	x	x	x	Water wetting
H$_2$S					x	Hydrogen sulphide
Year	1979-996	1998	1998	1998 - 1999	2007	Year of development
Ref.	13	14	15	16	17	References of developer(s)

Appendix 2: Summary of selected CO$_2$ corrosion semi-empirical models

Input	Model Name								
	DM 1	DM 2	DLM	DLD	IFE	CORMED	PREDICT	CASSAND	ECE
PCO$_2$	x	x	x	x	x	x	x	x	x
T	x	x	x	x	x	x	x	x	x
pH			x	x	x	x	x	x	x
FR			x	x	x	x	x	x	x
FRM				x	x	x	x	x	x
SF			x	x	x	x	x		
P$_{tot}$			x	x	x	x	x	x	x
SP				x	x	x			
WW		x	x	x		x	x	x	
H$_2$S						x	x		
Year	1975	1991	1993	1995	2000	1985-991	1996-2000	1999	2005
Ref.	2	10	11	12	18	19	20	21	22

Appendix 3: Summary of selected CO$_2$ corrosion mechanistic models

Input	TULSA	HYDROCOR	KSC	OHIO	OLI	DREAM	MULTICORP	WWCORP	FREECORP
				Model Name					
PCO$_2$	x	x	x	x	x	x	x	x	x
T	x	x	x	x	x	x	x	x	x
pH	x	x	x	x	x	x	x	x	x
FR	x	x	x	x	x	x	x	x	x
FRM		x		x			x	x	x
SF	x	x	x		x	x	x	x	x
P$_{tot}$	x	x	x	x	x	x	x	x	x
SP		x	x				x	x	x
WW	x	x	x	x	x	x	x	x	x
H$_2$S		x							x
Year	1995-1998	1995	1998	1995-2001	1999	1996-2000	2002	2004-2005	2009
Ref.	3	23	24	25	26	27	28	29	30

Appendix 4: Summary of the governing equations of experimental methods used in erosion-corrosion studies.

S/N	Method	Governing Equation		References
		Mass Transfer Coefficient	**Shear Stress**	
1.	Rotating Cylinder Electrode (RCE)	$k_m = \dfrac{0.0791 Re^{0.70} Sc^{0.356} D}{d}$	$\tau_{RCE} = 0.0791 Re^{-0.3} \rho . r_c^2 . \omega^2$	115
2.	Rotating Disc (RD)	$k_m = 0.62 D^{2/3} v^{-1/6} \omega^{1/2}$	$\tau_{RD} = 0.302 . v . Re^{0.5} \rho . \omega$	73
3.	Rotating Cage (RC)	-	$\tau_{RC} = 0.0791 Re^{-0.3} \rho . r_{RC}^2 . \omega^{2.3}$	73
4.	Flow Loop	$k_m = \dfrac{0.0165 Re^{0.86} Sc^{0.33} D}{d}$	$\tau_w = \dfrac{\Delta P}{4} . \dfrac{l}{d} = \dfrac{F \rho V^2}{2}$	40
5.	Jet Impingement	-	$\tau_w = 0.179 . \rho . V^2 . Re^{-0.182} \left(\dfrac{r}{r_o}\right)^{-2.0}$	41-43

where,

$Re = \dfrac{ul}{\mu}$, $h = \dfrac{k_m d}{D} = a Re^x Sc^y$, $x = 0.5 \ to \ 1$ and $y = 0.33$. Other terms have their usual meanings [73].

A comprehensive review of the range of validity of these methods with the governing equations is contained in ref. [73].

Corrosion rate (CR) can be calculated from shear stress as follows: $CR = a . \tau^b$

And from the mass transfer as follows: $CR \propto k_m \Delta C$

45

70

5.500

3.500

30

∅6.600

A

A

32

25

M3

24.500

M6

1.200

6.600

M6

SECTION A-A
SCALE 1 : 1

	NAME	DATE
DRAWN BY	J. Ukpai	04/07/11
CHECKED BY	Dr. X. Hu	
ENG APPR.		
MFG APPR.		
Q.A.		

MATERIAL: Nylon

UNLESS OTHERWISE SPECIFIED:
DIMENSIONS ARE IN MM
TOLERANCES: ±0.1

TITLE: Test Cell/Sample
Holder Design

SIZE **A** DWG. NO. Appendix 5 REV

SCALE: 1:1 WEIGHT: SHEET 1 OF 1